Dynamical Control of Many-Body Interactions in Driven Quantum Matter

Thesis by
Christopher Kai-Chen Yang

In Partial Fulfillment of the Requirements for the
Degree of
Doctor of Philosophy

CALIFORNIA INSTITUTE OF TECHNOLOGY
Pasadena, California

2025
Defended May 14th, 2025

Christopher Kai-Chen Yang
ORCID: 0000-0002-9462-9074

ACKNOWLEDGEMENTS

I would like to thank my advisor, Gil Refael, for his guidance and encouragement on this journey into the quantum world of electrons. Gil has a remarkable ability to explain quantum physics from a bird's eye view—without compromising on any precision or accuracy. From his unique perspective of the quantum world, Gil taught me to look further into the horizons of physics, identify the boundaries of our knowledge, and establish unlikely connections with seemingly distant research topics. Most importantly, Gil taught me that research was a responsibility in the greater context of things: a commitment to guide the broader scientific community—and the general public—with honest results rooted in a fundamental respect for scientific integrity.

Caltech's Bridge Hall of Physics is an inspiring place where numerous brilliant physicists have visited and worked over the years. I thank Jason Alicea, Lesik Motrunich, and David Hsieh for always encouraging me, sharing their wisdom during daily condensed matter lunch meetings, and providing me with concrete advice on my research. I've also had the great pleasure of working with former Caltech postdocs Cyprian Lewandowski, Iliya Esin, and Frederik Nathan.

Cyprian was my first postdoctoral mentor at Caltech. He always encouraged me to take the lead in meetings, even when he understood the research topics better than I did. He taught me how to navigate the academic world and build a network in the community. During my nearly annual trips to Tallahassee, Florida, Cyprian and his wife, Marilena, would invite me to their home for board games and dinner. I thank him for teaching me much of what I know about solid-state systems and for making my PhD journey possible. He is a true friend and mentor.

I feel deeply fortunate to have worked with Iliya over the past five years. I increasingly find that my approach to physics and research is influenced by Iliya's example as a scientist. From my perspective, Iliya's research abilities are analogous to conducting an orchestra—he has a remarkable intuition for what details of which components to tune and perfect, an effort that pays off when the components play together in a beautiful symphony. His commitment to scientific rigor complements his enthusiasm for quantum dynamics, which is always grounded in solid factual evidence. Iliya also taught me how to communicate science effectively, patiently leaving hundreds of suggestions on my early drafts and referee replies, even though

I knew it would've been easier for him to edit the paper directly. I am particularly grateful for his belief in me throughout my PhD—for reminding me to celebrate small progress and focus on putting forth solid results, even if they may not seem to lead anywhere at first. I thank him for teaching me how to produce quality work as a scientist.

Frederik has been an equally exceptional mentor. Despite living thousands of miles away and across multiple time zones, he involved me in his projects on Weyl semimetals, for which I am deeply grateful. Frederik has a remarkable ability to simplify complex results, and he'd often predict results that would typically require extensive calculations. His excitement for research is contagious, inspiring me to think visually about electronic physics.

I would also like to thank the condensed matter theory group at Caltech, including the members of the institute I've had the pleasure of knowing: Loly Ekmekjian, Liam O'Brien, Andrew Ivanov, Swati Chaudhary, Nandu Manoj, Sara Vanovac, Yue Liu, Yinan Chen, Stephen Naus, Valerio Peri, Étienne Lantagne-Hurtubise, Gal Shavit, Federica Surace, and others. The greatest gift they gave me was their genuine deep interest in my research.

Beyond Caltech, I feel grateful for the quantum experts with whom I've interacted. I remember, in particular, meeting Mikael Rechtsman during one of Caltech's colloquium lunches at the Athenaeum. Mikael asked me why I hadn't attempted to realize my theoretical work experimentally and offered some new angles to pursue. In retrospect, his encouragement played an important role at the start of my first theory-experiment collaboration a few years later.

Speaking of the experimental collaboration, I would like to thank Yijing Liu and the Paola Barbara and Nikolai Kalugin groups for the privilege of working with them on experimental Floquet physics. I met Yijing by chance at the APS exhibition hall in Minnesota in 2024, having previously attended his talk. The resulting collaboration has been a true delight. I am grateful to the Georgetown University and New Mexico Tech groups for giving me a real-world view of the quantum world. Paola has also been incredibly supportive of my postdoc and career endeavors.

Beyond quantum physics, I have many people to thank. I thank the DOE for its fellowship support during my PhD and for inspiring me early on through its internship program. I thank my early mentors—Robin Rehagen, Jay Salmonson, Christopher Young, and Aritoki Suzuki for teaching me how to become a researcher

and showing me the beauty of science on all length scales—from the galaxies in the skies to atoms at ultra-low temperatures. I also want to acknowledge my friends at Caltech, especially Jerry Zhang, who introduced me to photography. Without Jerry, I wouldn't have discovered the beauty of California and explored its stunning landscapes and wildlife. I am thankful to Jerry for the encouragement and laughter that helped me overcome the challenging aspects of my PhD. His kindness and generosity define what it means to be a genuine friend.

My parents have been the source of my strength and motivation. I thank my mom for packing my childhood days with every possible creative activity to spark my imagination. I thank her for sharing laughter and tears and ensuring I never weather the storms alone. She made great sacrifices for my career on the unconditional basis of love. I thank my dad for inspiring my interest in science. He shows his care for me in unique ways–taking me on bike trips, adding new accessories to my bike and car, and teaching me how to build and fix things. I thank my grandmother for taking care of every aspect of my life and for bravely coming to this country as a single mother. She could not speak much English, yet she navigated this country better than I ever could, working until age 77 and building a remarkable life and family for her children.

I thank Tzu Chi and Dharma Master Cheng Yen for shaping how I see the world and teaching me to hold love and care for others close to my heart. I thank Mr. Joe Wang and Mrs. Shiu-Yun Tsai for taking care of me just like their own child and inspiring me to go to Tijuana for charity missions. During my near-weekly trips to Tijuana with Tzu Chi, I've gotten to know children living in houses made of cardboard and styrofoam. It makes me reflect on how lucky I am and how challenges make us stronger. In both Floquet physics and Buddhism, periodicity appears as a common theme. It may not be possible to comprehend the periodicity if you stand on just one trough of the wave. Nevertheless, the gift of persistence gives you a new perspective, revealing remarkable phenomena that only emerge on long timescales.

ABSTRACT

Strongly driven Floquet systems have emerged as promising platforms for exotic non-equilibrium physics, but their instability to heating motivates practical questions about how Floquet engineering can be useful. Although drive-induced heating is often attributed to interactions, this thesis adopts a different perspective, identifying regimes where dissipative many-body dynamics can stabilize Floquet physics and define remarkable new drive-tunable properties. This principle enables highly tunable many-body steady states with minimal heating, leading to a novel regime where drive control over single-particle Floquet states can extend to many-body interactions. Our theoretical and experimental results in Parts II and III center around two themes. The first theme focuses on discovering controllable and stable many-body Floquet states. The second explores further into what the future holds—envisioning the prospects for unconventional Floquet physics with nontraditional driving fields and three-dimensional materials.

Part II of this thesis leverages kinematic constraints on low-dimensional many-body scattering as new principles for tuning and stabilizing Floquet phases. First, we predict that a circularly polarized laser can drive slow electrons of moiré systems into a subsonic regime where they decouple from the intrinsic 2D acoustic phonons of the system. This "slow-electron regime" enables optical control over the steady-state occupation of topological Floquet states and the resulting anomalous Hall conductivity. Second, we present experimental transport signatures of steady Floquet physics in graphene irradiated by a continuous-wave laser. Our experiment, performed at 3-4 K lattice temperatures with lasers off-resonant to optical phonons, creates electron-phonon scattering bottlenecks that stabilize persistent low-temperature phases with light-induced longitudinal transport characteristics. The long-lived many-body phase represents the first experimental signatures of steady Floquet physics in a metallic solid.

Part III presents emerging opportunities for many-body Floquet engineering beyond traditional optically-driven, low-dimensional materials. We first explore beyond-optical driving fields, revealing the emergence of quantized charge transport in 1D systems driven by coherent phonons. Incoherent phonons relax electrons into a topological spatiotemporal Floquet state with quantized group velocity set by the coherent phonon, realizing topological charge pumping in a highly non-adiabatic setting. Finally, we address the topological effects of time-periodic drives beyond

low-dimensional systems, revealing that THz-frequency, circularly polarized light can induce topological chiral plasmons in Weyl semimetals with band anisotropy, broken time-reversal symmetry, and broken inversion symmetry.

The theoretical and experimental work in this thesis represent key progress towards realizing persistent Floquet physics for diverse applications in quantum device engineering.

PUBLISHED CONTENT AND CONTRIBUTIONS

[1] Yijing Liu*, Christopher Yang*, Gabriel Gaertner, John Huckabee, Alexey V. Suslov, Gil Refael, Frederik Nathan, Cyprian Lewandowski, Luis E. F. Foa Torres, Iliya Esin, Paola Barbara, and Nikolai G. Kalugin. Signatures of floquet electronic steady states in graphene under continuous-wave mid-infrared irradiation. *Nature Communications*, 16(1), February 2025. ISSN 2041-1723. doi: 10.1038/s41467-025-57335-2. URL http://dx.doi.org/10.1038/s41467-025-57335-2.
*indicates equal contribution. C.K.Y. participated in the conception of the theory-experiment collaboration, carried out the steady-state Floquet simulations, and participated in the writing of the manuscript.

[2] Christopher Yang, Gil Refael, and Frederik Nathan. Chiral plasmons and topological photocurrent in weyl semimetals. *in preparation*. This work is in preparation. C.K.Y. participated in the conception of the project, carried out the analytical and numerical calculations, and participated in the writing of the manuscript.

[3] Christopher Yang, Iliya Esin, Cyprian Lewandowski, and Gil Refael. Optical control of slow topological electrons in moiré systems. *Phys. Rev. Lett.*, 131: 026901, Jul 2023. doi: 10.1103/PhysRevLett.131.026901. URL https://link.aps.org/doi/10.1103/PhysRevLett.131.026901.
C.K.Y. participated in the conception of the project, carried out the analytical and numerical calculations, and participated in the writing of the manuscript.

[4] Christopher Yang, Will Hunt, Gil Refael, and Iliya Esin. Quantized acoustoelectric floquet effect in quantum nanowires. *Phys. Rev. Lett.*, 133:226301, Nov 2024. doi: 10.1103/PhysRevLett.133.226301. URL https://link.aps.org/doi/10.1103/PhysRevLett.133.226301.
C.K.Y. participated in the conception of the project and the analytical and numerical calculations, and participated in the writing of the manuscript.

TABLE OF CONTENTS

Acknowledgements . . . iii
Abstract . . . vi
Published Content and Contributions . . . viii
Table of Contents . . . viii
List of Illustrations . . . xii
List of Tables . . . xxx

I Introduction 1
Chapter I: General Introduction . . . 2
Chapter II: Topology in Adiabatic Dynamics . . . 9
2.1 Adiabatic Evolution . . . 9
2.2 Berry Curvature and Chern Number . . . 10
2.3 Manifestations of Topology in Adiabatic Transport Dynamics . . . 12
2.4 Edge States and Topology in Graphene . . . 16
Chapter III: Coherent Dynamics and Topology of Floquet Systems . . . 19
3.1 Floquet Theory: Separating Stroboscopic Dynamics from Micromotion 20
3.2 Analytic Approximations to the Floquet Hamiltonian . . . 24
3.3 Numerical Approach: Frequency-Space Expansion . . . 27
3.4 Floquet Hamiltonian of Irradiated Graphene and Semiconducting Systems . . . 28
3.5 The Floquet Topological Insulator . . . 31
3.6 Topological Transport in Floquet Systems . . . 35
Chapter IV: Incoherent Dynamics of Floquet Systems . . . 37
4.1 Floquet-Boltzmann Equation . . . 38
4.2 Solving for the Steady State . . . 40
4.3 Survival of Floquet-Bloch States Under Continuous-Wave Driving . . 45

II Persistent Floquet Quantum Matter 48
Chapter V: Optical Control of Slow Topological Electrons in Moiré Systems . 49
5.1 Introduction . . . 49
5.2 The System . . . 50
5.3 Transport Properties . . . 52
5.4 Phenomenological Analysis . . . 53
5.5 Numerical Analysis . . . 55
5.6 Conclusion . . . 57
5.7 Acknowledgements . . . 58
Chapter A: Appendix . . . 59

A.1 Details of the Models . . . 59
A.2 Choice of Physical Parameters . . . 62
A.3 Anomalous Hall Conductivity Calculations for the Continuum Model 63
A.4 Direct Variation of the Phonon Speed c_{ph} . . . 64
A.5 Symmetries and Berry Curvature Distributions of the Toy and Continuum Models . . . 64
A.6 Full Phenomenological Model . . . 67
A.7 Formal Definition, Numerical Evaluation, and Phenomenological Model of $\mathcal{A}_{in}$ . . . 70
A.8 Predicting $\mathcal{E}^*$ for the Toy Model . . . 74
A.9 Different Frequencies . . . 77
A.10 Gap Sizes . . . 77
A.11 Floquet Boltzmann Equation . . . 78
A.12 Form Factor Details . . . 80
A.13 Validity of the Diagonal Density Matrix Approximation . . . 81
A.14 Dielectric Function of Strontium Titanate . . . 82
A.15 Monkhorst-Pack Grid, Numerical Integration, and Convergence . . . 83
A.16 Berry Curvature Calculations . . . 84
A.17 The Drive Amplitude Perturbative Regime at Different Twist Angles 85
Chapter VI: Signatures of Floquet Electronic Steady States in Graphene Under Continuous-Wave Mid-Infrared Irradiation . . . 86
6.1 Introduction . . . 86
6.2 Devices and photoconductive measurements . . . 88
6.3 Theory of Floquet Steady States . . . 89
6.4 Optically-controlled photoresponse . . . 91
6.5 Discussion . . . 94
6.6 Methods . . . 96
6.7 Acknowledgements . . . 97
Chapter B: Appendix . . . 99
B.1 Sample Irradiation with a Continous-Wave Mid-Infrared Laser Beam 99
B.2 Measurement Sequence . . . 100
B.3 Transmission property of ITO top gate for Mid-IR irradiation . . . 102
B.4 Cyclotron Resonance of the Top-Gated Epitaxial Graphene Samples . 103
B.5 Gate Efficiency Calibration . . . 104
B.6 Device Fabrication . . . 105
B.7 Characterization of Single-Particle Dynamics via Floquet States . . . 107
B.8 Steady State Simulations of Laser-Illuminated Graphene . . . 108
B.9 Transport in the Floquet Steady State . . . 110
B.10 Density of States and Berry Curvature Calculation . . . 112
B.11 Transverse Hall Voltage . . . 112
B.12 Reproducibility of the Results . . . 114
B.13 Effect of Hall contact misalignment on the transverse signal measured under illumination . . . 115
B.14 Linearity in the device response . . . 116
B.15 Chopper frequency dependence of the photoresponse . . . 116

B.16 Error Analysis . . . 117

III Floquet Physics Beyond Optical Drives and Beyond Low-Dimensional Systems 120

Chapter VII: Quantized Acoustoelectric Floquet Effect in Quantum Nanowires 121
7.1 Introduction . . . 121
7.2 Phonon-Driven Carbon Nanotube. . . . 123
7.3 Floquet-Boltzmann Equation. . . . 125
7.4 Phenomenological Rate Equation . . . 126
7.5 Numerical Analysis . . . 128
7.6 Acknowledgements . . . 130
Chapter C: Appendix . . . 131
C.1 Microscopic Details of the Carbon Nanotube . . . 131
C.2 Details of the coherent phonon drive . . . 133
C.3 Details on the Steady State Calculation . . . 137
C.4 Effective Description Using Lindblad Master Equation . . . 138
Chapter VIII: Chiral Plasmons and Topological Photocurrent in Weyl Semimetals . . . 145
8.1 Introduction . . . 145
8.2 System . . . 147
8.3 Origin of Topological Response . . . 147
8.4 Nonzero Filling . . . 148
8.5 Photoresponse of a Single WN . . . 149
8.6 Symmetry Constraints . . . 151
8.7 Numerical Verification . . . 152
8.8 Plasmon Enhancement . . . 153
8.9 Chiral Plasmons in WSMs with broken TRS . . . 154
8.10 Conclusions . . . 154
8.11 Acknowledgments . . . 155
Chapter D: Appendix . . . 156
D.1 Steady State Electronic Distribution . . . 157
D.2 Photoresponse of an Isolated, Untilted Weyl Node . . . 157
D.3 Consequences of Finite tilt . . . 165
Bibliography . . . 173

LIST OF ILLUSTRATIONS

Number *Page*

3.1 Schematic illustration of slow (stroboscopic-timescale) dynamics and fast (micromotion) dynamics of a Floquet system with a time-periodic Hamiltonian $H(t) = H(t+T)$. A system is initialized at time t_0 in the state $|\Psi(t_0)\rangle$. We compare the time-dependence of the expectation value of an operator $\hat{O}$ under evolution by the full time-dependent Schrodinger equation $|\Psi(t)\rangle = U(t,t_0)|\Psi(t_0)\rangle$ (orange curve), where $U(t,t_0) = \mathcal{T}\exp\left[-(i/\hbar)\int_{t_0}^{t} H(t')dt'\right]$, and under the effective time-independent Floquet Hamiltonian $|\tilde{\Psi}(t)\rangle = e^{iH_F(t-t_0)}|\Psi(t_0)\rangle$ (blue curve). The Floquet Hamiltonian H_F captures the slow course-grained dynamics of the system on timescales longer than the period of the drive T (see blue curve), while the full solution to the time-dependent Schrodinger equation captures the fast dynamics (micromotion) within each time period (see orange curve). The orange and blue curves agree at stroboscopic times given by t_0+nT, where $n \in \mathbb{Z}$, where $|\Psi(t_0+nT)\rangle = |\tilde{\Psi}(t_0+nT)\rangle$. Figure based on Ref. [290]. . . . 21

3.2 Floquet electronic bands of graphene irradiated by a circularly-polarized laser. (a) Energy spectrum of graphene as a function of k_x for fixed $k_y = 0$. (b) Quasienergy spectrum of graphene under circularly polarized laser irradiation, exhibiting an off-resonant Haldane gap of size Δ_K and a resonant gap of size Δ_R. 30

3.3 Pseudospin winding under circularly polarized irradiation. (a) Here we box in orange the $\alpha = -$ quasienergy band. (b) Plot of $\alpha = -$ quasienergy band vs. k_x and k_y. Red arrows indicate the orientation of the pseudospin $\hat{n}_{\boldsymbol{k}-}(0)$. We focus on the pseudospin along the rings sketched in green. (c) Pseudospin in the region $k < k_R$, which is roughly aligned with the $\hat{z}$-axis, with orientation set by the sign of the mass gap at $k = 0$. (d) Pseudospin along the resonance ring $k = k_R$. (e) Pseudospin in the region $k > k_R$, which approaches the equator, parameterized by $\hat{n}_{\boldsymbol{k}-}(0) = \hat{\boldsymbol{k}}$. 32

3.4 Path (red curve) traced out by the pseudospin $\hat{n}_{\boldsymbol{k}-}(0)$ upon variation across the resonance ring [see Figure 3.3(d)]. (a) The case of $\mathrm{sign}(\Delta_\xi \xi \eta) > 0$, in which case the pseudospin winds around the polar axis (sketched by a black line) 2 times. (b) The case of $\mathrm{sign}(\Delta_\xi \xi \eta) < 0$, in which case the pseudospin does not wind around the polar axis. 34

4.1 The quasienergy of the driven system is defined modulo $\hbar\omega$. In our discussion of the Floquet Boltzmann equation, it is convenient to consider two choices of the quasienergy bands. (a) The "folded" Floquet Brillouin Zone (FBZ) picture is analogous to the rotating frame in the rotating wave approximation, where states with band character corresponding to the valence band of the undriven system are shifted in energy by $+\hbar\Omega$. (b) The "unfolded" picture where the quasienergies are shifted such that quasienergy spectrum resembles the original bands, except with a gap opening at resonance. Dashed lines indicate $\pm\hbar\Omega/2$. 41

4.2 Sketch of "regular" electron-phonon and electron-electron scattering processes that do not rely on photoemission and photoabsorption to conserve energy and momentum. In the folded picture [panels (a) and (c)], these scattering processes only connect the same Floquet copies [i.e. states sketched with the same color]. When the processes are sketched on the unfolded bands [see panels (b) and (d)], it becomes clear that no photoabsorption or emission is required to conserve energy-momentum in the scattering processes. 42

4.3 Sketch of electron-phonon Floquet-Umklapp scattering processes that absorb or emit a single photon. In the folded picture [panel (a)], these scattering processes connect different Floquet copies [i.e., states sketched with different color]. When the processes are sketched on the unfolded bands [see panels (b-d)], it is clear that the scattering relies on an absorption or emission of a single photon (squiggly blue lines) to conserve energy and momentum. 43

4.4 Sketch of electron-electron Floquet-Umklapp scattering processes that absorb or emit a single photon, categorized as Floquet-Auger I and II which transfer a single or pair of electrons across distinct Floquet bands. We sketch the scattering processes in the folded picture in panels (a) and (c) and the unfolded picture in panels (b) and (d). In the unfolded picture, it is clear that the scattering relies on an absorption or emission of a single photon (squiggly blue lines) to conserve energy and momentum. 44

4.5 Sketch of an electron-electron collision process (green arrows) facilitating interband electronic scattering across the Floquet gap. 46

5.1 (a) Schematic experimental design. Circularly polarized laser induces non-trivial Berry-curvature in the narrow bands (see Figure 5.2(b-c)), resulting in an anomalous Hall conductivity σ_{xy}. TBG lies on top of a dielectric and metallic gate that screen electron-electron interactions. (b) Anomalous Hall conductivity vs. drive amplitude $\mathcal{E}$ for $\zeta \approx 0.5$ and various values of χ indicated on the scale (see below Eqs. 5.4 and 5.7 for definitions of ζ and χ). The σ_{xy} features a rapid drop with $\mathcal{E}$ below the critical amplitude $\mathcal{E}^*$ (dashed line). Here, $\mathcal{E}_0 = \hbar v_F/(eL_M^2) \approx 7.2 \times 10^4$ V/m. (c) Critical amplitude vs. $c_{\rm ph}/v^0_{\rm eff}$, where $v^0_{\rm eff} = v_{\rm eff}(0)$ is an effective electron velocity defined in the text. Enlarged red circle: $\mathcal{E}^*$ in (b). 50

5.2 (a) Zoom-in on schematic narrow bands in a moiré system. Drive with angular frequency Ω resonantly couples states along resonance rings (green curves). (b) Undriven spectrum of TBG along a line in the Brillouin Zone indicated by the orange curve in (c). Dashed frame encloses optically-active, narrow central bands $\nu = \pm 1$. (c) Berry curvature $\mathcal{B}^{(\xi)}_{\boldsymbol{k}+}$ in the upper Floquet band, with blue color intensity proportional to $\tanh\left(2\mathcal{B}^{(\xi)}_{\boldsymbol{k}+}/L_M^2\right)$ (color bar) so $\mathcal{B}^{(\xi)}_{\boldsymbol{k}+}$ peaks are more visible. Dashed lines indicate areas enclosing $\mathcal{B}^{(\xi)}_{\boldsymbol{k}+}$ peaks at the Dirac points and resonance ring. (d) Periodic quasienergy Floquet spectrum of the driven system, having two central bands shown in (a). The Floquet spectrum exhibits the upper (UFB, $\alpha = +$) and lower (LFB, $\alpha = -$) Floquet bands, separated by off-resonant gaps Δ_K at the Dirac K, K' points and a Rabi-like gap Δ_R along the resonance ring [130, 236, 239]. 51

5.3 (a) Schematics of the Floquet spectrum and one of the phonon light-cones originating from the area $\mathcal{S}_K$ in the UFB. The intersection between the UFB (LFB) and all cones centered in $\mathcal{S}_K$ form $\mathcal{S}_{\text{in}}$ ($\mathcal{S}_{\text{out}}$). As $\mathcal{E} \to \mathcal{E}^*$, the area of $\mathcal{S}_{\text{in}}$ vanishes. (b-d) Numerical verification of the phenomenological model. (b) Area of $\mathcal{S}_{\text{in}}$, $\mathcal{A}_{\text{in}}$, vs. $\mathcal{E}$ for three values of $c_{\text{ph}}/v^0_{\text{eff}}$. (c) Average occupation in $\mathcal{S}_K$. (d) Anomalous Hall conductivity σ_{xy} for same parameters as (b, c). At $\mathcal{E}^*$ (dashed lines), $\mathcal{A}_{\text{in}}$, $F^{(\xi)}_{K+}$, and σ_{xy} sharply change. 55

5.4 (a) Left column: steady-state occupation of the UFB when $\chi = \infty$ (calculated on a 163×163 momentum grid). Right column: steady-state occupation when $\chi = 0.24$ (calculated on a 73×73 momentum grid). Bottom row: strong-drive case ($\mathcal{E} = 4.3\mathcal{E}_0 > \mathcal{E}^*$). Top row: weak-drive case ($\mathcal{E} = 0.97\mathcal{E}_0 < \mathcal{E}^*$). Zoom-in boxes: the K, K' points have reduced occupation when $\mathcal{E} > \mathcal{E}^*$ relative to when $\mathcal{E} < \mathcal{E}^*$. (b) Visibility $\mathcal{V}$ vs. χ. (c) Value of χ for various ϵ and gate distances d. (d) Value of η for various ϵ and deformation potentials D, with $d = 4$ nm. Points in (b, d): parameters used in Figure 5.1(b). 57

A.1 (a) The quasienergy band structure of the toy model with for the parameters used in the main text. (b) The quasienergy band structure of the continuum model at valley $\xi = +1$. In both panels, the first Floquet Brillouin zone is shaded. See Section A.2 for details and justification for the parameters we have used. 61

A.2 (a) Left: the steady-state occupation of the lower Floquet band in valley $\xi = +1$ of the continuum model [25, 149]. Right: the Berry curvature of the same band, which peaks near the Dirac points and the resonance ring. (b) The anomalous Hall conductivity σ_{xy} as a function of drive strength $\mathcal{E}$. 64

A.3 Anomalous Hall conductivity of the toy model as a function of the ratio $c_{\text{ph}}/v^0_{\text{eff}}$ for three different drive field strengths $\mathcal{E}/\mathcal{E}_0$. The same electron-phonon decoupling process is visible as σ_{xy} plateaus. 65

A.4 Comparing the Berry curvature distribution in the upper Floquet band in the (a) continuum model and (b) toy model at a drive amplitude of $\mathcal{E}/\mathcal{E}_0 \approx 3.1$. 67

A.5 The occupation $F^{(\xi)}_{K+}$ as predicted by the phenomenological model in Section A.6 for different ratios $\chi \equiv \tau^{\mathrm{el}}_K/\tau^{\mathrm{ph}}_K$. Note that for large χ, the occupation is *lower* than the non-interacting case at weak drive amplitudes, an effect of reduced Pauli blocking in the electron-phonon interactions. 69

A.6 (a) The intersection $\mathcal{S}_K$ (Figure 3(a)) as viewed on the Brillouin zone. The outer radius along the path KR is $h_b(\mathcal{E})$. (b) Quasienergy (pink) along the path KR, with the phonon light cone (grey) that determines the *outer* radius of $\mathcal{A}_{\mathrm{in}}$. The intersections k_+ and k_- between the cone and the upper Floquet band determines $h_b(\mathcal{E}) = k_+ - k_-$. 72

A.7 (a) Width of the intersection $\mathcal{S}_K$, $w_b(\mathcal{E})$. (b) Circular coordinate system with arc length w (increasing counterclockwise) that we use to determine $w_b(\mathcal{E}) = w_+ - w_-$. 73

A.8 Comparing numerical evaluation of $\mathcal{E}^*$ (points) to an analytic fit to Eq. A.65. We use the same fitting parameters $f_2 = 0.778$, $f_1 = 0$, and $\delta(N) = 0.006$ for both panels. 75

A.9 Comparing the dependence of σ_{xy} on $\mathcal{E}$ for (a) the frequency considered in the main text and (b) a lower frequency where Floquet-Umklapp processes are stronger. Note that the frequency in panel (b) is inaccessible without generating two-photon resonances in the continuum model due to the peaked shape of the $\nu = \pm 1$ bands near the Γ point. 76

A.10 Comparison of the fitted Δ_R and predicted Δ_K in Equations A.72 and A.76 (solid lines) to those obtained from numerics (points), using $\hbar\Omega = 5$ meV in the toy model. Here, we fit Δ_R with factors of $f^R_1 = 0.04$ and $f^R_2 = 0.0184$ (see Eq. A.72). 77

A.11 Comparing the average toy and continuum model form factors $\mathcal{W}^{\xi\nu'\nu}_{\boldsymbol{k},\boldsymbol{q}+\boldsymbol{G}}$, with $|\boldsymbol{q}+\boldsymbol{G}|$ measured in units of 10^8 m^{-1}. (a-c) The intraband ($\nu = \nu'$) form factors at the K, M, and Γ points. (d-f) The interband ($\nu \neq \nu'$) form factors at the K, M, and Γ points. 80

A.12 The color represents the ratio $\hbar/(\tau^{\mathrm{tot}}_{\boldsymbol{k}}\Delta\varepsilon_{\boldsymbol{k}})$ at different points in momentum space (a) for the upper Floquet band and (b) for the lower Floquet band for the case $\chi \approx 2.8$ and $\zeta \approx 0.5$. 82

A.13 Convergence of anomalous conductivity with grid size for (a) $N(\mathrm{mod}\ 3) = 1$ and (b) $N(\mathrm{mod}\ 3) = 2$. Due to the positioning of grid points near the K point, the results at low grid resolutions show significant disagreement. 83

A.14 The requirement that the laser drive strength $\mathcal{E}$ is perturbative, i.e. a fraction of electron bandwidth $e\mathcal{E}L_M < W$, narrows the range of $\mathcal{E}$ values that can be used. As a result, the range of c_{ph} whose $\mathcal{E}^*$ is visible is limited as well - we postulate that they are pushed to higher drive strengths $\mathcal{E}$. 84

6.1 (a) Device layout with two contacts for longitudinal bias, V_{Bias}, and two contacts for measurements of the transverse voltage, V_y. The device has a square geometry with a 5-μm side and an indium tin oxide (ITO) top gate with an Al2O3 dielectric sublayer, for applying a gate voltage V_{Gate}. (b) Drive-modified Floquet bands of the graphene Dirac cone, which exhibits a Floquet gaps of size at the resonance energies $\varepsilon = \pm\hbar\Omega/2$, where $\hbar$ is the reduced Planck constant and Ω is the angular frequency of the laser. (c) Density of states of the Floquet bands calculated numerically for a circularly and linearly polarized laser of power density $P = 3\ \mathrm{mW}/\mu\mathrm{m}^2$. (d) Photo-induced change of source-drain current (ΔI) as a function of Fermi energy E_F for circularly and linearly polarized laser irradiation, as measured at a constant source-drain voltage of 6 mV. ΔI is measured with a lock-in amplifier using a chopper modulation as a reference. The circles represent data points and the solid lines are obtained by adjacent point averaging. The dotted lines mark the E_F values corresponding to $\pm\hbar\Omega/2$, with the related uncertainty indicated by the gray stripes. The uncertainty is attributed to the gate efficiency calibration and the detail is described in Appendix B. The dips in ΔI at energies $\pm\hbar\Omega/2$ are much broader than the Floquet gap Δ(see c) and arise from the non-equilibrium steady-state distribution of electrons. The measurements were performed on sample A at a cryostat temperature of ~ 3.5 K, laser photon energy of 117 meV, and laser power density of $1.1\ \mathrm{mW}/\mu\mathrm{m}^2$. 87

6.2 (a) Key scattering processes between the graphene K and K' valleys facilitated by photons (arrow 1), surface acoustic phonons (arrows 2, 3), and graphene acoustic phonons (arrow 4) that contribute to the steady state. (b) Steady state distribution (black solid curve) for $P = 1.9\ \mathrm{mW}/\mu\mathrm{m}^2$ and equilibrium distribution (blue dashed curve) of electrons at doping $E_F = 0$, where the longitudinal photoconductivity is enhanced relative to equilibrium. Here, ε denotes the quasienergy and $F_{k\alpha}$ denotes the electronic occupation. (c) Steady state distribution (black solid curve) of electrons at doping $E_F = 0.35\hbar\Omega$ and $P = 0.8\ \mathrm{mW}/\mu\mathrm{m}^2$, where the photoconductivity is suppressed relative to an equilibrium distribution expectation (blue dashed curve). (d) Same as (c) but for a larger power density $P = 1.9\ \mathrm{mW}/\mu\mathrm{m}^2$, where the steady state distribution exhibits additional electron density above the Floquet gap. e Steady state distribution (black solid curve) of electrons for $P = 1.9\ \mathrm{mW}/\mu\mathrm{m}^2$ at doping $E_F = 0.75\hbar\Omega$, where the photoconductivity is approximately identical to that of an equilibrium distribution (blue dashed curve), with a slightly raised effective temperature due to multi-photon heating processes. The horizontal dotted lines in (b–e) mark ε values corresponding to $\pm\hbar\Omega/2$. 90

6.3 (a) Photo-induced change of source-drain current (ΔI) as a function of E_F under irradiation at various peak power densities, as measured on sample C at a constant source-drain voltage of 6 mV and a cryostat temperature of 3.2 K. The photon energy is $\hbar\Omega$ = 117 meV. The laser beam is circularly polarized. The circles represent data points and the solid lines are the fitted curve by a Gaussian-like function described in the Methods. The dotted line marks the E_F value corresponding to $-\hbar\Omega/2$, with the related uncertainty indicated by the gray stripes. (b) Theoretically predicted ΔI as calculated from the Floquet Boltzmann equation. The dotted line marks the E_F value corresponding to $-\hbar\Omega/2$. (c) Depth a_0 of the photocurrent dip and associated error, as calculated from a Gaussian-like fit (see details in the Methods section). For both the theoretical and experimental data, a_0 decreases with the power density P for large P due to enhanced heating processes in the Floquet steady state. (d) Experimental and theoretical FWHM of the photocurrent dip and the Floquet gap size (red dotted line), Δ, as a function of the power density. The FWHM exceeds Δ, indicating the emergence of photoexcited electrons in the non-equilibrium Floquet steady state. The detailed error analysis of FWHM is described in Appendix B. The uncertainty in the laser power density due to power fluctuation in (c) and (d) are estimated by the change in the laser power before and after each transport measurement. 92

6.4 (a) Longitudinal photocurrent as a function of at a fixed source-drain voltage of 6 mV, with laser spot in focus and defocused. For all three curves, the laser power is ∼ 3.6 W, corresponding to a peak power density of 0.6 mW/μm^2 at focus. Under defocused irradiation, with the laser spot slightly moved to the side, the power density drops by ∼ 3 times (gray curves). Circular polarization of 10.6 μm wavelength laser radiation. The cryostat temperature stabilized at ∼ 3.4 K. b Theoretically calculated photocurrent for weak drives, exhibiting shallower dips near resonance as a function of decreasing driving power, in agreement with (a). (c) Temperature dependence of the longitudinal photocurrent as a function of E_F. The photocurrent decreases, and the dips at $E_F = \pm\hbar\Omega/2$ disappear at high temperatures. The laser beam is circularly polarized. (d) Theoretically calculated photocurrent for laser power density 1.4 mW/μm^2, the photocurrent dip becomes less visible at higher temperatures. The dotted lines in (a)–(d) mark the E_F value corresponding to $\pm\hbar\Omega/2$, where the related uncertainty is indicated by the gray stripes in (a) and (c). 93

B.1 Scheme of the sample illumination system. Schematic illustration of the optical setup used for delivering and focusing the mid-infrared irradiation. The beamsplitters are used only during the preliminary alignment of optical elements. The inset image shows the visible laser spot on the sample used for the preliminary alignment of the molybdenum mirrors and the ZnSe focusing lens. 99

B.2 Measurement sequence in time. Experimentally measured cryostat temperature (top panel) and longitudinal current (bottom panel) with laser blocked and unblocked intervals. Note that the actual graphene lattice temperature, $T(t)$, is expected to be further elevated relative to the cryostat temperature. When the laser is blocked, the sample cools down to $T_{\rm bg}$, giving rise to a strong bolometric effect in the longitudinal current. The laser illumination is blocked/unblocked in the optical path between the chopper and the sample (light coral stripes indicate when laser is unblocked), the average laser power density is 0.125 mW/μm^2 and the peak power density is 1.25 mW/μm^2, $\hbar\Omega$ = 117 meV (10.6 μm wavelength). 100

B.3 Laser intensity and temperature dependence of the longitudinal conductance. Gate voltage dependence of the source-drain current at different temperatures with laser blocked (gray) and under irradiation at the base temperature (red), with $P = 0.6$ mW/μm^2 and with source-drain voltage fixed at 50 mV. 101
B.4 Mid-Infrared transmission spectrum of ITO. Example of spectrum measured from our typical 110-nm thick ITO layer in the range around 10.6 μm wavelength (corresponding to the wavenumber 943 cm^{-1}). . 102
B.5 Longitudinal photoresponse vs. carrier density at different B fields. Longitudinal voltage photoresponse as a function of magnetic field and carrier density, under chopper-modulated irradiation with circular polarization, at a laser intensity of 20 μW/μm^2 and photon energy $\hbar\Omega = 117$ meV. The sample is biased at a fixed current I_x of 1 μA, and the photoinduced change in source-drain voltage ΔV_{xx} is measured with a lock-in amplifier. 103
B.6 Gate efficiency calibration. (a) (Black) Source-drain voltage and (blue) transverse voltage from the Hall effect measurements for $V_g = 7$ V and a constant bias (source-drain) current $I_{sd} = 1$ μA. The green and red lines are examples of the set of "4 points" used for extracting the actual transverse voltage. (b) (Black) Conductance at different gate voltages. (Blue) Carrier density at different V_g from Hall measurements. (Red) Linear fitting of carrier density at different V_g. 104
B.7 Scheme of key steps in top-gated graphene device fabrication. (a) Patterning of graphene Hall bars with a thin Pd/Au protection layer. (b) Optical image of the graphene devices prior to removing the metal protection layer and the top gate fabrication. (c) Illustration of top gate fabrication using Al_2O_3 as the dielectric layer and ITO as the gate contact. (d) Optical image of the top-gated devices. The dashed line marks the area of devices shown in (b). 107

B.8 Characteristics of the single-particle quasienergy spectrum. (a) Single-particle quasienergy bandgap ΔE_1 opening at $\varepsilon_{k\alpha} = \pm\hbar\Omega/2$, with $\varepsilon_{k\alpha} = 0$ corresponding to the Dirac point. The axes indicate the laser power density and photon energy. (b) Predicted light-induced modifications of the time-averaged density of states of graphene (see section J for definition) as a function of Fermi energy shift from the Dirac point for different power densities, with circular polarization (top) and linear polarization (bottom). Notice that the laser-induced gap at the Dirac point, which is a second-order process, is not resolved in the experiment for the chosen laser intensities. (See the main text for details.) The vertical dotted lines mark the E_F, value at $\pm\hbar\Omega/2$. . 109

B.9 Temperature dependence of the longitudinal conductivity at $E_F = 0$ without irradiation, which indicates charge puddle effects. 111

B.10 Transverse voltage response under different conditions. Transverse voltage as a function of E_F, under light irradiation ($\hbar\Omega = 117$ meV) with left-hand circular polarization. The dotted lines mark the values corresponding to $E_F = \pm\hbar\Omega/2$, with the related uncertainties indicated by the gray stripes. (a) Transverse voltage measured at different bias voltage values. The cryostat temperature is 3.1 K, and the laser beam is circularly polarized. (b) Transverse voltage measured under different irradiation power. The curves are vertically shifted for clarity. The cryostat temperature ranges from 3.0-3.3 K depending on laser intensity. The laser beam is circularly polarized. The circles represent data points, and the solid lines are obtained by adjacent point averaging. (c) Transverse voltage measured at different temperatures. For both (a) and (c), the laser intensity is 0.8 mW/μm^2 and for (b) and (c) the bias voltage is 50 mV. The measurements are from sample C. 113

B.11 Transverse voltage response under different conditions. (a) Transverse voltage as a function of E_F, under light irradiation ($\hbar\Omega$ = 117 meV) with different polarizations of the laser. (b) helicity-dependent Hall voltage in Sample A. (c) Hall conductivity in Sample A. Here, the laser intensity is 1.4 mW/μm^2, bias source-drain voltage is 6 mV, and cryostat temperature is 3.4 K. (d) Theoretically calculated Floquet Hall conductivity with nontrivial E_F-dependence arising from the tunable electronic steady state. The dotted lines in (a)-(d) mark the values corresponding to $E_F = \pm\hbar\Omega/2$, with the related uncertainties indicated by the gray stripes in (a)-(c). In (a)-(c), the circles represent data points, and the solid lines are obtained by adjacent point averaging. 114

B.12 Floquet signatures in the longitudinal photocurrent in additional devices. The dotted lines mark the E_F values corresponding to $\pm\hbar\Omega/2$, with the related uncertainty described by the gray stripes. (a) Longitudinal photocurrent as a function of E_F under different polarization illumination in sample B. Parameters: Laser power density 1.4 mW/μm^2 and bias voltage 6 mV. (b) Longitudinal photocurrent as a function of E_F, under different polarization illumination in sample C. Parameters: Laser power density 1.6 mW/μm^2, bias voltage 6 mV, and cryostat temperature 3.4 K. 115

B.13 Transverse voltage response in additional devices. Transverse voltage as a function of E_F, under irradiation with different polarizations in sample C [panel (a)] and the difference between the transverse voltage response from circular polarizations of the laser beam with opposite chirality extracted from the curves in panel (a) [see panel (b)], and upon reversing the source-drain bias V_{sd}. Laser power density 0.5 mW/μm^2, cryostat temperature 3.1 K. The dotted lines mark the E_F values corresponding to $\pm\hbar\Omega/2$, with the related uncertainty described by the gray stripes. 116

B.14 Effect of Hall contacts misalignment. (a) (Red) $V_{\text{Misalignment}}$ and (black) V_{sd} measured at the same source-drain current. Room temperature. (b) Misalignment contribution to the measured transverse voltage for (top) circular and (bottom) linear irradiation. Solid lines represent the transverse voltages measured by the lock-in amplifier; dotted lines represent the contribution resulting from misalignment in the Hall contacts. The experimental data from Figure B.11 are shown for reference. 117

B.15 Bias dependence of sample response. (a) I-V curve from sample C at different values of V_g. (b) Photo-induced current change ΔI as a function of bias voltage at different values of V_g. (c) Normalized longitudinal photoresponse ΔI as a function of E_F at different bias voltages, under circularly polarized irradiation, with a power density of 1.5 mW/μm^2. The curves are vertically shifted for clarity. The cryostat temperature is 3.4 K. The dotted lines mark the E_F values corresponding to $\pm\hbar\Omega/2$, with the related uncertainty described by the gray stripes. 118

B.16 Longitudinal photoresponse as a function of chopper frequency. Photo-induced current change measured in sample C under 1.5 mW/μm^2 of circularly polarized irradiation. The sample is biased at a fixed 6 mV. The cryostat temperature is 3.4 K. Error bars indicate the maximum deviation in the lock-in amplifier reading during the measurement. 119

7.1 (a) Schematic experimental setup. A THz-frequency coherent phonon wave (with atomic displacements sketched by orange arrows) of momentum q and angular frequency ω propagates from the phonon source on the right to the absorbing material on the left. A screening material of dielectric constant ϵ is placed below the CNT. Black sinusoid represents the coherent phonon potential. Electrons (black dots) generate quantized current $J = e\omega/\pi$ when confined to the troughs of the potential, achieved when incoherent phonon relaxation (ep) is much faster than electron-electron heating (ee). (b) Current J vs. Floquet gap $\Delta/\hbar\omega$ for different ϵ (see inset). Vertical line denotes $\Delta = \hbar\omega$. Inset: Δ^* vs. ϵ, where Δ^* is the minimal Floquet gap at which J is nearly quantized, set as $0.96e\omega/\pi$. (c) Band structure of a $(10, 0)$ armchair CNT. Inset: Fermi energy lies near the band bottom of the lowest positive-energy band, and the electronic density n_e is chosen to be commensurate to q. (d) Quasienergy spectrum of the driven system. Blue shading on the $\alpha = 0$ band indicates the optimal filling resulting in quantized current. Incoherent phonon scattering transitions (black arrows) relax electrons into the $\alpha = 0$ band. 122

7.2 (a) Floquet bands upon driving by a coherent phonon wave. Dashed light purple arrows (1-3): dominant electron-phonon intraband and cooling processes relaxing electrons into the $\alpha = 0$ band. Solid red arrows (4-5): electron-phonon heating processes exciting electrons into the $\alpha = 1$ band, which are kinematically suppressed when $\Delta \gg \delta\varepsilon$. (b) Pairs of zigzag and squiggly red arrows: electron-electron scattering exciting electrons into the $\alpha = 1$ band. Dashed light purple arrow: electron-phonon process relaxing excited electrons into $\mathcal{S}_+$. (c)-(e) Occupation F_i of the patch $\mathcal{S}_i$ for $i = +, -, 0$ [see panel (a)] vs Δ for various dielectric constants ϵ. Vertical lines: $\Delta = \Delta^*(\epsilon)$. Note $F_+ \to 0, F_- \to 1$ as $\Delta \to \Delta^*$, resulting in quantized current. 126

7.3 (a) Steady state occupation of the phonon-driven CNT for a weak phonon drive ($\Delta < \Delta^*$), dielectric constant $\epsilon = 80$, and optimal doping $n_e = q$. Inset shows excitations in the $\alpha = 1$ band near the Floquet gap. (b) Same as (a) but for a strong drive amplitude ($\Delta > \Delta^*$) where the occupation of the $\alpha = 1$ band is negligible, and the $\alpha = 0$ band is fully occupied. (c)-(d) Same as (b), but with two different electronic densities n_e away from optimal doping. (e) Steady state current vs n_e evaluated at $\Delta = 0.8\hbar\omega > \Delta^*$ for $\epsilon = 80$. 128

C.1 Phonon transfer mechanism when a phonon source (grey block) is placed under the right end of the carbon nanotube [see Figure 1(a) in the main text for the complete, proposed experimental setup]. A carbon atom of mass M_c (grey circle in magnified picture) experiences a Van der Waals force across the interface, with effective spring constant k. 135

C.2 The ratio ζ of the maximum interband scattering rate to the Floquet band energy separation vs. Floquet gap Δ for various dielectric constants ϵ. Note that $\zeta \ll 1$, so steady state coherences are suppressed. 139

C.3 Simplified model of the quantized acoustoelectric Floquet effect. The black curve represents the moving coherent phonon potential $V(x,t)$, and the grey dashed curve sketches the potential at a slightly later time. Electrons (green dots) generate quantized current when confined to the troughs of the potential, which is achieved when the incoherent phonon relaxation time $\tau_{\rm ep}$ is much faster than the heating time $\tau_{\rm h}$. . . 140

C.4 Steady state current J as calculated from the Lindblad master equation [Eq. (C.33)]. (a) Steady state current in the regime $\hbar/(\bar{\tau}\Delta) \ll 1$ analyzed in the main text using the Floquet Boltzmann equation. The current is quantized when the system is driven adiabatically, i.e., $\log(\hbar\omega/\Delta) < 0$. In the non-adiabatic regime $\log(\hbar\omega/\Delta) > 0$, the current attains a quantized value in the regime where incoherent phonon relaxation dominates $\tau_{\rm ep} \ll \tau_{\rm h}$. (b) Steady state current for a weak driving potential amplitude Δ satisfying $(\bar{\tau}\Delta)/\hbar = 0.3$. In contrast to panel (a), the current deviates from quantization in the adiabatic regime $\log(\hbar\omega/\Delta) < 0$, and instead only attains a quantized value when $\tau_{\rm ep} \ll \tau_{\rm h}$. 143

8.1 Light-induced charge pumping and chiral plasmons. (a) We consider the optical response of a noncentrosymmetric WSMs, where opposite-chirality Weyl nodes (WNs) can have distinct effective chemical potentials ($\mu_\pm$) and tilts ($\chi_\pm$). We show that circularly polarized driving in the near-adiabiatic regime can induce a topological charge pumping effect leading to a strong photocurrent $\bar{j}^z_\eta$ along the beam axis, where $\eta = \circlearrowleft, \circlearrowright$ denotes the helicity of the laser. (b) Numerically computed photocurrent, $\bar{j}^z_\circlearrowleft$, for $\mu_- = 15\,\mathrm{m}eV$, $\mu_+ = 30\ \mathrm{m}eV$, and $hf = 5$ meV, with $\chi_\pm = \pm\chi$. (c) Maximal $\bar{j}^z_\eta$, denoted $j^z_{\max}$, attained numerically (scatter points) and predicted semiclassically (dashed line) [Eq. (8.7)]. Discrepancies arise as hf is raised beyond the adiabatic limit. (d) Plasmon enhancement factor $G^\eta \equiv E/E_{\text{ext}}$ vs hf and E, where E_{ext} (E) denotes the drive-field amplitude outside (inside) the WSM. Dashed curve indicates plasmon resonance predicted semiclassically. (e) Same as (d), but for a WSM with broken TRS and a pair of WNs with opposite chirality and tilt. Here, the chiral plasmon resonance differs for left (left panel) and right (right panel) circular polarizations. 146

8.2 Topological photocurrent as quantized charge pumping. (a) Brillouin zone region (purple) surrounding a single WN (bright yellow) at $\mu = 0$. Under illumination by circularly polarized light, all electronic states with a given k_x and k_y (yellow vertical line) traces out a cylinder (pink) in momentum space during a period of the drive. This generates a quantized charge transfer per cycle along the z direction, given by $-e$ times the total flux of Berry curvature through the surface of the cylinder (differential area element indicated by dark purple). When the cylinder encloses the WN, this integral is nonzero and given by ± 1. (b) Total time-averaged current $\mathcal{I}^z_\circlearrowleft(\boldsymbol{k}_\perp)$ in the system generated by electrons with a fixed in-plane momentum $\boldsymbol{k}_\perp = (k_x, k_y)$. Left and right panels depict $v_F eA/\hbar \approx 5hf$ and $v_F eA/\hbar \approx 0.2hf$, respectively, corresponding to adiabatic and nonadiabatic driving. The dashed curve indicates the trajectory of the WN. 150

8.3 Photoresponse from doped and tilted WNs, with parameters $E = 1.5$ MV/m, $hf = 5$ meV and $\tau = 5$ ps, corresponding to $\tau f \approx 6$. (a) Photocurrent $\bar{j}^z_\eta$ vs. μ for an isolated, untilted WN. The orange curve indicates semiclassical prediction [see discussion below Eq. (8.6)]. (b)-(c) Photocurrent $\bar{j}^z_\eta$ from a pair of opposite-chirality WNs with opposite tilts, $\chi \equiv \chi_+ = -\chi_-$ under left (b) and right (c) laser polarization. In the limit $\chi \to 0$, the photoresponse is dominated by the chirality-dependent component generated by the anomalous velocity. (d) Chirality-independent component $\bar{j}^z_G = (\bar{j}^z_\circlearrowleft + \bar{j}^z_\circlearrowright)/2$ of $\bar{j}^z_\eta$. Dashed line indicates prediction from semiclassical analysis [Eq. (8.6)]. (e) Steady state occupation function $g_1(\boldsymbol{k}, 0)$ at time $t = 0$ in the $\nu = 1$ band, for the same parameters as panel (a). Black dot indicates the position of the WN, and vectors indicate the oscillating current components generated parallel $j_\parallel$ and perpendicular $j_\perp$ to the internal electric field $\boldsymbol{E}(t)$ and the resulting polarization $\boldsymbol{P}^\eta(t)$, along with induced field $\boldsymbol{E}_{\text{ind}}(t)$. 151

D.1 (a) Topological current produced by conduction band ($\nu = 1$) states in an isolated Weyl node, calculated by numerically integrating the semiclassical equations of motion [see Eq. (D.14)]. Here, $j_{\text{top}} = -ef(eA/\hbar)^2/(4\pi)$ denotes the topological current magnitude produced by a fully-occupied valence band [see Eq. (1) in the main text], and $x_F = \hbar k_F/(eA)$. (b) Log-scale plot of panel (a), with fits (solid lines) to the numerical data. 160

D.2 Illustration of the coordinate system used to calculate the saturation value of $j^z_{1,\eta}$ for $k_F \gg 2eA/\hbar$. Here, $\boldsymbol{k}' = \boldsymbol{k} + e\boldsymbol{A}(t)/\hbar$ is the shifted coordinate system, which fixes the WN at the origin. Purple sphere indicates the Fermi volume in the conduction band, which is centered at the WN (center white dot). Under illumination by circularly polarized light, populated electronic states with a given $\boldsymbol{k}_\perp = (k_x, k_y)$ traces out a cylinder $\mathcal{S}_t(\boldsymbol{k}_\perp)$ (dark purple) in momentum space during a period of the drive. Due to the finite Fermi momentum k_F, finite Berry curvature $\boldsymbol{\Omega}_1$ penetrates the "caps" $\mathcal{S}_t(\boldsymbol{k}_\perp)$ (light green) of the cylinder located at $k_z = \pm\sqrt{k_F^2 - |\boldsymbol{k}_\perp|^2}$. The Berry flux through the caps $\mathcal{S}_t(\boldsymbol{k}_\perp)$ produces a saturation value of $j^z_{1,\eta}$ in the limit $k_F \gg 2eA/\hbar$. 160

D.3 (a) Illustration of the characteristic in-plane momentum dynamics relevant for analyzing the photocurrent. Solid black circle indicates the edge of the instantaneous equilibrium Fermi volume of $H(\boldsymbol{k}, t)$ as a function of in-plane momentum, $\boldsymbol{k}_\perp = (k_x, k_y)$, for an arbitrary, fixed value of k_z. Black dot indicates the instantaneous location of the Weyl node, which is located at an azimuthal angle of $2\pi f t$ from the k_x axis (red arrow). We approximate the instantaneous equilibrium occupation $f_1^{\text{eq}}(\boldsymbol{k}, t)$ [Eq. (D.30)] to be given by 1 if $\boldsymbol{k}_\perp$ is located within the annulus segment (shaded blue) and between the two angles indicated by green lines, and 0 otherwise. (For the choice of $\boldsymbol{k}_\perp$ sketched in the figure, $\boldsymbol{k}_\perp$ is positioned such that $f_1^{\text{eq}}(\boldsymbol{k}, t) = 0$.) Such an approximation is accurate in the limit where the Fermi momentum k_F is much less than the vector potential $eA/\hbar$. (b) Occupation function $g_1(\boldsymbol{k}, t)$ as a function of the in-plane momentum magnitude $k_\perp = \sqrt{k_x^2 + k_y^2}$ in the slow relaxation time limit $\tau f \gg 1$, plotted for several values of the z-momentum k_z. 164

D.4 Origin of the laser helicity-independent photocurrent in a tilted WN. In the limit $\tau f \gg 1$, the steady state occupation of bands at any given time t is the time average of the instantaneous equilibrium occupation function $\theta(\varepsilon_{\boldsymbol{k}1}(t') - \mu)$ at all other times t'. The black solid and dashed gray curves represent the electronic bands at representative times t and t', respectively. The instantaneous equilibrium distribution at time t' (orange) preferentially fills states with $\partial \varepsilon_{\boldsymbol{k}1}(t)/\partial k_z < 0$, producing a net helicity-independent current. 169

LIST OF TABLES

Number *Page*

B.1 Fitting results of Hall measurements at different gate voltages 106

B.2 V_g corresponds to $E_F = \hbar\Omega/2$ 106

Part I

Introduction

Chapter 1

GENERAL INTRODUCTION

The length scales and timescales in the quantum and macroscopic worlds differ by many orders of magnitude, inspiring questions about how quantum degrees of freedom can be manipulated in a laboratory. Efforts to control quantum phenomena have set the stage for highly tunable platforms to study quantum information and matter. Time-periodic fields, in particular, offer versatile methods for controlling quantum systems, with wide-ranging applications across condensed matter physics. For example, ultra-low-frequency driving fields can unveil the adiabatic topological dynamics of quantum matter, such as the Thouless charge pumping effect [7, 29, 32, 47, 71, 82, 111, 126, 133, 154, 159, 173, 201, 201, 221, 234, 278, 279, 302]. Low-amplitude time-periodic fields can also serve as a probe of quantum phases by inducing perturbative responses through optical spectroscopy [53, 195, 303]. While these examples already illustrate some practical applications of time-periodic fields, this thesis primarily focuses on the strong and non-adiabatic driving regime far beyond linear response theory, where *Floquet engineering* can fundamentally design nonequilibrium quantum phases with exotic properties [15, 36, 45, 64, 74–76, 80, 81, 83, 99, 131, 140, 152, 165, 167, 169, 189, 214, 235, 239, 258, 260, 281, 291–294, 304].

Floquet-engineered systems exhibit dynamics that roughly separate into "micromotion" and "stroboscopic dynamics," with frequencies faster and slower than the driving frequency, respectively [216, 239, 241, 290]. Micromotion can underlie exotic magnetic properties [204], reveal anomalous Floquet topological phases [240], and be detected with high-resolution time-resolved probes [65]. On the other hand, the coarse-grained stroboscopic dynamics can be modeled by a time-independent *Floquet Hamiltonian* that captures the time-averaged dynamics of the system on timescales much longer than the driving period. The Floquet Hamiltonian could generally differ significantly from the Hamiltonian of the equilibrium system and even exhibit drive-induced topology [167, 215, 216]. Additionally, the Floquet Hamiltonian governs the low-frequency stroboscopic dynamics, allowing its properties to be probed with conventional DC or low-frequency measurements as long as the drive pulse duration is sufficiently long. These properties highlight a key motivation for pursuing Floquet engineering: the Floquet Hamiltonian behaves like

a tunable static Hamiltonian, with potentially exotic phases that can be manipulated in situ.

Despite the promising opportunities for Floquet engineering to control and manipulate quantum matter, the statistical mechanics of Floquet systems is a challenging problem that poses several issues [195, 196]. First, experimental observables depend not just on the single-particle electronic dynamics governed by the Floquet Hamiltonian but also on how the Floquet states are populated. In particular, the chemical potential of Floquet systems is ill-defined because Floquet states are coherent superpositions of distinct energy levels, potentially above and below the chemical potential of the equilibrium system [74, 76, 196, 239, 257, 258]. The resulting highly-nonequilibrium distribution of electrons are also susceptible to absorption of energy from the driving field, facilitated by electronic interactions, that could heat the distribution to a high-temperature state [54, 138, 158]. Lastly, in any heated system, incoherent scattering processes facilitated by electron-phonon and electron-electron scattering are also enhanced, drawing questions about whether Floquet states can remain coherent in the presence of rapid incoherent scattering processes [6, 257, 258]. These problems have become such a concern that the uncontrolled heating of Floquet systems is sometimes referred to as the "heat death" of Floquet physics [238].

The field of Floquet engineering has introduced several potential solutions to stabilize low-temperature driven phases. The umbrella term for these solutions is sometimes called the "non-thermal pathway" to Floquet engineering, which manipulates quantum properties not through heating but by accessing and controlling low-temperature degrees of freedom through coherent coupling to the driving field [59]. One promising opportunity for non-thermal Floquet engineering is to drive systems with ultra high-frequencies, which can produce a long-lived, low-temperature Floquet phase known as the Floquet pre-thermal state [1, 3, 4, 155, 223]. On the other hand, ultrafast laser pulses with frequencies resonant with the level spacing of the system can also produce transient Floquet effects at high driving intensities while minimizing heating due to its short pulse duration [143, 174, 185, 187, 260, 263, 301, 329].

In this thesis, we seek to use the intrinsic coupling of low-dimensional Floquet solid-state systems to their surrounding environment—the phonons in the lattice and the screening from surrounding dielectrics—as a primary mechanism for stabilizing low-temperature Floquet physics under continuous-wave (CW) driving. The

dissipation of energy to a low-temperature bath of phonons, combined with the CW driving, leads electrons to relax into a steady-state electronic distribution with stable transport effects. Furthermore, we show that Pauli blocking in the steady state can suppress scattering rates between Floquet states, enabling Floquet states to remain coherent even with driving amplitudes much weaker than those used in ultrashort-pulsed laser experiments. Our theoretical and experimental results provide key principles to realize Floquet physics in CW-driven solid-state systems and *enhance* their controllability with many-body interactions.

This thesis is organized as follows. Part I reviews Floquet engineering and the incoherent dynamics of Floquet systems. In Chapter 2, we provide an overview of the connection between topology in solid-state quantum systems and its response to adiabatic driving fields. The topological adiabatic dynamics inspire questions about whether similar universal topological signatures of quantum matter can also emerge when the driving source is non-adiabatic. In Chapter 3, we relax the assumptions of adiabaticity by introducing Floquet theory, which describes the quantum dynamics of systems driven by time-periodic fields. We discuss the emergence of fast micromotion and slow stroboscopic dynamics in Floquet systems and introduce the time-independent Floquet Hamiltonian to model the stroboscopic dynamics. We derive the effective Floquet Hamiltonian for gapless systems such as graphene and semiconducting systems such as TMDs, characterize the topology of the Floquet Hamiltonian, and discuss how its band geometry can be probed through transport measurements. In Chapter 4, we discuss the effects of weak many-body interactions in Floquet systems and introduce the Floquet-Boltzmann equation.

The remainder of the thesis, Parts II and III, are centered around two key themes.

Part II: Tunability and Stability of Many-Body Floquet Topological Phases

Part II of this thesis presents theoretical and experimental results centered around two primary goals. The first objective is to optically control many-body interactions in Floquet systems, and the second is to stabilize Floquet physics on long timescales by leveraging dissipative dynamics.

Optical Control of Many-Body Interactions

To understand how periodic drives can manipulate many-body interactions, it is helpful to review how optical drives can control single-particle electronic physics. A notable example of this is drive-induced topology in Floquet systems. In 2009, Takashi Oka and Hideo Aoki predicted that monolayer graphene systems irradiated

by a circularly polarized laser drive could be described by an effective Floquet Hamiltonian with a topological *Haldane gap* and a drive-induced DC anomalous Hall conductivity [215]. This drive-induced Haldane gap was a first demonstration of an *off-resonant* topological Floquet gap—where the gap opening (centered at the zero-energy Dirac point between the conduction and valence bands) was energetically far-separated from the single-photon resonance in the bands. In 2011, Netanel Lindner, Gil Refael, and Victor Galitski noticed that nontrivial band topology could also be induced in trivial bands by *resonantly-driving* the bands with a laser field [167]. The drive-induced topological system was named the "Floquet topological insulator" (FTIs). Further work formalized the topological characterization of Floquet states and elucidated its transport properties [139, 152]. Importantly, these works presented Floquet engineering as a novel method to optically control single-particle electronic physics on demand.

While the single-particle dynamics of Floquet systems already present remarkable opportunities to engineer new quantum matter, an accurate modeling of Floquet systems must also consider many-body interactions. In driven quantum matter, many-body collisions only conserve energy up to an integer multiple of the driving frequency, enabling a dramatically different population distribution from equilibrium. In 2015, Seetharam et al. inroduced a microscopic modeling of many-body interactions in optically-driven semiconducting systems through the Floquet Boltzmann equation (FBE) approach [257, 258], which built on previous theoretical works studying interacting driven open quantum systems [90, 144]. The FBE leveraged Fermi's golden rule for driven states to microscopically model perturbative many-body collisions. Crucially, it demonstrated that low-temperature *steady states* under continuous-wave irradiation could be induced by coupling the Floquet system to a low-temperature bosonic bath and suppressing heating processes via external leads. Further work by Esin et al. [74–76, 78] elucidated how many-body interactions in Floquet systems could be engineered to produce finite, and even quantized, topological transport characteristics and symmetry broken phases. Overall, these groundbreaking examples extended optical control over single-particle dynamics in continuously-driven Floquet systems to many-body interactions.

This thesis seeks to leverage many-body interactions in low-dimensional systems as new principles for controlling Floquet topological insulators. Previous works that analyzed Floquet systems with the FBE (mentioned above) considered low-dimensional systems coupled to 3D phononic baths, where energy-momentum

constraints on electron-phonon scattering were relaxed. Chapter 5 of this thesis considers a new regime where phonons and electrons are both low-dimensional. Here, kinematic bottlenecks on electron-phonon scattering are highly constrained in phase space and can become highly sensitive to driving parameters. We identify a tunable kinematic constraint uniquely possible in moiré materials, where electronic and phononic speeds are comparable. In particular, we show that variations in the laser amplitude can drive Floquet states into a slow regime where their group velocity is subsonic to acoustic phonons, weakening electron-phonon coupling. In this regime, the drive-induced topological transport signatures are sharply modified, providing a novel example of optically-controllable topological electronic physics.

Stabilizing Persistent Floquet Physics

Having discussed theoretical proposals for Floquet topological insulators, we now discuss the experimental feasibility of Floquet engineering. Most experimental realizations of Floquet physics in solid-state systems thus far have utilized ultrafast lasers with pulse times in the range of femto to picoseconds to limit the effect of heating and leverage the intense laser amplitudes achievable by ultrafast laser sources. Notably, Floquet modifications to the single-particle electronic bandstructure have been confirmed by ARPES experiments [174, 187, 301, 329]. ARPES experiments have also offered some insights into the stability of Floquet states under many-body scattering in solid-state systems, establishing that large Floquet gaps, combined with low lattice temperatures, could be a necessity for Floquet-Bloch states to survive in the presence of the scattering of photoexcited carriers [6]. While ARPES experiments have provided direct probes of the hallmark Floquet bandstructure of periodically-driven systems, the signatures of Floquet bands have also been detected through optical signatures such as second-harmonic generation [260] and transport experiments such as the light-induced anomalous Hall effect in graphene [185].

Ultrafast laser experiments have been remarkably successful in producing transient Floquet effects, but stabilizing long-living signatures of Floquet physics in solids remains a long-sought goal. A truly continuous-wave (CW) irradiated Floquet system could increase the accessibility of Floquet effects and extend its tunability and utility. However, the heating and stability of continuously-driven Floquet systems seem to pose serious problems to its experimental realization. In this thesis, we seek to understand what experimental considerations are necessary to leverage dissipation dynamics to stabilize CW irradiated Floquet systems. Chapter 6 presents the first experimental signatures of Floquet steady states in a CW irradiated solid-state

metallic system. The frequency of the drive and temperature of the lattice were deliberately chosen to maintain low-temperature phonons, providing principles for cooling the system to a low-temperature steady state. We show that the longitudinal transport signatures are consistent with the predictions of the Floquet-Boltzmann equation and that Pauli blocking in the steady state can preserve the coherence of Floquet-Bloch states in the presence of scattering.

Part III: Floquet Topological Physics Beyond Optical Driving Fields and Low-Dimensional Systems

While Part II of this thesis primarily addresses the stability and topological characteristics of low-dimensional driven systems under continuous optical driving, Part III of this thesis seeks to extend persistent topological Floquet physics to (i) beyond-optical drives and (ii) 3D systems.

The intense theoretical and experimental research on Floquet engineering has motivated new efforts to realize Floquet physics with novel driving sources, such as angular-momentum carrying light [8, 137], spatially-patterned light fields [255], multi-tone laser drives [180, 205], and spatiotemporal drives such as coherent phonon lasers [77, 224]. The remarkable topological signatures of these effects extend far beyond the predictions of Floquet topological physics driven by single-tone optical lasers. For example, a simultaneous application of incommensurate driving frequencies can produce the topological frequency conversion effect [180, 205]. Coherent phonon lasers, which transfer both *energy* and *momentum*, can also produce exotic topological bands with spatiotemporal symmetries [40, 91, 114, 224].

A notable new category of driving sources consists of high-frequency coherent phonon sources in the THz range. Historically, coherent phonon sources have been limited to ultra-low frequencies around the MHz or GHz range. While MHz and GHz frequency phonon sources are suitable for producing adiabatic dynamics, the more recent emergence of THz-frequency phonon sources offers exciting potential for Floquet engineering. These THz-frequency coherent phonon waves can be generated optically, by directly driving an IR-active phonon mode [68], by excitation of electrons that produce coherent phonons through electron-phonon coupling [67, 274, 317], or by biasing metals to produce the acoustic Cerenkov [10, 151, 213, 327], Klein-Zehner [5, 104], or phaser effect [77]. Chapter 7 of this thesis establishes new Floquet engineering applications for these high-frequency coherent phonon laser sources. In particular, we introduce a new type of Floquet phase with quantized

transport driven by THz-frequency coherent phonons. We use Floquet-Boltzmann theory to show that incoherent phonon dissipation in the system can relax electrons into a topological spatiotemporal Floquet band with a quantized group velocity. The resulting topological charge pumping effect remains remarkably robust in a highly non-adiabatic regime, producing currents orders of magnitude stronger than those in an adiabatic Thouless pump setup [7, 29, 32, 47, 71, 82, 111, 159, 201, 201, 278, 279].

Finally, Chapter 8 discusses the emergence of topological plasmons and photocurrents in Weyl semimetals irradiated by THz-frequency circularly-polarized lasers. In contrast with the works in other chapters of this thesis, the phenomenon is adiabatic in nature, but importantly highlights the interplay between time-periodic driving fields and transport phenomena beyond low-dimensional systems.

In summary, this thesis presents key progress towards realizing persistent Floquet physics with optical and beyond-optical driving fields, addressing critical questions about the role of many-body interactions in the stability and tunability of Floquet quantum matter.

Chapter 2

TOPOLOGY IN ADIABATIC DYNAMICS

We begin by reviewing some of the earliest demonstrations of topology in solid-state systems. These examples establish the intricate connection between topology and the adiabatic evolution of quantum systems. Section 2.1 defines when the dynamics of a time-dependent Hamiltonian can be classified as adiabatic. Section 2.2 reveals the connection between adiabatic electronic dynamics, Berry curvature, and topology. Section 2.3 derives explicit relations between the Berry curvature and electronic transport dynamics. Finally, Section 2.4 closes with discussions of the topology of 2-level systems and edge states, all of which will be extended to Floquet topological systems in Chapter 3.

2.1 Adiabatic Evolution

The following section is based on Refs. [97, 287, 307, 330].

In this section, we model the adiabatic evolution of quantum systems and define the adiabatic condition.

To study the dynamics produced by a time-dependent Hamiltonian, we consider a Hamiltonian $H_{\lambda(t)}$ parameterized by a time-dependent vector of parameters, $\boldsymbol{\lambda}(t)$. By diagonalizing the *instantaneous* Hamiltonian at each time t, we obtain the instantaneous eigenstates $|n_{\lambda(t)}\rangle$ and eigenenergies $E^n_{\lambda(t)}$, which satisfy the eigenvalue relation

$$H_{\lambda(t)}|n_{\lambda(t)}\rangle = E^n_{\lambda(t)}|n_{\lambda(t)}\rangle, \tag{2.1}$$

where n indexes the eigenstates. In our analysis, we assume that the instantaneous eigenenergies are non-degenerate at all times. To find the solutions to the time-dependent Schrodinger equation, given by

$$i\hbar\partial_t|\Psi(t)\rangle = H_{\lambda(t)}|\Psi(t)\rangle, \tag{2.2}$$

we expand the solution $|\Psi(t)\rangle$ in terms of the instantaneous eigenstates:

$$|\Psi(t)\rangle = \sum_n c_m(t)e^{\frac{i}{\hbar}\int_0^t E^m_{\lambda(t')}dt'}|n_{\lambda(t)}\rangle, \tag{2.3}$$

where the form of the coefficients $c_m(t)$ is chosen for convenience. The Schrodinger equation, Eq. (2.2), can now be written as a matrix equation in terms of the

coefficients $c_n(t)$, described by the rate equations

$$\partial_t c_m(t) = -\sum_n \langle m_{\lambda(t)}|\partial_t n_{\lambda(t)}\rangle c_n(t) e^{\frac{i}{\hbar}\int_0^t (E^m_{\lambda(t')} - E^n_{\lambda(t')})dt'}. \tag{2.4}$$

Eq. (2.4) indicates that the time-dependence of the Hamiltonian generates transitions between distinct pairs of eigenstates $|n_{\lambda(t)}\rangle$ and $|m_{\lambda(t)}\rangle$, with a transition rate of magnitude $|\langle m_{\lambda(t)}|\partial_t n_{\lambda(t)}\rangle c_n(t)|$.

We will now prove that the probability of tunneling transitions is suppressed if the parameters $\boldsymbol{\lambda}(t)$ are varied slowly. To simplify the analysis, we consider the time evolution of a system initialized at time $t = 0$ in the n-th eigenstate of the instantaneous Hamiltonian, i.e., $|\Psi(0)\rangle = |n_{\lambda(0)}\rangle$. We focus on a regime where $\boldsymbol{\lambda}(t)$ is varied slowly such that $\langle m_{\lambda(t)}|\partial_t n_{\lambda(t)}\rangle$ and $c_m(t)$ vary with frequencies much slower than the level spacing $(E^m_{\lambda(t)} - E^n_{\lambda(t)})/\hbar$ between eigenstates of the instantaneous Hamiltonian. In this limit, Eq. (2.4) can be integrated by parts to obtain

$$c_m(t) \approx -i\hbar \frac{\langle m_{\lambda(t)}|\partial_t n_{\lambda(t)}\rangle}{E^m_{\lambda(t')} - E^n_{\lambda(t')}} e^{\int_0^t (E^m_{\lambda(t')} - E^n_{\lambda(t')})dt'} c_n(t) \tag{2.5}$$

for $n \neq m$. The solution to the time-dependent Schrodinger equation can therefore be written as

$$|\Psi(t)\rangle \propto |n_{\lambda(t)}\rangle - i\hbar \sum_{m\neq n} \frac{\langle m_{\lambda(t)}|\partial_t n_{\lambda(t)}\rangle}{E^m_{\lambda(t')} - E^n_{\lambda(t')}} |m_{\lambda(t)}\rangle, \tag{2.6}$$

where we have dropped the normalization factor for clarity.

The *adiabatic limit* is realized when $\boldsymbol{\lambda}(t)$ varies sufficiently slowly that the second term in Eq. (2.6) is negligible, and $|\Psi(t)\rangle \propto |n_{\lambda(t)}\rangle$ at all times. To quantify the adiabatic limit, we note that differentiation of Eq. (2.1) yields

$$\langle m_{\lambda(t)}|\partial_t n_{\lambda(t)}\rangle = \frac{\langle m_{\lambda(t)}|\partial_t H_{\lambda(t)}|n_{\lambda(t)}\rangle}{E^n_{\lambda(t)} - E^m_{\lambda(t)}}. \tag{2.7}$$

Upon substitution into Eq. (2.6), we find that the adiabatic condition is given by

$$|\langle m_{\lambda(t)}|\hbar\partial_t H_{\lambda(t)}|n_{\lambda(t)}\rangle| \ll (E^n_{\lambda(t)} - E^m_{\lambda(t)})^2. \tag{2.8}$$

2.2 Berry Curvature and Chern Number

The following section is based on Refs. [307].

As we showed in Section 2.1, an adiabatically-evolved system initialized in an instantaneous eigenstate of the Hamiltonian remains in the eigenstate at all times, satisfying $|\Psi(t)\rangle \propto |n_{\lambda(t)}\rangle$. However, the state vector $|\Psi(t)\rangle$ can acquire a nontrivial

modulus-1 phase factor during the evolution. To restore the phase factor, we note that the matrix equation given in Eq. (2.4) contains only one nonzero element in the adiabatic limit, $\partial_t c_n(t) = -\langle n_{\lambda(t)}|\partial_t n_{\lambda(t)}\rangle c_n(t)$. The solution to this equation is given by

$$|\Psi(t)\rangle = e^{i\gamma_n(t)}|n_{\lambda(t)}\rangle, \tag{2.9}$$

where $\gamma_n(t) = i\int_0^t \langle n_{\lambda(t')}|\partial_t n_{\lambda(t')}\rangle dt'$. This phase $\gamma_n(t)$ can be expressed in terms of the *Berry connection*,

$$\boldsymbol{A}_n(\boldsymbol{\lambda}) = \langle n_{\lambda(t)}|\nabla_\lambda|n_{\lambda(t)}\rangle, \tag{2.10}$$

using the relation

$$\gamma_n = i\int_C \boldsymbol{A}_n(\boldsymbol{\lambda})\cdot d\boldsymbol{\lambda}, \tag{2.11}$$

where C defines the path traced out by $\boldsymbol{\lambda}(t)$ as a function of time. Furthermore, if C is a *closed loop* in 3D parameter space, then $\gamma_n(t)$ is called the *Berry phase*. For such a closed path, C encloses a closed surface, denoted $\mathcal{S}$, and Stokes' theorem implies that

$$\gamma_n = \int_{\mathcal{S}} \boldsymbol{\Omega}_{\lambda n}\cdot d\boldsymbol{S}, \tag{2.12}$$

where $d\boldsymbol{S}$ is a differential area element on the surface $\mathcal{S}$, and

$$\boldsymbol{\Omega}_{\lambda n} = \nabla_\lambda \times \boldsymbol{A}_n(\boldsymbol{\lambda}) = i\langle\nabla_\lambda n_{\lambda(t)}|\times|\nabla_\lambda n_{\lambda(t)}\rangle \tag{2.13}$$

is the *Berry curvature*. A special case worth noting is that of a *closed* surface $\mathcal{S}$, where $e^{i\gamma_n(t)}$ is singled value, so $\gamma_n = 2\pi C$, and $C \in \mathbb{Z}$ is known as the Chern number.

Example: two-level system. Throughout this thesis, we will primarily focus on the dynamics and topological properties of low-temperature quantum matter, whose electronic physics can often be captured by a two-level Hamiltonian. In its most generic form, the Hamiltonian for a 2-level system is given by $H = \boldsymbol{d}\cdot\boldsymbol{\sigma}$, where $\boldsymbol{\sigma} = (\sigma_x, \sigma_y, \sigma_z)$ is the vector of Pauli matrices and $\boldsymbol{d}$ is parameterized by three variables, θ, ϕ, and r as follows:

$$\boldsymbol{d} = r(\cos\theta\cos\phi, \cos\theta\sin\phi, \sin\theta). \tag{2.14}$$

The eigenstates of the Hamiltonian are given by

$$|\psi_0\rangle = \begin{pmatrix} -e^{-i\phi}\sin(\theta/2) \\ \cos(\theta/2)\end{pmatrix} \quad \text{and} \quad |\psi_1\rangle = \begin{pmatrix} e^{-i\phi}\cos(\theta/2) \\ \sin(\theta/2)\end{pmatrix}, \tag{2.15}$$

with eigenenergies $E_0 = -r$ and $E_1 = r$, respectively. In the cartesian coordinates defined by $x = r\cos\theta\cos\phi$, $y = r\cos\theta\sin\phi$, and $z = r\sin\theta$, explicit calculation yields the Berry curvature given by

$$\boldsymbol{\Omega}_{\boldsymbol{d}n} = i\langle\nabla_{\boldsymbol{d}}\psi_n| \times |\nabla_{\boldsymbol{d}}\psi_n\rangle = (-1)^n \frac{\boldsymbol{d}}{|\boldsymbol{d}|^3}. \tag{2.16}$$

where $n = 0, 1$ indexes the eigenstates $|\psi_n\rangle$. The Chern number of the system emerges when considering the Berry curvature along a closed surface $\mathcal{S}$ in parameter space, which is quantized with an integer value given by

$$C_n = \frac{1}{2\pi} \oint_{\mathcal{S}} \boldsymbol{\Omega}_{\boldsymbol{d}n} \cdot d\boldsymbol{S}, \tag{2.17}$$

where $d\boldsymbol{S}$ is a differential element on the surface $\mathcal{S}$. To prove the quantization of C_n, note that $\nabla_{\boldsymbol{d}}\boldsymbol{\Omega}_{\boldsymbol{d}n} = (-1)^n\delta(\boldsymbol{d})$, where $\delta(\boldsymbol{d})$ is the Dirac-Delta function. Therefore, applying the divergence theorem yields $C_n = (-1)^n$ if $\mathcal{S}$ encloses the origin $\boldsymbol{d} = 0$, and $C_n = 0$ otherwise.

2.3 Manifestations of Topology in Adiabatic Transport Dynamics

The Berry curvature can be detected in systems evolving adiabatically in time, producing robust topological transport signatures in electronic systems. Below, we provide two examples.

Thouless Pumping in a Slow-Moving Turnstile

The following section is based on Ref. [232].

The Thouless pump provides a simple example of topological transport in a 1D system. The system consists of electrons in a slowly-propagating wave potential, described by the Hamiltonian

$$\hat{H} = \frac{\hbar^2\hat{k}^2}{2m} + 2V\cos\big(qx - \omega t\big), \tag{2.18}$$

where $\hat{k} = -i\partial_x$ is the momentum operator, m is the mass of the electron, V is the energy scale of the potential wave, $1/q$ is the wavelength of the wave, and ω is its frequency. Because the moving wave potential is periodic in space, the electronic band structure can be folded into a Brillouin zone covering the crystal momenta $k \in [0, q]$. We will focus on the effective Hamiltonian of the system surrounding $q/2$, given by

$$H_{\text{eff}} = \begin{pmatrix} \frac{1}{2m}\left(\frac{q}{2} + k\right)^2 & Ve^{-i\omega t} \\ Ve^{i\omega t} & \frac{1}{2m}\left(-\frac{q}{2} + k\right)^2 \end{pmatrix}. \tag{2.19}$$

Up to a constant energy offset, H_{eff} can be expressed in the form $H_{\text{eff}} = \boldsymbol{d}\cdot\boldsymbol{\sigma}$, with $\boldsymbol{d}$ given in Eq. (2.14) and $r = \sqrt{(kq/2m)^2 + V^2}$, $\cos\theta = (kq/2m)/\sqrt{(kq/2m)^2 + V^2}$ and $\phi = \omega t$. The Hamiltonian has two instantaneous eigenstates, given by

$$|\psi_-\rangle = \begin{pmatrix} -e^{-i\phi}\sin(\theta/2) \\ \cos(\theta/2) \end{pmatrix} \quad \text{and} \quad |\psi_+\rangle = \begin{pmatrix} e^{-i\phi}\cos(\theta/2) \\ \sin(\theta/2) \end{pmatrix} \tag{2.20}$$

with energy $E_- = -r$ and $E_+ = r$, respectively. We assume that the system is initialized in the state $|\psi_-\rangle$ at $t = 0$ and consider the current produced by the adiabatic evolution of the system as a function of t.

To calculate the current, we consider the solution $|\Psi(t)\rangle$ to the time-dependent Schrodinger equation $i\hbar\partial_t|\Psi(t)\rangle = H_{\text{eff}}(t)|\Psi(t)\rangle$ to the first order non-adiabatic correction, given by

$$|\Psi(t)\rangle \approx |\psi_-\rangle - i\hbar\frac{\langle\psi_+|\partial_t\psi_-\rangle}{E_+ - E_-}|\psi_+\rangle \tag{2.21}$$

up to an overall phase factor [see Eq. (2.6)]. The time-averaged total current therefore is given by

$$J = \frac{e\omega}{2\pi}\int_0^{2\pi/\omega} dt \int_{-q/2}^{q/2} dk\ \langle\Psi(t)|\frac{1}{\hbar}\frac{\partial H_{\text{eff}}}{\partial k}|\Psi(t)\rangle, \tag{2.22}$$

where e is the electron charge. Using Eq. (2.21), we find that

$$\langle\Psi(t)|\frac{1}{\hbar}\frac{\partial H_{\text{eff}}}{\partial k}|\Psi(t)\rangle = \langle\psi_-|\frac{1}{\hbar}\frac{\partial H_{\text{eff}}}{\partial k}|\psi_-\rangle - \Omega(k,t), \tag{2.23}$$

where $\Omega(k,t) = i\left[\langle\partial_k\psi_-|\partial_t\psi_-\rangle - \langle\partial_t\psi_-|\partial_k\psi_-\rangle\right]$ is the Berry curvature in (k,t)-space. The first term on the right side of Eq. (2.23) is the group velocity contribution to the current, and the second term is the quantum geometric contribution—the anomalous velocity.

To calculate J, we note that the group velocity [first term in Eq. (2.23)], is zero after integration, because $E_-|_{k=q/2} - E_-|_{k=-q/2} = 0$. Therefore, only the anomalous velocity remains:

$$J = -\frac{e\omega}{2\pi}\int_0^{2\pi/\omega} dt \int_{-q/2}^{q/2} dk\ \Omega(k,t). \tag{2.24}$$

Already, we can see that the current should be quantized in integer multiples of $e\omega/2\pi$, because the integral over t and k traces out a curve in $\boldsymbol{d}$-space fully enclosing the origin. We can arrive at the same result by performing the calculation explicitly, first through computation of the Berry connection

$$\mathcal{A}(k,t) = \langle\psi_-(\theta,\phi)|\partial_k|\psi_-(\theta,\phi)\rangle\hat{k} + \langle\psi_-(\theta,\phi)|\partial_t|\psi_-(\theta,\phi)\rangle\hat{t}, \tag{2.25}$$

where $\hat{k}$ and $\hat{t}$ are unit vectors in the (k,t) phase space. Using Eq. (2.20), we find that

$$\mathcal{A}(k,t) = \frac{1-\cos\theta}{2}\left(\frac{\partial\theta}{\partial k}\hat{k} + \frac{\partial\phi}{\partial t}\hat{t}\right) \quad \text{and} \quad \Omega(k,t) = \frac{d}{dk}\left(\frac{1-\cos\theta}{2}\right). \tag{2.26}$$

Upon substitution into Eq. (2.24), we find that

$$J = \frac{\omega}{2\pi}\left[\frac{1-\cos\theta}{2}|_{k=q/2} - \frac{1-\cos\theta}{2}|_{k=-q/2}\right] = \frac{e\omega}{2\pi}, \tag{2.27}$$

implying that a single electron is pumped across the system per driving period.

Weak Electric Field and Quantized Hall Conductivity

The following section is based on Refs. [97, 232, 307].

The Berry curvature of electronic states in a 2D lattice can be detected from the current response to a weak, DC electric field $\boldsymbol{E}$. We consider a Bloch Hamiltonian $H(\boldsymbol{k})$ parameterized by the crystal momentum $\boldsymbol{k}$. The weak electric field is equivalent to a slowly-varying vector potential $\boldsymbol{A}(t) = \boldsymbol{E}(t)t$, which produces adiabatic electronic dynamics via minimal coupling $\boldsymbol{k} \to \boldsymbol{k}' = \boldsymbol{k} + e\boldsymbol{A}(t)/\hbar$, yielding the time-dependent Hamiltonian $H(\boldsymbol{k}')$ with instantaneous eigenstates $|u_{\boldsymbol{k}'n}\rangle$ and eigenenergies $E_{\boldsymbol{k}'n}$ indexed by the integer n, which satisfy the eigenvalue relation

$$H(\boldsymbol{k}')|u_{\boldsymbol{k}'n}\rangle = E_{\boldsymbol{k}'n}|u_{\boldsymbol{k}'n}\rangle. \tag{2.28}$$

Here, we have absorbed the time dependence into $\boldsymbol{k}'$ for simplicity of the notation. We consider the solution $|\psi_{\boldsymbol{k}n}(t)\rangle$ to the time-dependent Schrodinger equation $i\hbar\partial_t|\psi_{\boldsymbol{k}n}(t)\rangle = H(\boldsymbol{k}')|\psi_{\boldsymbol{k}n}(t)\rangle$ initialized in the n-th instantaneous eigenstate at time $t = 0$. To the first order non-adiabatic correction,

$$|\psi_{\boldsymbol{k}n}(t)\rangle \approx |u_{\boldsymbol{k}'n}\rangle - i\hbar\sum_{m\neq n}\frac{\langle u_{\boldsymbol{k}'m}|\partial_t u_{\boldsymbol{k}'n}\rangle}{E_{\boldsymbol{k}'m} - E_{\boldsymbol{k}'n}}|u_{\boldsymbol{k}'m}\rangle \tag{2.29}$$

up to an overall phase factor. The group velocity, given by

$$\boldsymbol{v}_{\boldsymbol{k}n} = \langle\psi_{\boldsymbol{k}n}(t)|\frac{1}{\hbar}\frac{\partial H(\boldsymbol{k})}{\partial\boldsymbol{k}}|\psi_{\boldsymbol{k}n}(t)\rangle, \tag{2.30}$$

can be evaluated by using the relation $\partial/\partial t = -(e/\hbar)\boldsymbol{E}\cdot\nabla_{\boldsymbol{k}}$ and noting that $\langle\psi_{\boldsymbol{k}m}(t)|(\partial H(\boldsymbol{k})/\partial\boldsymbol{k})|\psi_{\boldsymbol{k}n}(t)\rangle = (E_{\boldsymbol{k}m} - E_{\boldsymbol{k}n})\langle\psi_{\boldsymbol{k}m}(t)|\nabla_{\boldsymbol{k}}|\psi_{\boldsymbol{k}n}(t)\rangle$ [as determined by differentiating both sides of Eq. (2.28) with respect to $\boldsymbol{k}$]. Combining these results, we find that

$$\boldsymbol{v}_{\boldsymbol{k}n} = \frac{1}{\hbar}\frac{\partial E_{\boldsymbol{k}n}}{\partial\boldsymbol{k}} - \frac{e}{\hbar}\boldsymbol{E}\times\boldsymbol{\Omega}_{\boldsymbol{k}n}, \tag{2.31}$$

where

$$\boldsymbol{\Omega}_{\boldsymbol{k}n} = i\langle \nabla_{\boldsymbol{k}} u_{\boldsymbol{k}n}| \times |\nabla_{\boldsymbol{k}} u_{\boldsymbol{k}n}\rangle \tag{2.32}$$

is the Berry curvature. Eq. (2.31) is the semiclassical equations of motion for electrons under weak electric fields, and the second term in Eq. (2.31) is known as the *anomalous velocity*.

The semiclassical equations of motion enable us to estimate the current flowing through the system, given by

$$\boldsymbol{J} = e \sum_n \int_{\mathrm{BZ}} \frac{d^2\boldsymbol{k}}{(2\pi)^2} \boldsymbol{v}_{\boldsymbol{k}n} f_{\boldsymbol{k}n}, \tag{2.33}$$

where n sums over the bands of the system, the integral over $\boldsymbol{k}$ covers the full Brillouin zone (BZ), and $f_{\boldsymbol{k}n}$ denotes the occupation function of the state $|u_{\boldsymbol{k}n}\rangle$. Without loss of generality, we can align $\boldsymbol{E} = E_x\hat{x}$ and compute Hall conductivity $\sigma_{xy} = J_y/E_x$, given by

$$\sigma_{xy} = \sum_n \frac{e^2}{\hbar} \int_{\mathrm{BZ}} d^2\boldsymbol{k}\ \boldsymbol{\Omega}_{\boldsymbol{k}n} \cdot \hat{z}\ f_{\boldsymbol{k}n}. \tag{2.34}$$

If the chemical potential of the system is chosen such that an integer number of bands are fully-filled, then the Hall conductivity is proportional to the sum over the Chern numbers C_n of the fully-filled bands, where

$$\sigma_{xy} = \sum_{n\in\text{filled}} \frac{e^2}{2\pi\hbar} C_n \quad \text{and} \quad C_n = \frac{1}{2\pi} \int_{\mathrm{BZ}} d^2\boldsymbol{k}\ \boldsymbol{\Omega}_{\boldsymbol{k}n} \cdot \hat{z}. \tag{2.35}$$

In the Brillouin zone, it can be shown that $C_n \in \mathbb{Z}$ by noting that

$$C_n = \frac{1}{2\pi} \int_{\mathrm{BZ}} d^2\boldsymbol{k}\ \boldsymbol{\Omega}_{\boldsymbol{k}n} \cdot \hat{z} = \frac{i}{2\pi} \oint d\boldsymbol{k} \cdot \langle u_{\boldsymbol{k}n}|\nabla_{\boldsymbol{k}}|u_{\boldsymbol{k}n}\rangle \tag{2.36}$$

where the integral on the left hand side is performed along the boundary of the first Brillouin zone (1BZ). To prove the quantization of C_n, we leverage the periodicity of the Brillouin zone, noting that the Bloch function $|u_{\boldsymbol{k}n}\rangle$ should return to itself upon the transformation $\boldsymbol{k} \to \boldsymbol{k}+\boldsymbol{G}$, where $\boldsymbol{G}$ is a reciprocal lattice vector, but only up to a phase factor. We can account for the phase factor by defining $|u_{\boldsymbol{k}n}\rangle = e^{-i\theta_n(\boldsymbol{k})}|\tilde{u}_{\boldsymbol{k}n}\rangle$, where $\theta_n(\boldsymbol{k})$ is a real-valued phase factor and $|\tilde{u}_{\boldsymbol{k}n}\rangle$ is invariant upon $\boldsymbol{k} \to \boldsymbol{k}+\boldsymbol{G}$. Noting that $\oint d\boldsymbol{k} \cdot \langle \tilde{u}_{\boldsymbol{k}n}|\nabla_{\boldsymbol{k}}|\tilde{u}_{\boldsymbol{k}n}\rangle = 0$ due to the periodicity of $|\tilde{u}_{\boldsymbol{k}n}\rangle$ upon the transformation $\boldsymbol{k} \to \boldsymbol{k}+\boldsymbol{G}$, we find that

$$C_n = \frac{1}{2\pi} \oint d\boldsymbol{k} \cdot \nabla_{\boldsymbol{k}} \theta_n(\boldsymbol{k}). \tag{2.37}$$

Furthermore, because $e^{-i\theta_n(\boldsymbol{k})}$ is single-valued on a closed loop around the 1BZ, C_n must be *quantized*.

Two-level system. In a two-level system [see definition above Eq. (2.14)], we can derive the Chern number from a simple geometric picture. It can be shown [see Ref. [232]] that the Chern number can be expressed as

$$C_n = (-1)^n \frac{1}{4\pi} \int_{\mathrm{BZ}} d^2\boldsymbol{k}\ \hat{\boldsymbol{d}} \cdot (\partial_{k_x}\hat{\boldsymbol{d}} \times \partial_{k_y}\hat{\boldsymbol{d}}), \tag{2.38}$$

where $n = 0, 1$ which counts the oriented solid angle swept by $\hat{\boldsymbol{d}} \equiv \boldsymbol{d}/|\boldsymbol{d}|$ upon variation across the Brillouin zone (BZ), divided by 4π. Because the BZ is a closed manifold, C is quantized. Thus, we can interpret C as the number of times $\hat{\boldsymbol{d}}$ fully-covers the Bloch sphere (or, equivalently, the number of times the surface traced out by $\boldsymbol{d}$ fully encloses the origin $\boldsymbol{d} = 0$) upon variation across the BZ.

2.4 Edge States and Topology in Graphene

The following section is based on Ref. [97].

To illustrate the emergence of topology in a solid-state system, we consider the Hamiltonian of graphene modified by the addition of a mass gap. Near the K and K' valleys, indexed by $\xi = +1, -1$, respectively, the system can be described by the Dirac Hamiltonian

$$H_\xi(\boldsymbol{k}) = \hbar v_F(k_x\sigma_x + \xi k_y\sigma_y) + m_\xi\sigma_z, \tag{2.39}$$

where v_F is the Fermi velocity and m_ξ is the mass gap. The eigenergies of the Hamiltonian are given by $E_n(\boldsymbol{k}) = (-1)^n\sqrt{(\hbar v_F k)^2 + m_\xi^2}$, where $k = \sqrt{k_x^2 + k_y^2}$ and $n = 0, 1$ indexes the quasienergy.

Topology

To determine the topology of the system, we consider the winding of the pseudospin

$$\hat{\boldsymbol{d}}(k, \phi) = (\hbar v_F k \cos\phi_{\boldsymbol{k}}, \hbar v_F k \sin\phi_{\boldsymbol{k}}, m_\xi)/\sqrt{(\hbar v_F k)^2 + m_\xi^2} \tag{2.40}$$

within each valley, where we have used the polar coordinates $k = \sqrt{k_x^2 + k_y^2}$ and $\phi_{\boldsymbol{k}} = \arctan(k_y/k_x)$. To count the winding of the pseudospin, we track the evolution of $\hat{\boldsymbol{d}}(k, \phi)$ as a function of of k, starting at $k = 0$. At $k = 0$, $\hat{\boldsymbol{d}}(k, \phi) = \mathrm{sign}(m_\xi)\hat{z}$ is aligned with the z-axis, with an orientation determined by the sign of the mass term m_ξ. As k is increased, the pseudospin begins to approach the k_x-k_y plane, winding

clockwise as a function of increasing $\phi_{\boldsymbol{k}}$ if $\xi = +1$, or counterclockwise if $\xi = -1$. Thus, the pseudospin covers half of the Bloch sphere, tracing out a solid angle of $2\pi\ \mathrm{sign}(m_\xi)\xi$ and contributing a Chern number of $C_n^\xi = (-1)^n \mathrm{sign}(m_\xi)\xi/2$ to the band indexed by $n = 0, 1$.

In order to calculate the total Chern number C_n of the electronic bands in the Brillouin zone, we add the contributions from the K and K' valleys, using the relation $C_n = C_n^{+1} + C_n^{-1}$. For a *regular mass term*, given by $m_\xi = m$, the bands are trivial ($C_n = 0$) because $C_n^{+1} = -C_n^{-1}$. For a *Haldane* (topological) mass term, given $m_\xi = \xi m$ with opposite signs in the K and K' valleys, we find that $C_n = (-1)^n \mathrm{sign}(m)$, giving rise to topologically-nontrivial Chern bands.

Edge States

An important consequence of topologically-nontrivial bands is the emergence of edge states localized to the spatial interfaces between topologically-distinct phases. Let us consider a slab of graphene with a Haldane mass gap, extending infinitely along the y-direction but with a finite length along the x-direction, terminating at the right and left edges positioned at $x = x_R$ and $x = x_L$, respectively, where $x_L < x_R$. The edges in the x-direction are interfaced with graphene with a regular mass gap.

To understand the emergence of edge states, we analyze the Schrodinger equation near the right edge for different values of k_y, first for a single valley indexed by ξ. Starting at $k_y = 0$, we find that the Schrodinger equation is given by

$$\begin{pmatrix} m_\xi(x) & -i\hbar v_F \partial_x \\ -i\hbar v_F \partial_x & -m_\xi(x) \end{pmatrix} \begin{pmatrix} \psi_1 \\ \psi_2 \end{pmatrix} = \varepsilon \begin{pmatrix} \psi_1 \\ \psi_2 \end{pmatrix} \tag{2.41}$$

where $m_\xi = \xi m$ (corresponding to a Haldane gap) in the region $x_L < x < x_R$, and $m_\xi = m$ elsewhere. To determine the energy ε of the edge mode, we focus on the Hamiltonian H_ξ evaluated at $k_y = 0$, which *anticommutes* with σ_y, i.e., $\{H_\xi, \sigma_y\} = 0$. This symmetry relation implies that an eigenstate $|\psi\rangle$ with energy ε must come in a pair with an eigenstate $\sigma_y|\psi\rangle$ with energy $-\varepsilon$, except if $\varepsilon = 0$, implying that the edge mode must have zero energy, $\varepsilon = 0$. Solving Eq. (2.45) for the zero-energy state, we find that

$$-i\hbar v_F \partial_x \psi_2 = -m_\xi \psi_1 \quad \text{and} \quad -i\hbar v_F \partial_x \psi_1 = m_\xi \psi_2, \tag{2.42}$$

whose solutions are given by

$$\begin{pmatrix} \psi_1 \\ \psi_2 \end{pmatrix} = \frac{1}{\sqrt{2}} \begin{pmatrix} -i\ \mathrm{sign}(m_\xi) \\ 1 \end{pmatrix} e^{-|m||x-x_R|/(\hbar v_F)}, \tag{2.43}$$

and

$$\begin{pmatrix}\psi_1\\ \psi_2\end{pmatrix} = \frac{1}{\sqrt{2}}\begin{pmatrix} i\ \mathrm{sign}(m_\xi)\\ 1\end{pmatrix} e^{-|m||x-x_L|/(\hbar v_F)} \tag{2.44}$$

near the right and left edges, respectively. Notice that the edge states are localized to the edges of the system, located at $x = x_L, x_R$. We can now generalize the analysis to nonzero values of k_y, where the Schrodinger equation now reads

$$\left[\begin{pmatrix} m_\xi(x) & -i\hbar v_F\partial_x\\ -i\hbar v_F\partial_x & -m_\xi(x)\end{pmatrix} + \xi\hbar v_F k_y\sigma_y\right]\begin{pmatrix}\psi_1\\ \psi_2\end{pmatrix} = \varepsilon\begin{pmatrix}\psi_1\\ \psi_2\end{pmatrix}. \tag{2.45}$$

The wave vectors given in Eqs. (2.43)-(2.44) remain solutions to the Eq. (2.45), except with an energy shifted to $E_R(k_y) = \xi\ \mathrm{sign}(m_\xi)\hbar v_F k_y$ at $x = x_R$ and $E_L(k_y) = -\xi\ \mathrm{sign}(m_\xi)\hbar v_F k_y$ at $x = x_L$. Importantly, when combining the results for the K and K' valleys, the edge states are *chiral*, because the edge states exhibit opposite group velocity in the y-direction on the right and left edges.

Chapter 3

COHERENT DYNAMICS AND TOPOLOGY OF FLOQUET SYSTEMS

The topological transport properties of adiabatically driven systems, reviewed in Chapter 2, motivate questions about how topology could play a role in the universal properties of non-adiabatically driven systems. Floquet theory leverages a common feature of many driving fields—time-periodicity—to model its effects on quantum systems without assumptions of adiabaticity. A remarkable prediction of Floquet theory is the emergence of drive-induced band topology, which leads to transport signatures such as an anomalous Hall conductivity. We provide an overview of these predictions in this chapter.

Before discussing the topological properties of Floquet systems, we begin with a broad overview of the key results of Floquet theory. Floquet theory provides a framework to solve the time-dependent Schrodinger equation,

$$i\hbar\partial_t|\Psi(t)\rangle = H(t)|\Psi(t)\rangle, \tag{3.1}$$

when the Hamiltonian is time-periodic: $H(t) = H(t+T)$. In particular, the Schrodinger equation is solved by computing the unitary evolution operator

$$U(t,t_0) = \mathcal{T}\, e^{-\frac{i}{\hbar}\int_{t_0}^{t} H(t')dt'} \tag{3.2}$$

relating the state $|\Psi(t)\rangle = U(t,t_0)|\Psi(t_0)\rangle$ at arbitrary times t to the initial state $|\Psi(t_0)\rangle$ at time t_0, where $\mathcal{T}$ denotes time-ordering. The key result of Floquet theory is that a *time-independent* effective Floquet Hamiltonian $H_F[t_0]$ can fully capture the dynamics of the system at stroboscopic times $t = t_0 + mT$, where $m \in \mathbb{Z}$ [196, 241, 290]. In particular, we can write

$$U(t_0 + mT, t_0) = e^{-iH_F[t_0]\times mT/\hbar}. \tag{3.3}$$

Furthermore, the set of eigenvectors $|u_n\rangle$ and eigenvalues ε_n ("quasienergy") of the Floquet Hamiltonian $H_F[t_0]$, indexed by the integer n, provides a simple expression for $|\Psi(t)\rangle$ at stroboscopic times,

$$|\Psi(t_0 + mT)\rangle = \sum_n a_n e^{-i\varepsilon_n mT}|u_n\rangle, \tag{3.4}$$

where a_n are *time-independent* coefficients dependent only on the initial state $|\Psi(t_0)\rangle$. The Floquet Hamiltonian $H_F[t_0]$ therefore provides a simple description of the coarse-grained, slow dynamics of the system on stroboscopic timescales longer than the period of the drive. These slow dynamics are often sufficient to describe the salient properties of Floquet systems. For instance, many-body scattering processes and low-frequency transport measurements of optically-driven systems, which are the primary focus of this thesis, occur on timescales much longer than the period of most laser drives [74, 258]. Importantly, under certain conditions, $H_F[t_0]$ can also possess topological properties [167, 215].

The rest of the chapter is structured as follows. In Section 3.1, we introduce the Floquet Hamiltonian H_F and the micromotion operator K_F, which respectively describe the dynamics of Floquet systems on timescales longer and shorter than the period of the drive. Section 3.2 seeks to find approximate analytic forms for H_F using the high-frequency expansion and the rotating wave approximation, respectively applicable when the driving frequency is off-resonant and resonant to the energy level spacing of the equilibrium system. Section 3.3 describes a numerical scheme to solve for $|\Psi(t)\rangle$ using a frequency-space expansion when the approximation methods in Section 3.2 may not apply. Section 3.4 provides an example of the Floquet Hamiltonian for graphene-based systems. Section 3.5 describes the emergence of topology in Floquet systems. And, finally, Section 3.6 describes how drive-induced topology can emerge in the transport properties of Floquet systems.

3.1 Floquet Theory: Separating Stroboscopic Dynamics from Micromotion

The following section is based on Refs. [196, 241, 290].

In this section, we seek to separate the evolution operator

$$U(t, t_0) = \mathcal{T} e^{-\frac{i}{\hbar}\int_{t_0}^{t} H(t')dt'} \tag{3.5}$$

into components that dictate the dynamics of Floquet systems on timescales longer and shorter than the period of the drive. As we will see in Section 3.3 of this chapter, the slow dynamics can often be approximated in analytic form and provide key insights into the behavior of Floquet systems on long timescales.

Slow and Fast Dynamics

The evolution of a Floquet system from time t_0 to time t can be separated into two steps: a stroboscopic evolution from time t_0 to time $t_0 + nT$, where $n \in \mathbb{Z}$, and a

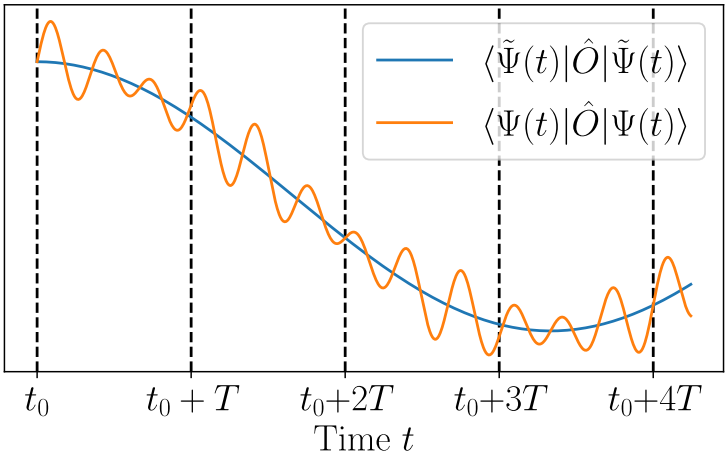

Figure 3.1: Schematic illustration of slow (stroboscopic-timescale) dynamics and fast (micromotion) dynamics of a Floquet system with a time-periodic Hamiltonian $H(t) = H(t+T)$. A system is initialized at time t_0 in the state $|\Psi(t_0)\rangle$. We compare the time-dependence of the expectation value of an operator $\hat{O}$ under evolution by the full time-dependent Schrodinger equation $|\Psi(t)\rangle = U(t,t_0)|\Psi(t_0)\rangle$ (orange curve), where $U(t,t_0) = \mathcal{T}\exp\left[-(i/\hbar)\int_{t_0}^{t} H(t')dt'\right]$, and under the effective time-independent Floquet Hamiltonian $|\tilde{\Psi}(t)\rangle = e^{iH_F(t-t_0)}|\Psi(t_0)\rangle$ (blue curve). The Floquet Hamiltonian H_F captures the slow course-grained dynamics of the system on timescales longer than the period of the drive T (see blue curve), while the full solution to the time-dependent Schrodinger equation captures the fast dynamics (micromotion) within each time period (see orange curve). The orange and blue curves agree at stroboscopic times given by $t_0 + nT$, where $n \in \mathbb{Z}$, where $|\Psi(t_0 + nT)\rangle = |\tilde{\Psi}(t_0 + nT)\rangle$. Figure based on Ref. [290].

sub-cycle evolution from the stroboscopic time $t_0 + nT$ to the final time $t = s + nT$, where n is chosen such that $0 \leq s - t_0 < T$. The evolution operator $U(t,t_0)$ can therefore be written as

$$U(t,t_0) = U(s+nT, t_0+nT)U(t_0+nT,t_0). \tag{3.6}$$

Noting that $U(s+nT,t_0+nT) = U(t,t_0)$, we find that

$$U(t,t_0) = U(s,t_0)U(t_0+nT,t_0). \tag{3.7}$$

The operators $U(s,t_0)$ and $U(t_0+nT,t_0)$ capture the micromotion and stroboscopic time evolution, respectively, which we now analyze separately:

- *Stroboscopic dynamics and the Floquet Hamiltonian.* The stroboscopic evolution operator $U(t_0+nT,t_0)$ can be separated into n single-period evolutions:

$U(t_0 + nT, t_0) = [U(t_0 + T, t_0)]^n$. By definition, the evolution operator across each period is given by

$$U(t_0 + T, t_0) = e^{-iH_F[t_0]T/\hbar} \tag{3.8}$$

where the time-dependent operator $H_F[t_0]$ is called the Floquet Hamiltonian.

- *Micromotion and micromotion operator.* If we wish to determine the state $|\Psi(t)\rangle$ at an arbitrary time $t = s + nT$, it would be incorrect to evolve the state with the Floquet Hamiltonian $H_F[t_0]$, i.e., $|\Psi(t)\rangle \neq e^{-iH_F[t_0]\times(t-t_0)/\hbar}|\Psi(t_0)\rangle$. Instead, another operator $K_F[t_0](s)$ is needed to restore information about the sub-cycle micromotion of the system from time t_0 to s, such that

$$|\Psi(t)\rangle = e^{-iK_F[t_0](s)/\hbar}e^{-iH_F[t_0]\times(t-t_0)/\hbar}|\Psi(t_0)\rangle. \tag{3.9}$$

  The operator $K_F[t_0](s)$ is called the micromotion (or kick) operator.

The definitions of $H_F[t_0]$ and $K_F[t_0]$ can be used to rewrite the evolution operator in the form

$$U(t, t_0) = e^{-iK_F[t_0](s)/\hbar}e^{-iH_F[t_0]\times(t-t_0)/\hbar}. \tag{3.10}$$

State Vector

With knowledge of the Floquet Hamiltonian $H_F[t_0]$ and the micromotion operator $K_F[t_0]$, we can now find an explicit form for $|\Psi(t)\rangle$ using the eigenstates $|u_n\rangle$ and quasienergies ε_n of the Floquet Hamiltonian H_F, which satisfy the eigenvalue relation

$$H_F[t_0]|u_n\rangle = \varepsilon_n|u_n\rangle. \tag{3.11}$$

We assume that the system is initialized in the state $|\Psi(t_0)\rangle$ at time $t = t_0$, which can be expanded in terms of $|u_n\rangle$ as follows:

$$|\Psi(t_0)\rangle = \sum_n a_n|u_n\rangle. \tag{3.12}$$

Using Eq. (3.10) to evaluate $|\Psi(t)\rangle = U(t, t_0)|\Psi(t_0)\rangle$ yields

$$|\Psi(t)\rangle = \sum_n a_n e^{-i\varepsilon_n(t-t_0)/\hbar}|\Phi_n(t)\rangle, \tag{3.13}$$

where

$$|\Phi_n(t)\rangle = e^{-iK_F[t_0](t)/\hbar}|u_n\rangle \tag{3.14}$$

is periodic in time, i.e., $|\Phi_n(t)\rangle = |\Phi_n(t+T)\rangle$. The primary result here is that solutions to the time-dependent Schrodinger equation, $|\Psi(t)\rangle$, [see Eq. (3.13)] can be expanded in the complete basis given by the *Floquet states*

$$|\psi_n(t)\rangle = e^{-i\varepsilon_n t/\hbar}|\Phi_n(t)\rangle, \tag{3.15}$$

where ε_n is the quasienergy of the Floquet state.

Coarse-Grained Dynamics

When only the coarse-grained dynamics of the system on timescales much longer than the driving period are relevant, we can approximate the expectation values of observables by using the state

$$|\tilde{\Psi}(t)\rangle = \sum_n a_n e^{-i\varepsilon_n(t-t_0)}|u_n\rangle, \tag{3.16}$$

which is exact at stroboscopic times, i.e., $|\tilde{\Psi}(t_0+mT)\rangle = |\Psi(t_0+mT)\rangle$, where $m \in \mathbb{Z}$. This can be deduced from Eq. (3.14) by noticing that $|\Phi_n(t_0+mT)\rangle = |u_n\rangle$, because $K_F[t_0](t_0) = 0$ by definition [see Eq. (3.10)].

In Figure 3.1, we provide a schematic illustration of how the expectation values of an operator $\hat{O}$ may differ when evaluated with $|\tilde{\Psi}(t)\rangle$ and $|\Psi(t)\rangle$. Notice that the two results agree at stroboscopic times and $|\tilde{\Psi}(t)\rangle$ can capture the coarse-grained dynamics on slow timescales. Only knowledge of the Floquet Hamiltonian $H_F[t_0]$ is necessary to solve for $|\tilde{\Psi}(t)\rangle$. In Figure 3.1, we have schematically illustrated micromotion oscillations with amplitudes weaker than the stroboscopic dynamics. This can be justified more rigorously with the frequency space expansion, introduced in Section 3.3, which predicts a Wannier-Stark like localization of the Fourier harmonics of Floquet states that suppresses the amplitude of micromotion with frequencies much higher than the driving frequency [241].

Gauge Choice

In the discussion above, we implicitly chose a gauge given by $K_F[t_0] = 0$. The gauge choice is not unique. For instance, a choice of a different initial time t_0' gives rise to a different Floquet Hamiltonian and micromotion operator given by

$$H_F[t_0'] = U(t_0', t_0)H_F[t_0]U^\dagger(t_0', t_0) \quad \text{and} \quad e^{iK_F[t_0'](t)} = U(t_0', t_0)e^{iK_F[t_0](t)}, \tag{3.17}$$

respectively. Alternatively, the gauge defined by

$$H_F = e^{iK_F(t_0)}H_F[t_0]e^{-iK_F(t_0)} \quad \text{and} \quad e^{iK_F(t)} = e^{iK_F(t_0)}e^{iK_F[t_0](t)} \tag{3.18}$$

can be chosen to obtain a Floquet Hamiltonian H_F and micromotion operator $K_F(t)$ with no initial time dependence. In the latter gauge choice, the evolution operator also takes a form $U(t_f, t_i) = e^{-iK_F(t_f)}e^{-iH_F(t_f-t_i)}e^{iK_F(t_i)}$ independent of t_0. Note that substitution of the evolution operator into the Schrodinger equation provides another equivalent definition of H_F and K_F. In particular, the micromotion operator K_F is the operator that transforms the operator $Q(t) = H(t) - i\hbar\partial_t$, sometimes known as the "quasienergy operator," into a time-independent operator, which is precisely the Floquet Hamiltonian:

$$H_F = e^{iK_F(t)}[H(t) - i\hbar\partial_t]e^{-iK_F(t)}. \tag{3.19}$$

This definition can sometimes be useful when the form of $Q(t)$ is simple and the form of $e^{iK_F(t)}$ can be guessed by observation, such as in the rotating wave approximation that will be presented in Section 3.2. Note that the form of $K_F(t)$ and H_F are still not unique, and Eq. (3.19) can still be satisfied by a different set of operators $H'_F = MH_FM^\dagger$ and $e^{iK'_F(t)} = Me^{iK_F(t)}$ related by the unitary operator M. For instance, a choice of $K_F(t_0) = 0$ restores the gauge choice used at the beginning of this section.

3.2 Analytic Approximations to the Floquet Hamiltonian

It is sometimes impossible to obtain closed analytic forms for the operators K_F and H_F. In this section, we discuss two limits in which approximate forms for K_F, H_F, or both can be obtained. Throughout this section, we will consider a generic time-periodic system described by the Hamiltonian

$$H(t) = H_0 + H_1(t), \tag{3.20}$$

where H_0 is the static Hamiltonian, $H_1(t) = H_1(t + 2\pi/\omega)$, and ω is the angular frequency of the driving field.

High-Frequency Expansion

The following section is based on Refs. [196, 236].

The high-frequency expansion approximates the Floquet Hamiltonian H_F when the spectral level spacing between relevant states of the static Hamiltonian H_0 is much smaller than the frequency $\hbar\omega$ of the drive. To perform the expansion, we first rewrite

$$H_1(t) = \sum_m H_1^{(m)} e^{im\omega t} \tag{3.21}$$

and seek a Floquet Hamiltonian and micromotion operator of the form

$$H_F = H_0 + \sum_{m=1}^{\infty} \frac{\Omega_m}{\omega^m} \quad \text{and} \quad K_F(t) = \sum_{m=1}^{\infty} \frac{\Lambda_m(t)}{\omega^m}, \tag{3.22}$$

satisfying Eq. (3.19). Depending on the gauge choice, two types of expansions can be obtained.

Floquet-Magnus expansion. This expansion is obtained by imposing the gauge choice $K_F(t_0) = 0$. In this case, we obtain the leading order terms

$$\Omega_1 = \sum_{m\neq 0} \left\{ \frac{[H_1^{(-m)}, H_1^{(m)}]}{2m} + \frac{[H_1^{(m)}, H_0]}{m} e^{-im\omega t_0} \right\}, \tag{3.23}$$

and

$$\Lambda_1(t) = i \sum_{m\neq 0} \frac{H_1^{(m)}}{m} (e^{-im\omega t} - e^{-im\omega t_0}) \tag{3.24}$$

by substitution of Eq. (3.22) into Eq. (3.19).

Van-Vleck expansion. This expansion removes the t_0 dependence by imposing the gauge choice $\int_0^T K_F(t)dt = 0$. In this case,

$$\Omega_1 = \sum_{m\neq 0} \frac{[H_1^{(-m)}, H_1^{(m)}]}{2m} \quad \text{and} \quad \Lambda_1(t) = i \sum_{m\neq 0} \frac{H_1^{(m)}}{m} e^{-im\omega t}. \tag{3.25}$$

Rotating Wave Approximation

The rotating wave approximation (RWA) [86, 251] approximates the Floquet Hamiltonian in regions of phase space where the level spacing between states of H_0 is nearly resonant to the frequency $\hbar\omega$ of the drive.

To illustrate the RWA, we consider a generic two-level Bloch Hamiltonian described by the static Hamiltonian $H_0 = \boldsymbol{d} \cdot \boldsymbol{\sigma}$, where

$$\boldsymbol{d} = E_{\boldsymbol{k}}(\sin\theta_{\boldsymbol{k}} \cos\phi_{\boldsymbol{k}}, \sin\theta_{\boldsymbol{k}} \sin\phi_{\boldsymbol{k}}, \cos\theta_{\boldsymbol{k}}) \tag{3.26}$$

is parameterized by the crystal momentum $\boldsymbol{k}$, and $\boldsymbol{\sigma} = (\sigma_x, \sigma_y, \sigma_z)$ is the vector of Pauli matrices. The Hamiltonian H_0 has two eigenstates denoted $|v\rangle$ and $|c\rangle$ with energy $-E_{\boldsymbol{k}}$ and $E_{\boldsymbol{k}}$, respectively. We also assume that the time-dependent Hamiltonian $H_1(t)$ of the system only oscillates with a single frequency ω, i.e.,

$$H_1(t) = \boldsymbol{V} \cdot \boldsymbol{\sigma} e^{i\omega t} + \boldsymbol{V}^* \cdot \boldsymbol{\sigma} e^{-i\omega t}, \tag{3.27}$$

where $\boldsymbol{V}$ is a 3-component vector of complex numbers. The RWA provides an approximate Floquet Hamiltonian in the limit where $\hbar\omega \approx |2E_{\boldsymbol{k}}|$.

To perform the RWA, we transform to the diagonal basis of H_0, where

$$\tilde{H}_0 = U(\theta_{\boldsymbol{k}}, \phi_{\boldsymbol{k}}) H_0 U^\dagger(\theta_{\boldsymbol{k}}, \phi_{\boldsymbol{k}}) = \begin{pmatrix} -E_{\boldsymbol{k}} & 0 \\ 0 & E_{\boldsymbol{k}} \end{pmatrix}, \tag{3.28}$$

and

$$U(\theta_{\boldsymbol{k}}, \phi_{\boldsymbol{k}}) = e^{-i(\phi_{\boldsymbol{k}}/2)\sigma_z} e^{-i(\theta_{\boldsymbol{k}}/2)\sigma_y} \tag{3.29}$$

relates the two bases (i.e., rotates $\boldsymbol{d}$ into a new basis where it is aligned with the z-axis). Similarly, the driven Hamiltonian in this basis is given by

$$\tilde{H}_1(t) = \tilde{\boldsymbol{V}} \cdot \boldsymbol{\sigma} e^{i\omega t} + \tilde{\boldsymbol{V}}^* \cdot \boldsymbol{\sigma} e^{i\omega t}, \tag{3.30}$$

where $\tilde{\boldsymbol{V}}^*$ is related to $\boldsymbol{V}$ by a rotation [see Eq. (3.29)]. We use $\tilde{H}(t) = \tilde{H}_0 + \tilde{H}_1(t)$ to denote the full Hamiltonian in the diagonal basis of H_0.

Now, we perform the rotating wave approximation (RWA). In the interacting picture [115], where the Hamiltonian is given by $\tilde{H}^I(t) = e^{i\tilde{H}_0 t/\hbar} \tilde{H}(t) e^{-i\tilde{H}_0 t/\hbar}$, we discard terms oscillating with frequency ω and $\omega + 2E_{\boldsymbol{k}}/\hbar$ (i.e., "counter-rotating" terms), keeping only low frequency terms oscillating with frequency $\omega - 2E_{\boldsymbol{k}}/\hbar$. Transforming back to the Schrodinger picture yields $\tilde{H}(t) \approx H_{\mathrm{RWA}}(t)$, where the RWA-approximated Hamiltonian is given by

$$H_{\mathrm{RWA}}(t) \equiv \begin{pmatrix} 0 & (\tilde{V}_x - i\tilde{V}_y) e^{-i\omega t} \\ (\tilde{V}_x + i\tilde{V}_y) e^{i\omega t} & 0 \end{pmatrix}. \tag{3.31}$$

The utility of the RWA is that it allows us to easily find an effective Floquet Hamiltonian for the system. To see this, we note that the approximate quasienergy operator

$$\tilde{Q}(t) \approx H_{\mathrm{RWA}}(t) - i\hbar\partial_t \tag{3.32}$$

[see discussion above Eq. (3.19) for the definition] can be made time-independent by a transformation to a rotating frame, where $H_F = U(t)^\dagger \tilde{Q}(t) U(t)$ is the effective Floquet Hamiltonian and

$$U(t) = \begin{pmatrix} e^{i\omega t} & 0 \\ 0 & 1 \end{pmatrix} \tag{3.33}$$

implements the transformation. Explicitly, the Floquet Hamiltonian is given by

$$H_F = (-E_{\boldsymbol{k}} + \hbar\omega/2)\sigma_z + \tilde{V}_x \sigma_x + \tilde{V}_y \sigma_y, \tag{3.34}$$

and the eigenspectrum of H_F contains two quasienergies, given by

$$\varepsilon_{\boldsymbol{k}\alpha} = (-1)^{\alpha}\sqrt{(-E_{\boldsymbol{k}} + \hbar\omega/2)^2 + \tilde{V}_x^2 + \tilde{V}_y^2}, \tag{3.35}$$

where $\alpha = 0, 1$ enumerates the quasienergy bands. From Eq. (3.35), it is clear that the spectrum exhibits a *resonant Floquet gap* of size

$$\Delta_K = 2\sqrt{\tilde{V}_x^2 + \tilde{V}_y^2}, \tag{3.36}$$

which opens at momenta $\boldsymbol{k}_R$ satisfying the *resonance condition* given by $2E_{\boldsymbol{k}_R} = \hbar\omega$.

3.3 Numerical Approach: Frequency-Space Expansion

So far, we have seen that the high-frequency expansion and RWA can provide approximate expressions for H_F in certain limits. Alternatively, we can calculate the full (stroboscopic and micromotion) time-dependence of the Floquet state $|\Phi_n(t)\rangle$ by solving the time-dependent Schrodinger equation numerically in Fourier space. Here, we expand the Floquet state in a Fourier series:

$$|\Phi_n(t)\rangle = \sum_m e^{-im\omega t}|\phi_n^{(m)}\rangle, \tag{3.37}$$

where $|\phi_n^{(m)}\rangle$ are referred to as *Floquet harmonics* and $\omega = 2\pi/T$ is the angular frequency of the drive. Expanding the Hamiltonian

$$H(t) = \sum_m e^{-im\omega t}H^{(m)}, \tag{3.38}$$

in terms of its harmonic components $H^{(m)}$, we use the time-dependent Schrodinger equation to obtain the matrix equation

$$(\varepsilon_n + m\hbar\omega)|\phi_n^{(m)}\rangle = \sum_{m'} H^{(m-m')}|\phi_n^{(m')}\rangle, \tag{3.39}$$

which can be solved by the eigenvalue relation $\mathcal{H}\boldsymbol{\phi}_n = \varepsilon_n\boldsymbol{\phi}_n$, where

$$\mathcal{H} = \begin{pmatrix} & \vdots & \vdots & \vdots & \vdots & \\ \dots & H_0 - (m-1)\hbar\omega & H^{(-1)} & H^{(-2)} & H^{(-3)} & \dots \\ \dots & H^{(1)} & H_0 - m\hbar\omega & H^{(-1)} & H^{(-2)} & \dots \\ \dots & H^{(2)} & H^{(1)} & H_0 - (m+1)\hbar\omega & H^{(-1)} & \dots \\ & \vdots & \vdots & \vdots & \vdots & \end{pmatrix} \tag{3.40}$$

is an infinite-dimensional matrix and

$$\boldsymbol{\phi}_n = \begin{pmatrix} \vdots \\ |\phi_n^{(m-1)}\rangle \\ |\phi_n^{(m)}\rangle \\ |\phi_n^{(m+1)}\rangle \\ \vdots \end{pmatrix} \tag{3.41}$$

is the vector of Floquet harmonics [241]. The eigenvalue relation can be solved numerically by restricting $|m| < m_c$ in the frequency expansion of the Floquet state $|\Phi(t)\rangle$, see Eq. (3.37), where $m_c \gg 1$ is a large cutoff. Such a cutoff captures the micromotion of the system roughly up to a cutoff angular frequency of $m_c\omega$.

3.4 Floquet Hamiltonian of Irradiated Graphene and Semiconducting Systems

This section is based on, and extends upon, the analysis in Refs. [167, 239, 284].

Having discussed numerical and analytical methods to study the dynamics of Floquet systems, we now use Floquet theory to reveal the properties of optically-driven graphene and semiconducting systems. In the absence of driving, the low-energy physics of such a system near a single valley of its Brillouin zone is described by the Hamiltonian

$$H_0 = \boldsymbol{d} \cdot \boldsymbol{\sigma} \quad \text{where} \quad \boldsymbol{d} = (\hbar v_F k_x, \xi \hbar v_F k_y, \Delta_\xi/2), \tag{3.42}$$

and its eigenenergies are given by $\pm E_{\boldsymbol{k}}$, where $E_{\boldsymbol{k}} = \sqrt{(\hbar v_F k)^2 + (\Delta_\xi/2)^2}$ and $k = \sqrt{k_x^2 + k_y^2}$. Here, Δ_ξ defines the semiconducting gap size, and $\xi = +1, -1$ indexes the K and K' valleys, respectively. This Hamiltonian can describe a wide class of electronic systems. For example, the gapless $\Delta_\xi = 0$ limit of the Hamiltonian can be used to model a sheet of monolayer graphene, and a finite gap $\Delta_\xi \neq 0$ can be used to model the low-energy Hamiltonian for a single spin and valley sector of a direct-bandgap transition metal dichalcogenide. The coupling of the system to an optical drive is described by minimal coupling, $\boldsymbol{k} = \boldsymbol{k} + e\boldsymbol{A}(t)/\hbar$, to the magnetic vector potential $\boldsymbol{A}(t)$ of the laser field. Due to the linearity of H_0 in $\boldsymbol{k}$, the driven Hamiltonian can be written in the form $H(t) = H_0 + H_1(t)$, with

$$H_1(t) = \boldsymbol{V} \cdot \boldsymbol{\sigma} e^{i\omega t} + \boldsymbol{V}^* \cdot \boldsymbol{\sigma} e^{-i\omega t}, \tag{3.43}$$

where $\boldsymbol{V}$ is a 3-component vector of complex numbers that depends on the details of $\boldsymbol{A}(t)$. Our goal is to determine the the Floquet Hamiltonian of the system for different types of laser fields.

Circularly Polarized Laser

A circularly polarized laser field is described by the magnetic vector potential $\boldsymbol{A}(t) = A(\cos\omega t, \eta\sin\omega t, 0)$, where $\eta = -1$ and $\eta = +1$ for left and right circularly polarized lasers, respectively. By minimal coupling to the static Hamiltonian H_0, we find that the driven Hamiltonian $H_1(t)$ is parameterized by $\boldsymbol{V} = \frac{1}{2}v_F eA(-i, \xi\eta, 0)$.

Off-Resonant Floquet Hamiltonian. We can use the Van Vleck high-frequency expansion [196, 215, 236] to derive the Floquet Hamiltonian for crystal momenta satisfying $2E_{\boldsymbol{k}} \ll \hbar\omega$. Substitution into Eqs. (3.25) and (3.22) yields

$$H_F = H_0 - \Delta_K\sigma_z, \quad \text{where} \quad \Delta_K = \eta\xi\frac{e^2v_F^2A^2}{\omega}, \tag{3.44}$$

and the quasienergy

$$\varepsilon_{\boldsymbol{k}\alpha} = (-1)^\alpha\sqrt{E_{\boldsymbol{k}}^2 + [(\Delta_\xi - \Delta_K)/2]^2}. \tag{3.45}$$

is obtained by diagonalizing H_F. In a gapped systems, the second term in Eq. (3.44) indicates that the drive renormalizes the bandgap in a valley and laser helicity dependent manner. In graphene, notice that the drive-induced mass term, see Eq. (3.44), has opposite signs in opposite valleys, indicating that the drive dynamically produces a *Haldane gap*, a result first predicted by Takashi Oka and Hideo Aoki in 2009 [215].

Resonant Floquet Hamiltonian. Next, we use the RWA to estimate the Floquet Hamiltonian in the region of momentum space characterized by $2E_{\boldsymbol{k}} \approx \hbar\omega$. Following the RWA presented in Section 3.3, we find that the effective Floquet Hamiltonian in the rotating frame is given by

$$H_F = (-E_{\boldsymbol{k}} + \hbar\omega/2)\sigma_z + \tilde{V}_x\sigma_x + \tilde{V}_y\sigma_y, \tag{3.46}$$

where

$$\tilde{V}_x = v_F eA\sin\phi_{\boldsymbol{k}}[\delta_{\xi\eta,-1}\cos^2(\theta_{\boldsymbol{k}}/2) - \delta_{\xi\eta,1}\sin^2(\theta_{\boldsymbol{k}}/2)], \tag{3.47}$$

and

$$\tilde{V}_y = v_F eA\cos\phi_{\boldsymbol{k}}[\delta_{\xi\eta,-1}\cos^2(\theta_{\boldsymbol{k}}/2) + \delta_{\xi\eta,1}\sin^2(\theta_{\boldsymbol{k}}/2)]. \tag{3.48}$$

The quasienergy spectrum is therefore given by

$$\varepsilon_{\boldsymbol{k}\alpha} = (-1)^\alpha\sqrt{(-E_{\boldsymbol{k}} + \hbar\omega/2)^2 + (\Delta_R/2)^2}, \tag{3.49}$$

where $\alpha = 0, 1$ enumerates the Floquet bands. Note that the quasienergy spectrum exhibits a Floquet gap along the *resonance ring* paramaterized by $2E_{\boldsymbol{k}} \approx \hbar\omega$, of size

$$\Delta_R = \begin{cases} (v_F eA)\cos^2(\theta_{\boldsymbol{k}}/2) & \text{if } \xi\eta = 1, \\ (v_F eA)\sin^2(\theta_{\boldsymbol{k}}/2) & \text{if } \xi\eta = -1. \end{cases} \tag{3.50}$$

Here, we can immediately infer the valley selection rules for transition metal dichalcogenides. When the helicity of the laser is of opposite sign than the chirality ξ sign(Δ_ξ) of the valley, then the valley is more optically transparent because Δ_R is suppressed relative to the opposite valley [263].

Note that the same selection rule does not apply to graphene, where $\Delta = 0$ and the Floquet gap size $\Delta_R = v_F eA$ is independent of the laser helicity [284].

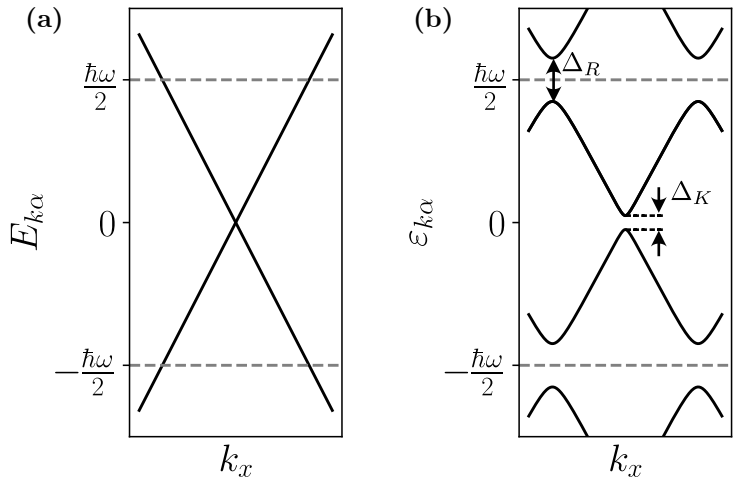

Figure 3.2: Floquet electronic bands of graphene irradiated by a circularly-polarized laser. (a) Energy spectrum of graphene as a function of k_x for fixed $k_y = 0$. (b) Quasienergy spectrum of graphene under circularly polarized laser irradiation, exhibiting an off-resonant Haldane gap of size Δ_K and a resonant gap of size Δ_R.

Visualization of the Floquet Bands in Graphene. The quasienergy near the K point and near the resonance ring, presented in Eqs. (3.45) and (3.49), respectively, can be stitched together to obtain the quasienergy spectrum for arbitrary $\boldsymbol{k}$. To visualize the resulting Floquet bands, we show the undriven bands of graphene ($\Delta = 0$) in Figure 3.2(a) and the driven Floquet bands in Figure 3.2(b). We indicate the opening of the resonance and Haldane gaps denoted Δ_R and Δ_K, respectively.

Linearly Polarized Laser

We now consider the effect of a linearly polarized laser field, described by the magnetic vector potential $\boldsymbol{A}(t) = (A_x \cos(\omega t), A_y \cos(\omega t), 0)$. In this case, the driven Hamiltonian is parameterized by $\boldsymbol{V} = \frac{1}{2} v_F e (A_x, A_y, 0)$.

Off-Resonant Floquet Hamiltonian. In the region of the Brillouin zone satisfying $2E_{\boldsymbol{k}} \ll \hbar\omega$, the Van Vleck high frequency expansion, see Eq. (3.25), yields the Floquet Hamiltonian $H_F \approx H_0$ to first order in ω^{-1}. Thus, the drive-induced Haldane gap predicted by Oka and Aoki [215] does not emerge for linearly-polarized irradiation.

Resonant Floquet Hamiltonian. Using the RWA, we derive an approximate Floquet Hamiltonian for crystal momenta near the resonance ring parameterized by $2E_{\boldsymbol{k}} \approx \hbar\omega$. For a linearly polarized laser field, we find that

$$\tilde{V}_x = \frac{1}{2} e v_F (A_x \cos\phi_{\boldsymbol{k}} + A_y \sin\phi_{\boldsymbol{k}}) \cos\theta_{\boldsymbol{k}}, \tag{3.51}$$

and

$$\tilde{V}_y = \frac{1}{2} e v_F (A_y \cos\phi_{\boldsymbol{k}} - A_x \sin\phi_{\boldsymbol{k}}). \tag{3.52}$$

A notable case is graphene, where $\theta_{\boldsymbol{k}} = \pi/2$, $\tilde{V}_y = v_F e (A_x \cos\phi_{\boldsymbol{k}} + A_y \sin\phi_{\boldsymbol{k}})$, $\tilde{V}_x = 0$, and the Floquet gap along the resonance ring $2E_{\boldsymbol{k}} = \hbar\omega$ is *momentum-dependent*, given by

$$\Delta_F = v_F e |A_x \cos\phi_{\boldsymbol{k}} + A_y \cos\phi_{\boldsymbol{k}}|. \tag{3.53}$$

The Floquet gap vanishes when the polarization of the laser field (A_x, A_y) is perpendicular to the crystal momentum $\boldsymbol{k}$.

3.5 The Floquet Topological Insulator

This section is based on, and extends upon, the analysis in Refs. [167, 239, 284].

In Sections 3.2 and 3.4, we discussed analytical methods to estimate the Floquet Hamiltonian and its quasienergy spectrum. Already, we have seen some potential signatures of topology in the Floquet Hamiltonian, such as the drive-induced Haldane gap in graphene, see Eq. (3.44). In this section, we provide a more complete discussion of the topological properties of Floquet systems.

As an example, we focus on a gapped graphene-like system driven by a circularly polarized laser, described by the time-periodic Hamiltonian $H(t) = H_0 + H_1(t)$,

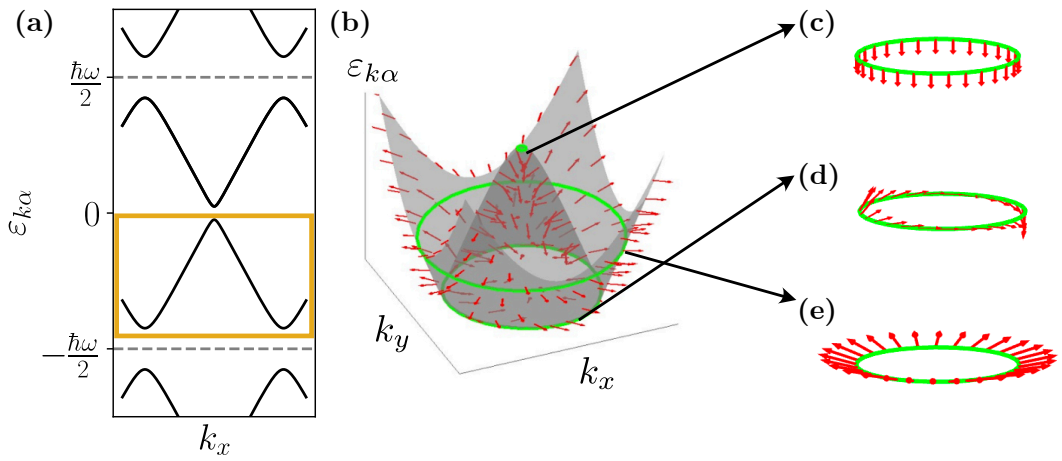

Figure 3.3: Pseudospin winding under circularly polarized irradiation. (a) Here we box in orange the $\alpha = -$ quasienergy band. (b) Plot of $\alpha = -$ quasienergy band vs. k_x and k_y. Red arrows indicate the orientation of the pseudospin $\hat{n}_{\boldsymbol{k}-}(0)$. We focus on the pseudospin along the rings sketched in green. (c) Pseudospin in the region $k < k_R$, which is roughly aligned with the $\hat{z}$-axis, with orientation set by the sign of the mass gap at $k = 0$. (d) Pseudospin along the resonance ring $k = k_R$. (e) Pseudospin in the region $k > k_R$, which approaches the equator, parameterized by $\hat{n}_{\boldsymbol{k}-}(0) = \hat{\boldsymbol{k}}$.

defined in Section 3.4. In order to characterize the topology of the Floquet bands, we consider the pseudospin of electronic states in the α-th Floquet band, defined by

$$\hat{n}_{\boldsymbol{k}\alpha}(t) = \langle \psi_{\boldsymbol{k}\alpha}(t)|\boldsymbol{\sigma}|\psi_{\boldsymbol{k}\alpha}(t)\rangle, \tag{3.54}$$

where $|\psi_{\boldsymbol{k}\alpha}(t)\rangle$ denotes the Floquet state [see Eq. (3.15) for definition] with quasienergy $\varepsilon_{\boldsymbol{k}\alpha}$. The Chern number counts the number of times $\hat{n}_{\boldsymbol{k}\alpha}$ covers the Bloch sphere upon variation across a the Brillouin zone (BZ) [167, 239]:

$$C_\alpha = \int_{\mathrm{BZ}} \frac{d^2\boldsymbol{k}}{(2\pi)^2} \hat{n}_{\boldsymbol{k}\alpha}(t) \cdot [\partial_{k_x}\hat{n}_{\boldsymbol{k}\alpha}(t) \times \partial_{k_y}\hat{n}_{\boldsymbol{k}\alpha}(t)], \tag{3.55}$$

which is a generalization of the definition for a two-level static Hamiltonian, see Eq. (2.38). For a gapped graphene system, variations of the pseudospin are confined to regions around the K and K' valley, so it is easiest to compute contributions to C_α from the K and K' valley separately. In what follows, we use C^α_{+1} and C^α_{-1} to respectively denote the contributions to the Chern number from the K and K' valleys, the sum of which is the total Chern number of the band α, i.e., $C_\alpha = C^\alpha_{+1} + C^\alpha_{-1}$.

For concreteness, we begin by focusing on the $\alpha = -$ Floquet band [see band boxed in orange in Figure 3.3(a)] near the K valley of the gapped graphene system. To

count the winding of the pseudospin in the region near the K valley, our approach is to consider the pseudospin along "rings" in momentum space with radius k and centered around the K point [see green curves in Figure 3.3(b) for an illustration]. We begin near the K point and track the changes in the pseudospin configuration as the ring radius k is increased. It is useful to first start by considering momenta far from the resonance ring (defined by $|\boldsymbol{k}| = k_R$ and $2E_{\boldsymbol{k}} = \hbar\omega$) where the pseudospin configuration is particularly simple:

- Region $k \ll k_R$: near $k = 0$, the pseudospin is roughly aligned with the polar axis ($\hat{z}$-axis), with a direction set by the sign of mass gap Δ, i.e., $\hat{n}_{\boldsymbol{k}-} \approx \text{sign}(\Delta_\xi)\hat{z}$ [see Figure 3.3(c)].
- Region $k \gg k_R$: in this regime, the pseudospin is roughly identical to the pseudospin of the undriven valence band, so $\hat{n}_{\boldsymbol{k}-} \approx \hat{\boldsymbol{k}}$, where $\hat{\boldsymbol{k}} = \boldsymbol{k}/k$ [see Figure 3.3(e)].

Thus, as the "rings" in momentum space [green curves in Figure 3.3(b)] increase in radius, the pseudospin is initially aligned with the polar axis of the Bloch sphere ($\hat{n}_{\boldsymbol{k}-} = \text{sign}(\Delta_\xi)\hat{z}$) and eventually winds to its equator ($\hat{n}_{\boldsymbol{k}-} = \hat{\boldsymbol{k}}$) at large k, covering a solid angle of $2\pi\ \text{sign}(\Delta_\xi)$. However, it would be incorrect to immediately conclude that the Chern number is given by $C_{+1} = \frac{1}{2}\text{sign}(\Delta_\xi)$. In fact, there are multiple paths that the pseudospin can take to wind from the polar axis to the equator, which can in general cover the Bloch sphere an additional integer number of times. Therefore, we expect that $C_{+1} = \frac{1}{2}\text{sign}(\Delta_\xi) + n$, where $n \in \mathbb{Z}$. Our next task is to determine n based on the RWA Hamiltonian.

The value of n can be determined by counting the number of times the pseudospin winds around the polar axis along the resonance ring [see Figure 3.3(d)] [130, 167, 239]. To proceed, we use the RWA Hamiltonian,

$$H_{\text{RWA}}(t) \equiv \begin{pmatrix} 0 & (\tilde{V}_x - i\tilde{V}_y)e^{-i\omega t} \\ (\tilde{V}_x + i\tilde{V}_y)e^{i\omega t} & 0 \end{pmatrix}, \tag{3.56}$$

to calculate the pseudospin configuration on the resonance ring. We focus on the pseudospin texture at time $t = 0$, but the results can be shown to be equivalent at all other times. We first transform $H_{\text{RWA}}(0)$ to the original sublattice basis of the Hamiltonian:

$$U^\dagger(\theta_{\boldsymbol{k}}, \phi_{\boldsymbol{k}})H_{\text{RWA}}(0)U(\theta_{\boldsymbol{k}}, \phi_{\boldsymbol{k}}) = \boldsymbol{d}_{\text{RWA}} \cdot \boldsymbol{\sigma}, \tag{3.57}$$

where

$$\boldsymbol{d}_{\mathrm{RWA}} = \frac{1}{2}\begin{pmatrix} \tilde{V}_x \cos\phi_{\boldsymbol{k}} \cos\theta_{\boldsymbol{k}} - \tilde{V}_y \sin\phi_{\boldsymbol{k}} \\ \tilde{V}_x \sin\phi_{\boldsymbol{k}} \cos\theta_{\boldsymbol{k}} + \tilde{V}_y \cos\phi_{\boldsymbol{k}} \\ -2\tilde{V}_x \sin\theta_{\boldsymbol{k}} \end{pmatrix}. \tag{3.58}$$

The expression for $\boldsymbol{d}_{\mathrm{RWA}}$ allows us to compute the pseudospin along the resonance ring, given by $\hat{n}_{\boldsymbol{k}-}(0) = -\hat{\boldsymbol{d}}_{\mathrm{RWA}}$, where $\hat{\boldsymbol{d}}_{\mathrm{RWA}} = \boldsymbol{d}_{\mathrm{RWA}}/|\boldsymbol{d}_{\mathrm{RWA}}|$. In Figure 3.4, we plot the trajectory traced out by $\hat{n}_{\boldsymbol{k}-}(0)$ (red curve) as a function of $\phi_{\boldsymbol{k}}$, with $\theta_{\boldsymbol{k}}$ fixed by the resonance condition:

$$\theta_{\boldsymbol{k}} = \arctan\left(\frac{\Delta_\xi/2}{\hbar v_F k_R}\right). \tag{3.59}$$

Figure 3.4(a) considers the case $\mathrm{sign}(\Delta_\xi \xi \eta) > 0$ and shows that $\hat{\boldsymbol{d}}_{\mathrm{RWA}}$ winds twice around the polar axis. Whether the pseudospin winds counterclockwise or clockwise around the polar axis is determined by η, so $n = 2\eta$. Figure 3.4(b) considers the case $\mathrm{sign}(\Delta_\xi \xi \eta) < 0$ and shows that $\hat{\boldsymbol{d}}_{\mathrm{RWA}}$ does not wind around the polar axis, in which case $n = 0$.

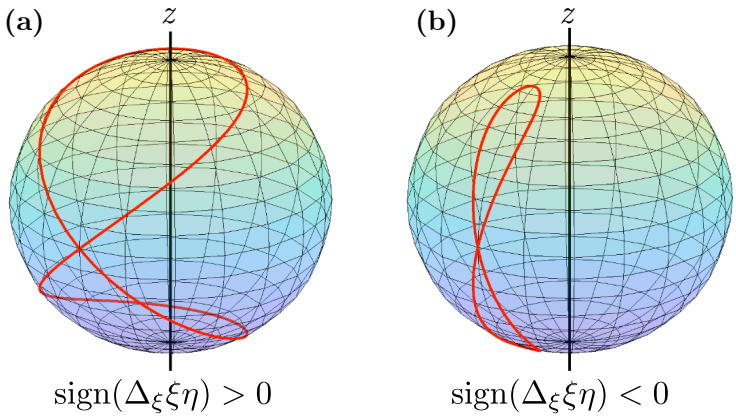

Figure 3.4: Path (red curve) traced out by the pseudospin $\hat{n}_{\boldsymbol{k}-}(0)$ upon variation across the resonance ring [see Figure 3.3(d)]. (a) The case of $\mathrm{sign}(\Delta_\xi \xi \eta) > 0$, in which case the pseudospin winds around the polar axis (sketched by a black line) 2 times. (b) The case of $\mathrm{sign}(\Delta_\xi \xi \eta) < 0$, in which case the pseudospin does not wind around the polar axis.

The arguments can be generalized to the K' valley. In general, the valley indexed by ξ contributes a Chern number given by [239],

$$C_\xi^- = \frac{1}{2}\mathrm{sign}(\Delta_\xi \xi) + \begin{cases} 2\eta & \text{if } \mathrm{sign}(\Delta_\xi \xi \eta) > 0 \\ 0 & \text{if } \mathrm{sign}(\Delta_\xi \xi \eta) < 0. \end{cases} \tag{3.60}$$

Case of graphene. In graphene, although there is no mass gap in the equilibrium system, the K and K' points are not gapless due to the opening of the drive-induced Haldane gap, see Eq. (3.44). In the analysis above, we therefore replace Δ_ξ with Δ_K, defined in Eq. (3.44). Because $\text{sign}(\Delta_K) = -\xi\eta$, substitution into Eq. (3.60) yields

$$C_\xi^- = -\frac{1}{2}\eta + 2\eta. \tag{3.61}$$

In a gapless graphene system, the circularly polarized driving field therefore induces a Floquet band with a net Chern number of $C_\alpha = -3\eta(-1)^\alpha$.

3.6 Topological Transport in Floquet Systems

The following section is based on Ref. [74].

Having understood the origin of drive-induced topology in Floquet systems, we now discuss how drive-induced topology can be detected from the transport responses of Floquet systems to weak electric fields.

First, we introduce the anomalous velocity in the Floquet basis by defining the Berry curvature of a Floquet state, given by

$$\boldsymbol{\Omega}_{\boldsymbol{k}\alpha}(t) = \nabla_{\boldsymbol{k}} \times \boldsymbol{A}_{\boldsymbol{k}n}(t), \tag{3.62}$$

where $\boldsymbol{A}_{\boldsymbol{k}n}(t) = i\langle\psi_{\boldsymbol{k}n}(t)|\nabla_{\boldsymbol{k}}|\psi_{\boldsymbol{k}n}(t)\rangle$ denotes the Berry connection and $|\psi_{\boldsymbol{k}n}(t)\rangle$ is the Floquet state of a time-periodic Hamiltonian $H(t)$. Note that the Chern number of the Floquet band, introduced in Eq. (3.55), can equivalently be calculated via integration of $\boldsymbol{\Omega}_{\boldsymbol{k}\alpha}(t)$ across the Brillouin zone:

$$C_\alpha = \frac{1}{2\pi}\int d^2\boldsymbol{k}\ \boldsymbol{\Omega}_{\boldsymbol{k}\alpha}(t)\cdot\hat{z}. \tag{3.63}$$

For our purposes, we are interested in transport responses or many-body collision processes on timescales much longer than the frequency of the drive [257, 258]. In this case, we focus on the time-averaged anomalous velocity of electrons, which can be calculated using the time-averaged Berry curvature given by

$$\boldsymbol{\Omega}_{\boldsymbol{k}\alpha} = \nabla_{\boldsymbol{k}} \times \boldsymbol{A}_{\boldsymbol{k}n}. \tag{3.64}$$

Here, $\boldsymbol{A}_{\boldsymbol{k}n}(t) = i\sum_n\langle\phi^n_{\boldsymbol{k}n}|\nabla_{\boldsymbol{k}}|\phi^n_{\boldsymbol{k}n}\rangle$ denotes the time-averaged Berry connection and $|\phi^n_{\boldsymbol{k}n}\rangle$ are the Floquet harmonics, obtained by expanding the Floquet state in the harmonic series:

$$|\psi_{\boldsymbol{k}n}(t)\rangle = e^{-i\varepsilon_{\boldsymbol{k}n}}\sum_n e^{-im\omega t}|\phi^n_{\boldsymbol{k}n}\rangle. \tag{3.65}$$

In the presence of a weak electric field $\boldsymbol{E}$, the average group velocity of electrons is therefore given by

$$\boldsymbol{v}_{\boldsymbol{k}\alpha} = \frac{1}{\hbar}\nabla_{\boldsymbol{k}}\varepsilon_{\boldsymbol{k}\alpha} + \frac{e}{\hbar}\boldsymbol{E}\times\boldsymbol{\Omega}_{\boldsymbol{k}\alpha}, \tag{3.66}$$

which is derived in a similar manner as Section 2.3, by assuming that the weak electric field produces an *adiabatic* evolution of the Floquet states.

To determine the current produced by the electric field, we estimate the occupation $\tilde{F}_{\boldsymbol{k}\alpha}$ of the Floquet state $|\psi_{\boldsymbol{k}n}(t)\rangle$ in the presence of the electric field. When the occupation is spatially homogenous across the system, its time evolution can be estimated from the Boltzmann transport equation given by

$$\partial_t\tilde{F}_{\boldsymbol{k}\alpha} - \frac{e}{\hbar}\boldsymbol{E}\cdot\nabla_{\boldsymbol{k}}\tilde{F}_{\boldsymbol{k}\alpha} = -\frac{\tilde{F}_{\boldsymbol{k}\alpha} - F_{\boldsymbol{k}\alpha}}{\tau_{\boldsymbol{k}\alpha}}. \tag{3.67}$$

Here, we have used the relaxation time approximation, which assumes that the occupation relaxes to its value $F_{\boldsymbol{k}\alpha}$ in the absence of the electric field within a relaxation time $\tau_{\boldsymbol{k}\alpha}$. We are interested in the population distribution of electrons in the steady state, defined by $\partial_t\tilde{F}_{\boldsymbol{k}\alpha} = 0$, which is given by

$$\tilde{F}_{\boldsymbol{k}\alpha} = F_{\boldsymbol{k}\alpha} - \frac{e}{\hbar}\tau_{\boldsymbol{k}\alpha}E\partial_{k_x}F_{\boldsymbol{k}\alpha}. \tag{3.68}$$

The Hall conductivity in the steady state is therefore given by

$$\sigma_{xy} = \frac{e^2}{\hbar}\sum_{\alpha}\int\frac{d^2\boldsymbol{k}}{(2\pi)^2}\boldsymbol{\Omega}_{\boldsymbol{k}\alpha}\cdot\hat{z}\,F_{\boldsymbol{k}\alpha}, \tag{3.69}$$

and the longitudinal conductivity is given by

$$\sigma_{xx} = \frac{e^2}{\hbar}\sum_{\alpha}\int\frac{d^2\boldsymbol{k}}{(2\pi)^2}\tau_{\boldsymbol{k}\alpha}(\partial_{k_x}\varepsilon_{\boldsymbol{k}\alpha})(\partial_{k_x}F_{\boldsymbol{k}\alpha}). \tag{3.70}$$

The discussion of transport signatures in Floquet systems thus far inspires questions about what sets the steady-state occupations of Floquet states $F_{\boldsymbol{k}\alpha}$ *before* the application of the weak electric field. The steady state is governed by the incoherent dynamics of electrons generated by many-body collisions, which will be the topic of Chapter 4.

Chapter 4

INCOHERENT DYNAMICS OF FLOQUET SYSTEMS

In an interacting electronic Floquet system, the laws of equilibrium statistical mechanics that normally guarantee Fermi-Dirac statistics no longer apply [257, 258]. Photo-assisted many-body collisions sharply modify the occupation of electronic states, producing a dramatically different population distribution from equilibrium. In this chapter, we show that electron-phonon coupling to a low-temperature phonon bath, in particular, can serve as a mechanism to stabilize a low-temperature "ideal Floquet topological insulator" population distribution supporting topological transport signatures.

We focus on a model of a many-body interacting system coupled to an external phonon bath, described by the Hamiltonian

$$\hat{H} = \hat{H}_0 + \hat{H}_{\text{el-ph}} + \hat{H}_{\text{el-el}}. \tag{4.1}$$

Here, the single-particle Hamiltonian is given by

$$\hat{H}_0 = \sum_{\boldsymbol{k},\nu} E_{\boldsymbol{k}\nu} \hat{c}^\dagger_{\boldsymbol{k}\nu} \hat{c}_{\boldsymbol{k}\nu}, \tag{4.2}$$

where $\hat{c}^\dagger_{\boldsymbol{k}\nu}$ creates a Bloch state $|\boldsymbol{k}\nu\rangle$ with energy $E_{\boldsymbol{k}\nu}$. The electron-phonon interactions are described by the Hamiltonian

$$\hat{H}_{\text{el-ph}} = \sum_{\boldsymbol{k},\boldsymbol{q},j,\nu,\nu'} M^{\nu\nu'}_{\boldsymbol{k},\boldsymbol{q}} \hat{c}^\dagger_{\boldsymbol{k}+\boldsymbol{q},\nu'} c_{\boldsymbol{k}\nu} (\hat{b}^\dagger_{\boldsymbol{q},j} + \hat{b}_{-\boldsymbol{q},j}) + \text{H.c.} \tag{4.3}$$

and the electron-electron interactions are modeled by

$$\hat{H}_{\text{el-el}} = \sum_{\boldsymbol{k}_1,\boldsymbol{k}_2,\boldsymbol{q},\{\nu_i\}} V^{\{\nu_i\}}_{\boldsymbol{k}_1,\boldsymbol{k}_2,\boldsymbol{q}} \hat{c}^\dagger_{\boldsymbol{k}_1+\boldsymbol{q},\nu_1} \hat{c}^\dagger_{\boldsymbol{k}_2-\boldsymbol{q},\nu_2} \hat{c}_{\boldsymbol{k}_2\nu_3} \hat{c}_{\boldsymbol{k}_1\nu_4}, \tag{4.4}$$

where $\hat{b}^\dagger_{\boldsymbol{q},j}$ creates a phonon of frequency $\omega_j(\boldsymbol{q})$ with momentum $\boldsymbol{q}$ and mode indexed by j, and $M^{\nu\nu'}_{\boldsymbol{k},\boldsymbol{q}}$ and $V^{\{\nu_i\}}_{\boldsymbol{k}_1,\boldsymbol{k}_2,\boldsymbol{q}}$ are the matrix elements for electron-phonon and electron-electron interactions, respectively [258]. Upon driving the system with a laser field of magnetic vector potential $\boldsymbol{A}(t)$ and angular frequency Ω, the Hamiltonian becomes time-dependent $\hat{H}_0(t)$ via minimal coupling $\boldsymbol{k} \to \boldsymbol{k} + e\boldsymbol{A}(t)/\hbar$, and the time-dependent Schrodinger equation is solved by the Floquet states $|\psi_{\boldsymbol{k}\alpha}(t)\rangle$

with quasienergies $\varepsilon_{\boldsymbol{k}\alpha}$, as discussed in Chapter 3. The occupations of the Floquet states, given by $F_{\boldsymbol{k}\alpha}(t) = \langle \hat{f}^\dagger_{\boldsymbol{k}\alpha}(t)\hat{f}_{\boldsymbol{k}\alpha}(t)\rangle$, where $\hat{f}^\dagger_{\boldsymbol{k}\alpha}(t)$ denotes the creation operator for $|\psi_{\boldsymbol{k}\alpha}(t)\rangle$, are determined by the incoherent dynamics of the electrons generated by $\hat{H}_{\text{el-ph}}$ and $\hat{H}_{\text{el-el}}$. Our goal is to evaluate the occupations in the long time limit, when the system approaches a steady state with occupation given by $F_{\boldsymbol{k}\alpha}$, which is time-independent, $\dot{F}_{\boldsymbol{k}\alpha} = 0$, up to micromotion. In Section 4.1, we introduce the Floquet-Boltzmann equation, which models the population dynamics of Floquet systems when the interactions $\hat{H}_{\text{el-el}}$ and $\hat{H}_{\text{el-ph}}$ are weak perturbations to the single-particle Hamiltonian $\hat{H}_0(t)$. The remainder of the chapter is concerned with solving for the steady state and finding conditions that stabilize low-temperature phases, see Section 4.2, and understanding the stability of Floquet-Bloch states in a steady state, see Section 4.3.

4.1 Floquet-Boltzmann Equation

The following section is based on Refs. [257–259].

The Floquet-Boltzmann equation provides a framework to characterize the many-body steady state of Floquet systems under the following assumptions:

1. *Born-Markov approximation.* We assume that the incoherent phonons thermalize much faster than the rate of electron-phonon scattering, such that the incoherent phonons remain in thermal equilibrium at all times and can be described by a Bose-Einstein distribution.

2. *Diagonal ensemble and perturbative interactions.* We assume that coherences between the Floquet states are negligible, i.e., $\langle \hat{f}^\dagger_{\boldsymbol{k}'\alpha'}(t)\hat{f}_{\boldsymbol{k}\alpha}(t)\rangle \approx 0$ for $\boldsymbol{k}' \neq \boldsymbol{k}$ or $\alpha \neq \alpha'$. This is an appropriate approximation when the steady state is translation invariant and the interactions are *perturbative*, such that the scattering time τ_{scat} between Floquet states is much larger than the inverse spectral gap Δ between the Floquet states, i.e., $\tau_{\text{scat}} \gg \hbar/\Delta$.

3. *Slow scattering dynamics.* We assume that the characteristic timescale for scattering τ_{scat} is much longer than the period of the drive, i.e., $\tau_{\text{scat}} \gg 2\pi/\Omega$, such that only the slow (stroboscopic-timescale) evolution of the electronic occupations affect the incoherent scattering processes. In this limit, we can simplify the analysis by discarding the micromotion of the population dynamics.

Explicitly, the Floquet-Boltzmann equation is given by

$$\dot{F}_{\boldsymbol{k}\alpha} = I^{\text{el-ph}}_{\boldsymbol{k}\alpha}[\{F_{\boldsymbol{k}\alpha}\}] + I^{\text{el-el}}_{\boldsymbol{k}\alpha}[\{F_{\boldsymbol{k}\alpha}\}], \tag{4.5}$$

where $I^{\text{el-ph}}_{\boldsymbol{k}\alpha}[\{F_{\boldsymbol{k}\alpha}\}]$ and $I^{\text{el-el}}_{\boldsymbol{k}\alpha}[\{F_{\boldsymbol{k}\alpha}\}]$ are respectively the collision integrals for electron-phonon and electron-electron scattering. In the following subsections, we provide the explicit forms for $I^{\text{el-ph}}_{\boldsymbol{k}\alpha}[\{F_{\boldsymbol{k}\alpha}\}]$ and $I^{\text{el-el}}_{\boldsymbol{k}\alpha}[\{F_{\boldsymbol{k}\alpha}\}]$ and provide an intuitive explanation for the population dynamics generated by the many-body collisions.

Electron-Phonon Scattering

The electron-phonon collision integral is given by

$$\begin{aligned} I^{\text{el-ph}}_{\boldsymbol{k}\alpha}[\{F_{\boldsymbol{k}\alpha}\}] = \frac{2\pi}{\hbar}\frac{1}{N}\sum_{\boldsymbol{k}'\in\text{BZ}}\sum_{\alpha'}\sum_{j}\sum_{n}|\mathcal{G}^{\boldsymbol{k}'\alpha'}_{\boldsymbol{k}\alpha}(n,j)|^2 \\ \times\Big[\left\{F_{\boldsymbol{k}'\alpha'}(1-F_{\boldsymbol{k}\alpha})\mathcal{N}(\hbar\omega_j(\boldsymbol{k}'-\boldsymbol{k})) - F_{\boldsymbol{k}\alpha}(1-F_{\boldsymbol{k}'\alpha'})[1+\mathcal{N}(\hbar\omega_j(\boldsymbol{k}'-\boldsymbol{k}))]\right\} \\ \times\delta(\varepsilon_{\boldsymbol{k}'\alpha'}+n\hbar\Omega-\varepsilon_{\boldsymbol{k}\alpha}+\hbar\omega_j(\boldsymbol{q})) \\ +\left\{F_{\boldsymbol{k}'\alpha'}(1-F_{\boldsymbol{k}\alpha})[1+\mathcal{N}(\hbar\omega_j(\boldsymbol{k}'-\boldsymbol{k}))] - F_{\boldsymbol{k}\alpha}(1-F_{\boldsymbol{k}'\alpha'})\mathcal{N}(\hbar\omega_j(\boldsymbol{k}'-\boldsymbol{k}))\right\} \\ \times\delta(\varepsilon_{\boldsymbol{k}'\alpha'}+n\hbar\Omega-\varepsilon_{\boldsymbol{k}\alpha}-\hbar\omega_j(\boldsymbol{q}))\Big], \end{aligned} \tag{4.6}$$

where

$$\mathcal{G}^{\boldsymbol{k}'\alpha'}_{\boldsymbol{k}\alpha}(n,j) = \sum_{m}\sum_{\nu,\nu'} M^{\nu\nu'}_{\boldsymbol{k},\boldsymbol{q}}\langle\phi^{n+m}_{\boldsymbol{k}'\alpha'}|\nu'\boldsymbol{k}'\rangle\langle\nu\boldsymbol{k}|\phi^{m}_{\boldsymbol{k}\alpha}\rangle \tag{4.7}$$

is the photon dressed electron-phonon matrix element in the Floquet basis, $\mathcal{N}(\varepsilon) = (e^{\varepsilon/k_BT}-1)^{-1}$ is the Bose-Einstein distribution for the incoherent phonons maintained at temperature T, and k_B is the Boltzmann constant. To provide intuition for the collision integral, it is useful to consider the low-temperature limit $T\to 0$, in which case $\mathcal{N}(\varepsilon)\to 0$. In this limit, the collision integral, Eq. (4.6), reduces to:

$$\begin{aligned} \lim_{T\to 0} I^{\text{el-ph}}_{\boldsymbol{k}\alpha}[\{F_{\boldsymbol{k}\alpha}\}] = \frac{2\pi}{\hbar}\frac{1}{N}\sum_{\boldsymbol{k}'\in\text{BZ}}\sum_{\alpha'}\sum_{j}\sum_{n}|\mathcal{G}^{\boldsymbol{k}'\alpha'}_{\boldsymbol{k}\alpha}(n,j)|^2 \\ \times\Big[-F_{\boldsymbol{k}\alpha}(1-F_{\boldsymbol{k}'\alpha'})\delta(\varepsilon_{\boldsymbol{k}'\alpha'}+n\hbar\Omega-\varepsilon_{\boldsymbol{k}\alpha}+\hbar\omega_j(\boldsymbol{q})) \\ +F_{\boldsymbol{k}'\alpha'}(1-F_{\boldsymbol{k}\alpha})\delta(\varepsilon_{\boldsymbol{k}'\alpha'}+n\hbar\Omega-\varepsilon_{\boldsymbol{k}\alpha}-\hbar\omega_j(\boldsymbol{q}))\Big]. \end{aligned} \tag{4.8}$$

The first term in brackets represents a sink term, scattering an electron out of the state with quasienergy $\varepsilon_{\boldsymbol{k}\alpha}$ into a state with quasienergy $\varepsilon_{\boldsymbol{k}'\alpha'}+n\hbar\Omega$. Since the phonon frequency is a positive quantity, $\hbar\omega_j(\boldsymbol{q})>0$, the Dirac Delta function ensures the process is only possible when the quasienergy is lowered during the process, i.e.,

$\varepsilon_{\boldsymbol{k}'\alpha'}+n\hbar\Omega < \varepsilon_{\boldsymbol{k}\alpha}$, corresponding to a phonon *emission*. This kinematic constraint is imposed because phonons can only be emitted to, and not be absorbed from, a zero-temperature phonon bath. The second term is a source term, scattering an electron with quasienergy $\varepsilon_{\boldsymbol{k}'\alpha'} + n\hbar\Omega$ into the state with quasienergy $\varepsilon_{\boldsymbol{k}\alpha}$. Once again, the Dirac Delta function ensures that the quasienergy is lowered during the process, i.e., $\varepsilon_{\boldsymbol{k}'\alpha'} + n\hbar\Omega > \varepsilon_{\boldsymbol{k}\alpha}$, such that a phonon is emitted. The occupation functions appearing in Eq. (4.8) account for Pauli blocking, ensuring that no scattering process can be completed if the initial state is empty or the final state is full.

Electron-Electron Scattering

The electron-electron collision integral is given by

$$I^{\text{el-el}}_{\boldsymbol{k}\alpha}[\{F_{\boldsymbol{k}\alpha}\}] = \frac{4\pi}{\hbar}\frac{1}{N^2}\sum_{\boldsymbol{k}_2\in\text{BZ}}\sum_{\boldsymbol{k}_3\in\text{BZ}}\sum_{\alpha_2,\alpha_3,\alpha_4}\sum_{n}\sum_{\boldsymbol{G}}|\mathcal{V}^{(\boldsymbol{k}_3,\alpha_3),(\boldsymbol{k}_1+\boldsymbol{k}_2-\boldsymbol{k}_3,\alpha_4)}_{(\boldsymbol{k},\alpha),(\boldsymbol{k}_2,\alpha_2)}(n,\boldsymbol{G})|^2\times$$
$$\times\,\delta(\varepsilon_{\boldsymbol{k}\alpha}+\varepsilon_{\boldsymbol{k}_2\alpha_2}-\varepsilon_{\boldsymbol{k}_3\alpha_3}-\varepsilon_{\boldsymbol{k}+\boldsymbol{k}_2-\boldsymbol{k}_3,\alpha_4}+n\hbar\Omega)\big[(1-F_{\boldsymbol{k}\alpha})(1-F_{\boldsymbol{k}_2\alpha_2})F_{\boldsymbol{k}_3\alpha_3}F_{\boldsymbol{k}_1+\boldsymbol{k}_2-\boldsymbol{k}_3,\alpha_4}$$
$$-F_{\boldsymbol{k}\alpha}F_{\boldsymbol{k}_2\alpha_2}(1-F_{\boldsymbol{k}_3\alpha_3})(1-F_{\boldsymbol{k}_1+\boldsymbol{k}_2-\boldsymbol{k}_3,\alpha_4})\big], \tag{4.9}$$

where

$$\mathcal{V}^{(\boldsymbol{k}_3,\alpha_3),(\boldsymbol{k}_1+\boldsymbol{k}_2-\boldsymbol{k}_3,\alpha_4)}_{(\boldsymbol{k},\alpha),(\boldsymbol{k}_2,\alpha_2)}(n) = \sum_{\nu_1,\nu_2}\sum_{\nu_3,\nu_4}\sum_{n_2,n_3,n_4}V^{\{\nu_i\}}_{\boldsymbol{k},\boldsymbol{k}_2,\boldsymbol{k}_4-\boldsymbol{k}_2}\langle\phi^{n-n_2+n_3+n_4}_{\boldsymbol{k}\alpha}|\nu_1\boldsymbol{k}\rangle\langle\phi^{n_2}_{\boldsymbol{k}_2\alpha_2}|\nu_2\boldsymbol{k}_2\rangle\times$$
$$\times\,\langle\nu_3\boldsymbol{k}_3|\phi^{n_3}_{\boldsymbol{k}_3\alpha_3}\rangle\langle\nu_4\boldsymbol{k}_4|\phi^{n_4}_{\boldsymbol{k}+\boldsymbol{k}_2-\boldsymbol{k}_3,\alpha_4}\rangle \tag{4.10}$$

is the photon-dressed electron-electron matrix element in the Floquet basis. The collision integral, Eq. (4.9), describes a two-electron scattering process. Note that, although the total momentum is conserved, the total quasienergy is conserved only up to an integer multiple of $\hbar\Omega$ [see Dirac Delta function in Eq. (4.9)], which accounts for photoabsorption and emission, as will be discussed in Section 4.2.

4.2 Solving for the Steady State

The following section is based on Refs. [75, 258].

To solve for the steady state condition, given by $\dot{F}_{\boldsymbol{k}\alpha} = 0$, we first identify the microscopic collision processes that enter the FBE. For concreteness, we focus on a simple resonantly-driven semiconducting system, with the quasienergy band structure shown in Figure 4.1. Because the quasienergy is defined modulo $\hbar\omega$, we can sketch two equivalent representations of the quasienergy bands. The first is the

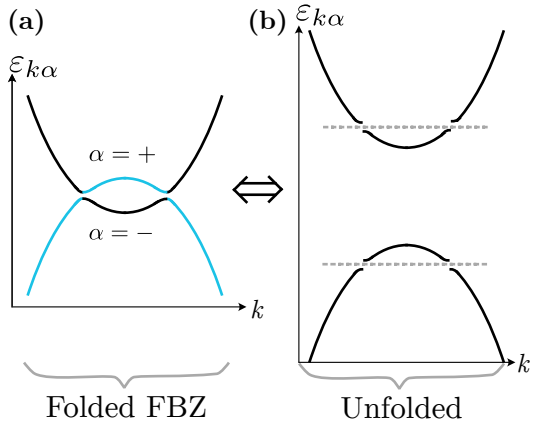

Figure 4.1: The quasienergy of the driven system is defined modulo $\hbar\omega$. In our discussion of the Floquet Boltzmann equation, it is convenient to consider two choices of the quasienergy bands. (a) The "folded" Floquet Brillouin Zone (FBZ) picture is analogous to the rotating frame in the rotating wave approximation, where states with band character corresponding to the valence band of the undriven system are shifted in energy by $+\hbar\Omega$. (b) The "unfolded" picture where the quasienergies are shifted such that quasienergy spectrum resembles the original bands, except with a gap opening at resonance. Dashed lines indicate $\pm\hbar\Omega/2$.

"folded" Floquet Brillouin zone (FBZ) picture analogous to the rotating frame in the rotating wave approximation, where states with band character corresponding to the valence band of the undriven system are shifted in energy by $+\hbar\omega$ [Figure 4.1(a)]. In the folded representation, we sketch the original electronic band in black and the shifted valence band in blue. The second representation is the "unfolded" picture where the quasienergies are shifted such that quasienergy spectrum resembles the original bands, except with a gap opening at resonance [Figure 4.1(b)]. We will interchange between the two equivalent representations of the quasienergy structure, depending on which allows for a more convenient visualization the many-body scattering process in question.

The weak electron-phonon and electron-electron interactions described by the FBE scatter electrons between single-particle Floquet states. These collision processes can be categorized into two types:

- Regular scattering processes, sketched in Figure 4.2 for electron-phonon interactions [panel (a) and (b)] and electron-electron interactions [panel (c) and (d)]. These processes exist even in the equilibrium setting and restore electronic populations back to the thermal Fermi-Dirac distribution in the undriven bands. In the unfolded picture [panels (b) and (d)], it is clear that these

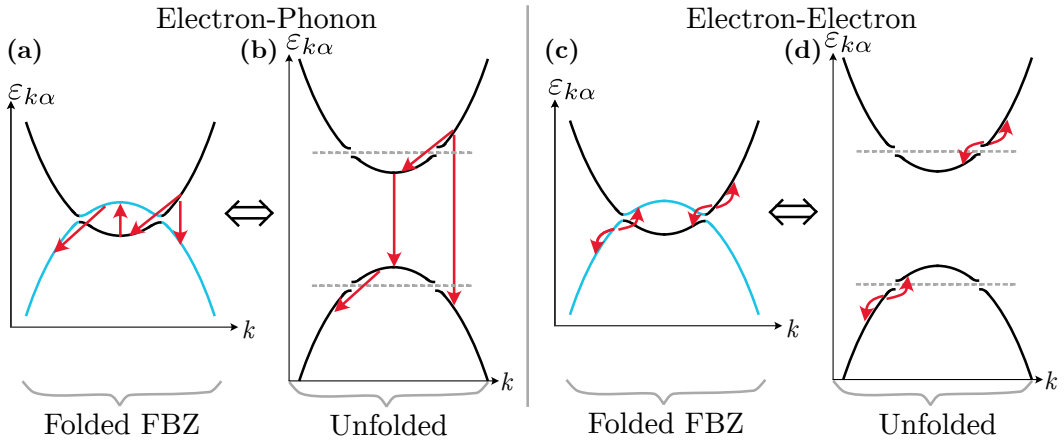

Figure 4.2: Sketch of "regular" electron-phonon and electron-electron scattering processes that do not rely on photoemission and photoabsorption to conserve energy and momentum. In the folded picture [panels (a) and (c)], these scattering processes only connect the same Floquet copies [i.e. states sketched with the same color]. When the processes are sketched on the unfolded bands [see panels (b) and (d)], it becomes clear that no photoabsorption or emission is required to conserve energy-momentum in the scattering processes.

scattering processes conserve energy and momentum without absorption or emission of photons.

- Floquet-Umklapp (FU) processes (photo-assisted scattering). These processes perturb the steady state distribution away from the equilibrium Fermi-Dirac distribution and rely on photon absorption or emission to achieve energy-momentum conservation. First-order FU processes are sketched in Figures 4.3 and 4.4 for electron-phonon and electron-electron interactions, respectively, emitting or absorbing a single photon. We show the FU scattering processes in the unfolded picture [Figures 4.3(b)-(d), 4.4(b), and 4.4(d)] to emphasize that these first-order FU processes conserve energy and momentum only up to $\pm\hbar\Omega$, which corresponds to an absorption or emission of a single photon (sketched by a blue squiggly line). Note that higher-order FU processes, which absorb or emit more than one photon, occur with suppressed probability for sufficiently weak drives [257, 258].

To approximate the electronic steady state in the presence of the scattering processes discussed above, we consider the FBE for the average density of electrons in each

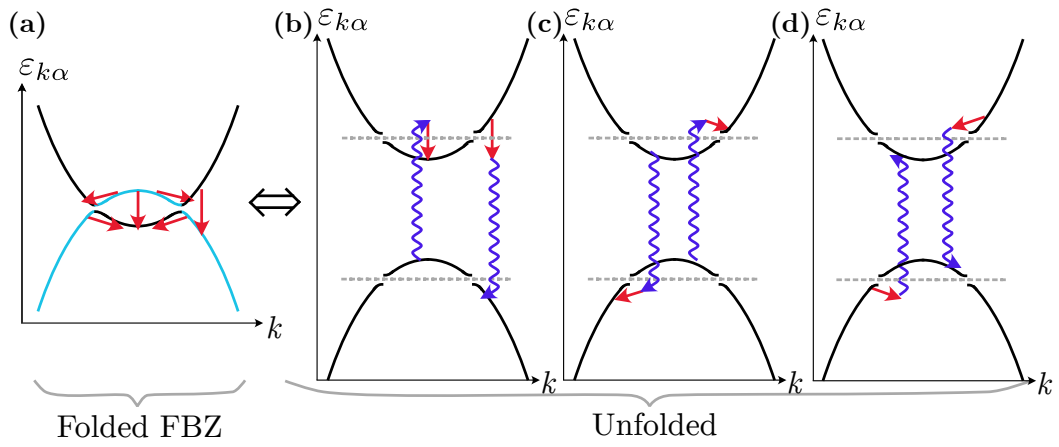

Figure 4.3: Sketch of electron-phonon Floquet-Umklapp scattering processes that absorb or emit a single photon. In the folded picture [panel (a)], these scattering processes connect different Floquet copies [i.e., states sketched with different color]. When the processes are sketched on the unfolded bands [see panels (b-d)], it is clear that the scattering relies on an absorption or emission of a single photon (squiggly blue lines) to conserve energy and momentum.

Floquet band, given by

$$n_\alpha = A \int \frac{d^2\boldsymbol{k}}{(2\pi)^2} F_{\boldsymbol{k}\alpha} \tag{4.11}$$

where A denotes the area of the unit cell and $\alpha = +, -$ indexes the upper (UFB) and lower Floquet bands (LFB), respectively, in the folded picture [see Figure 4.1(a)]. To further simplify the analysis, we focus on a charge neutral system, where a single variable, $n \equiv n_+ = 1 - n_-$, parameterizes the density of electrons (holes) in the LFB (UFB). To construct a rate equation for n, we consider the collisions sketched in Figures 4.2, 4.3, and 4.4 that connect different Floquet bands.

Electron-Phonon Scattering

The occupation function n is modified by interband electron-phonon scattering processes in the folded picture, sketched by vertical lines in Figures 4.2 and 4.3. Scattering processes connecting the UFB band to the LFB band are proportional to the density of electrons in the UFB and holes in the LFB, both given by $1 - n$. Therefore, such a process occurs with a rate given by $\dot{n}|^{\text{ph}}_{\text{in}} = W^{\text{ph}}_{\text{in}}(1-n)^2$, where $W^{\text{ph}}_{\text{in}}$ is an occupation-independent intrinsic scattering rate set by the electron-phonon matrix element [see Eq. (4.6)]. Similarly, we define an intrinsic scattering rate $W^{\text{ph}}_{\text{out}}$ for collision processes from the LFB to the UFB, which occur with a rate given by $\dot{n}|^{\text{ph}}_{\text{out}} = -W^{\text{ph}}_{\text{out}} n^2$.

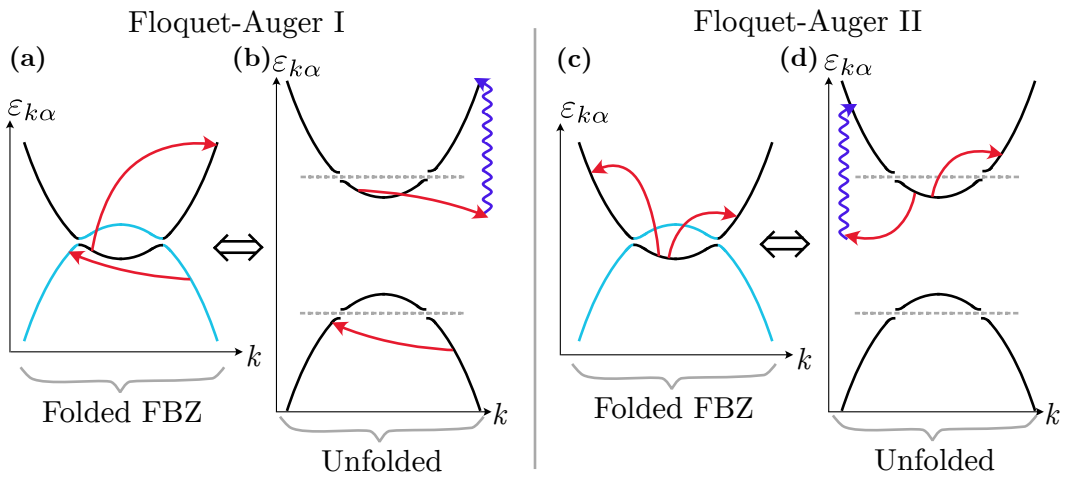

Figure 4.4: Sketch of electron-electron Floquet-Umklapp scattering processes that absorb or emit a single photon, categorized as Floquet-Auger I and II which transfer a single or pair of electrons across distinct Floquet bands. We sketch the scattering processes in the folded picture in panels (a) and (c) and the unfolded picture in panels (b) and (d). In the unfolded picture, it is clear that the scattering relies on an absorption or emission of a single photon (squiggly blue lines) to conserve energy and momentum.

Electron-Electron Scattering

Electron-electron scattering processes facilitate collision processes changing (interband) or preserving (intraband) the total particle density within each Floquet band. The interband scattering processes primarily arise from photo-assisted FU processes, which can be divided into two types: Floquet-Auger I (or "single" Floquet-Auger) collisions, transferring a single electron between distinct Floquet bands; and Floquet-Auger II (or "double" Floquet-Auger) collisions, transferring two electrons between distinct Floquet bands, see Figure 4.4. These Floquet-Auger processes are the primary electron-electron scattering processes affecting the LFB occupation n.

Electron-electron scattering processes of the Floquet Auger I and II type sketched in Figure 4.4 excite electrons from the LFB band to the UFB band, and therefore contribute the sink rates to the LFB occupation given by $\dot{n}|^{\mathrm{ee}}_{1-+} = -W^{\mathrm{ee}}_1 n^3(1-n)$ and $\dot{n}|^{\mathrm{ee}}_{2-+} = -W^{\mathrm{ee}}_2 n^4$, where W^{ee}_1 and W^{ee}_2 are intrinsic scattering rates independent of the occupation function. Owing to the particle-hole symmetry of the Floquet bands, reverse processes can be constructed that facilitate a net transfer of electrons from the UFB band to the LFB band, which contribute source rates $\dot{n}|^{\mathrm{ee}}_{1+-} = W^{\mathrm{ee}}_1 n(1-n)^3$ and $\dot{n}|^{\mathrm{ee}}_{2+-} = W^{\mathrm{ee}}_{2+-}(1-n)^4$ to the LFB occupation.

Phenomenological Rate Equation

Combining the electron-phonon and electron-electron scattering rates, the full rate equation for the average LFB occupation function n is given by

$$\begin{aligned}\dot{n} &= \dot{n}|^{\text{ph}}_{\text{in}} + \dot{n}|^{\text{ph}}_{\text{out}} + \dot{n}|^{\text{ee}}_{1-+} + \dot{n}|^{\text{ee}}_{2-+} + \dot{n}|^{\text{ee}}_{1+-} + \dot{n}|^{\text{ee}}_{2+-} \\ &= W^{\text{ph}}_{\text{in}}(1-n)^2 - W^{\text{ph}}_{\text{out}} n^2 + W^{\text{ee}}_1[n(1-n)^3 - n^3(1-n)] + W^{\text{ee}}_2[(1-n)^4 - n^4].\end{aligned} \tag{4.12}$$

To elucidate the role of the different processes on the steady state, we consider several limits

- Without electron-phonon interactions $W^{\text{ph}}_{\text{in}}, W^{\text{ph}}_{\text{out}} \to 0$, the steady state is given by $n = 1/2$, which corresponds to an infinite-temperature state. This limit highlights the importance of phonon cooling in stabilizing steady states.
- In the limit of strong phonon cooling, where $W^{\text{ph}}_{\text{out}} \gg W^{\text{ph}}_{\text{in}}, W^{\text{ee}}_1, W^{\text{ee}}_2$, the steady state is roughly given by $n \approx 0$. This corresponds to an "ideal Floquet topological insulator (FTI) state" where the LFB is nearly fully-occupied. The drive-induced Berry curvature of Floquet systems is usually isolated near regions of the Brillouin zone surrounding the resonant Floquet gap, with opposite signs of Berry curvature above and below the gap [74]. Thus, because the ideal FTI state creates an imbalance of occupations of states above and below the Floquet gap, it gives rise to a finite anomalous Hall conductivity.

4.3 Survival of Floquet-Bloch States Under Continuous-Wave Driving

So far, we have discussed how many-body scattering processes determine the occupation of Floquet states. However, for the Floquet states to remain coherent in the presence of these collision processes, the interband scattering rate of many-body collisions, denoted $\hbar/\tau_{\text{inter}}$, must be much smaller than the Floquet gap Δ [see condition 2 in Section 4.1]. Here, we show that steady states produced by continuous-wave (CW) irradiation can give rise to a Pauli-blocking effect suppressing the magnitude of $\hbar/\tau_{\text{inter}}$. Such a Pauli blocking effect enables CW lasers to induce coherent Floquet states, even though such CW laser sources are typically incapable of achieving the ultra-strong field amplitudes produced by ultrafast lasers (see, e.g., Ref. [1]).

To provide an estimate of the interband scattering rate near a resonant Floquet gap, we cannot use the simplified analysis in Section 4.2, which only captures the momentum-averaged scattering processes across the Brillouin zone (BZ). Instead,

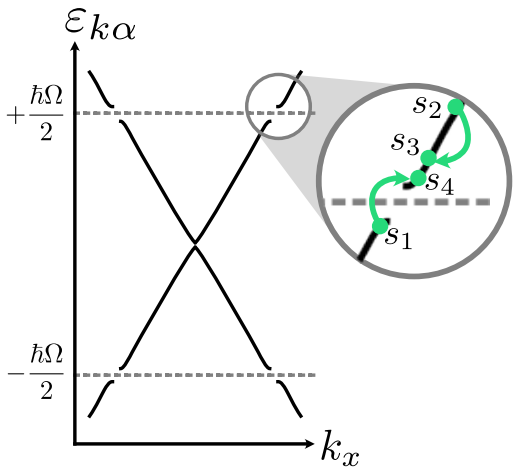

Figure 4.5: Sketch of an electron-electron collision process (green arrows) facilitating interband electronic scattering across the Floquet gap.

we need to consider the collision processes in regions of the BZ close to the Floquet gap, sketched in Figure 4.5. Because electron-electron collisions typically occur on timescales much faster than electron-phonon scattering [258], we focus on interband electron-electron Auger collisions near the Floquet gap, sketched in Figure 4.5. Here, electrons in the initial Floquet states denoted s_1 and s_2 are scattered into the final states s_3 and s_4. The resulting rate of electronic scattering out of the state s_1 can be estimated as

$$\tau_{\text{inter}}^{-1} \approx \frac{1}{\hbar}|V_q\langle\phi^0_{s_1}|\phi^0_{s_4}\rangle\langle\phi^0_{s_2}|\phi^0_{s_3}\rangle|^2 F_{s_2}(1-F_{s_4})(1-F_{s_3}), \tag{4.13}$$

where $|\phi^n_s\rangle$ denotes the n-th Floquet harmonic corresponding to the Floquet state s, F_s denotes the steady state occupation, and V_q denotes the bare electron-electron matrix element corresponding to the process with momentum transfer q. The electronic states near the Floquet gap are superpositions of the conduction and valence bands, and therefore have reduced spectral weight, i.e., $|\langle\phi^0_s|\phi^0_s\rangle| \approx 0.5$. Additionally, photoexcitation processes, see Figure 4.3, produce densities of electronic occupations near the gap, which are relaxed by regular electron-phonon collision processes, see Figure 4.2. When these photoexcitation and phonon relaxation processes are balanced in a steady state, we can roughly estimate that the occupation functions F_s are approximately half-filled near the gap, which can be more rigorously justified by numerical calculations, see Ref. [1]. Overall, we can estimate that

$$|\langle\phi^0_{s_1}|\phi^0_{s_4}\rangle\langle\phi^0_{s_2}|\phi^0_{s_3}\rangle|^2 F_{s_2}(1-F_{s_4})(1-F_{s_3}) \sim 10^{-2} \tag{4.14}$$

providing a roughly 100-times reduction in the bare interband scattering rate set by $\hbar^{-1}|V_q|^2$. As we have demonstrated, the Pauli blocking effect due to photoexcited population near the gap plays a key role in suppressing the scattering rate in the steady state. Crucially, this reduced interband scattering rate enables coherent Floquet-Bloch states to survive in continuous-wave setups, even when the laser amplitudes are weaker than those used in ultrafast laser experiments.

Part II

Persistent Floquet Quantum Matter

Chapter 5

OPTICAL CONTROL OF SLOW TOPOLOGICAL ELECTRONS IN MOIRÉ SYSTEMS

Floquet moiré materials possess optically-induced flat-electron bands with steady-states sensitive to drive parameters. Within this regime, we show that strong interaction screening and phonon bath coupling can overcome enhanced drive-induced heating. In twisted bilayer graphene (TBG) irradiated by a terahertz-frequency continuous circularly polarized laser, the extremely slow electronic states enable the drive to control the steady state occupation of high-Berry curvature electronic states. In particular, above a critical field amplitude, high-Berry-curvature states exhibit a slow regime where they decouple from acoustic phonons, allowing the drive to control the anomalous Hall response. Our work shows that the laser-induced control of topological and transport physics in Floquet TBG are measurable using experimentally available probes.

5.1 Introduction

Time-periodic fields can drive materials into exotic non-equilibrium phases [15, 36, 75, 76, 80, 81, 83, 99, 167, 169, 214, 235, 258, 293, 294], with unconventional transport and optical characteristics [45, 64, 74, 140, 152, 189, 260, 304] controllable by external parameters. In laser-driven twisted bilayer graphene (TBG) [131, 165, 281, 291, 292], a flat-band regime with pronounced electron-electron interaction effects is accessible away from the magic angles [25]. Generating low-temperature Floquet states in such a regime requires cooling processes that compensate for strong drive-induced electron-electron heating. A common cooling solution involves coupling Floquet systems to low-temperature phonon baths [62, 63, 258].

We demonstrate that intrinsic electron-phonon coupling in TBG and Coulomb screening can stabilize low-temperature steady-states in Floquet TBG under terahertz (THz) frequency, circularly polarized laser drives. In this steady-state, the drive amplitude controls the filling of electronic states with large Berry curvature, resulting in a highly tunable anomalous conductivity σ_{xy} [74, 185, 215, 253, 254] (Figure 5.1(a-b)). The ability to tune the Floquet steady-state results from the unique slow electron regime in TBG where phonons travel faster than—and decouple from—many flat band electronic states [77, 261].

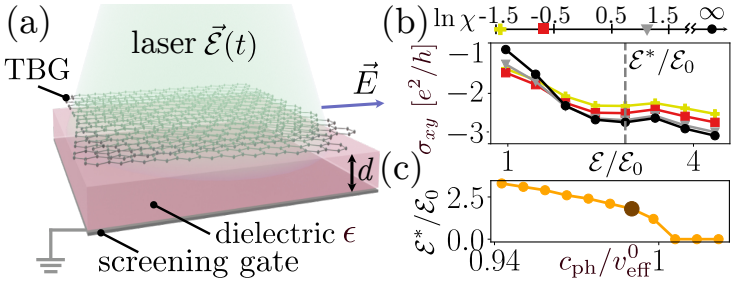

Figure 5.1: (a) Schematic experimental design. Circularly polarized laser induces non-trivial Berry-curvature in the narrow bands (see Figure 5.2(b-c)), resulting in an anomalous Hall conductivity σ_{xy}. TBG lies on top of a dielectric and metallic gate that screen electron-electron interactions. (b) Anomalous Hall conductivity vs. drive amplitude $\mathcal{E}$ for $\zeta \approx 0.5$ and various values of χ indicated on the scale (see below Eqs. 5.4 and 5.7 for definitions of ζ and χ). The σ_{xy} features a rapid drop with $\mathcal{E}$ below the critical amplitude $\mathcal{E}^*$ (dashed line). Here, $\mathcal{E}_0 = \hbar v_F/(eL_M^2) \approx 7.2\times10^4$ V/m. (c) Critical amplitude vs. $c_{\rm ph}/v^0_{\rm eff}$, where $v^0_{\rm eff} = v_{\rm eff}(0)$ is an effective electron velocity defined in the text. Enlarged red circle: $\mathcal{E}^*$ in (b).

5.2 The System

We begin by constructing the time-periodic, interacting Hamiltonian for laser-driven TBG near the charge neutrality point and at a twist angle θ. The single-particle effective Hamiltonian of undriven TBG is $\hat{H}_0 = \sum_{\boldsymbol{k}\nu\xi} E^{(\xi)}_{\boldsymbol{k}\nu} \hat{c}^{(\xi)\dagger}_{\boldsymbol{k}\nu} \hat{c}^{(\xi)}_{\boldsymbol{k}\nu}$, where $\hat{c}^{(\xi)\dagger}_{\boldsymbol{k}\nu}$ creates a Bloch state $|\xi\nu\boldsymbol{k}\rangle$ of crystal momentum $\boldsymbol{k}$, band ν, and energy $E^{(\xi)}_{\boldsymbol{k}\nu}$, near valley index $\xi = \pm1$ of the single-layer graphene Brillouin zone [25, 149]. The index $\nu = \pm$ labels the narrow central particle and hole bands (Figure 5.2(a, b)) with total bandwidth W, which are separated by a large energy gap from all other bands. We consider a circularly polarized laser of vector potential $\boldsymbol{A}(t) = (\mathcal{E}/\Omega)[\cos(\Omega t)\hat{\boldsymbol{x}} - \sin(\Omega t)\hat{\boldsymbol{y}}]$ with electric field amplitude $\mathcal{E}$ and angular-frequency Ω, which couples to electrons by minimal coupling $\boldsymbol{k} \to \boldsymbol{k} + e\boldsymbol{A}(t)/\hbar$, resulting in the time-periodic Hamiltonian $\hat{H}_0(t)$.

The periodic Hamiltonian $\hat{H}_0(t)$ gives rise to Floquet eigenstates $|\Phi^{(\xi)}_{\boldsymbol{k}\alpha}(t)\rangle$ with quasienergies $\varepsilon^{(\xi)}_{\boldsymbol{k}\alpha}$ satisfying $|\varepsilon^{(\xi)}_{\boldsymbol{k}\alpha}| < \frac{1}{2}\hbar\Omega$. We consider the regime $W \le \hbar\Omega < 2W$ corresponding to a single photon resonance within the central TBG bands. Specifically, we consider $\Omega = 5$ meV$/\hbar$ and TBG at a near-magic twist angle of $\theta = 1.13°$ whose Fermi velocity $v_F \approx 17$ km/s (corresponding to $W = 5$ meV in the Bistritzer-MacDonald model [25, 149]) is comparable to phonon speeds in TBG [148]. The drive mixes the two central bands $\nu = \pm1$, resulting in quasienergies $\varepsilon^{(\xi)}_{\boldsymbol{k}\alpha}$, with upper and lower Floquet bands denoted by $\alpha = \pm$ (Figure 5.2(d)) [131]. The drive opens off-resonant gaps of size $\Delta_K \approx 2e^2v_F^2\mathcal{E}^2/\hbar\Omega^3$ at the Dirac points K and

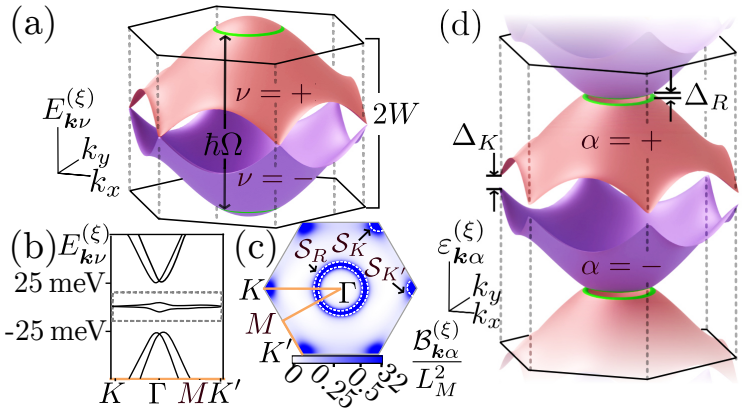

Figure 5.2: (a) Zoom-in on schematic narrow bands in a moiré system. Drive with angular frequency Ω resonantly couples states along resonance rings (green curves). (b) Undriven spectrum of TBG along a line in the Brillouin Zone indicated by the orange curve in (c). Dashed frame encloses optically-active, narrow central bands $\nu = \pm 1$. (c) Berry curvature $\mathcal{B}^{(\xi)}_{\boldsymbol{k}+}$ in the upper Floquet band, with blue color intensity proportional to $\tanh\left(2\mathcal{B}^{(\xi)}_{\boldsymbol{k}+}/L_M^2\right)$ (color bar) so $\mathcal{B}^{(\xi)}_{\boldsymbol{k}+}$ peaks are more visible. Dashed lines indicate areas enclosing $\mathcal{B}^{(\xi)}_{\boldsymbol{k}+}$ peaks at the Dirac points and resonance ring. (d) Periodic quasienergy Floquet spectrum of the driven system, having two central bands shown in (a). The Floquet spectrum exhibits the upper (UFB, $\alpha = +$) and lower (LFB, $\alpha = -$) Floquet bands, separated by off-resonant gaps Δ_K at the Dirac K, K' points and a Rabi-like gap Δ_R along the resonance ring [130, 236, 239].

K' of the moiré Brillouin zone and a Rabi-like gap of $\Delta_R \sim V$ along the resonance ring, which is the ring on the $\boldsymbol{k}$-plane satisfying $E^{(\xi)}_{\boldsymbol{k}+} - E^{(\xi)}_{\boldsymbol{k}-} = \hbar\Omega$ (green rings in Figure 5.2(a, d)). Here, v_F is the Fermi velocity of the undriven band structure, V is the energy scale of the drive, and the expression for Δ_K comes from the Van-Vleck perturbative expansion [6, 130, 215, 239, 241, 284].

The key component for stabilizing Floquet many-body states is the electron coupling to low-temperature longitudinal TBG acoustic phonons:

$$\hat{H}_{\text{el-ph}} = \sum_{\substack{\boldsymbol{k},\boldsymbol{q},\boldsymbol{G}\\ \nu,\nu',\xi}} M^{\nu\nu'\xi}_{\boldsymbol{k},\boldsymbol{q},\boldsymbol{G}} \hat{c}^{(\xi)\dagger}_{\boldsymbol{k}+\boldsymbol{q}+\boldsymbol{G},\nu'} \hat{c}^{(\xi)}_{\boldsymbol{k}\nu} (\hat{b}^\dagger_{\boldsymbol{q}} + \hat{b}_{-\boldsymbol{q}}) + \text{h.c.} \tag{5.1}$$

Here, $\boldsymbol{G}$ is a moiré Brillouin zone reciprocal lattice vector, and

$$M^{\nu\nu'\xi}_{\boldsymbol{k},\boldsymbol{q},\boldsymbol{G}} = D\sqrt{\hbar c_{\text{ph}} q}/(\sqrt{2A_M\rho}c_{\text{ph}})\mathcal{W}^{\xi\nu\nu'}_{\boldsymbol{k},\boldsymbol{q}+\boldsymbol{G}} \tag{5.2}$$

is the matrix element with deformation potential D, moiré unit cell area $A_M = \sqrt{3}L_M^2/2$, lattice vector length $L_M = a/[2\sin(\theta/2)]$, monolayer graphene density ρ, and monolayer lattice vector length $a = 0.246$ nm. The operator $\hat{b}^\dagger_{\boldsymbol{q}}$ creates an

acoustic phonon mode of momentum $\boldsymbol{q}$ with amplitude q, speed $c_{\rm ph}$, and energy $\hbar c_{\rm ph} q$. The speed of sound $c_{\rm ph}$ in TBG is roughly the same as that in monolayer graphene, but the small Brillouin zone in TBG folds the acoustic phonon dispersion into many branches [148]. The form-factor $\mathcal{W}^{\xi\nu\nu'}_{\boldsymbol{k},\boldsymbol{q}+\boldsymbol{G}} \equiv \langle \xi\nu'\boldsymbol{k}+\boldsymbol{q}+\boldsymbol{G}|\xi\nu\boldsymbol{k}\rangle$ captures the decreasing coupling of electrons to folded phonon branches with large $\boldsymbol{G}$ [119]. We also include electron-electron interactions:

$$\hat{H}_{\text{el-el}} = \sum_{\substack{\boldsymbol{k}_1,\boldsymbol{k}_2\\ \boldsymbol{q},\boldsymbol{G}\\ \{\nu_i\},\xi}} V^{\{\nu_i\}\xi}_{\boldsymbol{k}_1,\boldsymbol{k}_2,\boldsymbol{q},\boldsymbol{G}} \hat{c}^{(\xi)\dagger}_{\boldsymbol{k}_1+\boldsymbol{q},\nu_1} \hat{c}^{(\xi)\dagger}_{\boldsymbol{k}_2-\boldsymbol{q},\nu_2} \hat{c}^{(\xi)}_{\boldsymbol{k}_2,\nu_3} \hat{c}^{(\xi)}_{\boldsymbol{k}_1,\nu_4}, \tag{5.3}$$

where $V^{\{\nu_i\}\xi}_{\boldsymbol{k}_1,\boldsymbol{k}_2,\boldsymbol{q},\boldsymbol{G}} = V_{\boldsymbol{q}+\boldsymbol{G}} \mathcal{W}^{\xi\nu_1\nu_4}_{\boldsymbol{k}_1,\boldsymbol{q}+\boldsymbol{G}} \mathcal{W}^{\xi\nu_2\nu_3}_{\boldsymbol{k}_2,-\boldsymbol{q}-\boldsymbol{G}}$, with $i = 1,\ldots,4$, contains the screened Coulomb potential $V_{\boldsymbol{q}} = e^2/(2\epsilon_0 q A_M)(1+\epsilon\coth(qd))^{-1}$ for a gate separated from TBG by a dielectric of permittivity ϵ and thickness d, where ϵ_0 is the vacuum permittivity (Figure 5.1(a)).

We focus on electron dynamics in its Floquet basis, treating interactions $\hat{H}_{\text{el-ph}}$ and $\hat{H}_{\text{el-el}}$ as weak perturbations scattering electrons between single-particle Floquet states [75, 76, 253, 257, 258]. The occupation probability $F^{(\xi)}_{\boldsymbol{k}\alpha}(t) = \langle \hat{f}^{(\xi)\dagger}_{\boldsymbol{k}\alpha}(t) \hat{f}^{(\xi)}_{\boldsymbol{k}\alpha}(t)\rangle$ is described by the Floquet-Boltzmann Equation (FBE) [93, 110, 257, 258],

$$\dot{F}^{(\xi)}_{\boldsymbol{k}\alpha}(t) = I^{\text{el-ph}}_{\boldsymbol{k}\alpha}[\{F^{(\xi)}_{\boldsymbol{k}\alpha}(t)\}] + I^{\text{el-el}}_{\boldsymbol{k}\alpha}[\{F^{(\xi)}_{\boldsymbol{k}\alpha}(t)\}]. \tag{5.4}$$

Here, $\hat{f}^{(\xi)\dagger}_{\boldsymbol{k}\alpha}(t)$ creates a single-particle electron state $|\Phi^{(\xi)}_{\boldsymbol{k}\alpha}(t)\rangle$, and $I^{\text{el-ph}}_{\boldsymbol{k}\alpha}$ and $I^{\text{el-el}}_{\boldsymbol{k}\alpha}$ are respectively the electron-phonon and electron-electron collision integrals, evaluated by the Fermi golden rule (see Appendix A for FBE details). The steady-state distribution yields $\dot{F}^{(\xi)}_{\boldsymbol{k}\alpha} = 0$, and $\langle \hat{f}^{(\xi)\dagger}_{\boldsymbol{k}\alpha}(t) \hat{f}^{(\xi)}_{\boldsymbol{k}\alpha'}(t)\rangle$ is supressed for $\alpha \neq \alpha'$ when $1/\tau^{\text{tot}}_{\boldsymbol{k}} \equiv 1/\tau^{\text{el}}_{\boldsymbol{k}} + 1/\tau^{\text{ph}}_{\boldsymbol{k}} \ll \Delta\varepsilon_{\boldsymbol{k}}/\hbar$, where $\tau^{\text{el}}_{\boldsymbol{k}}$ and $\tau^{\text{ph}}_{\boldsymbol{k}}$ are the interband electron-electron and electron-phonon scattering times, respectively, and $\Delta\varepsilon_{\boldsymbol{k}} = \min_{n\in\mathbb{Z}} |\varepsilon_{\boldsymbol{k}+} - \varepsilon_{\boldsymbol{k}-} + n\hbar\Omega|$ [110, 145, 257]. Because $\Delta\varepsilon_K = 2\Delta_K$ is minimal, the condition is equivalently $\zeta \equiv \hbar/(2\Delta_K \tau^{\text{tot}}_K) \ll 1$ (see Figure 5.4(d)). In Figs. 5.1(b) and 5.4(c-d), we show the maximal ζ across fields $\mathcal{E}$ plotted in Figs. 5.1 and 5.3.

5.3 Transport Properties

To probe the electronic dynamics induced by the laser, we study the anomalous conductivity in the steady-state of the system [39, 61, 63, 74, 185, 215, 253, 254, 280]

$$\sigma_{xy} = \frac{2e^2}{\hbar} \sum_{\alpha,\xi=\pm} \int d^2\boldsymbol{k}\, \mathcal{B}^{(\xi)}_{\boldsymbol{k}\alpha} F^{(\xi)}_{\boldsymbol{k}\alpha}, \tag{5.5}$$

which averages the product of Berry curvature [74, 87, 239]

$$\mathcal{B}^{(\xi)}_{\boldsymbol{k}\alpha} = \frac{\Omega}{\pi}\int_0^{2\pi/\Omega} dt\ \mathrm{Im}\langle\partial_{k_x}\Phi^{(\xi)}_{\boldsymbol{k}\alpha}(t)|\partial_{k_y}\Phi^{(\xi)}_{\boldsymbol{k}\alpha}(t)\rangle, \tag{5.6}$$

and the steady-state fillings, $F^{(\xi)}_{\boldsymbol{k}\alpha}$. Without the drive, TBG has fragile topology with $\sigma_{xy} = 0$ at charge neutrality [212, 233, 308]. The circularly polarized laser breaks time-reversal symmetry between the valleys $\xi = \pm 1$, opens Haldane gaps in each valley, and produces nonzero σ_{xy}.

Our main finding is that σ_{xy} can be controlled by the field strength. It features a rapid drop as a function of the amplitude of the drive, $\mathcal{E}$, near the critical amplitude $\mathcal{E}^*$ (Figure 5.1(b)). This strong dependence on the external field indicates profound changes in the electronic steady-state distribution as the drive amplitude changes across $\mathcal{E} = \mathcal{E}^*$. Furthermore, this strong amplitude-dependence arises only when the undriven effective electronic velocity v^0_{eff} is close to c_{ph} in TBG (Figure 5.1(c)), a condition unique to TBG near the "slow-electron" regime [77, 261].

5.4 Phenomenological Analysis

We explain the origin of the strong dependence of σ_{xy} on the drive amplitude near $\mathcal{E} = \mathcal{E}^*$ (Figure 5.1(b)) by focusing on key processes affecting σ_{xy}, which involve momentum states (the K and K' points and resonance ring, see Figure 5.2(c)) with large Berry curvature $\mathcal{B}^{(\xi)}_{\boldsymbol{k}\alpha}$. We assume that the steady-state occupation of the upper Floquet band (UFB, $\alpha = +$) and valley index ξ near K are uniform, $F^{(\xi)}_{\boldsymbol{k}+} = F^{(\xi)}_{K+}$, for $\boldsymbol{k} \in \mathcal{S}_K$, where $\mathcal{S}_K$ is a small circle enclosing the full-width half maximum of the Berry curvature peak at K (Figure 5.2(c)).

The steady-state occupation emerges as a balance between the total incoming rate $\dot{F}^{(\xi)}_{K+}|_{\mathrm{in}}$ into $\mathcal{S}_K$ and outgoing rate $\dot{F}^{(\xi)}_{K+}|_{\mathrm{out}}$ from $\mathcal{S}_K$. Single phonon emission connecting the UFB $\mathcal{S}_{\mathrm{in}}$ (see Figure 5.3(a)) with $\mathcal{S}_K$ is the dominant contribution to $\dot{F}^{(\xi)}_{K+}|_{\mathrm{in}}$. The two regions are connected by the phonon light-cone (see Fig 5.3(a)). This rate is $\dot{F}^{(\xi)}_{K+}|_{\mathrm{ph,in}} \approx \mathcal{R}_{\mathrm{in}}(1 - F^{(\xi)}_{K+})F^{(\xi)}_{\mathrm{in}}$, where $F^{(\xi)}_{\mathrm{in}}$ is the average UFB occupation in $\mathcal{S}_{\mathrm{in}}$, and $\mathcal{R}_{\mathrm{in}}$ is the average intrinsic scattering rate. Importantly, $\mathcal{R}_{\mathrm{in}}$ is proportional to the momentum-space area of $\mathcal{S}_{\mathrm{in}}$, denoted $\mathcal{A}_{\mathrm{in}}$, estimated by counting the UFB states that may scatter to $\mathcal{S}_K$ by electron-phonon interactions. Hence, $\mathcal{S}_{\mathrm{in}}$ is the intersection between the UFB and phonon light-cones originating anywhere within $\mathcal{S}_K$ (Figure 5.3(a)). As Δ_R and Δ_K widen with $\mathcal{E}$, the Floquet bands become narrower [64, 131, 165], and $\mathcal{A}_{\mathrm{in}}$ shrinks, vanishing at $\mathcal{E} = \mathcal{E}^*$ (Figure 5.3(b)). The critical strength $\mathcal{E}^*$ is defined by $v_{\mathrm{eff}}(\mathcal{E}^*) = c_{\mathrm{ph}}$, where

$v_{\text{eff}}(\mathcal{E}) = \max_{\boldsymbol{k}'}(\varepsilon^{(\xi)}_{\boldsymbol{k}'+} - \varepsilon^{(\xi)}_{\boldsymbol{K}+})/|\boldsymbol{k}' - \boldsymbol{K}|$ is the electronic velocity near the K point. By estimating $v_{\text{eff}}(\mathcal{E})$, one finds that $\mathcal{E}^* \propto [1 - c_{\text{ph}}/v^0_{\text{eff}}]^\gamma$ for small $1 - c_{\text{ph}}/v^0_{\text{eff}}$, where γ depends on the quasienergy structure and $v^0_{\text{eff}} \equiv v_{\text{eff}}(0)$. One can also show $\mathcal{A}_{\text{in}} \propto \max(\mathcal{E} - \mathcal{E}^*, 0)$ as $\mathcal{E} \to \mathcal{E}^*$. (See Appendix A.)

Similarly, the phonon-mediated outgoing rate is $\dot{F}^{(\xi)}_{K+}|_{\text{ph,out}} \approx \mathcal{R}_{\text{out}} F^{(\xi)}_{K+}(1 - F^{(\xi)}_{\text{out}})$, where $F^{(\xi)}_{\text{out}}$ is the lower Floquet band (LFB, $\alpha = -$) average occupation in $\mathcal{S}_{\text{out}}$, and $\mathcal{R}_{\text{out}}$ is the average intrinsic rate, proportional to $\mathcal{A}_{\text{out}} = \int_{\mathcal{S}_{\text{out}}} d^2\boldsymbol{k}$, where $\mathcal{S}_{\text{out}}$ is the momentum region enclosing intersections between the LFB with phonon light cones originating from states in $\mathcal{S}_K$ (see Figure 5.3(a)). However, unlike $\mathcal{A}_{\text{in}}$, $\mathcal{A}_{\text{out}}$ does not vanish as $\mathcal{E} \to \mathcal{E}^*$ and instead expands as $\mathcal{E}$ increases.

Electron-electron interactions and photon-mediated Floquet-Umklapp (FU) processes introduce additional terms in the rate equation depending smoothly on $\mathcal{E}$ and roughly uniformly-spread in momentum. We thus include an incoming $\dot{F}^{(\xi)}_{K+}|_{\text{r,in}} = \Gamma_{\text{in}}(1 - F^{(\xi)}_{K+})$ and outgoing rate $\dot{F}^{(\xi)}_{K+}|_{\text{r,out}} = \Gamma_{\text{out}} F^{(\xi)}_{K+}$ with $\Gamma_{\text{in/out}} \equiv \Gamma^{\text{ph}}_{\text{in/out}} + \Gamma^{\text{el}}_{\text{in/out}}$, where $\Gamma^{\text{el(ph)}}_{\text{in/out}}$, are rates of electron-electron (electron-phonon FU) processes. The strength of FU processes is weaker than $\mathcal{R}_{\text{out}}$ by factors of $\approx (v_F e\mathcal{E}/\Omega^2)^{2n}$, where $|n| > 1$ is the number of photons emitted or absorbed [258]. FU processes also impart large phonon momentum transfers that the form-factor in Eq. C.6 suppresses.

In the steady-state, $\dot{F}^{(\xi)}_{K+}|_{\text{in}} = \dot{F}^{(\xi)}_{K+}|_{\text{ph,in}} + \dot{F}^{(\xi)}_{K+}|_{\text{r,in}}$ and $\dot{F}^{(\xi)}_{K+}|_{\text{out}} = \dot{F}^{(\xi)}_{K+}|_{\text{ph,out}} + \dot{F}^{(\xi)}_{K+}|_{\text{r,out}}$ are equal, and

$$F^{(\xi)}_{K+} = \frac{\mathcal{R}_{\text{in}} F^{(\xi)}_{\text{in}} + \Gamma_{\text{in}}}{\mathcal{R}_{\text{in}} F^{(\xi)}_{\text{in}} + \mathcal{R}_{\text{out}}(1 - F^{(\xi)}_{\text{out}}) + \Gamma_{\text{in}} + \Gamma_{\text{out}}}. \tag{5.7}$$

Note that $F^{(\xi)}_{\text{in}}, 1 - F^{(\xi)}_{\text{out}} \neq 0$ due to electron (hole) excitations in the UFB (LFB) generated by FU processes. Since $\mathcal{R}_{\text{in}} \propto \mathcal{A}_{\text{in}}$, $\mathcal{R}_{\text{in}}$ decreases as a function of $\mathcal{E}$, shrinking to zero for $\mathcal{E} \geq \mathcal{E}^*$ (see Figure 5.3(b) for numerical verification). We expect a similar $\mathcal{E}$-dependence of $F^{(\xi)}_{K+}$ and σ_{xy}, yet smeared by additional scattering rates appearing in Eq. 5.7, as verified numerically in Figure 5.1(b). Additionally, Eq. 5.7 elucidates the dependence of $F^{(\xi)}_{K+}$ on the ratio $\chi \equiv \tau^{\text{el}}_K/\tau^{\text{ph}}_K \approx \mathcal{R}_{\text{out}}/\Gamma^{\text{el}}_{\text{out}} \approx \mathcal{R}_{\text{out}}/\Gamma^{\text{el}}_{\text{in}}$ (see Figure 5.1(b)), with $F^{(\xi)}_{K+} \to 0.5$ as $\chi \to 0$. In Figs. 5.1(b) and 5.4(b-c), we display χ evaluated at the amplitude $\mathcal{E}$ where ζ is fixed.

A similar rate equation can be derived for the occupation probability of holes in the LFB. Due to the emergent, approximate anti-unitary particle-hole symmetry [23, 270, 271] at charge neutrality that is preserved by the drive, the transition rates in the LFB are roughly similar to those in the UFB, leading to approximately

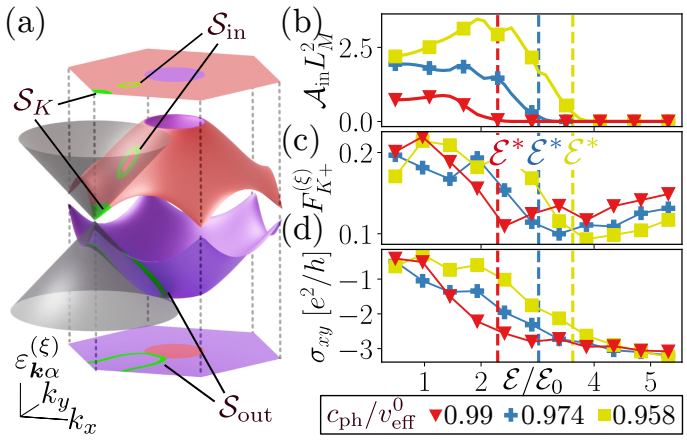

Figure 5.3: (a) Schematics of the Floquet spectrum and one of the phonon light-cones originating from the area $\mathcal{S}_K$ in the UFB. The intersection between the UFB (LFB) and all cones centered in $\mathcal{S}_K$ form $\mathcal{S}_{\rm in}$ ($\mathcal{S}_{\rm out}$). As $\mathcal{E} \to \mathcal{E}^*$, the area of $\mathcal{S}_{\rm in}$ vanishes. (b-d) Numerical verification of the phenomenological model. (b) Area of $\mathcal{S}_{\rm in}$, $\mathcal{A}_{\rm in}$, vs. $\mathcal{E}$ for three values of $c_{\rm ph}/v^0_{\rm eff}$. (c) Average occupation in $\mathcal{S}_K$. (d) Anomalous Hall conductivity σ_{xy} for same parameters as (b, c). At $\mathcal{E}^*$ (dashed lines), $\mathcal{A}_{\rm in}$, $F^{(\xi)}_{K+}$, and σ_{xy} sharply change.

equal electron and hole occupations near the Dirac points in the UFB and LFB ($F^{(\xi)}_{K+} \approx 1 - F^{(\xi)}_{K'-}$). Notice that the signs of the Berry curvatures near the Dirac points in the LFB and UFB are opposite, resulting in constructive contributions of electron and hole populations to σ_{xy}. Thus, we can reproduce qualitatively the sharp change of σ_{xy} with $\mathcal{E}$ in Figure 5.3 [131]. Occupations in the resonance ring vicinity (Figure 5.2(c)) yield a similar $\mathcal{E}$-dependence, but with a much lower critical field (not visible for $\mathcal{E}$ plotted in Figs. 5.1 and 5.3) due to different effective electronic velocities near the resonance ring.

5.5 Numerical Analysis

The results in Figure 5.3(b-d) utilized a simplified toy model describing TBG as a tight-binding hexagonal lattice, similar to graphene [42], but with parameters tuned to match v_F and the Brillouin zone size of TBG. This model misses some subtle details but captures the interplay between electron and phonon velocities and the large Berry curvature at the Dirac points and resonance ring. The model represents only the central $\nu = \pm 1$ bands of the undriven bandstructure, but since the low drive angular frequency Ω is only resonant to these narrow bands, we can ignore the $|\nu| > 1$ bands—valid when θ is near the magic angle where the $|\nu| > 1$ and $\nu = \pm 1$ bands are well-separated. In Appendix A, we present the numerical

analysis of a continuum model without electron-electron interactions [25, 149, 193], which yields qualitatively similar results, demonstrating that the controllable σ_{xy} is insensitive to model details. In the toy model, $v^0_{\text{eff}} = 18.9$ km/s, and we vary $c_{\text{ph}} \in [17.9 \text{ km/s}, 19.4 \text{ km/s}]$ in Figure 5.1(c). In the range $c_{\text{ph}} < v^0_{\text{eff}}$, the drive induces the regime $c_{\text{ph}} > v_{\text{eff}}(\mathcal{E})$ for $\mathcal{E} > \mathcal{E}^*$. To capture the decaying overlap of the wavefunctions for momentum Umklapp transitions, in the toy model, we take $\mathcal{W}^{\xi\nu\nu'}_{\boldsymbol{k},\boldsymbol{q}} \to \langle \xi\nu'\boldsymbol{k}+\boldsymbol{q}|\xi\nu\boldsymbol{k}\rangle e^{-l_w^2 q^2/4}$, with $l_w \approx L_M/(1.5\sqrt{3})$ representing the radius of Wannier orbitals localized to TBG layer alignment sites [119].

First, we show how solving the FBE (Eq. 5.4) for the steady-state distribution verifies the phenomenological model. Consider the non-interacting limit by solving Eq. 5.4 for $F^{(\xi)}_{\boldsymbol{k}\alpha}$ with $\chi \to \infty$ ($I^{\text{el-el}}_{\boldsymbol{k}\alpha} = 0$). The left-half column of Figure 5.4(a) shows the non-interacting steady-state distributions for a phonon bath temperature of 1 K and $c_{\text{ph}} = 0.99 v^0_{\text{eff}}$ in the $\mathcal{E} > \mathcal{E}^*$ and $\mathcal{E} < \mathcal{E}^*$ cases. When $\mathcal{E} > \mathcal{E}^*$ (left bottom quadrant), the Dirac points have reduced occupations (see zoom-in boxes) relative to when $\mathcal{E} < \mathcal{E}^*$ (left top quadrant), because incoming scattering rates into $\mathcal{S}_{K,K'}$ are suppressed (verifying the phenomenological model). Figure 5.3(c) shows the occupation near the K point, $F^{(\xi)}_{K+}$, as a function of $\mathcal{E}$ for three values of $c_{\text{ph}}/v^0_{\text{eff}}$ and verifies $\mathcal{A}_{\text{in}}$, $F^{(\xi)}_{K+}$, and σ_{xy} sharply change at the same critical field $\mathcal{E} = \mathcal{E}^*$. Heating induced by FU processes causes $F^{(\xi)}_{K+}$ to slowly increase with $\mathcal{E} > \mathcal{E}^*$ (see Eq. 5.7).

Next, we quantify the strength of Coulomb screening necessary to stabilize the steady-state, which depends on the balance between electron-phonon cooling processes and electron-electron heating processes. We include $I^{\text{el-el}}_{\boldsymbol{k}\alpha} \neq 0$ by taking finite χ. On the right-half column of Figure 5.4(a), we show the resulting steady-state occupations, which is slightly closer to the hot steady-state $F^{(\xi)}_{\boldsymbol{k}\pm} = 0.5$ and has more smeared occupations than the non-interacting case (left half of Figure 5.4(a)). To quantify the effect of interactions on σ_{xy}, note that, in Figure 5.1(b), σ_{xy} drops less rapidly with $\mathcal{E} < \mathcal{E}^*$ as χ decreases. We capture this behavior with the visibility parameter $\mathcal{V} \equiv -\max_{\mathcal{E}<\mathcal{E}^*}|\partial_{\mathcal{E}}\sigma_{xy}|/[(e^2/h)/\mathcal{E}_0]$. Figure 5.4(b) demonstrates how $\mathcal{V}$ increases with χ. Lastly, we relate χ and ζ to physical parameters in TBG. Figure 5.4(c) shows the necessary gate distances d and dielectrics ϵ to experimentally achieve various values of χ, and Figure 5.4(d) shows the values of ϵ and deformation potentials D satisfying $\zeta < 1$ for $d = 4$ nm. One suitable dielectric is $SrTiO_3$ with $\epsilon \sim 1600$ at $\Omega = 5$ meV$/\hbar$ angular frequencies [69, 243, 295]; note that surface optical phonons in $SrTiO_3$ are of higher frequencies than Ω and would not interact

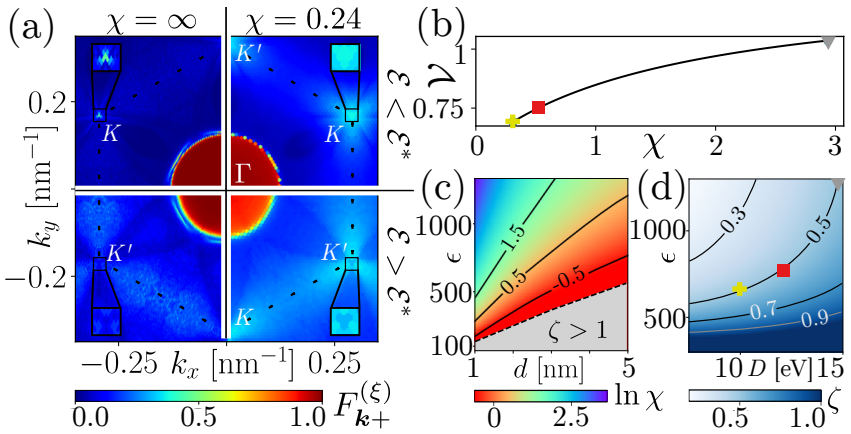

Figure 5.4: (a) Left column: steady-state occupation of the UFB when $\chi = \infty$ (calculated on a 163×163 momentum grid). Right column: steady-state occupation when $\chi = 0.24$ (calculated on a 73×73 momentum grid). Bottom row: strong-drive case ($\mathcal{E} = 4.3\mathcal{E}_0 > \mathcal{E}^*$). Top row: weak-drive case ($\mathcal{E} = 0.97\mathcal{E}_0 < \mathcal{E}^*$). Zoom-in boxes: the K, K' points have reduced occupation when $\mathcal{E} > \mathcal{E}^*$ relative to when $\mathcal{E} < \mathcal{E}^*$. (b) Visibility $\mathcal{V}$ vs. χ. (c) Value of χ for various ϵ and gate distances d. (d) Value of η for various ϵ and deformation potentials D, with $d = 4$ nm. Points in (b, d): parameters used in Figure 5.1(b).

with electrons in TBG via direct (non-FU) scattering processes [245].

5.6 Conclusion

TBG is a remarkable system whose Fermi velocity is comparable to the speed of sound. Upon THz-laser driving, the electronic population dynamics exhibits bottlenecks for electron-phonon scattering into high-Berry curvature Floquet states, strongly affecting the anomalous Hall transport. These bottlenecks can be sensitively controlled by the drive amplitude. If the undriven effective electron speed is faster than sound $v^0_{\text{eff}} > c_{\text{ph}}$, a drive with $\mathcal{E} > \mathcal{E}^*$ induces the opposite regime $v_{\text{eff}}(\mathcal{E}) < c_{\text{ph}}$, weakening the electron-phonon coupling and suppressing the Hall conductivity (Figure 5.1(b)). We also find that a strong $\mathcal{E}$-dependence of σ_{xy} arises for efficient Coulomb screening by a close-by gate or a strong dielectric [49, 248, 289]. Experimental advances in Floquet engineering [185], and THz laser sources [52, 160], show that our predicitions should be accessible experimentally.

Analysis of UV-visible or X-ray driven TBG is a subject of future work, which must account for optically-active dispersive bands [131, 291]. High-frequency drives could reduce heating, facilitating fewer electron-electron FU processes [258] while activating electron-phonon Umklapp cooling processes arising from tightly-

localized Wannier orbitals in TBG [119]. (In this work, these cooling processes are suppressed FU processes.) Another interesting direction involves developing a Hartree-Fock treatment for symmetry-broken phases in the steady-state of strongly coupled TBG [76]. We leave these exciting directions to future studies.

5.7 Acknowledgements

We thank Netanel Lindner, Mark Rudner, Or Katz, Gaurav Gupta, Seamus O'Hara, Jason Alicea, Alex Thomson, Felix von Oppen, Kryštof Kolář, Étienne Lantagne-Hurtubise, and Valerio Peri for valuable discussions. C.Y. gratefully acknowledges support from the DOE NNSA Stewardship Science Graduate Fellowship program, which is provided under cooperative agreement number DE-NA0003960. C.L. acknowledges support by the Gordon and Betty Moore Foundation's EPiQS Initiative, Grant GBMF8682, start-up funds from Florida State University and the National High Magnetic Field Laboratory. The National High Magnetic Field Laboratory is supported by the National Science Foundation through NSF/DMR-1644779 and the state of Florida. G.R. and I.E. are grateful for support from the Simons Foundation and the Institute of Quantum Information and Matter, as well as support from the NSF DMR grant number 1839271. This work is supported by ARO MURI Grant No. W911NF-16-1-0361, and was performed in part at Aspen Center for Physics, which is supported by National Science Foundation grant PHY-1607611.

Appendix A

APPENDIX

A.1 Details of the Models

In both the toy and continuum models, we take the undriven Hamiltonians $H(\boldsymbol{k})$ and obtain the time-dependent Hamiltonian $H(\boldsymbol{k},t)$ via minimal coupling $\boldsymbol{k} \to \boldsymbol{k} + e\boldsymbol{A}(t)/\hbar$. Here,

$$\boldsymbol{A}(t) = A[\cos(\Omega t)\hat{\boldsymbol{x}} - \sin(\Omega t)\hat{\boldsymbol{y}}] \tag{A.1}$$

is the magnetic vector potential of the circularly polarized laser. We can expand the time-dependent eigenstates of the Hamiltonian in a Floquet-Bloch basis [241]:

$$|\psi_{\boldsymbol{k}\alpha}(t)\rangle = e^{-i\varepsilon_\alpha^{(\xi)}t/\hbar}|\Phi^m_{\boldsymbol{k}\alpha}(t)\rangle, \tag{A.2}$$

where $|\Phi^m_{\boldsymbol{k}\alpha}(t)\rangle$ is periodic in time ($|\Phi^m_{\boldsymbol{k}\alpha}(t)\rangle = |\Phi^m_{\boldsymbol{k}\alpha}(t+2\pi/\Omega)\rangle$), $\varepsilon_\alpha^{(\xi)}$ are the quasienergies plotted in Figure 5.2(d), and α enumerates the Floquet quasienergy bands. To determine the Floquet-Bloch basis, it is easiest to expand the time-dependent $|\Phi^m_{\boldsymbol{k}\alpha}(t)\rangle$ in terms of time-independent Fourier harmonics $|\phi^m_{\boldsymbol{k}\alpha}\rangle$,

$$|\Phi^m_{\boldsymbol{k}\alpha}(t)\rangle = \sum_m e^{-im\Omega t}|\phi^m_{\boldsymbol{k}\alpha}\rangle, \tag{A.3}$$

take a Fourier transform the Hamiltonian,

$$H(\boldsymbol{k},t) = \sum_m e^{-im\Omega t}H^{(m)}(\boldsymbol{k}), \tag{A.4}$$

and solve the Schrödinger equation in the basis of Floquet harmonics:

$$(\varepsilon_\alpha^{(\xi)} + m\hbar\Omega)|\phi^m_{\boldsymbol{k}\alpha}\rangle = \sum_{m'} H^{(m-m')}(\boldsymbol{k})|\phi^{m'}_{\boldsymbol{k}\alpha}\rangle. \tag{A.5}$$

In the following subsections, we detail the exact form of the Floquet Hamiltonians.

Tight binding Floquet toy Hamiltonian

We use a rescaled, two-band tight binding model for graphene to replicate the flat conduction and valence bands of TBG. In the rescaled Hamiltonian

$$H_{\text{toy}}(\boldsymbol{k}) = \begin{pmatrix} 0 & h_{\boldsymbol{k}} \\ h^*_{\boldsymbol{k}} & 0 \end{pmatrix}, \tag{A.6}$$

$$h_{\boldsymbol{k}} = \frac{W}{3}\sum_j e^{i\boldsymbol{k}\cdot\boldsymbol{\delta}_j}, \tag{A.7}$$

we choose long hopping vectors

$$\boldsymbol{\delta}_j = L_M/\sqrt{3}[\sin(2\pi m/3)\hat{\boldsymbol{x}} + \cos(2\pi m/3)\hat{\boldsymbol{y}}], \tag{A.8}$$

with $L_M = 0.246\ \text{nm}/(2\sin\theta/2)$, and a narrow bandwidth W. The corresponding rescaled energies and Bloch states are

$$E_\nu(\boldsymbol{k}) = \nu|h_{\boldsymbol{k}}|, \tag{A.9}$$

and

$$|\nu\boldsymbol{k}\rangle = \frac{1}{\sqrt{2}}\begin{pmatrix}\nu e^{i\arg(h_{\boldsymbol{k}})}\\ 1\end{pmatrix}, \tag{A.10}$$

respectively, with $\nu = \pm 1$ enumerating the narrow Bloch bands.

Following Ref. [42], we perform minimal coupling, which turns the functions $h_{\boldsymbol{k}}$ into time-dependent quantities with Fourier transforms

$$\begin{aligned} h_{\boldsymbol{k}}^{(n)} &= \frac{1}{2\pi/\Omega}\int_0^{2\pi/\Omega} h_{\boldsymbol{k}+e\boldsymbol{A}(t)/\hbar}e^{-in\Omega t}dt \\ &= \sum_j t e^{i\boldsymbol{k}\cdot\boldsymbol{\delta}_j}e^{in\phi_j}J_n(-\tilde{\mathcal{E}}), \end{aligned} \tag{A.11}$$

where $\tilde{\mathcal{E}}$ is the dimensionless drive strength

$$\tilde{\mathcal{E}} = \frac{eL_M}{\sqrt{3}\hbar}A = \frac{eL_M}{\sqrt{3}\hbar}\frac{\mathcal{E}}{\Omega}; \tag{A.12}$$

the phase angles are $\phi_0 = \pi/2$, $\phi_1 = -5\pi/6$, and $\phi_2 = -\pi/6$; and

$$J_n(z) = \frac{1}{2\pi i^n}\int_0^{2\pi} e^{iz\cos\theta}e^{in\theta}d\theta. \tag{A.13}$$

The Fourier-transformed Hamiltonian is

$$H_{\text{toy}}^{(n)}(\boldsymbol{k}) = \begin{pmatrix}0 & h_{\boldsymbol{k}}^{(n)}\\ h_{\boldsymbol{k}}^{*(n)} & 0\end{pmatrix}. \tag{A.14}$$

Note that

$$h_{\boldsymbol{k}}^{*(n)} = \sum_j t e^{-i\boldsymbol{k}\cdot\boldsymbol{\delta}_j}e^{in\phi_j}J_n(\tilde{\mathcal{E}}) \tag{A.15}$$

is the Fourier transform of the conjugate of $h_{\boldsymbol{k}}$. In simulations, we generally truncate the Fourier Hamiltonian (Eq. A.5) to $-12 \le m \le 12$, so that we account for a sufficient number of high-order Floquet-Umklapp processes in the Floquet-Boltzmann equation. We do not perform the gauge transformation $h_{\boldsymbol{k}}^{(n)} \to ie^{-i\boldsymbol{k}\cdot\boldsymbol{\delta}_0}h_{\boldsymbol{k}}^{(n)}$ so as to preserve the C_3 symmetry of the matrix element in the Floquet-Boltzmann equation (see Eq. C.21).

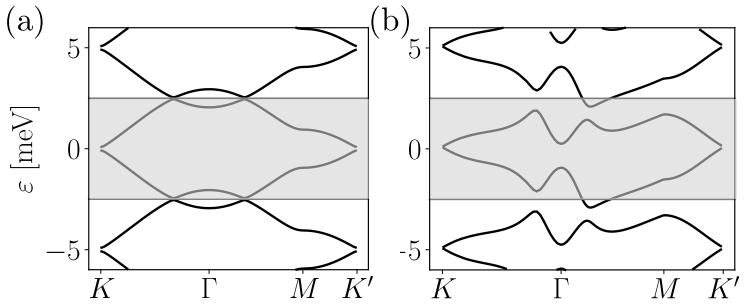

Figure A.1: (a) The quasienergy band structure of the toy model with for the parameters used in the main text. (b) The quasienergy band structure of the continuum model at valley $\xi = +1$. In both panels, the first Floquet Brillouin zone is shaded. See Section A.2 for details and justification for the parameters we have used.

Continuum Model Floquet Hamiltonian

The undriven continuum model for TBG [149] describes the bandstructure of TBG near the valley $\xi = \pm 1$ of the monolayer graphene Brillouin zone. Its Hamiltonian

$$H_\xi(\boldsymbol{k}) = \begin{pmatrix} H_1^\xi(\boldsymbol{k}) & U_\xi^\dagger \\ U_\xi & H_2^\xi(\boldsymbol{k}) \end{pmatrix} \tag{A.16}$$

is diagonalized in the basis $\psi_{n\boldsymbol{k}} = (\psi_{n\boldsymbol{k}}^{A_1}, \psi_{n\boldsymbol{k}}^{B_1}, \psi_{n\boldsymbol{k}}^{A_2}, \psi_{n\boldsymbol{k}}^{B_2})^T$ with

$$\psi_{n\boldsymbol{k}}^X(\boldsymbol{r}) = e^{i\boldsymbol{k}_{\text{mic}}\cdot\boldsymbol{r}} \sum_{\boldsymbol{G}} C_{n\boldsymbol{k}}^X(\boldsymbol{G}) e^{i\boldsymbol{G}\cdot\boldsymbol{r}} \tag{A.17}$$

where $X = A_l, B_l$ represents sublattice A or B degree of freedom in layer index $l = \pm 1$, $\boldsymbol{k}_{\text{mic}} = \boldsymbol{k} + (\boldsymbol{K}_\xi^{+1} + \boldsymbol{K}_\xi^{-1})/2 + \hat{\boldsymbol{x}}\sqrt{3}\xi/2|\boldsymbol{K}_\xi^{+1} - \boldsymbol{K}_\xi^{-1}|$ is the microscopic momentum of the electrons, $\boldsymbol{k}$ is the mini Brillouin zone momentum, and

$$\boldsymbol{K}_\xi^l = -\xi\frac{4\pi}{3a} R(-l\theta/2)\hat{\boldsymbol{x}} \tag{A.18}$$

for layer $l = \pm 1$ and $a = 0.246$ nm. In Eq. A.16, H_l^ξ are the monolayer graphene Hamiltonians, which, in close vicinity of the $\xi = \pm 1$ valleys, resemble Dirac cones:

$$H_l^\xi(\boldsymbol{k}) = -\hbar v_F^{\text{ml}} \left[R(l\theta/2)(\boldsymbol{k}_{\text{mic}} - \boldsymbol{K}_\xi^l)\right] \cdot (\xi\sigma_x, \sigma_y) \tag{A.19}$$

where $R(\varphi)$ is the 2×2 rotation matrix, and v_F^{ml} is the monolayer Graphene Fermi velocity. The interlayer coupling is

$$\begin{aligned} U_\xi = &\begin{pmatrix} u & u' \\ u' & u \end{pmatrix} + \begin{pmatrix} u & u'v^{-\xi} \\ u'v^{\xi} & u \end{pmatrix} e^{i\xi\boldsymbol{G}_1\cdot\boldsymbol{r}} \\ &+ \begin{pmatrix} u & u'v^{\xi} \\ u'v^{-\xi} & u \end{pmatrix} e^{i\xi(\boldsymbol{G}_2+\boldsymbol{G}_3)\cdot\boldsymbol{r}} \end{aligned} \tag{A.20}$$

Using minimal coupling, we obtain time-dependent monolayer graphene Hamiltonians, with Fourier transform

$$H_l^{\xi(n)}(\boldsymbol{k}) = -\hbar v \Big\{ R(l\theta/2) \Big([\boldsymbol{k}_{\text{mic}} - \boldsymbol{K}_\xi^{(l)}] \delta_{n,0} + \frac{e}{\hbar} \frac{1}{2} \mathcal{E} [(\delta_{n,1} + \delta_{n,-1}) \hat{\boldsymbol{y}} - i(\delta_{n,-1} - \delta_{n,1}) \hat{\boldsymbol{x}}] \Big) \Big\} \cdot (\xi \sigma_x, \sigma_y). \tag{A.21}$$

Then,

$$H_\xi^{(n)} = \begin{pmatrix} H_1^{\xi(n)}(\boldsymbol{k}) & U_\xi^\dagger \delta_{n,0} \\ U_\xi \delta_{n,0} & H_2^{\xi(n)}(\boldsymbol{k}) \end{pmatrix} \tag{A.22}$$

is the Fourier transform of the continuum model Hamiltonian. For the continuum model, we truncate the Floquet Hamiltonian (Eq. A.16) to $-6 \leq m \leq 6$.

Upon diagonalizing the Floquet Hamiltonian, we obtain a large number of Floquet states per energy interval $[-\hbar\Omega/2, \hbar\Omega/2]$. We select two states per $\boldsymbol{k}$-point whose spectral weights $A_\alpha^0(\boldsymbol{k}) = |\langle \phi_{\boldsymbol{k}\alpha}^0 | \phi_{\boldsymbol{k}\alpha}^0 \rangle|^2$ are large (which makes their contribution to the Floquet-Boltzmann equation most important, see Section C).

Quasienergy Bands

In Section A.2, we provide and motivate the choices of physical parameters that we use in the main text. In Figure A.1, we preview the quasienergy bands for our choice of toy and continuum model parameters.

A.2 Choice of Physical Parameters

First, we present the physical parameters we use for the electronic Hamiltonian in the TBG continuum model (see Section A.1 for the Hamiltonian). We consider the non-interacting continuum model [25, 149] at a near-magic twist angle of $\theta = 1.13°$. The bandwidth of the central bands at this angle is $W \approx 5$ meV, and a perturbative expansion of the Hamiltonian around the Brillouin zone Dirac points [25] estimates the Fermi velocity as

$$v_F(\theta) = v_F^{\text{ml}}(1 - 3\beta^2)/(1 + 3\beta^2(1 + \eta^2)), \tag{A.23}$$

where $\beta = u'/(\hbar k_\theta v_F^{\text{ml}})$ and $\eta = u/u'$ with $v_F^{\text{ml}} = 8 \times 10^5$ m/s, $k_\theta = 4\pi/(3L_M)$, $u = 0.0797$ eV, and $u' = 0.0975$ eV [25, 149]. Eq. A.23 predicts that the Fermi velocity at the chosen twist angle is $v_F = 27$ km/s. However, the derivation of Eq. A.23 approximates that H_l^ξ is roughly θ-independent and tends to overestimate v_F (see Figure 4 inset in [25]). We can obtain a better estimate by numerically

calculating the Fermi velocity along the path K-M in $\boldsymbol{k}$-space of the $\nu = +1$ band in the $\xi = +1$ valley. (This is the direction of maximum Fermi velocity.) The estimate yields $v_F = 17.5$ km/s, and we hereafter use this value. In our Floquet Hamiltonian, we use a laser angular-frequency of $\Omega \approx W/\hbar \approx 5$ meV$/\hbar$.

Second, we present the parameters we use for the electronic Hamiltonian of the TBG two-band toy tight binding model (see Section A.1 for the Hamiltonian). We choose our toy model Fermi velocity, frequency, and twist angle to roughly match those of the continuum model. Specifically, we use a twist angle of $\theta = 1.13°$ and choose $W = 3.1$ meV so that the Fermi velocity $v_F = WL_M/(2\sqrt{3}\hbar) = 17$ km/s roughly matches that of the continuum model at the same angle. In the toy model Floquet Hamiltonian, we choose $\Omega \approx 5$ meV$/\hbar$.

Third, we discuss the parameters we use for the TBG phonons. For both the continuum and toy models, we consider phonons speeds in the range of $c_{\text{ph}} \in [17.9 \text{ km/s}, 19.4 \text{ km/s}]$. In the toy model, $v^0_{\text{eff}} = 18.9$ km/s, and, in the continuum model, $v^0_{\text{eff}} = 19.5$ km/s, so the range of c_{ph} we choose covers the regime $c_{\text{ph}} < v^0_{\text{eff}}$, in which the drive induces the opposite regime $c_{\text{ph}} > v_{\text{eff}}(\mathcal{E})$ when $\mathcal{E} > \mathcal{E}^*$. We also use the same phonon bath temperature of $T_{\text{ph}} = 1$ K for the toy and continuum model calculations.

Please see Section A.15 for details of the numerical $\boldsymbol{k}$-point grid and Section A.12 for details of the toy model form factor.

A.3 Anomalous Hall Conductivity Calculations for the Continuum Model

In this section, we repeat the calculations in the main text on the TBG continuum model [25, 149]. We consider the non-interacting limit, setting $\epsilon \to \infty$ so that $I^{\text{el-el}}_{\boldsymbol{k}\alpha} = 0$.

First, we discuss differences in the bandstructure and topology at valleys $\xi = +$ and $\xi = -$. The circularly polarized laser opens a gap at the Dirac points, Δ_K, effectively adding a mass term $\xi\Delta_K\sigma_z$ to the Hamiltonian (see Section A.1 and [131] for a derivation) in the vicinity of the Dirac points. Because the sign of the mass term depends on ξ, the $\xi = \pm 1$ superlattice valley contributions to σ_{xy} do not trivially cancel to zero. In fact, in reciprocal space, the Berry curvature and occupations near $\xi = +1$ are simple $\pi/3$ rotations of those in $\xi = -1$, so

$$\sigma_{xy} = \frac{4e^2}{h} \sum_{\alpha=\pm} \int_{\text{MBZ}} \frac{d^2\boldsymbol{k}}{(2\pi)^2} \mathcal{B}^{(+1)}_{\boldsymbol{k}\alpha} F^{(+1)}_{\boldsymbol{k}\alpha}. \tag{A.24}$$

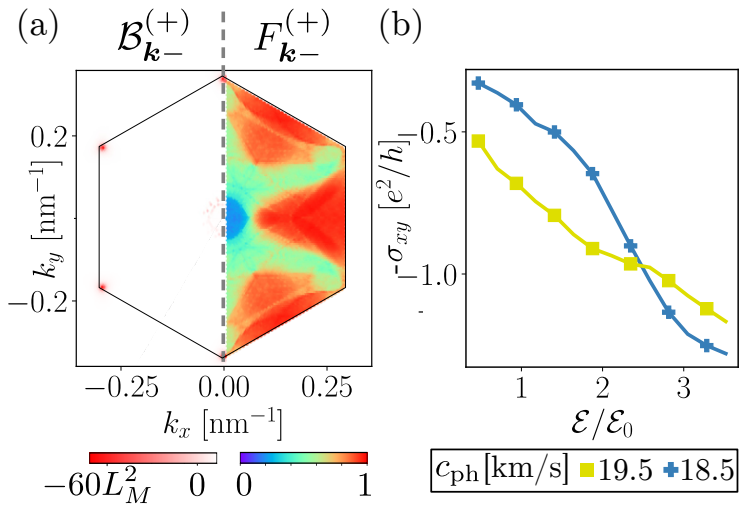

Figure A.2: (a) Left: the steady-state occupation of the lower Floquet band in valley $\xi = +1$ of the continuum model [25, 149]. Right: the Berry curvature of the same band, which peaks near the Dirac points and the resonance ring. (b) The anomalous Hall conductivity σ_{xy} as a function of drive strength $\mathcal{E}$.

In Figure A.2, we show the steady-state and σ_{xy} for the continuum model calculation. Note that we use the full form factor $\mathcal{W}^{\xi\nu'\nu}_{\boldsymbol{k},\boldsymbol{q}} = \langle \xi\nu'\boldsymbol{k}+\boldsymbol{q}|\xi\nu\boldsymbol{k}\rangle$ as calculated from the continuum model wavefunctions (see Section A.12).

A.4 Direct Variation of the Phonon Speed c_{ph}

Throughout the main text, we use the drive strength $\mathcal{E}$ to control electron speeds. We could achieve similar results by keeping $\mathcal{E}$ fixed and varying c_{ph} instead. Figure A.3 shows the variation of σ_{xy} as a function of c_{ph}. The curves resemble the dependence of σ_{xy} on $\mathcal{E}$ in the main text (see, for e.g., Figure 1(b)).

A.5 Symmetries and Berry Curvature Distributions of the Toy and Continuum Models

In this section, we compare the symmetries of the toy and continuum models with and without the drive, and we show that the Berry curvature distributions of the models with the drive are consistent near the Dirac points.

Symmetries

The symmetries of the undriven BM continuum model are $C_{2z}T = \sigma_x\mathcal{K}$, $C_3 = e^{i2\pi/3\sigma_z}$, and $C_{2x} = \sigma_x\tau_x$, where τ_i and σ_i are in the layer and sublattice degrees of freedom, $i = 0, x, y, z$, and $\mathcal{K}$ is conjugation. At charge neutrality, undriven TBG also has an emergent, approximate unitary particle-hole symmetry $P = i\tau_y$ and anti-

unitary particle-hole symmetry $\mathcal{P} = PC_{2z}T$ within each superlattice valley, which ensures $PH_\xi(\boldsymbol{k})P^{-1} \approx -H_\xi(-\boldsymbol{k})$ and $\mathcal{P}H_\xi(\boldsymbol{k})\mathcal{P}^{-1} \approx -H_\xi(-\boldsymbol{k})$ (see Eq. A.16 for the definition of $H_\xi(\boldsymbol{k})$) [23, 270, 271].

We now discuss the effect of the drive on the symmetries of the BM model. The drive induces a dynamical Haldane mass term $\Delta_K \xi \sigma_z$ (see Section A.5). It also resonantly-couples states around the resonance ring, where the effective Hamiltonian is

$$H_R^\xi(\boldsymbol{k}) = V_R(\boldsymbol{k})|\xi - \boldsymbol{k}\rangle\langle\xi + \boldsymbol{k}| + V_R^*(\boldsymbol{k})|\xi + \boldsymbol{k}\rangle\langle\xi - \boldsymbol{k}| \tag{A.25}$$

as derived from degenerate perturbation theory, where $V_R(\boldsymbol{k}) = \langle\xi - \boldsymbol{k}|H_\xi^{(1)}(\boldsymbol{k})|\xi + \boldsymbol{k}\rangle$ and $|\xi \pm \boldsymbol{k}\rangle$ are the undriven single-particle Bloch states (see the main text for the definition) [130]. We can see that the drive breaks $C_{2z}T$ symmetry by opening the Haldane gap. The drive also breaks P symmetry because the drive-induced Haldane mass term $\Delta_K \xi \sigma_z$ commutes with P. However, the drive preserves the anti-unitary $\mathcal{P}$ symmetry. One can see this by first noting that $(C_{2z}T)\sigma_z(C_{2z}T)^{-1} = -\sigma_z$, so $\mathcal{P}\Delta_K \xi \sigma_z \mathcal{P}^{-1} = -\Delta_K \xi \sigma_z$. Secondly, since $\mathcal{P}|\xi -, \pm\boldsymbol{k}\rangle = |\xi +, \mp\boldsymbol{k}\rangle$,

$$\begin{aligned}\mathcal{P}H_R(\boldsymbol{k})\mathcal{P}^{-1} = V_R(\boldsymbol{k})|\xi +, -\boldsymbol{k}\rangle\langle\xi -, -\boldsymbol{k}| \\ + V_R^*(\boldsymbol{k})|\xi -, -\boldsymbol{k}\rangle\langle\xi +, -\boldsymbol{k}|.\end{aligned} \tag{A.26}$$

Noting that $\mathcal{P}H_\xi^{(1)}(\boldsymbol{k})\mathcal{P}^{-1} = -H_\xi^{(-1)}(-\boldsymbol{k})$ and $|\xi + \boldsymbol{k}\rangle = \mathcal{P}^{-1}|\xi -, -\boldsymbol{k}\rangle$, we find that

$$V_R(\boldsymbol{k}) = -\langle\xi +, -\boldsymbol{k}|H_\xi^{(-1)}(-\boldsymbol{k})|\xi -, -\boldsymbol{k}\rangle = -V_R^*(-\boldsymbol{k}). \tag{A.27}$$

Therefore, $\mathcal{P}H_R(\boldsymbol{k})\mathcal{P}^{-1} = -H_R(-\boldsymbol{k})$, and the Hamiltonian is also particle-hole symmetric along the resonantly-coupled states. Lastly, the drive preserves C_3 symmetry

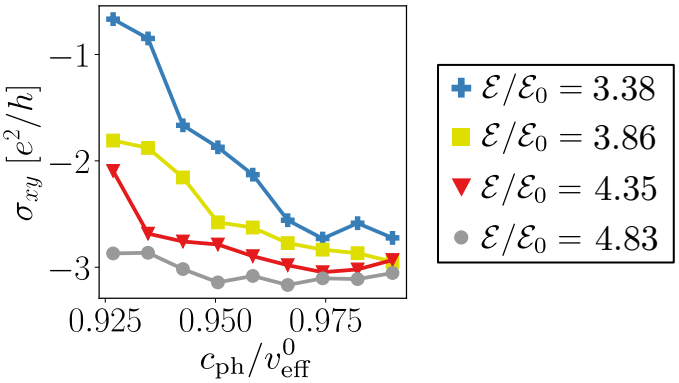

Figure A.3: Anomalous Hall conductivity of the toy model as a function of the ratio $c_{\mathrm{ph}}/v_{\mathrm{eff}}^0$ for three different drive field strengths $\mathcal{E}/\mathcal{E}_0$. The same electron-phonon decoupling process is visible as σ_{xy} plateaus.

and C_{2x} symmetry, which one can see by noting the following:

$$C_3 H_\xi(\boldsymbol{k}) C_3^{-1} = H_\xi(\boldsymbol{k}),\ C_{2x} H_\xi(\boldsymbol{k}) C_{2x}^{-1} = H_{-\xi}(\boldsymbol{k}), \tag{A.28}$$

$$C_3 \Delta_K \xi \sigma_z C_3^{-1} = \Delta_K \xi \sigma_z,\ C_{2x} \Delta_K \xi \sigma_z C_{2x}^{-1} = -\Delta_K \xi \sigma_z, \tag{A.29}$$

and

$$C_3 H_R^\xi(\boldsymbol{k}) C_3^{-1} = H_R^\xi(\boldsymbol{k}),\ C_{2x} H_R^\xi(\boldsymbol{k}) C_{2x}^{-1} = H_R^{-\xi}(\boldsymbol{k}). \tag{A.30}$$

Thus, the Hamiltonian near the Dirac points and resonantly-coupled states respect the C_3 and C_{2x} symmetries.

Now, we discuss the symmetries of the toy model. In the undriven limit, the toy model has exact particle-hole symmetry $P = \sigma_z \mathcal{K}$. It also has the symmetries $C_{2z}T = \sigma_x \mathcal{K}$, $C = \sigma_z$ (sublattice/chiral symmetry), and $C_3 = e^{i2\pi/3\sigma_z}$. The drive opens a Haldane mass gap $\Delta_K \xi_{\mathrm{MBZ}} \sigma_z$, where $\xi_{\mathrm{MBZ}} = 1$ (-1) for the mini Brillouin zone K (K') point. We can now see that the drive breaks $C_{2z}T$, C, and T symmetry via the Haldane mass term, while preserving $P = CT$ symmetry. One can see that P is preserved by noting that $P \Delta_K \xi_{\mathrm{MBZ}} \sigma_z P^{-1} = -\Delta_K \xi_{\mathrm{MBZ}} \sigma_z$ since conjugation $\mathcal{K}$ inverts the momentum and hence the sign of the mass term. Similar arguments as the continuum model case can be made to show that the Hamiltonian near the resonance ring respects P.

Importantly, the drive preserves the emergent particle-hole symmetry in the continuum model while preserving the exact particle-hole symmetry in the toy model. As we note in the phenomenological analysis section of the main text, the emergent particle-hole symmetry ensures that the electron and hole scattering rates in the UFB and LFB are similar. Secondly, the drive breaks $C_{2z}T$ symmetry in both models by opening a Haldane gap. In Section A.5, we show that the Haldane gap ensures the Berry curvature distributions of the models near the Dirac points are consistent.

Berry Curvature

The tunable conductivity σ_{xy} relies only on the large Berry curvature and electron-phonon scattering bottlenecks near the Dirac points of the mini Brillouin zone. In this section, we detail how the Berry curvature distributions for the toy and continuum models are consistent near the Dirac points, as the numerical calculations of Berry curvature demonstrate in Figure A.4. We now prove the agreement analytically. The Hamiltonian for the mini Brillouin zone Dirac cone in the toy model is given by

$$H_{\mathrm{Dirac}}^{\mathrm{toy}}(\boldsymbol{q}) = \hbar v_F \boldsymbol{q} \cdot (\xi_{\mathrm{MBZ}} \sigma_x, \sigma_y), \tag{A.31}$$

where $\boldsymbol{q}$ is the momentum measured from the K or K' point, v_F is the Fermi velocity of TBG, and $\xi_{\mathrm{MBZ}} = +$ for the K point and $\xi_{\mathrm{MBZ}} = -$ for the K' point in the mini Brillouin zone. The corresponding Hamiltonian for the continuum model is

$$H^{\mathrm{cont}}_{\mathrm{Dirac}}(\boldsymbol{q}) = \hbar v_F \boldsymbol{q} \cdot (\xi\sigma_x, \sigma_y) \tag{A.32}$$

where ξ is the superlattice valley index. Upon applying minimal coupling and the Van-Vleck perturbative expansion (see Section A.10 for details), one finds the effective Floquet Hamiltonians

$$H^{\mathrm{toy}}_{\mathrm{Dirac,eff}}(\boldsymbol{q}) = \hbar v_F \boldsymbol{q} \cdot (\xi_{\mathrm{MBZ}}\sigma_x, \sigma_y) + \xi_{\mathrm{MBZ}}\Delta_K\sigma_z \tag{A.33}$$

$$H^{\mathrm{cont}}_{\mathrm{Dirac,eff}}(\boldsymbol{q}) = \hbar v_F \boldsymbol{q} \cdot (\xi\sigma_x, \sigma_y) + \xi\Delta_K\sigma_z. \tag{A.34}$$

We note that in both models, the Berry curvature does not alternate signs between the K and K' points in mini Brillouin zone. Additionally, Eq. A.34 shows that the drive breaks time-reversal symmetry between the superlattice valleys $\xi = \pm 1$ in the BM model, permitting nonzero σ_{xy} when contributions to the conductivity from both superlattice valleys are combined.

A.6 Full Phenomenological Model

In this section, we derive a detailed phenomenological model that qualitatively reproduces the dependence of σ_{xy} on $\mathcal{E}$ and the effect of interactions presented in the main text.

Let us begin by adding more details to the phenomenological model for the K-point

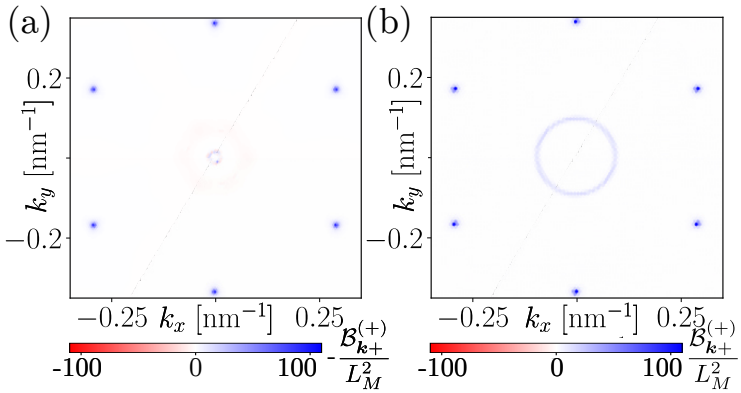

Figure A.4: Comparing the Berry curvature distribution in the upper Floquet band in the (a) continuum model and (b) toy model at a drive amplitude of $\mathcal{E}/\mathcal{E}_0 \approx 3.1$.

occupation. We write

$$\begin{aligned} F_{K+}^{(\xi)} = [&\mathcal{R}_{\text{in}} F_+ + \Gamma_{\text{in}}^{\text{el}} + \Gamma_{\text{in}}^{\text{el,FU}} + \mathcal{R}_{\text{in}}^{\text{FU}} F_-]/ \\ &[\mathcal{R}_{\text{in}} F_+ + \mathcal{R}_{\text{out}}(1 - F_-) \\ &+ \Gamma_{\text{in}}^{\text{el}} + \Gamma_{\text{in}}^{\text{el,FU}} + \Gamma_{\text{out}}^{\text{el}} + \Gamma_{\text{out}}^{\text{el,FU}} \\ &+ \mathcal{R}_{\text{in}}^{\text{FU}} F_- + \mathcal{R}_{\text{out}}^{\text{FU}}(1 - F_+)], \end{aligned} \tag{A.35}$$

where $\Gamma_{\text{in/out}}^{\text{el}}$, $\Gamma_{\text{in/out}}^{\text{el, FU}}$ and $\mathcal{R}_{\text{in/out}}^{\text{FU}}$ are the non-FU electron-electron, FU electron-electron, and FU electron-phonon scattering rates, respectively. Here, F_α is the average occupation of Floquet band α outside the resonance ring, and $F_+ = 1 - F_-$. We drop the superscript (ξ) on the occupations for simplicity and work within a single superlattice valley. Let us now make the following approximations and definitions:

$$\Gamma_{\text{in}}^{\text{el}} \approx \Gamma_{\text{out}}^{\text{el}} \equiv \Gamma, \text{ and } \Gamma_{\text{in}}^{\text{el,FU}} \approx \Gamma_{\text{out}}^{\text{el,FU}} \approx S\Gamma, \tag{A.36}$$

where FU processes are suppressed by a factor of $S \equiv (V/\hbar\Omega)^2$, with $V \approx v_F e\mathcal{E}/\Omega$. For phonon transitions, let us make the following definitions:

$$\mathcal{R}_{\text{out}} \equiv \mathcal{R}, \text{ and } \mathcal{R}_{\text{in}} = r\mathcal{R}, \tag{A.37}$$

where $r \equiv \mathcal{R}_{\text{in}}/\mathcal{R}_{\text{out}}$. Let us also define $r^{\text{FU}} \equiv \mathcal{R}_{\text{in}}^{\text{FU}}/\mathcal{R}_{\text{out}}^{\text{FU}}$, and approximate $\mathcal{R}_{\text{out}}^{\text{FU}} \approx Sa^{\text{FU}}\mathcal{R}$, where the factor $a^{\text{FU}} > 1$ accounts for the fact that the phase space area of states connected to the UFB K point by FU processes is much larger than area of states connected to the UFB K point by non-FU processes. We therefore obtain

$$\mathcal{R}_{\text{out}}^{\text{FU}} = Sa^{\text{FU}}\mathcal{R}, \text{ and } \mathcal{R}_{\text{in}}^{\text{FU}} = Sa^{\text{FU}} r^{\text{FU}}\mathcal{R}. \tag{A.38}$$

Now, Eq. A.35 reduces to

$$F_{K+}^{(\xi)} = \frac{rF_+\mathcal{R} + SF_- a^{\text{FU}} r^{\text{FU}}\mathcal{R} + (1+S)\Gamma}{(1+r)F_+\mathcal{R} + S(1+r^{\text{FU}})F_- a^{\text{FU}}\mathcal{R} + 2(1+S)\Gamma}. \tag{A.39}$$

Let us further define $x \equiv \Gamma/\mathcal{R}$ as a ratio of electron-electron to electron-phonon scattering rates and use $F_- \approx 1 - F_+$ (ensured by emergent particle-hole symmetry, see Section A.5) to obtain

$$F_{K+}^{(\xi)} = \frac{rF_+ + S(1-F_+)a^{\text{FU}} r^{\text{FU}} + (1+S)x}{(1+r)F_+ + S(1+r^{\text{FU}})(1-F_+)a^{\text{FU}} + 2(1+S)x}. \tag{A.40}$$

We will determine the dependence of $F_{K+}^{(\xi)}$ on interaction strength x at strong and weak drive amplitudes.

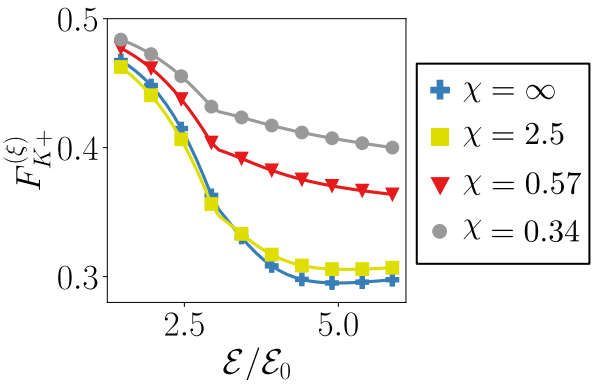

Figure A.5: The occupation $F_{K+}^{(\xi)}$ as predicted by the phenomenological model in Section A.6 for different ratios $\chi \equiv \tau_K^{\text{el}}/\tau_K^{\text{ph}}$. Note that for large χ, the occupation is *lower* than the non-interacting case at weak drive amplitudes, an effect of reduced Pauli blocking in the electron-phonon interactions.

We now derive the phenomenological equation for F_α. The rate equation is roughly

$$\begin{aligned}\dot{F}_+ \approx &\Lambda_{\text{in}} F_-(1-F_+) - \Lambda_{\text{out}} F_+(1-F_-) \\ &+ \Gamma(1+S)(1-F_+) - \Gamma(1+S)F_+\end{aligned} \tag{A.41}$$

where Λ_{in} and Λ_{out} are electron-phonon scattering rates into and out of the UFB. Note that $\Lambda_{\text{in}} \approx S\Lambda_{\text{out}}$ since scattering processes described by Λ_{in} are FU processes. We also approximate $\Lambda_{\text{out}} \approx f_b \mathcal{R}$, with a factor $f_b > 1$, because we expect $\mathcal{R}$, which is suppressed by strong electron-phonon scattering bottlenecks near the K point, to be smaller than Λ_{out}, the total scattering rate into the UFB. We can then find the steady-state solution F_+ in terms of x and substitute the results into Eq. A.40.

In Figure A.5, we show the occupation $F_{K+}^{(\xi)}$ as a function of $\mathcal{E}$ for different values of $\chi = \tau_K^{\text{el}}/\tau_K^{\text{ph}} \approx x^{-1} F_+|_{\mathcal{E}=\mathcal{E}^*}$ (c.f. $1/\tau_K^{\text{ph}} \sim \mathcal{R} F_+|_{\mathcal{E}=\mathcal{E}^*}$ and $1/\tau_K^{\text{el}} \sim \Gamma$) where $F_+|_{\mathcal{E}=\mathcal{E}^*}$ is F_+ evaluated at the drive ampltiude $\mathcal{E}^*$, which we choose to be $\mathcal{E}^* = 2.5\mathcal{E}_0$. To generate the figure, we choose $f_b = 3$ and $a^{\text{FU}} = 28$. Note that a^{FU} estimates that the total area of momentum states connected to $\mathcal{A}_K$ by electron-phonon FU processes covers roughly $1/6$ of the Brillouin zone. We write the following $\mathcal{E}$-dependent phenomenological equations for the ratios r and r^{FU} that capture very roughly their dependence on $\mathcal{E}$, inspired by Figure 4(b) in the main text. First, we approximate

$$r \approx \max\left[\frac{2}{e^{(\mathcal{E}-\mathcal{E}^*)/(0.8\mathcal{E}_0)}+1} - 1, 0\right]. \tag{A.42}$$

Note $r \sim 1$ for $\mathcal{E} \ll \mathcal{E}^*$ and $r = 0$ for $\mathcal{E} > \mathcal{E}^*$, capturing the behavior shown in

Figure 4(b) in the main text. Second, we choose

$$r^{\mathrm{FU}} \approx \frac{1/2}{e^{(\mathcal{E}-\mathcal{E}^*)/(0.5\mathcal{E}_0)}+1} + \frac{1}{2}. \tag{A.43}$$

Here, $r^{\mathrm{FU}} \sim 1$ for $\mathcal{E} \ll \mathcal{E}^*$ and decreases with $\mathcal{E}$, but never reaches 0 (since the electrons are never decoupled from electron-phonon FU processes).

Two features are notable in Figure A.5. First, the occupation decreases as a function of interaction strength for weak interactions (large χ) and weak drive amplitudes, a result of interactions reducing Pauli blocking of the phonon processes from patch $\mathcal{S}_{\mathrm{in}}$ to $\mathcal{S}_K$ and from $\mathcal{S}_K$ to $\mathcal{S}_{\mathrm{out}}$ (i.e., increasing $F_{\mathrm{in}}^{(\xi)}$ in Eq. 6 of the main text, correspondingly suppressing $F_{K+}^{(\xi)}$). When interactions are strong (small χ), $\Gamma_{\mathrm{in/out}}^{\mathrm{el}}$ dominates, and $F_{K+}^{(\xi)} \to 0.5$. Second, the occupation increases slowly for $\mathcal{E} > \mathcal{E}^*$, since FU processes strengthen as $(V/\hbar\Omega)^2$ grows with $\mathcal{E}$. Both of these behaviors are visible in Figure 3(c) in the main text.

A.7 Formal Definition, Numerical Evaluation, and Phenomenological Model of $\mathcal{A}_{\mathrm{in}}$

As described in the main text, a patch $\mathcal{S}_{\mathrm{in}}$ shaped as an elliptical annulus (see Figure 3(a)) with area $\mathcal{A}_{\mathrm{in}}$ in momentum space vanishes as $\mathcal{E} \to \mathcal{E}^*$. Here, we provide a formal definition of $\mathcal{A}_{\mathrm{in}}$ and explain how we estimate its dependence on $\mathcal{E}$ numerically and analytically.

Formal Definition

Let us first define $\mathcal{A}_{\mathrm{in}}$ formally. Consider a family of phonon cones centered throughout $\mathcal{S}_K$, the circular patch enclosing a K-point in the quasienergy spectrum (see Figure 3(a)). Suppose that a subset of the phonon cones are centered throughout a small quasienergy window $d\varepsilon_{\boldsymbol{k}+}$. The $\boldsymbol{k}$-space area of states $d\mathcal{A}_{\mathrm{in}}$ containing intersections of the cones with the upper Floquet band is

$$d\mathcal{A}_{\mathrm{in}} = d\varepsilon_{\boldsymbol{k}+} \sum_{s=\pm} \int d^2\boldsymbol{k}'\, \delta(\varepsilon_{\boldsymbol{k}+} - \varepsilon_{\boldsymbol{k}'+} + s\hbar c_{\mathrm{ph}}|\boldsymbol{k}' - \boldsymbol{k}|). \tag{A.44}$$

Next, we integrate over $\varepsilon_{\boldsymbol{k}+}$ contained in $\mathcal{S}_K$ to obtain

$$\begin{aligned} \mathcal{A}_{\mathrm{in}} = \int d\mathcal{A} = \int_{\boldsymbol{k}\in\mathcal{S}_K} d^2\boldsymbol{k} \frac{1}{D(\varepsilon_{\boldsymbol{k}+})} \times \\ \times \left[\sum_{s=\pm} \int d^2\boldsymbol{k}'\, \delta(\varepsilon_{\boldsymbol{k}+} - \varepsilon_{\boldsymbol{k}'+} + s\hbar c_{\mathrm{ph}}|\boldsymbol{k}' - \boldsymbol{k}|) \right], \end{aligned} \tag{A.45}$$

where

$$D(\varepsilon) = \sum_{\alpha} \int \frac{d^2\boldsymbol{k}}{(2\pi)^2} \delta(\varepsilon - \varepsilon_{\boldsymbol{k}\alpha}) \tag{A.46}$$

is the density of states in the quasienergy band structure. Exploiting the circular shape of $\mathcal{S}_K$,

$$\int_{\boldsymbol{k}\in\mathcal{S}_K} d^2\boldsymbol{k} \approx \int d^2\boldsymbol{k}\ \Theta(|\boldsymbol{k} - \boldsymbol{K}| - k_p) \tag{A.47}$$

where k_p is the radius of the circular area $\mathcal{A}_K$ of $\mathcal{S}_K$. Lastly, we calculate an approximate expression for k_p, the radius of $\mathcal{A}_K$. In the vicinity of the Dirac cone, the Hamiltonian is

$$H_K(\boldsymbol{k}, t) = \boldsymbol{d} \cdot \boldsymbol{\sigma}, \tag{A.48}$$

where $\boldsymbol{d} = \hbar v_F \xi k_x \hat{\boldsymbol{x}} + \hbar v_F k_y \hat{\boldsymbol{y}} + \xi \Delta_K \mathcal{E}^2 \hat{\boldsymbol{z}}$. (See Section A.10 for a detailed derivation.) The z-component of the Berry curvature is

$$\mathcal{B}^z_{k\alpha} = \alpha \frac{d_z}{2|\boldsymbol{d}|^3} = \alpha \frac{\Delta_K}{[(\hbar v_F k)^2 + \Delta_K^2]^{3/2}} \tag{A.49}$$

where $d_z = \xi\Delta_K$ and $\alpha = \pm$. At the half-maximum, $\mathcal{B}^z_{k_p\alpha} = 0.5\mathcal{B}^z_{0\alpha}$, so

$$k_p = (2^{2/3} - 1)^{1/2} \frac{\Delta_K}{\hbar v_F}. \tag{A.50}$$

Numerical Estimate

To generate the values of $\mathcal{A}_{\text{in}}$ we present in Figure 3(b), we evaluate the integrals in Eq. A.45 on a finite-sized grid of $\boldsymbol{k}$-points, smearing the step function by replacing $\Theta(|\boldsymbol{k} - \boldsymbol{K}| - k_p) \to [e^{(|\boldsymbol{k}-\boldsymbol{K}|-k_p)/\sigma_k} + 1]^{-1}$, where $\sigma_k = 2\pi/(L_M N)$ is the grid spacing between $\boldsymbol{k}$-points on an $N \times N$ Monkhorst-Pack grid (see Section A.15). Thus, we approximate

$$\begin{aligned} \mathcal{A}_{\text{in}} \approx \sum_{\boldsymbol{k}} [e^{(|\boldsymbol{k}-\boldsymbol{K}|-k_p)/\sigma_k} + 1]^{-1} \frac{1}{D(\varepsilon_{\boldsymbol{k}+})} \times \\ \times \left[\sum_{s=\pm} \sum_{\boldsymbol{k}'} \delta(\varepsilon_{\boldsymbol{k}+} - \varepsilon_{\boldsymbol{k}'+} + s\hbar c_{\text{ph}} |\boldsymbol{k}' - \boldsymbol{k}|) \right]. \end{aligned} \tag{A.51}$$

For more information on how we approximate the Dirac Delta function on the grid, please see Section A.15. Note that we numerically-estimate the K-point occupation in a similar way, by calculating

$$F^{(\xi)}_{K+} \approx \sum_{\boldsymbol{k}} [e^{(|\boldsymbol{k}-\boldsymbol{K}|-k_p)/\sigma_k} + 1]^{-1} F^{(\xi)}_{\boldsymbol{k}+}. \tag{A.52}$$

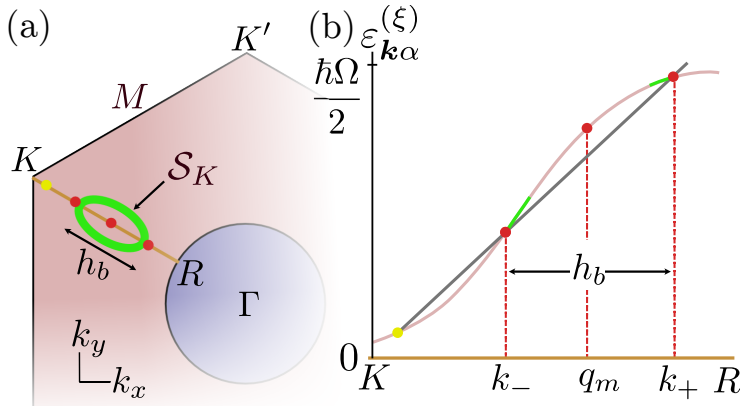

Figure A.6: (a) The intersection $\mathcal{S}_K$ (Figure 3(a)) as viewed on the Brillouin zone. The outer radius along the path KR is $h_b(\mathcal{E})$. (b) Quasienergy (pink) along the path KR, with the phonon light cone (grey) that determines the *outer* radius of $\mathcal{A}_{\text{in}}$. The intersections k_+ and k_- between the cone and the upper Floquet band determines $h_b(\mathcal{E}) = k_+ - k_-$.

Phenomenological Model

In this section, we prove that the intersection area $\mathcal{A}_{\text{in}} \propto \max(\mathcal{E}^* - \mathcal{E}, 0)$ as $\mathcal{E} \to \mathcal{E}^*$. The shape of $\mathcal{A}_{\text{in}}$ is an elliptical annulus as shown in Figure 3(a). Let us use $h_b(\mathcal{E})$ and $w_b(\mathcal{E})$ respectively to denote the *outer* major and minor axis radii of the elliptical annulus (see Figs. A.6(a) and A.7(a)). In the following sections, we begin by generating analytical estimates of $h_b(\mathcal{E})$ and $w_b(\mathcal{E})$.

Estimate of h_b

First, let us consider a slice of the upper Floquet band in $\boldsymbol{k}$-space from the K to the resonance ring (R) along the direction of $h_b(\mathcal{E})$, as we show in Figure A.6(b). Let us define a one-dimensional momentum component q along the path K-R. We sketch a phonon light cone (grey) originating from a point (yellow) in $\mathcal{S}_K$ that determines the outer radius of $\mathcal{A}_{\text{in}}$. The phonon cone intersects with the quasienergy at points k_+ and k_-, and the outer radius of $\mathcal{A}_{\text{in}}$ is therefore $h_b(\mathcal{E}) = k_+ - k_-$. First, consider the undriven limit $\mathcal{E} = 0$, where the gaps $\Delta_R = 0$ and $\Delta_K = 0$. We choose some point q_m such that $k_- < q_m < k_+$ and series expand the energy $E(q)$ of the undriven system around q_m:

$$\begin{aligned} E(q) &\approx E(q_m) + E'(q_m)(q - q_m) + \frac{1}{2}E''(q_m)(q - q_m)^2 \\ &= a_2 q^2 + a_1 q + a_0, \end{aligned} \tag{A.53}$$

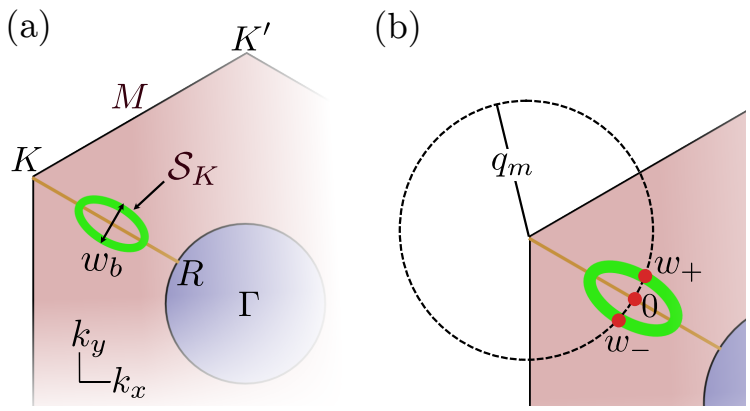

Figure A.7: (a) Width of the intersection $\mathcal{S}_K$, $w_b(\mathcal{E})$. (b) Circular coordinate system with arc length w (increasing counterclockwise) that we use to determine $w_b(\mathcal{E}) = w_+ - w_-$.

where $a_2 = E''(q_m)/2$, $a_1 = E'(q_m) - E''(q_m)q_m$, and $a_0 = E(q_m) - E'(q_m)q_m + E''(q_m)q_m^2/2$. As we increase $\mathcal{E}$, the gaps Δ_K and Δ_R widen. Let us write the quasienergy in the vicinity of q_m as

$$\varepsilon(q) \approx f(\mathcal{E})E(q) + \frac{\Delta_K}{2} \tag{A.54}$$

where $f(\mathcal{E}) \leq 1$ is a scaling factor that decreases as $\mathcal{E}$ increases and accounts for band flattening due to Δ_K and Δ_R. Let

$$f^{-1} = 1 - b_1\tilde{\mathcal{E}} - b_2\tilde{\mathcal{E}}^2, \tag{A.55}$$

where $b_1 \geq 0$ and $b_2 \geq 0$ are constants dependent on the exact bandstructure (i.e., how the widening of Δ_K and Δ_R with $\mathcal{E}$ affects the bandstructure near q_m). The roots of the equation $E(q) = \Delta_K/2 + \hbar c_{\text{ph}} q$ are $k_\pm$, and we may write the equation as

$$a_2 q^2 + a_1 q + a_0 = f\hbar c_s q, \tag{A.56}$$

from which we find that

$$h_b = k_+ - k_- = \sqrt{(a_1 - f\hbar c_s)^2 - 4a_2 a_0}. \tag{A.57}$$

Solving for $\mathcal{E}^*$ through the equation $h_b = 0$, and then series expanding the expression $(a_1 - f\hbar c_s)^2 - 4a_2a_0$ in powers of small $\mathcal{E} - \mathcal{E}^*$, we find that $(a_1 - f\hbar c_s)^2 - 4a_2a_0 \sim \mathcal{E}^* - \mathcal{E}$, so $h_b \sim \sqrt{\mathcal{E}^* - \mathcal{E}}$.

Estimate of w_b

To estimate w_b (see Figure A.7(a)), we define a circular coordinate system shown in Figure A.7(b) whose origin is the K point and arc length w is zero along the KR

slice, increasing counterclockwise. The quasienergy $\varepsilon(w)$ along the circle perimeter varies with w; let us approximate

$$\varepsilon(w) \approx \hbar\Omega/2 - (d_0 + d_2 w^2), \tag{A.58}$$

using some fitting parameters d_0 and d_2. (We assume that $w = 0$ is at local maximum of $\epsilon(w)$, so there is no linear term in Eq. A.58.) Roughly, $w_b = w_+ - w_-$, where we find w_+ and w_- by finding the roots of the equation

$$\hbar\Omega/2 - \Delta(w) = f\hbar c_s q_m. \tag{A.59}$$

Here, once again, we use the factor f in Eq. A.55 to account for band flattening as $\mathcal{E}$ increases from zero. So,

$$w_b = w_+ - w_- = 2\sqrt{(f\hbar c_s q_m + \hbar\Omega/2 - d_0)/d_2}. \tag{A.60}$$

Solving for $\mathcal{E}^*$ by setting $w_b = 0$ and series expanding $f\hbar c_s q_m + \hbar\Omega/2 - d_0$ in powers of $\mathcal{E}$, we find that $w_b \sim \sqrt{\mathcal{E}^* - \mathcal{E}}$.

Estimate of $\mathcal{A}_{\text{in}}$

In the limit $\mathcal{E} \to \mathcal{E}^*$, the elliptical annulus with finite thickness collapses into a filled ellipse. Thus, in the limit $\mathcal{E} \to \mathcal{E}^*$, we estimate that $\mathcal{A}_{\text{in}} = \pi h_b(\mathcal{E}) w_b(\mathcal{E}) \propto \max(\mathcal{E}^* - \mathcal{E}, 0)$.

A.8 Predicting $\mathcal{E}^*$ for the Toy Model

Here, we use the quasienergy dispersion of the toy model to predict $\mathcal{E}^*$. By writing an approximate, analytic expression for $v_{\text{eff}}(\mathcal{E})$ (see Eq. 6), we can find $\mathcal{E}^*$ using the relation $v_{\text{eff}}(\mathcal{E}^*) = c_{\text{ph}}$. From Eq. 6, $v_{\text{eff}}(\mathcal{E}) = (\varepsilon_{\boldsymbol{k}^*+} - \varepsilon_{\boldsymbol{K}+})/|\boldsymbol{k}^* - \boldsymbol{K}|$ for some appropriately-chosen $\boldsymbol{k}^*$ (dropping the superlattice valley index for notational simplicity). One can find numerically that $\boldsymbol{k}^*$ does not shift significantly with Ω or $\mathcal{E}$. We write an ansatz

$$\varepsilon_{\boldsymbol{k}^*+} \approx \hbar v^0_{\text{eff}} |\boldsymbol{k}^* - \boldsymbol{K}| - \frac{\hbar v_F}{L_M}\left(f_1'\tilde{\mathcal{E}} + f_2'\tilde{\mathcal{E}}^2\right)\frac{|\boldsymbol{k}^* - \boldsymbol{K}|}{\Omega/(2v^0_{\text{eff}})}, \tag{A.61}$$

where f_1' and f_2' are fitting constants dependent on the quasienergy bandstructure. Here, $\hbar v_F/L_M$ is the order of magnitude energy scale of the resonance ring gap Δ_R. The dependence of $\varepsilon_{\boldsymbol{k}^*+}$ on $\mathcal{E}$ arises predominantly from Δ_R. The dependence is stronger when $\boldsymbol{k}^*$ is close to the resonance ring, and we encode this behavior in the ratio $|\boldsymbol{k}^* - \boldsymbol{K}|/\Omega/(2v^0_{\text{eff}})$, where $\Omega/(2v^0_{\text{eff}})$ is the $\boldsymbol{k}$-space distance between the K

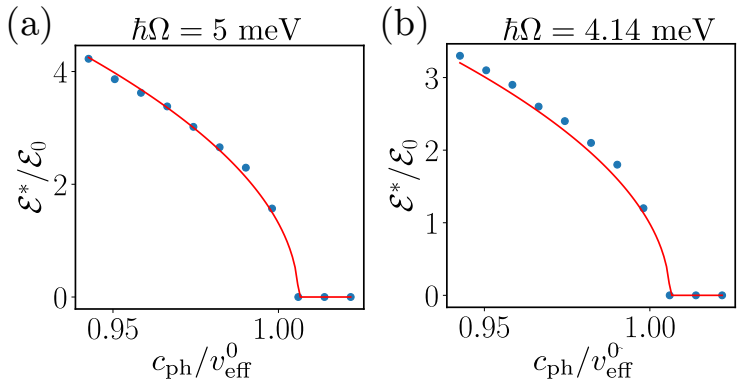

Figure A.8: Comparing numerical evaluation of $\mathcal{E}^*$ (points) to an analytic fit to Eq. A.65. We use the same fitting parameters $f_2 = 0.778$, $f_1 = 0$, and $\delta(N) = 0.006$ for both panels.

point and the resonance ring. Separately, we know that $\varepsilon_{\boldsymbol{K}+} = \Delta_K/2$. We use Eq. 6 to infer

$$v^0_{\rm eff}(\mathcal{E}) = v^0_{\rm eff} - \frac{\Delta_K}{2\hbar|\boldsymbol{k}^* - \boldsymbol{K}|} - \frac{2\hbar v_F v^0_{\rm eff}}{L_M\Omega}\left(f_1'\tilde{\mathcal{E}} + f_2'\tilde{\mathcal{E}}^2\right). \tag{A.62}$$

We know that $v^0_{\rm eff} \propto v_F$. We also assume that $|\boldsymbol{k}^* - \boldsymbol{K}|$ does not change significantly with $\mathcal{E}$, so it is independent of the drive and only dependent on the superlattice scale: $|\boldsymbol{k}^* - \boldsymbol{K}| \propto L_M^{-1}$. Thus, we can absorb some unknown coefficients into new coefficients f_1'' and f_2'' to obtain

$$v^0_{\rm eff}(\mathcal{E}) = v^0_{\rm eff} - \frac{\hbar v_F^2}{L_M\Omega}\left(f_1''\tilde{\mathcal{E}} + f_2''\tilde{\mathcal{E}}^2\right). \tag{A.63}$$

Upon solving for $\tilde{\mathcal{E}}^*$ from $c_s = v_{\rm eff}(\mathcal{E}^*)$, we find that

$$\tilde{\mathcal{E}}^* \approx \sqrt{\frac{L_M\Omega}{3f_2 v_F}}\left(\sqrt{1 - c_{\rm ph}/v^0_{\rm eff} + f_1^2} - f_1\right), \tag{A.64}$$

where f_1 and f_2 are new, rescaled fitting constants. Using the relation $\tilde{\mathcal{E}} = eL_M\mathcal{E}/(\sqrt{3}\hbar\Omega)$, we find

$$\mathcal{E}^* \approx \frac{\hbar\Omega^{3/2}}{f_2 e L_M^{1/2} v_F^{1/2}}\left(\sqrt{1 - c_{\rm ph}/v^0_{\rm eff} + f_1^2} - f_1\right), \tag{A.65}$$

As $c_{\rm ph} \to v^0_{\rm eff}$, $\mathcal{E}^* \propto (1 - c_{\rm ph}/v^0_{\rm eff})^\gamma$ where $\gamma = 1$ $(1/2)$ if $f_1 \neq 0$ $(= 0)$. See Figure A.8 for a fit for two different frequencies Ω.

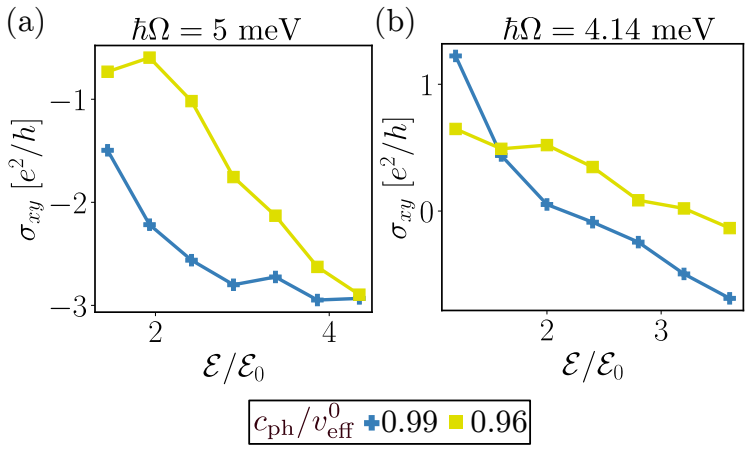

Figure A.9: Comparing the dependence of σ_{xy} on $\mathcal{E}$ for (a) the frequency considered in the main text and (b) a lower frequency where Floquet-Umklapp processes are stronger. Note that the frequency in panel (b) is inaccessible without generating two-photon resonances in the continuum model due to the peaked shape of the $\nu = \pm 1$ bands near the Γ point.

Finite grid size effects on an $N \times N$ Monkhorst-Pack grid (see Section A.15) generate a small numerical error $\delta(N)$ that enters A.65 as

$$\mathcal{E}^* \approx \frac{\hbar L_M^{1/2} \Omega^{3/2}}{f_2 e L_M v_F^{1/2}} \left(\sqrt{1 - c_{\rm ph}/v^0_{\rm eff} + \delta(N) + f_1^2} - f_1 \right). \tag{A.66}$$

To see this, let us consider the details of the finite-sized grid. We impose energy conservation through a broadened Dirac Delta function (see Section A.15), which we model as a Gaussian function in energy with a tiny width

$$\sqrt{2}\sigma \approx 0.1 \cdot \sqrt{2} \cdot \frac{W}{2N/3}. \tag{A.67}$$

(We motivate the choice of the prefactor of 0.1 in Section A.15.) Since we avoid the high symmetry K point in our grids, the $\boldsymbol{k}$-point with largest Berry curvature is, in fact, a point $\boldsymbol{k}_{\rm near}$ point shifted away from K by a small distance in momentum space of

$$|\delta \boldsymbol{k}| = |\boldsymbol{k}_{\rm near} - \boldsymbol{K}| \approx \frac{1}{2} \frac{\Omega/(2\hbar v^0_{\rm eff})}{2N/3} = \frac{\Omega}{4 v^0_{\rm eff}(2N/3)}. \tag{A.68}$$

This point is shifted in quasienergy by $\hbar v_F |\delta \boldsymbol{k}|$ relative to the actual K point. We can account for both of these effects by shifting $\varepsilon_{\boldsymbol{K}+} \to \varepsilon_{\boldsymbol{K}+} + \delta\varepsilon$, with $\delta\varepsilon = \sqrt{2}\sigma + \hbar v_F |\delta \boldsymbol{k}|$ and solve $v_{\rm eff}(\mathcal{E}^*) = c_{\rm ph}$ to find Eq. A.66 with $\delta(N) = \delta\varepsilon/(\hbar v^0_{\rm eff} |\boldsymbol{k}^* - \boldsymbol{K}|)$.

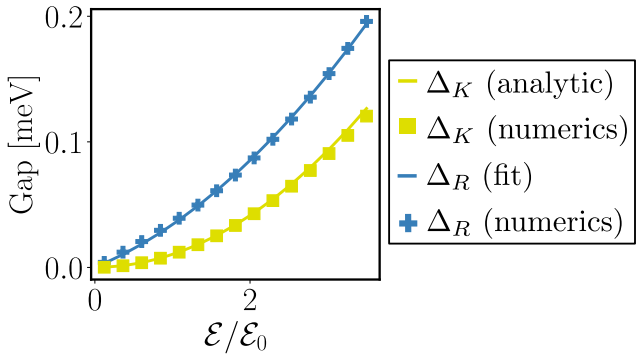

Figure A.10: Comparison of the fitted Δ_R and predicted Δ_K in Equations A.72 and A.76 (solid lines) to those obtained from numerics (points), using $\hbar\Omega = 5$ meV in the toy model. Here, we fit Δ_R with factors of $f_1^R = 0.04$ and $f_2^R = 0.0184$ (see Eq. A.72).

A.9 Different Frequencies

Reducing Ω below the value considered above will increase the ratio $(v_F e\mathcal{E}/\Omega^2)^2$ and in turn strengthen Floquet Umklapp processes, modifying the shape of the σ_{xy} curve. We demonstrate this in Figure A.9(b) for an angular frequency $\Omega = 4.135$ meV$/\hbar$. However, such a low-frequency regime is inaccessible in the continuum model (without generating two-photon resonances) due to the peaked shape of the continuum model $\nu = \pm 1$ band near the Γ point, so we do not consider this lower (doubly-resonant) frequency regime in the main text.

A.10 Gap Sizes

In this section, we estimate the size of the Floquet-induced gaps Δ_K and Δ_R. By the rotating wave approximation, the Floquet-induced gap at the resonance ring, Δ_R, is roughly proportional to the drive energy [239]. For a resonant drive that couples electronic states near the Dirac points, the drive energy is roughly

$$v_F eA/\hbar, \tag{A.69}$$

as predicted by minimal coupling $\boldsymbol{q} \to \boldsymbol{q} + e\boldsymbol{A}(t)/\hbar$ in the Dirac cone Hamiltonian

$$H_K(\boldsymbol{q}) = \hbar v_F \boldsymbol{q} \cdot (\xi\sigma_x, \sigma_y) \tag{A.70}$$

with $v_F = WL_M/(2\sqrt{3}\hbar)$. (We always use perturbative drives that generally fall in the range of $\tilde{\mathcal{E}} < 1$.) We expect that

$$\Delta_R \approx \frac{\hbar v_F}{L_M}\tilde{\mathcal{E}}. \tag{A.71}$$

Such an approximation works well for low-frequency resonant drives that couple states near the Dirac points. However, resonant drives with higher frequencies, like those used in the main text, couple states closer to the Γ-points of the TBG energy dispersion where the bands are nonlinear in q. In such a case, higher order (e.g., O($\tilde{\mathcal{E}}^2$)) contributions (from $O(q^2)$ contributions of the bandstructure) to Δ_R become dominant. In the present example, the energy of the tight binding model for graphene is quadratic in momentum near the Γ point, so we write an ansatz

$$\Delta_R \approx \frac{\hbar v_F}{L_M}(f_1^R \tilde{\mathcal{E}} + f_2^R \tilde{\mathcal{E}}^2), \tag{A.72}$$

and fit f_1^R and f_2^R to match Δ_R obtained by numerically diagonalizing the Floquet Hamiltonian, as shown in Figure A.10.

We can estimate the Floquet-induced K-point gap, Δ_K, by considering the time-dependent Dirac Hamiltonian

$$\begin{aligned} H_K(\boldsymbol{q}, t) = \hbar v_F(\xi q_x \sigma^x + q_y \sigma^y) \\ + v_F e A[\xi \cos(\Omega t)\sigma^x - \sin(\Omega t)\sigma^y]. \end{aligned} \tag{A.73}$$

and performing a Van Vleck expansion [140, 236, 239] to obtain an effective Floquet Hamiltonian

$$H_{K,\text{eff}}(\boldsymbol{q}) = H_K^{(0)} + \frac{[H_K^{(-1)}, H_K^{(1)}]}{\hbar\Omega} = H_K + \xi \frac{e^2 v_F^2 A^2}{\hbar\Omega}\sigma^z \tag{A.74}$$

with

$$H_K^{(n)}(\boldsymbol{q}) = \frac{1}{2\pi/\Omega}\int_0^{2\pi/\Omega} H_K(\boldsymbol{q}, t) e^{-in\Omega t} dt. \tag{A.75}$$

From Eq. A.74, we can extract

$$\Delta_K = \frac{2e^2 v_F^2}{\hbar\Omega} A^2 = \frac{6\hbar v_F^2}{L_M^2 \Omega}\tilde{\mathcal{E}}^2. \tag{A.76}$$

A.11 Floquet Boltzmann Equation

Here, we present the full expression for the Floquet-Boltzmann equation [258], $\partial_t F_{\boldsymbol{k}\alpha}(t) = I^{\text{el-ph}}_{\boldsymbol{k}\alpha}[\{F_{\boldsymbol{k}\alpha}(t)\}] + I^{\text{el-el}}_{\boldsymbol{k}\alpha}[\{F_{\boldsymbol{k}\alpha}(t)\}]$. The electron-phonon collision integral is

$$I^{\text{el-ph}}_{\boldsymbol{k}\alpha}[\{F_{\boldsymbol{k}\alpha}\}] = \frac{2\pi}{\hbar}\frac{1}{N}\sum_{\boldsymbol{k}'\in\text{BZ}}\sum_{\alpha'}\sum_{j}\sum_{n}|\mathcal{G}^{\boldsymbol{k}'\alpha'}_{\boldsymbol{k}\alpha}(n,j)|^2$$
$$\times\Big[\left\{F_{\boldsymbol{k}'\alpha'}(1-F_{\boldsymbol{k}\alpha})\mathcal{N}(\hbar\omega_j(\boldsymbol{k}'-\boldsymbol{k})) - F_{\boldsymbol{k}\alpha}(1-F_{\boldsymbol{k}'\alpha'})[1+\mathcal{N}(\hbar\omega_j(\boldsymbol{k}'-\boldsymbol{k}))]\right\}$$
$$\times\delta(\varepsilon_{\boldsymbol{k}'\alpha'}-\varepsilon_{\boldsymbol{k}\alpha}+\hbar\omega_j(\boldsymbol{q})+n\hbar\Omega)$$
$$+\left\{F_{\boldsymbol{k}'\alpha'}(1-F_{\boldsymbol{k}\alpha})[1+\mathcal{N}(\hbar\omega_j(\boldsymbol{k}'-\boldsymbol{k}))] - F_{\boldsymbol{k}\alpha}(1-F_{\boldsymbol{k}'\alpha'})\mathcal{N}(\hbar\omega_j(\boldsymbol{k}'-\boldsymbol{k}))\right\}$$
$$\times\delta(\varepsilon_{\boldsymbol{k}'\alpha'}-\varepsilon_{\boldsymbol{k}\alpha}-\hbar\omega_j(\boldsymbol{q})+n\hbar\Omega)\Big] \tag{A.77}$$

$$\mathcal{G}^{\boldsymbol{k}'\alpha'}_{\boldsymbol{k}\alpha}(n,j) = \frac{1}{\sqrt{A_{\text{Moiré}}}}\frac{D}{\sqrt{2\rho}c_{\text{ph}}}\sqrt{\hbar\omega_j(\boldsymbol{k}'-\boldsymbol{k})}\sum_{m}\sum_{\nu,\nu'}\langle\phi^{n+m}_{\boldsymbol{k}'\alpha'}|\nu'\boldsymbol{k}'\rangle\mathcal{W}^{\xi\nu'\nu}_{\boldsymbol{k},\boldsymbol{k}+\boldsymbol{G}_j}\langle\nu\boldsymbol{k}|\phi^{m}_{\boldsymbol{k}\alpha}\rangle \tag{A.78}$$

where $\rho = 7.61\times10^{-7}$ kg/m^2 is the 2D density of the graphene layers, D is the deformation potential, and the acoustic phonon mode j has frequency $\omega_j(\boldsymbol{q}) = \hbar c_{\text{ph}}|\boldsymbol{q}+\boldsymbol{G}_j|$ with $\{\boldsymbol{G}_j\}$ being the set of all possible reciprocal lattice vectors. The function $\mathcal{N}(\varepsilon) = (e^{-\varepsilon/k_BT_{\text{ph}}}-1)^{-1}$ is the Bose-Einstein occupation of the phonon bath at temperature T_{ph}. The electron-electron collision integral is

$$I^{\text{el-el}}_{\boldsymbol{k}\alpha}[\{F_{\boldsymbol{k}\alpha}\}] = \frac{4\pi}{\hbar}\frac{1}{N^2}\sum_{\boldsymbol{k}_2\in\text{BZ}}\sum_{\boldsymbol{k}_3\in\text{BZ}}\sum_{\alpha_2,\alpha_3,\alpha_4}\sum_{n}\sum_{\boldsymbol{G}}|\mathcal{V}^{(\boldsymbol{k}_3,\alpha_3),(\boldsymbol{k}_1+\boldsymbol{k}_2-\boldsymbol{k}_3,\alpha_4)}_{(\boldsymbol{k},\alpha),(\boldsymbol{k}_2,\alpha_2)}(n,\boldsymbol{G})|^2\times$$
$$\times\delta(\varepsilon_{\boldsymbol{k}\alpha}+\varepsilon_{\boldsymbol{k}_2\alpha_2}-\varepsilon_{\boldsymbol{k}_3\alpha_3}-\varepsilon_{\boldsymbol{k}+\boldsymbol{k}_2-\boldsymbol{k}_3,\alpha_4}+n\hbar\Omega)\times$$
$$\times\left[(1-F_{\boldsymbol{k}\alpha})(1-F_{\boldsymbol{k}_2\alpha_2})F_{\boldsymbol{k}_3\alpha_3}F_{\boldsymbol{k}_1+\boldsymbol{k}_2-\boldsymbol{k}_3,\alpha_4} - F_{\boldsymbol{k}\alpha}F_{\boldsymbol{k}_2\alpha_2}(1-F_{\boldsymbol{k}_3\alpha_3})(1-F_{\boldsymbol{k}_1+\boldsymbol{k}_2-\boldsymbol{k}_3,\alpha_4})\right] \tag{A.79}$$

$$\mathcal{V}^{(\boldsymbol{k}_3,\alpha_3),(\boldsymbol{k}_1+\boldsymbol{k}_2-\boldsymbol{k}_3,\alpha_4)}_{(\boldsymbol{k},\alpha),(\boldsymbol{k}_2,\alpha_2)}(n) = \sum_{\nu_1,\nu_2}\sum_{\nu_3,\nu_4}\sum_{n_2,n_3,n_4}V_{\boldsymbol{k}_2-\boldsymbol{k}_3+\boldsymbol{G}}\mathcal{W}^{\xi\nu_1\nu_4}_{\boldsymbol{k}_1,\boldsymbol{q}+\boldsymbol{G}}\mathcal{W}^{\xi\nu_2\nu_3}_{\boldsymbol{k}_2,-\boldsymbol{q}-\boldsymbol{G}}\times$$
$$\times\langle\phi^{n-n_2+n_3+n_4}_{\boldsymbol{k}\alpha}|\nu_1\boldsymbol{k}\rangle\langle\phi^{n_2}_{\boldsymbol{k}_2\alpha_2}|\nu_2\boldsymbol{k}_2\rangle\langle\nu_3\boldsymbol{k}_3|\phi^{n_3}_{\boldsymbol{k}_3\alpha_3}\rangle\langle\nu_4\boldsymbol{k}_4|\phi^{n_4}_{\boldsymbol{k}+\boldsymbol{k}_2-\boldsymbol{k}_3,\alpha_4}\rangle. \tag{A.80}$$

We solve for $\partial_t F_{\boldsymbol{k}\alpha} = 0$ using the Newton-Raphson algorithm. To ensure charge neutrality, we add a Lagrange multiplier term $\lambda(\sum_{\boldsymbol{k}\alpha}F_{\boldsymbol{k}\alpha} - N)$ to the Floquet-Boltzmann equation, choosing some large constant λ.

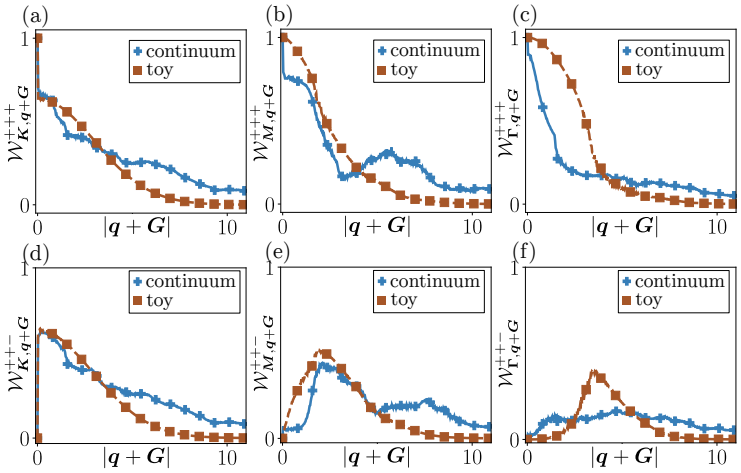

Figure A.11: Comparing the average toy and continuum model form factors $\mathcal{W}^{\xi\nu'\nu}_{\boldsymbol{k},\boldsymbol{q}+\boldsymbol{G}}$, with $|\boldsymbol{q}+\boldsymbol{G}|$ measured in units of 10^8 m^{-1}. (a-c) The intraband ($\nu = \nu'$) form factors at the K, M, and Γ points. (d-f) The interband ($\nu \neq \nu'$) form factors at the K, M, and Γ points.

A.12 Form Factor Details

Here, we discuss the details of the form factors $\mathcal{W}^{\xi\nu'\nu}_{\boldsymbol{k},\boldsymbol{q}+\boldsymbol{G}}$ used in the Boltzmann equation. In the continuum model, we calculate the form factor directly from the wavefunctions:

$$\mathcal{W}^{\xi\nu'\nu}_{\boldsymbol{k},\boldsymbol{q}+\boldsymbol{G}} = \sum_{X,\boldsymbol{G}'} C^{X*}_{\nu'\boldsymbol{k}+\boldsymbol{q}}(\boldsymbol{G}'-\boldsymbol{G})C^{X}_{\nu\boldsymbol{k}}(\boldsymbol{G}'). \tag{A.81}$$

For the toy model, we include, by hand, a suppression factor $e^{-l_w^2|\boldsymbol{q}+\boldsymbol{G}|^2/4}$, which accounts for the moiré periodicity that the toy model is unable to capture [119]:

$$\mathcal{W}^{\xi\nu'\nu}_{\boldsymbol{k},\boldsymbol{q}+\boldsymbol{G}} = \langle \xi\nu'\boldsymbol{k}+\boldsymbol{q}|\xi\nu\boldsymbol{k}\rangle e^{-l_w^2|\boldsymbol{q}+\boldsymbol{G}|^2/4}. \tag{A.82}$$

We choose $l_w = L_M/(1.5\sqrt{3})$ so that the form factor dependence on $|\boldsymbol{q}+\boldsymbol{G}|$ captures that of the continuum model.

To check the agreement between the toy and continuum model form factors, we calculate the form factors on a $\boldsymbol{k}$-grid, with a set of reciprocal lattice vectors $\{\boldsymbol{G}\}$, and plot the average value of $\mathcal{W}^{\xi\nu'\nu}_{\boldsymbol{k},\boldsymbol{q}+\boldsymbol{G}}$ as a function of $|\boldsymbol{q}+\boldsymbol{G}|$, for $\boldsymbol{k}$ at the K, Γ, and M points of the mini Brillouin zone. The results, shown in Figure A.11, show that the toy model form factor captures the general features of that of the continuum model.

We can show analytically that the toy and continuum model form factors agree when $\boldsymbol{k}$ and $\boldsymbol{k}+\boldsymbol{q}$ lie within the same K or K' valley in the mini Brillouin zone. These

low-momentum transfer processes are crucial to the tunable σ_{xy} presented in the text. Let us write $\boldsymbol{k} \equiv \boldsymbol{K} + \boldsymbol{p}$ (and $\boldsymbol{k} + \boldsymbol{q} = \boldsymbol{K} + \boldsymbol{p} + \boldsymbol{q}$), where $|\boldsymbol{q}|$ and $|\boldsymbol{p}|$ are small enough such that the energy dispersion still resembles a Dirac cone at momenta $\boldsymbol{k}$ and $\boldsymbol{k} + \boldsymbol{q}$. By utilizing the eigenfunctions of the Dirac cone Hamiltonian, one can show that the form factors are

$$\mathcal{W}^{\xi\nu'\nu}_{\boldsymbol{K}+\boldsymbol{p},\boldsymbol{q}} = \frac{1}{2}\left(1 + \nu\nu'\frac{\boldsymbol{p}\cdot(\boldsymbol{p}+\boldsymbol{q})}{|\boldsymbol{p}||\boldsymbol{p}+\boldsymbol{q}|}\right). \tag{A.83}$$

The formula holds true regardless of the chirality of the Dirac nodes. Note that form factors representing direct (non-FU) scattering transitions between different K and K' valleys in the mini Brillouin zone are not relevant since such scattering transitions are kinematically prohibited due to the slow-electron regime.

A.13 Validity of the Diagonal Density Matrix Approximation

In general, one needs to keep track of all coherences between the Floquet states, $\langle \hat{f}^{(\xi)\dagger}_{\boldsymbol{k}\alpha}(t)\hat{f}^{(\xi)}_{\boldsymbol{k}'\alpha'}(t)\rangle$, to fully-characterize the steady-state of a Floquet system. Translation symmetry suppresses the coherences for $\boldsymbol{k} \neq \boldsymbol{k}'$. The $\alpha \neq \alpha'$ interband coherences are suppressed for $\tau^{\text{tot}}_{\boldsymbol{k}} \gg \hbar/\Delta\varepsilon_{\boldsymbol{k}}$, where $1/\tau^{\text{tot}}_{\boldsymbol{k}} = 1/\tau^{\text{el}}_{\boldsymbol{k}} + 1/\tau^{\text{ph}}_{\boldsymbol{k}}$, $1/\tau^{\text{el}}_{\boldsymbol{k}}$ and $1/\tau^{\text{ph}}_{\boldsymbol{k}}$ are the interband electron-electron and electron-phonon scattering rates, respectively, and $\Delta\varepsilon_{\boldsymbol{k}} = \min_{n\in\mathbb{Z}}|\varepsilon_{\boldsymbol{k}+} - \varepsilon_{\boldsymbol{k}-} + n\hbar\Omega|$. In this section, we will explain how we numerically estimate the scattering rates.

Formal Definition of Scattering Times

Following Ref. [257], we define the interband scattering rates (fixing the initial Floquet band α) as

$$\begin{aligned}\frac{1}{\tau^{\text{ph}}_{\boldsymbol{k}}} = \frac{2\pi}{\hbar}\frac{1}{N}\sum_{\boldsymbol{k}'\in\text{BZ}}\sum_{\alpha'\neq\alpha}\sum_{j}\sum_{n}|\mathcal{G}^{\boldsymbol{k}'\alpha'}_{\boldsymbol{k}\alpha}(n,j)|^2\Big[&(1-F_{\boldsymbol{k}'\alpha'})[1+\mathcal{N}(\hbar\omega_j(\boldsymbol{k}'-\boldsymbol{k}))]\times\\ &\times\delta(\varepsilon_{\boldsymbol{k}'\alpha'} - \varepsilon_{\boldsymbol{k}\alpha} + \hbar\omega_j(\boldsymbol{q}) + n\hbar\Omega)\\ &+(1-F_{\boldsymbol{k}'\alpha'})\mathcal{N}(\hbar\omega_j(\boldsymbol{k}'-\boldsymbol{k}))\delta(\varepsilon_{\boldsymbol{k}'\alpha'} - \varepsilon_{\boldsymbol{k}\alpha} - \hbar\omega_j(\boldsymbol{q}) + n\hbar\Omega)\Big],\end{aligned} \tag{A.84}$$

$$\begin{aligned}\frac{1}{\tau^{\text{el}}_{\boldsymbol{k}}} = \frac{4\pi}{\hbar}\frac{1}{N^2}\sum_{\boldsymbol{k}_2\in\text{BZ}}\sum_{\boldsymbol{k}_3\in\text{BZ}}\sum_{\substack{\alpha_2,\alpha_3,\alpha_4\\ \alpha_3 \text{ or } \alpha_4\neq\alpha}}\sum_{n}\sum_{\boldsymbol{G}}|\mathcal{V}^{(\boldsymbol{k}_3,\alpha_3),(\boldsymbol{k}_1+\boldsymbol{k}_2-\boldsymbol{k}_3,\alpha_4)}_{(\boldsymbol{k},\alpha),(\boldsymbol{k}_2,\alpha_2)}(n,\boldsymbol{G})|^2\times\\ \times\delta(\varepsilon_{\boldsymbol{k}\alpha}+\varepsilon_{\boldsymbol{k}_2\alpha_2}-\varepsilon_{\boldsymbol{k}_3\alpha_3}-\varepsilon_{\boldsymbol{k}+\boldsymbol{k}_2-\boldsymbol{k}_3,\alpha_4}+n\hbar\Omega)F_{\boldsymbol{k}_2\alpha_2}(1-F_{\boldsymbol{k}_3\alpha_3})(1-F_{\boldsymbol{k}_1+\boldsymbol{k}_2-\boldsymbol{k}_3,\alpha_4}).\end{aligned} \tag{A.85}$$

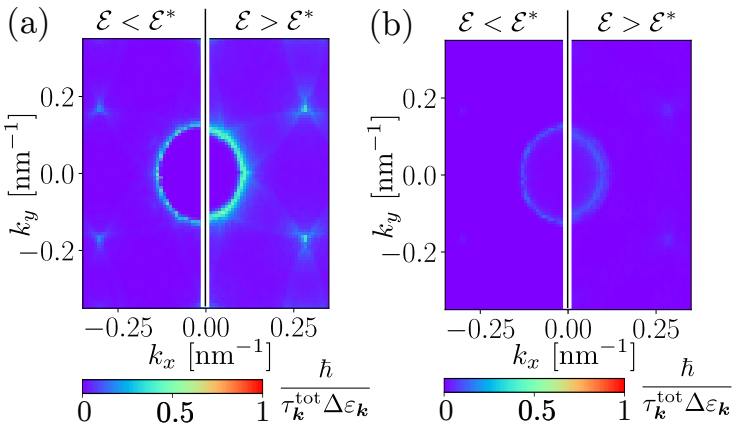

Figure A.12: The color represents the ratio $\hbar/(\tau_{\boldsymbol{k}}^{\mathrm{tot}}\Delta\varepsilon_{\boldsymbol{k}})$ at different points in momentum space (a) for the upper Floquet band and (b) for the lower Floquet band for the case $\chi \approx 2.8$ and $\zeta \approx 0.5$.

Numerical Calculation of Scattering Rates

In Figure A.12, we show the ratio $\hbar/(\tau_{\boldsymbol{k}}^{\mathrm{tot}}\Delta\varepsilon_{\boldsymbol{k}})$ in the regimes $\mathcal{E}/\mathcal{E}_0 = 0.966 < \mathcal{E}^*/\mathcal{E}_0$ and $\mathcal{E}/\mathcal{E}_0 = 2.898 > \mathcal{E}^*/\mathcal{E}_0$ for the case $\chi = \tau_K^{\mathrm{el}}/\tau_K^{\mathrm{ph}} \approx 2.8$ and $\zeta = \hbar/(2\tau_K^{\mathrm{tot}}\Delta_K) \approx 0.5$, where ζ is the maximum value across the range of $\mathcal{E}$ considered in Figure 1(b) in the main text, and χ is evaluated at the drive amplitude at which ζ is fixed. One sees that $\hbar/(\tau_{\boldsymbol{k}}^{\mathrm{tot}}\Delta\varepsilon_{\boldsymbol{k}}) \ll 1$ for most of the Brillouin zone and $\hbar/(\tau_{\boldsymbol{k}}^{\mathrm{tot}}\Delta\varepsilon_{\boldsymbol{k}}) < 1$ where the interband gaps are the smallest; by analysis of the Floquet-Redfield equation in Refs. [257, 259], the diagonal density matrix was shown to be a good approximation in this regime. Note that the definitions in Eqs. C.24 and C.25 calculate the electron (rather than hole) scattering times, and hence Pauli blocking results in different scattering times for the upper and lower Floquet bands; the scattering rates quoted in the main text take the maximum rate. Separately, we also note that the toy model underestimates the resonance gap (see Figure A.1) relative to the continuum model, and therefore overestimates $\hbar/(\tau_{\boldsymbol{k}}^{\mathrm{tot}}\Delta\varepsilon_{\boldsymbol{k}})$ around the resonance ring.

A.14 Dielectric Function of Strontium Titanate

The dielectric function for $SrTiO_3$ is

$$\epsilon(\Omega) = \epsilon_\infty \prod_{j=1}^{3} \frac{\omega_{Lj}^2 - \Omega^2}{\omega_{Tj}^2 - \Omega^2} \tag{A.86}$$

at angular frequency Ω, with the experimentally-determined longitudinal and transverse optical phonon frequencies, ω_{Lj} and ω_{Tj}, respectively, given in Ref. [69, 243, 295]. One finds that $|\epsilon(5\text{ meV})| = 1682$.

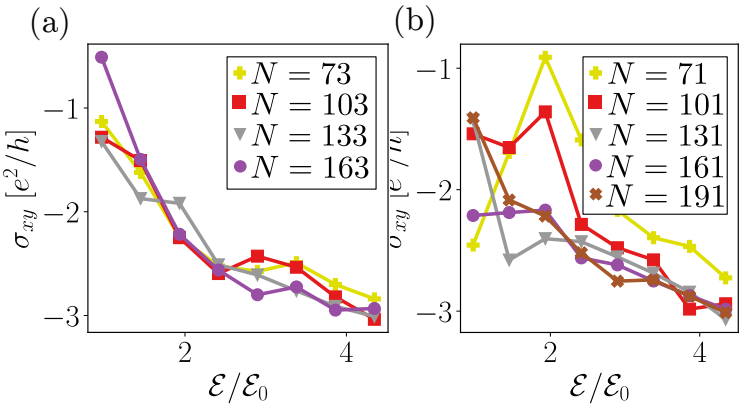

Figure A.13: Convergence of anomalous conductivity with grid size for (a) $N(\mathrm{mod}\ 3) = 1$ and (b) $N(\mathrm{mod}\ 3) = 2$. Due to the positioning of grid points near the K point, the results at low grid resolutions show significant disagreement.

A.15 Monkhorst-Pack Grid, Numerical Integration, and Convergence

In this section, we describe the methods we use to discretize the momentum Brillouin zone. We perform the Boltzmann equation integrals, introduced in Equations C.20 and C.22, over an $N \times N$ Monkhorst-Pack (MP) set of grid points [193], with $\boldsymbol{k}$-points

$$\boldsymbol{k}_{m,n} = \frac{m\boldsymbol{G}_1 + n\boldsymbol{G}_2}{N}, \tag{A.87}$$

odd N, and $m, n = 0, \ldots, N-1$. Specifically, we avoid values of $N(\mathrm{mod}\ 3) = 0$ that generate a $\boldsymbol{k}$-point exactly at the high-symmetry point of K, because such grids converge poorly when the drive strength is weak and Floquet-induced gap Δ_K is small.

Energy and Momentum Conservation

Here, we discuss in detail how we impose momentum and energy conservation on this MP grid. The space of MP $\boldsymbol{k}$ vectors are closed under addition and subtraction (modulo a reciprocal lattice vector), so conservation of momentum (e.g., $\boldsymbol{k} + \boldsymbol{k}_2 - \boldsymbol{k}_3$ in Eq. C.22), is simple to implement. We impose energy conservation via a smeared Dirac Delta function

$$\delta(\varepsilon) = \begin{cases} 1.04766 e^{-\varepsilon^2/2\sigma^2}/(2.5066283\sigma), & \text{if } |\varepsilon| < 2\sigma, \\ 0, & \text{otherwise,} \end{cases} \tag{A.88}$$

where we have chosen numerical factors so that

$$\int_{-\infty}^{\infty} \delta(\varepsilon) d\varepsilon = 1. \tag{A.89}$$

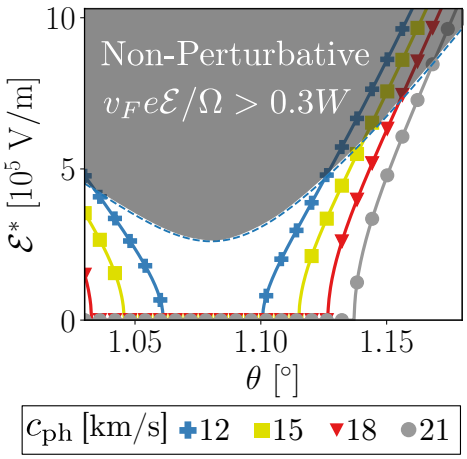

Figure A.14: The requirement that the laser drive strength $\mathcal{E}$ is perturbative, i.e. a fraction of electron bandwidth $e\mathcal{E}L_M < W$, narrows the range of $\mathcal{E}$ values that can be used. As a result, the range of $c_{\rm ph}$ whose $\mathcal{E}^*$ is visible is limited as well - we postulate that they are pushed to higher drive strengths $\mathcal{E}$.

The smearing parameter σ is one-tenth of the maximum quasienergy spacing between nearest-neighbor MP $\boldsymbol{k}$-points

$$\sigma = 0.1 \max_{\langle \boldsymbol{k},\boldsymbol{k}'\rangle,\alpha} |\varepsilon^{(\xi)}_{\boldsymbol{k}\alpha} - \varepsilon^{(\xi)}_{\boldsymbol{k}'\alpha}|, \tag{A.90}$$

where $\langle \boldsymbol{k},\boldsymbol{k}'\rangle$ restricts $\boldsymbol{k}'$ to be a nearest-neighbor of $\boldsymbol{k}$, and we have tuned the prefactor of 0.1 so that upon calculating the steady-state without Floquet-Umklapp processes, we obtain a Fermi-Dirac distribution, $F^{(\xi)}_{\boldsymbol{k}\alpha} = (e^{\varepsilon_{\boldsymbol{k}\alpha}/k_B T_{\rm ph}} + 1)^{-1}$ with temperature $T_{\rm ph}$ of the phonon bath [90].

Convergence of Conductivities

In Figure A.13, we show the convergence of the Hall conductivity σ_{xy} with grid size, using $\hbar\Omega = 5$ meV. In the main text, we use a 163×163 MP grid for non-interacting calculations, and a 73×73 grid for interacting calculations.

A.16 Berry Curvature Calculations

We follow the Berry curvature calculation presented in [87], defining U(1) link variables

$$U_\mu(\boldsymbol{k},t) = \frac{\langle\alpha(\boldsymbol{k},t)|\alpha(\boldsymbol{k}+\hat{\boldsymbol{\mu}},t)\rangle}{|\langle\alpha(\boldsymbol{k},t)|\alpha(\boldsymbol{k}+\hat{\boldsymbol{\mu}},t)\rangle|} \tag{A.91}$$

where $\mu = x, y$, $\hat{\boldsymbol{\mu}} = \boldsymbol{G}_\mu/N$, and $|\alpha(\boldsymbol{k}, t)\rangle$ are the Bloch vectors (i.e., $|\psi_{\boldsymbol{k}\alpha}(t)\rangle = e^{-i\boldsymbol{k}\cdot\boldsymbol{r}}|\alpha(\boldsymbol{k}, t)\rangle$). The Berry curvature is

$$\mathcal{B}_{\boldsymbol{k}\alpha}(t) = \frac{(2\pi)^2}{N^2 A_M} \arg\left[\frac{U_x(\boldsymbol{k}, t)U_y(\boldsymbol{k} + \hat{\boldsymbol{x}}, t)}{U_x(\boldsymbol{k} + \hat{\boldsymbol{y}}, t)U_y(\boldsymbol{k}, t)}\right] \tag{A.92}$$

and we use the time-averaged Berry curvature

$$\mathcal{B}_{\boldsymbol{k}\alpha} \equiv \frac{1}{2\pi/\Omega}\int_0^{2\pi/\Omega} \mathcal{B}_{\boldsymbol{k}\alpha}(t)dt \tag{A.93}$$

in transport calculations.

A.17 The Drive Amplitude Perturbative Regime at Different Twist Angles

We have treated the laser drive as a perturbation to the undriven TBG Hamiltonian, which restricts the range of field strengths $\mathcal{E}$ we can use to a weak perturbative regime. This also narrows the range of phonon speeds c_{ph} that will generate a critical field strength $\mathcal{E}^*$ in the perturbative regime, hence the narrow range of c_{ph} we have considered in, e.g., Figure 1(c). For various twist angles, we estimate the range of drive strengths $\mathcal{E}$ that are perturbative in the unshaded region of Figure A.14 and overlap in solid lines the predicted value of $\mathcal{E}^*$ for different speeds of sound. The shaded, non-perturbative regime corresponds to drive energy scales $v_F e\mathcal{E}/\Omega$ greater than a fraction, e.g., 0.3, of the bandwidth W. Here, we follow the analysis in [25] to estimate the undriven Fermi velocity

$$v_F(\theta) = \sqrt{\left((1 - 3\alpha^2)/(1 + 3\alpha^2(1 + \eta^2)) \times v_F^{\text{ml}}\right)^2 + v_{\text{min}}^2}, \tag{A.94}$$

where $v_{\text{min}} = 10^4$ m/s is a manually set minimum Fermi velocity of the undriven flat bands, and we use the same parameters as in Section A.2. We also adjust Ω such that $\Omega/v_F(\theta)$ is constant and equal to those considered in Figs. 1-4.

Chapter 6

SIGNATURES OF FLOQUET ELECTRONIC STEADY STATES IN GRAPHENE UNDER CONTINUOUS-WAVE MID-INFRARED IRRADIATION

Light-induced phenomena in materials can exhibit exotic behavior that extends beyond equilibrium properties, offering new avenues for understanding and controlling electronic phases. So far, non-equilibrium phenomena in solids have been predominantly explored using femtosecond laser pulses, which generate transient, ultra-fast dynamics. Here, we investigate the steady non-equilibrium regime in graphene induced by a continuous-wave (CW) mid-infrared laser. Our transport measurements reveal signatures of a long-lived Floquet phase, where a non-equilibrium electronic population is stabilized by the interplay between coherent photoexcitation and incoherent phonon cooling. The observation of non-equilibrium steady states using CW lasers stimulates further investigations of low-temperature Floquet phenomena towards Floquet engineering of steady-state phases of matter.

6.1 Introduction

Since the inception of quantum theory, light-matter interaction has been a significant source of fascinating discoveries and innovative technologies. In the last few years, Floquet engineering, the use of light to control the properties of a material, emerged as a focus of intense research [59, 124, 140, 167, 215, 216, 225, 239, 256]. This upsurge has been mainly driven by theoretical efforts [17, 63, 84, 153, 216, 239, 242, 253], with a few key experiments in the condensed matter realm, including the detection of Floquet-Bloch states through time- and angle-resolved photoemission spectroscopy [174, 187, 301, 329], second harmonic generation [260], as well as the observation of light-induced shifts of exciton resonances in WS_2 [143, 263] and light-induced Hall effect in graphene [185]. These experiments predominantly explored the transient phenomena induced by ultrafast pulsed lasers, uncovering some of the physics predicted by the Floquet theory [120]. Other studies explored the continuous-wave (CW) regime by inducing discrete Andreev-Floquet bound states in Josephson junctions under CW microwave irradiation [108, 220]. However, so far, solid-state experiments in the CW regime have not accessed the Floquet physics of delocalized Bloch states due to challenges related to population transfer effects

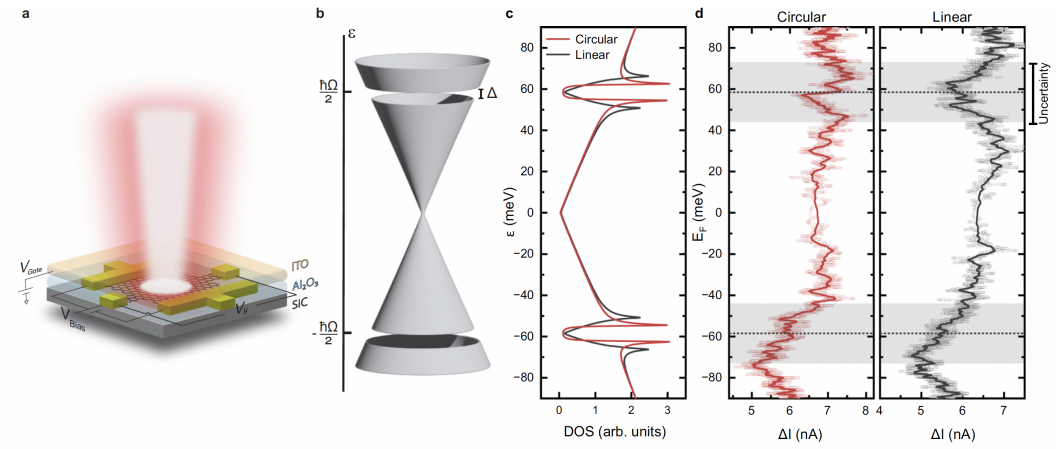

Figure 6.1: (a) Device layout with two contacts for longitudinal bias, V_{Bias}, and two contacts for measurements of the transverse voltage, V_y. The device has a square geometry with a 5-μm side and an indium tin oxide (ITO) top gate with an Al2O3 dielectric sublayer, for applying a gate voltage V_{Gate}. (b) Drive-modified Floquet bands of the graphene Dirac cone, which exhibits a Floquet gaps of size at the resonance energies $\varepsilon = \pm\hbar\Omega/2$, where $\hbar$ is the reduced Planck constant and Ω is the angular frequency of the laser. (c) Density of states of the Floquet bands calculated numerically for a circularly and linearly polarized laser of power density $P = 3$ mW/μm^2. (d) Photo-induced change of source-drain current (ΔI) as a function of Fermi energy E_F for circularly and linearly polarized laser irradiation, as measured at a constant source-drain voltage of 6 mV. ΔI is measured with a lock-in amplifier using a chopper modulation as a reference. The circles represent data points and the solid lines are obtained by adjacent point averaging. The dotted lines mark the E_F values corresponding to $\pm\hbar\Omega/2$, with the related uncertainty indicated by the gray stripes. The uncertainty is attributed to the gate efficiency calibration and the detail is described in Appendix B. The dips in ΔI at energies $\pm\hbar\Omega/2$ are much broader than the Floquet gap Δ(see c) and arise from the non-equilibrium steady-state distribution of electrons. The measurements were performed on sample A at a cryostat temperature of $\sim$ 3.5 K, laser photon energy of 117 meV, and laser power density of 1.1 mW/μm^2.

and heating. In this work, we demonstrate that under intermediate intensity CW mid-infrared (mid-IR) irradiation [see Figure 6.1(a)], the electronic population in graphene forms a non-equilibrium steady state with signatures of the underlying single-particle Floquet physics. In particular, the resulting electronic steady state relies on the Rabi-like Floquet gaps and a suppressed density of states (DOS) around electronic energies of half the photon energy in graphene's Floquet band structure [see Figure 6.1(b) and (c)]. Importantly, we demonstrate that photoinduced transport can be used as a probe of the emergent Floquet steady state in the system.

Specifically, we report on signatures of these steady Floquet effects in the gate voltage dependence of the laser-induced longitudinal photoresponses of graphene samples at cryogenic temperatures ranging from 2.5 K to 50 K.

6.2 Devices and photoconductive measurements

Our graphene devices were fabricated from large-area epitaxial graphene grown on SiC. The typical electron mobility of our material is about 5000 cm^2/Vs for the carrier concentration range studied in this work. (Figure B.7 shows an image of a cluster with 4 devices.) Each device was a 5 μm × 5 μm graphene square, with two source-drain contacts for the longitudinal electrical transport, two contacts to measure the transverse voltage, and a separate top gate electrode, as depicted in Figure 1a. The top gate comprised a 90-nm-thick dielectric Al_2O_3 layer and a gate electrode of sputtered 110-nm-thick indium tin oxide (ITO). The properties of our epitaxial graphene, the details of the fabrication process, and the optical properties of the gate electrode are outlined in Appendix B. Our laser operates with a photon energy of $\hbar\Omega$ = 117 meV, deliberately chosen to be below the optical phonon generation threshold in graphene (160-200 meV), in contrast to previous experiments that utilized photon energies above this threshold [185]. Importantly, this approach minimizes photo-induced phonon generation, guaranteeing acoustic phonons remain at low cryogenic temperatures and providing cooling channels for photoexcited electrons.

Overall, we measured three top-gated graphene devices on two different chips: samples A and B on the first chip, and sample C on the second chip. The devices were cooled in a closed-cycle optical cryostat with a base temperature of 2.5 K and were irradiated with a 10.6-μm-wavelength CW CO2 laser, providing up to 25 W of linearly polarized light. The laser polarization was controlled with a $\lambda/4$ plate. The radiation was delivered using high-power-withstanding molybdenum mirrors, and it was focused on the sample to a spot with a waist of about 50 μm using a ZnSe lens with a focal distance of 50.8 mm. The maximum power used to irradiate the sample was 16 W, yielding a power density P up to 2.6 $mW/\mu m^2$ after considering energy attenuation in the cryostat window and in the top gate of the graphene devices. Further details of the experimental setup are described in Appendix B.

We performed photoconductive measurements on the Floquet system by measuring the longitudinal current using a lock-in amplifier, with the reference signal to the lock-in provided by a chopper. The source-drain bias was mV unless otherwise

noted. The chopper modulated the laser beam with a frequency of around 23 Hz and a duty cycle of $\sim$ 10%. This procedure provided a direct measurement of the photocurrent, denoted and defined as the difference in the source-drain current between the irradiated and equilibrium systems. To explore the doping dependence of the photocurrent, we also extracted the equilibrium Fermi energy, E_F, as a function of the applied gate voltage using the classical Hall effect at different gate voltages, as described in detail in Appendix B.

The experimentally measured photocurrent ΔI [see Figure 6.1(d)] exhibits dips as a function of near doping close to the Floquet gaps for both circular and linear polarization of the laser beam. We note that due to the size of the sample chosen to optimize the coupling to the incident beam [146], the circular polarization might be distorted by the proximity to metallic electrodes [24] (see Appendix B for details). Nonetheless, the photocurrent dips are robust to changes in polarization and are sensitive only to the electronic photoexcitation rate set by the laser power density and frequency. Importantly, the broadness of the dips, significantly exceeding the width of the Floquet gaps in the graphene density of states [see Figure 6.1(d)], cannot be explained with single-particle Floquet physics and instead indicates strong non-equilibrium electronic population effects.

6.3 Theory of Floquet Steady States

Under CW illumination, the electronic population forms a non-equilibrium steady state distribution predominantly stabilized by electron-phonon scattering processes [see Figure 6.2(a)]. To understand the photo-assisted population dynamics, we focus on the low-energy band dispersion of graphene, which exhibits two Dirac cones with Fermi velocity corresponding to the graphene K and K' valleys [see Figure 6.2(a)]. Here, $\boldsymbol{k}$ denotes the crystal momentum, and α enumerates the energy bands. In our theoretical analysis, we focus on circular laser polarization for concreteness. We expect the longitudinal photocurrent to be qualitatively the same for linear polarization parallel to the current. The primary effect of a circularly polarized laser drive is the opening of dynamical gaps at the resonance energies with a size [33, 140, 215]. An additional Haldane gap opens at the Dirac point1, but the gap is too small to be resolved for the power densities used in the experiment, and is therefore not shown in Figure 6.2(a) citation of the electron to a virtual state (arrow 1) through photon absorption followed by the phonon-emission process relaxing the electron to the conduction band (arrow 2). The electronic population excited by this process is subsequently spread across a small window of energies assisted by

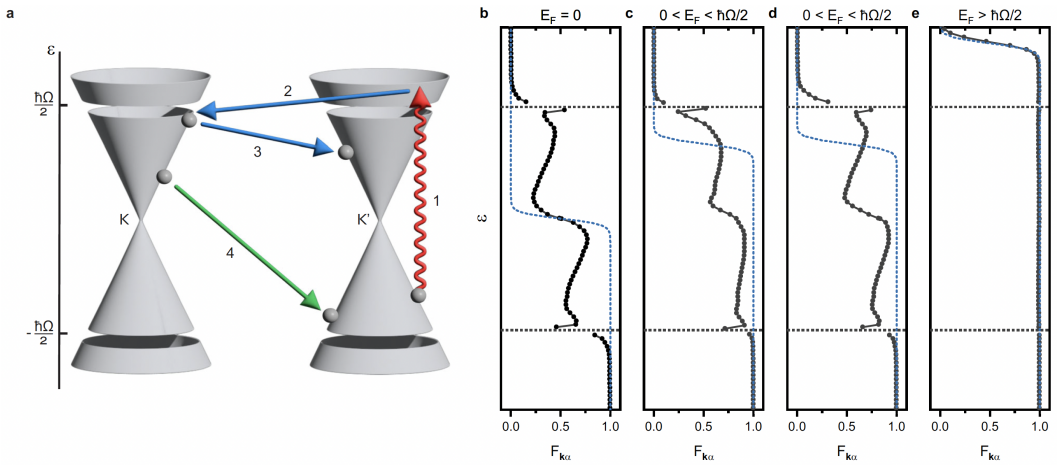

Figure 6.2: (a) Key scattering processes between the graphene K and K' valleys facilitated by photons (arrow 1), surface acoustic phonons (arrows 2, 3), and graphene acoustic phonons (arrow 4) that contribute to the steady state. (b) Steady state distribution (black solid curve) for $P = 1.9$ mW/μm^2 and equilibrium distribution (blue dashed curve) of electrons at doping $E_F = 0$, where the longitudinal photoconductivity is enhanced relative to equilibrium. Here, ε denotes the quasienergy and $F_{k\alpha}$ denotes the electronic occupation. (c) Steady state distribution (black solid curve) of electrons at doping $E_F = 0.35\hbar\Omega$ and $P = 0.8$ mW/μm^2, where the photoconductivity is suppressed relative to an equilibrium distribution expectation (blue dashed curve). (d) Same as (c) but for a larger power density $P = 1.9$ mW/μm^2, where the steady state distribution exhibits additional electron density above the Floquet gap. e Steady state distribution (black solid curve) of electrons for $P = 1.9$ mW/μm^2 at doping $E_F = 0.75\hbar\Omega$, where the photoconductivity is approximately identical to that of an equilibrium distribution (blue dashed curve), with a slightly raised effective temperature due to multi-photon heating processes. The horizontal dotted lines in (b–e) mark ε values corresponding to $\pm\hbar\Omega/2$.

the emission of low-energy acoustic phonons (arrow 3) and can be subsequently relaxed through additional acoustic phonon emission processes (arrow 4) back into the valence band. Ultimately, in the steady state, the excited electronic occupation in the conduction band is set by the balance between phonon-assisted photo-excitations (arrows 1-3) and phonon-assisted cooling processes (arrow 4). In Figure 6.2(a) and throughout our theoretical calculations, we include two phonon branches: a slow surface acoustic phonon branch with Rayleigh wave speed 1.3 km/s [arrows 2 and 3 in Figure 6.2(a)] and a faster graphene acoustic phonon branch with speed 11 km/s [arrow 4 in Figure 6.2(a)] [50]. The surface acoustic phonon speed used in our simulations captures the order of magnitude of the Rayleigh wave speed of the SiC [210]. To find the steady state electronic population $F_{k\alpha}$, we solved numerically

the full Floquet-Boltzmann equation, which includes all the microscopic electron-phonon scatterings between Floquet-Bloch states in the laser-driven graphene (see Appendix B for details) [74, 257, 258, 312]. The resulting steady state occupations at various electronic dopings are plotted in Figure 6.2(b)-(e), and the photocurrent is calculated from the steady state occupations using linear response theory in the weak source-drain bias regime. In our theory, we also account for charge puddles and a small, intensity-dependent lattice temperature difference between the driven and undriven systems. We estimate the conductivity in the presence of charge puddles using a phenomenological formula detailed in Appendix B.

Remarkably, the steady state distributions denoted by black curves in Figure 6.2(b)-(e) exhibit multiple step-like features associated with large $|\partial F_{\boldsymbol{k}\alpha}/\partial\varepsilon_{\boldsymbol{k}\alpha}|$, resembling effective Fermi surfaces, which significantly affect transport. The electron-like effective Fermi surfaces ($\partial F_{\boldsymbol{k}\alpha}/\partial\varepsilon_{\boldsymbol{k}\alpha} < 0$) contribute to a longitudinal current parallel to the direction of an applied electric field, while hole-like effective Fermi surfaces ($\partial F_{\boldsymbol{k}\alpha}/\partial\varepsilon_{\boldsymbol{k}\alpha} > 0$) suppress the overall photocurrent by contributing current antiparallel to the applied field. This is in strict contrast to an equilibrium distribution, where a single Fermi surface appears in the electronic distribution [see blue dashed curves in Figure 6.2(b)-(e)], and only electrons near the Fermi surface contribute to the longitudinal transport. The Fermi surfaces in the distribution predominantly arise from the scattering processes 1-4 sketched in Figure 6.2(a). Most notable is the non-equilibrium distribution for an electron-doped system $0 < E_F < \hbar\Omega/2$ [see Figure 6.2(c) and (d)], where the equilibrium Fermi surface located at finite density of states (see blue dashed curve) is separated into three electron-like Fermi surfaces (see black solid curve) which are located near the dips of the density of states and therefore contribute very few electronic carriers. In particular, two electron-like Fermi surfaces are centered at the Floquet gaps, where electronic group velocities and density of states are reduced, and another is positioned at zero energy, where the density of states vanishes. The reduced concentration of electronic carriers gives rise to a suppressed conductivity in the driven system. This phenomenon persists for both weak and strong driving amplitudes, as shown in Figure 6.2(c) and (d), respectively. For doping above resonance $E_F > \hbar\Omega/2$, processes 1–4 are Pauli-blocked, giving rise to an equilibrium-like distribution [see Figure 6.2(e)].

6.4 Optically-controlled photoresponse

Having understood the interplay of the Floquet bands, steady state occupation, and photocurrent ΔI, we now compare the theoretically calculated and experimentally

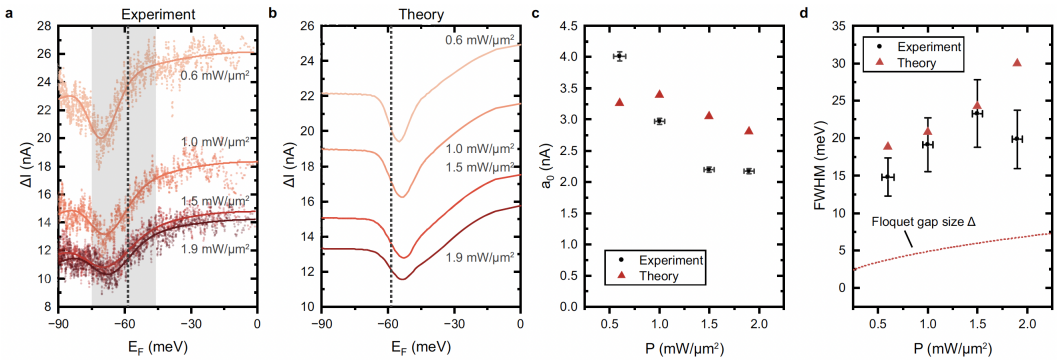

Figure 6.3: (a) Photo-induced change of source-drain current (ΔI) as a function of E_F under irradiation at various peak power densities, as measured on sample C at a constant source-drain voltage of 6 mV and a cryostat temperature of 3.2 K. The photon energy is $\hbar\Omega = 117$ meV. The laser beam is circularly polarized. The circles represent data points and the solid lines are the fitted curve by a Gaussian-like function described in the Methods. The dotted line marks the E_F value corresponding to $-\hbar\Omega/2$, with the related uncertainty indicated by the gray stripes. (b) Theoretically predicted ΔI as calculated from the Floquet Boltzmann equation. The dotted line marks the E_F value corresponding to $-\hbar\Omega/2$. (c) Depth a_0 of the photocurrent dip and associated error, as calculated from a Gaussian-like fit (see details in the Methods section). For both the theoretical and experimental data, a_0 decreases with the power density P for large P due to enhanced heating processes in the Floquet steady state. (d) Experimental and theoretical FWHM of the photocurrent dip and the Floquet gap size (red dotted line), Δ, as a function of the power density. The FWHM exceeds Δ, indicating the emergence of photoexcited electrons in the non-equilibrium Floquet steady state. The detailed error analysis of FWHM is described in Appendix B. The uncertainty in the laser power density due to power fluctuation in (c) and (d) are estimated by the change in the laser power before and after each transport measurement.

measured value of ΔI and discuss the tunability of the photoresponse by the laser power. In Figure 6.3(a), we focus on the experimentally measured photocurrent dip at negative E_F and plot the photocurrent for various laser power densities. In Figure 6.3(b), we show the theoretically calculated photocurrent for the same power densities. Let us discuss a few salient features captured by the theoretical model. A key feature is the broad width of the photocurrent dip, which we estimate by fitting the photocurrent to a Gaussian-like function detailed in the Methods section. The amplitude of the Gaussian a_0 quantifies the depth of the photocurrent dip, while the full width at half maximum (FWHM) quantifies its width. Notably, our theoretical prediction of the decrease in a_0 with the power density P, agrees with the experimental observation [see Figure 6.3(c)], indicating a power dependence of

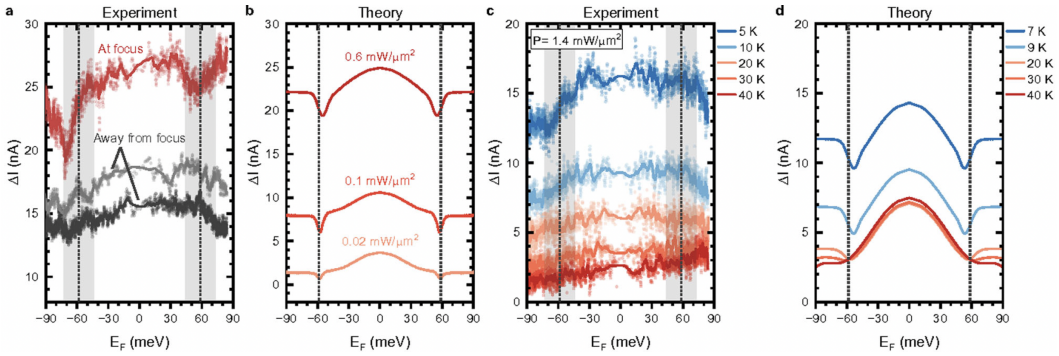

Figure 6.4: (a) Longitudinal photocurrent as a function of at a fixed source-drain voltage of 6 mV, with laser spot in focus and defocused. For all three curves, the laser power is $\sim$ 3.6 W, corresponding to a peak power density of 0.6 mW/μm^2 at focus. Under defocused irradiation, with the laser spot slightly moved to the side, the power density drops by $\sim$ 3 times (gray curves). Circular polarization of 10.6 μm wavelength laser radiation. The cryostat temperature stabilized at $\sim$ 3.4 K. b Theoretically calculated photocurrent for weak drives, exhibiting shallower dips near resonance as a function of decreasing driving power, in agreement with (a). (c) Temperature dependence of the longitudinal photocurrent as a function of E_F. The photocurrent decreases, and the dips at $E_F = \pm\hbar\Omega/2$ disappear at high temperatures. The laser beam is circularly polarized. (d) Theoretically calculated photocurrent for laser power density 1.4 mW/μm^2, the photocurrent dip becomes less visible at higher temperatures. The dotted lines in (a)–(d) mark the E_F value corresponding to $\pm\hbar\Omega/2$, where the related uncertainty is indicated by the gray stripes in (a) and (c).

the steady state distribution. The reduction of a_0 with P arises due to the increase of the photoexcited carrier density above the Floquet gap, which scales as $\sim P^{1/2}$, effectively increasing the photocurrent [cf. the shift of the effective Fermi surface near $\hbar\Omega/2$ in Figure 6.3(c) and (d)] [33]. The FWHM of the photocurrent dip observed in the experiment and predicted by the theory are both broader than the size of the Floquet gap, see Figure 6.3(d), indicating a Floquet-induced electronic population inversion in the steady state. We note that $\Delta I > 0$ for $0 < E_F < \hbar\Omega/2$ due to charge puddle and lattice heating effects (see Appendix B for more details). Finally, we note that the horizontal offset in the theoretically calculated photocurrent shown in Figure 6.3(b) relative to the experimental data in Figure 6.3(a) may arise from changes in the total electronic carrier density in the sample during laser illumination, which were not accounted for in the experimental assignment of the chemical potential.

To further verify that the transport signatures observed in the experiment arise from

photo-induced dynamics, we explore the experimentally measured photo-response for out-of-focus lasers, which reduce the irradiation power density by roughly a factor of three. Figure 6.4(a) demonstrates that the visibility of the photocurrent dip is significantly suppressed as the power density is reduced. This behavior, reproduced in theory [see Figure 6.4(b)], reflects the suppressed probability of drive-induced photoexcitation processes under weak laser irradiation.

Next, we explore the lattice temperature dependence of the electronic steady state and conductivity. Figure 6.4(c) and (d), respectively, show the measured and the theoretically predicted ΔI as a function of E_F, for several values of the lattice temperature. At higher temperatures, the distribution of the photoexcited electrons spreads over larger energy support, relaxing the sharp energy-momentum bottlenecks in the steady state distribution [see processes 1-4 in Figure 6.2(a)]. As a result, the dips in ΔI become less pronounced, virtually disappearing around 20 K. The discrepancy of the temperature dependence around charge neutrality between the experimental and theoretical plots is attributed to the finite-temperature physics of the charge puddles, which could modify the relaxation time of electrons at different temperatures under weak source-drain bias [163], which is not captured in the theory. The strong lattice temperature dependence of both the theoretically calculated and experimentally observed photocurrent, however, highlights the role of low phonon temperatures in stabilizing low-temperature electronic phenomena of Floquet effects in our system.

6.5 Discussion

The photoconductivity dip discussed above has been reproduced for other samples, which we present in the Appendix B. Different samples with different charge inhomogeneities showed similar widths of the photocurrent dip. This observation is consistent with the emergence of a Floquet steady state, which is predicted to be weakly sensitive to disorder. The positions of the dips in the electron and hole regions of the gate dependence are also slightly asymmetric, similar to particle-hole asymmetric results reported in McIver et al. [185].

So far, we have not discussed the transverse photoconductivity of the system. Our transverse voltage measurements displayed a laser helicity-dependent component on the μV scale, which amounts to a Hall conductivity of the order of $\sigma_{xy}^{\text{Hall}} \sim 10^{-3} e^2/h$, see Figure B.11. This range of values undershoots the prediction of $\sigma_{xy}^{\text{Hall}} \sim e^2/h$, from our theoretical model, which is mainly designed as a simple model for the longitudinal component of the photocurrent. We believe that a key reason for this

discrepancy is the distortion of the circular polarization by the metallic contacts, leading to regions of the sample with nearly linear polarization [24] (see Appendix B for details). In these regions, the Berry curvature can have large off-diagonal elements, reducing the photoresponse. Additionally, our theoretical calculation of the Hall voltage does not account for electron-electron interactions and charge puddles. Electron-electron scattering could suppress the Hall conductivity by raising the effective temperature of the steady-state electron-like Fermi surfaces [see Figure 6.2(b)–(e)] near the resonant Floquet gaps [258, 312]. Charge puddles could further suppress the Hall voltage by producing regions in the sample with low conductivity, which exhibit weak longitudinal source drain current and heavily suppressed local Hall voltage. More details of the transverse photoresponse measurements are provided in Appendix B.

In summary, we have explored the transport properties of graphene driven by a CW mid-infrared laser. In such metallic systems, the Floquet dressing of single-particle bands by resonant periodic drives is intertwined with many-body effects, such as electron scattering and population dynamics. Notably, we demonstrate that the interplay between these processes at intermediate driving intensities and cryogenic temperatures facilitates the formation of low-entropy electronic steady states. These steady states emerge from a cascade of photo-assisted electron-phonon scattering events that effectively cool the photoexcited electrons to low entropy states.

Our findings suggest that, in graphene on SiC, these processes are dominated by the emission of surface acoustic phonons at the graphene-SiC interface, along with acoustic phonons in the graphene itself. Furthermore, the formation of these steady states is crucially dependent on the underlying single-particle Floquet physics, such as the presence of Floquet gaps in the single-particle spectrum and scattering into replica Floquet bands. We interpret the observed pronounced dip in longitudinal conductivity in our samples as evidence of Floquet steady states. The characteristics of this dip—its position, depth, and width as functions of doping—align closely with predictions from Floquet many-body theory. Our results indicate a promising approach to perform Floquet engineering in metallic systems for sustained operation, potentially leading to the creation of Floquet steady-state phases, such as drive-induced symmetry broken phases [76], laser-induced flat bands [3, 131, 165], and optically-controlled topological transport [74, 312].

6.6 Methods

Experiment

The CW source was a 10.6 μm-wavelength, air-cooled Synrad J48-2 CO_2 laser, providing up to 25 W of linearly polarized light, modulated with a chopper (Scitec Instruments 300CD) with 27 Hz modulation frequency. The circular polarization of the laser radiation was controlled by a custom-made zero-order $\lambda/4$ plate, provided by Optogama UAB. For the delivery of the optical beam, we used molybdenum mid-IR high power mirrors.

The samples were cooled down to 2.5 K with a closed-cycle cryostat Oxford Instruments Optistat AC-V14. For optical access to our samples, we used a 2-mm thick ZnSe window. The beam delivery was done using an Edmund Optics cage focusing system mounted on a custom-made mechanical attachment to the cryostat. For beam focusing, we used a 50.8-mm focal distance, 1-inch diameter, ZnSe lens. Focusing and alignment of the mid-IR beam was controlled by a system of micrometers [127]. The estimation of the beam diameter at the lens focus is based on a Gaussian beam with our experimental parameters (18-19 mm laser beam waist before lens and 50.8 mm lens focal distance), and it yields ~35-38 μm. Experimentally, we were able to achieve focusing down to a 50 μm spot. This was confirmed during the fine alignment of the laser beam: the magnitude of was changing from the noise level to a maximum signal and then back to the noise level (about 10-12-times drop of signal magnitude) within 4-5 readout thimble divisions of in-plane alignment micrometers (e.g., within 40-50 μm distance). The maximum applied laser power in our experiments was 16 W, corresponding to a peak power density $\sim 8\ \mathrm{mW}/\mu\mathrm{m}^2$ for ~ 50 μm-diameter beam spot. Taking into account the transmission coefficients of the cryostat window and the gate electrode, we estimate the applied laser intensity as $\sim 2.6\ \mathrm{mW}/\mu\mathrm{m}^2$.

The measurements of photoinduced currents and voltages were performed using a home-made bias box, an HP 6177 C DC current/voltage source (for generation of gate voltages), a National Instruments BNC-2110 junction box, an Ametek 5110 lock-in amplifier, a DL Instruments 1211 current preamplifier, and a custom-made differential voltage preamplifier. The data collection system was controlled using a customized LabVIEW-based program.

The calibration of gate efficiencies of our samples (calibration of gate voltage in units of electron Fermi energy) was performed using a 9 Tesla Quantum Design Physical Property Measurement System at the NHMFL in Tallahassee, FL. The

details about gate efficiency calibration are provided in Appendix B.

Device Fabrication

For the device fabrication we adapted the process developed by Yang et al. [313]. to electron-beam lithography (EBL) [73] with additional lithography steps to deposit and pattern a top gate. The details of the device fabrication are provided in Appendix B. The epitaxial graphene on SiC was purchased from Graphene Waves.

Fitting

We estimate the full width at half maximum (FWHM) of the photocurrent dip by fitting the photocurrent to the function $\Delta I_{\text{fit}} = a_0 \exp\left[-(V_g - B)^2/2\sigma^2\right] + CV_g + D$, where a_0, B, σ, C, and D are fitting parameters, and V_g is the gate voltage. We extract the full width half maximum using the relation $\text{FWHM} = E_F(B+\sqrt{2\ln 2}\sigma) - E_F(B - \sqrt{2\ln 2}\sigma)$, where $E_F(V_g) = \hbar v_F\sqrt{\pi k(V_g - V_d)}$. Here, k is estimated from Hall measurements, and V_d is estimated to be the gate voltage at which σ_{xx} is minimized (see Appendix B).

6.7 Acknowledgements

We acknowledge support from NSF (projects DMR CMP #2104755, DMR CMP #2104770, and OSI #2329006), ANID FondeCyT (Chile) through grant number 1211038, and the Institute for Quantum Information and Matter, an NSF Physics Frontiers Center (PHY-2317110). C.Y. gratefully acknowledges support from the DOE NNSA Stewardship Science Graduate Fellowship program, which is provided under cooperative Agreement No. DE-NA0003960. G.R. and I.E. are grateful to the AFOSR MURI program, under agreement number FA9550-22-1-0339, as well as the Simons Foundation. Part of this work was done at the Aspen Center for Physics, which is supported by the NSF grant PHY-1607611. F.N. gratefully acknowledges support from the Carlsberg Foundation, grant CF22-0727. C.L. was supported by start-up funds from Florida State University and the National High Magnetic Field Laboratory. The National High Magnetic Field Laboratory (NHMFL) is supported by the National Science Foundation through NSF/DMR-1644779, NSF/DMR-2128556 and the State of Florida. L. E. F. F. T. acknowledges partial support from the EU Horizon 2020 research and innovation program under the Marie-Sklodowska-Curie Grant Agreement No. 873028 (HYDROTRONICS Project), and of The Abdus Salam International Centre for Theoretical Physics and the Simons Foundation. The authors thank Dr. Michael Jackson, Dr. Yanfei Yang,

Eli Adler, DaVonne Henry, Amjad Alqahtani, and Thy Le for helpful discussions, Taylor Terrones, Michael Chavez, and Leon Der for help with our experimental setup, and Dr. David Graf for help with experiments at NHMFL.

Appendix B

APPENDIX

B.1 Sample Irradiation with a Continous-Wave Mid-Infrared Laser Beam

The optical setup, with the components described in the Materials and Methods section, is shown in Figure B.1. A pair of molybdenum mid-infrared (Mid-IR) high-power mirrors were used for the delivery of the laser beam. For the pre-alignment of the orientation of the molybdenum mirrors and for the initial positioning of ZnSe lens closer to the position in focus, we used a visible laser (λ = 520 nm) collimated with the Mid-IR irradiation, with a camera to monitor the laser spot on the sample (see the inset in Figure B.1). After this initial alignment, the visible laser and the beamsplitters were removed, and the fine adjustment of the beam positioning with the Mid-IR laser was performed by using the photo-generated current in our devices as a reference. The illumination caused a change in the source-drain current due to the photo-generated hot electrons, as described in the main text. An example of current change under 10.6-μm-wavelength laser illumination is Figure B.2 below. We adjust the beam position by maximizing the photocurrent response. The devices were irradiated with a 10.6-μm-wavelength CW CO_2 laser, providing up to 25 W of

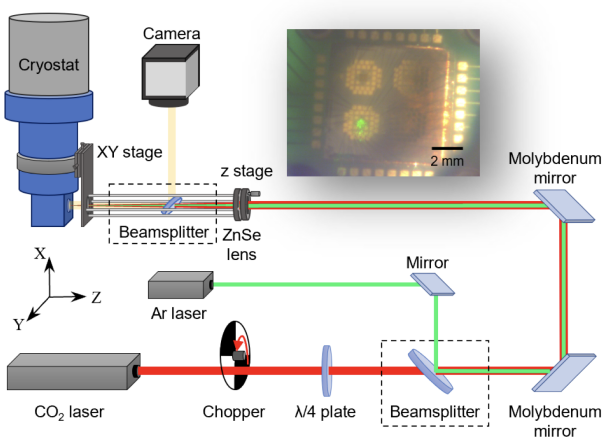

Figure B.1: Scheme of the sample illumination system. Schematic illustration of the optical setup used for delivering and focusing the mid-infrared irradiation. The beamsplitters are used only during the preliminary alignment of optical elements. The inset image shows the visible laser spot on the sample used for the preliminary alignment of the molybdenum mirrors and the ZnSe focusing lens.

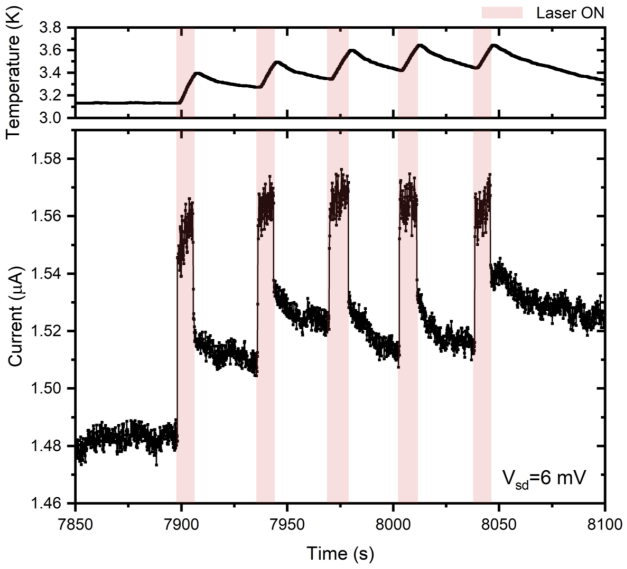

Figure B.2: Measurement sequence in time. Experimentally measured cryostat temperature (top panel) and longitudinal current (bottom panel) with laser blocked and unblocked intervals. Note that the actual graphene lattice temperature, $T(t)$, is expected to be further elevated relative to the cryostat temperature. When the laser is blocked, the sample cools down to T_{bg}, giving rise to a strong bolometric effect in the longitudinal current. The laser illumination is blocked/unblocked in the optical path between the chopper and the sample (light coral stripes indicate when laser is unblocked), the average laser power density is 0.125 mW/μm^2 and the peak power density is 1.25 mW/μm^2, $\hbar\Omega$ = 117 meV (10.6 μm wavelength).

linearly polarized light. The laser beam polarization was controlled with a $\lambda/4$ plate. Experimental samples were designed to maximize efficiency of the beam-sample coupling for the mid-IR irradiation [146]. At the same time, the half-wavelength size of the graphene devices and the attachment of the metallic electrodes to its edges result in predominantly linear polarization of the incident electromagnetic field near the edges of the graphene sample, regardless of the initial polarization of the laser source [24]. The presence of linearly polarized fields in some parts of the sample is expected to influence helicity-dependent effects.

B.2 Measurement Sequence

The laser beam was modulated by a chopper (the modulation frequencies were in the range of 10-50 Hz) with a duty cycle of $\sim$ 10%. During the on period, the system forms a non-equilibrium electronic state characterized by a photocurrent I_{dr} that relaxes during the off period to an equilibrium state with temperature T_{eq} and corresponding photocurrent $I_{\mathrm{eq}}(T_{\mathrm{eq}})$. The relaxation occurs over the phonon

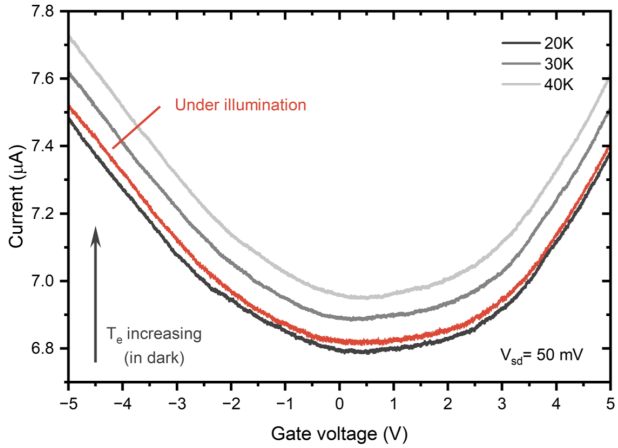

Figure B.3: Laser intensity and temperature dependence of the longitudinal conductance. Gate voltage dependence of the source-drain current at different temperatures with laser blocked (gray) and under irradiation at the base temperature (red), with $P = 0.6\ \mathrm{mW}/\mu\mathrm{m}^2$ and with source-drain voltage fixed at 50 mV.

scattering time, typically on the picosecond scale. The measured photocurrent is, therefore, given by $\Delta I = |I_{\mathrm{dr}} - I_{\mathrm{eq}}(T_{\mathrm{eq}})|$, which is detected directly using a lock-in amplifier, with the reference signal to the lock-in provided by a chopper. Figure B.2 shows the theoretically predicted photocurrent as a function of time, switching between I_{dr} and $I_{\mathrm{eq}}(T_{\mathrm{eq}})$, within the duty cycle.

Due to the illumination, the system temperature T_{eq} is elevated above the background temperature T_{bg}. To test the temperature change and the corresponding bolometric effect, we blocked the beam in the optical path between the chopper and the sample for extended times of a few seconds. During a timescale denoted τ_r, the system's temperature relaxed back to T_{bg} corresponding a reduction of the current to the value $I_{\mathrm{eq}}(T_{\mathrm{bg}})$. We note that the background itself is slightly heated by the laser, leading to gradual changes in T_{bg}. The bottom panel of Figure B.2 shows the longitudinal (source-drain) current measured as a function of time and at constant source-drain voltage while the laser beam was blocked or unblocked. The time dependence of the current can be fit to the function $I_{\mathrm{eq}}(T(t))$, where $T(t) = T_{\mathrm{bg}} + (T_{\mathrm{eq}} - T_{\mathrm{bg}})e^{-t/\tau_r}$ within one unblocking-blocking interval.

The relation of the photoresponse ΔI to effects of electron heating may be illustrated further in the following supplementary experiment. Figure B.3 shows the current vs. gate voltage curves of a graphene device at three different temperatures and at a fixed source-drain bias voltage without any laser irradiation (gray curves). The temperature dependence of the electrical resistance in graphene is determined by

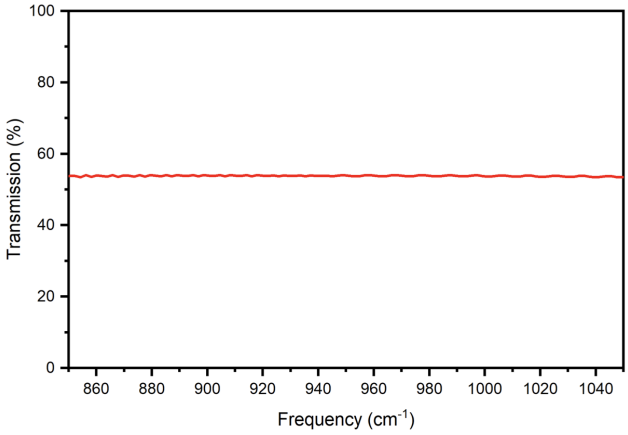

Figure B.4: Mid-Infrared transmission spectrum of ITO. Example of spectrum measured from our typical 110-nm thick ITO layer in the range around 10.6 μm wavelength (corresponding to the wavenumber 943 cm^{-1}).

different intrinsic and extrinsic sources of scattering, including phonons, defects in the crystal lattice or deformation in the graphene sheet (wrinkles or steps), as well as impurities in the substrate or on the graphene surface [26, 37, 41, 60, 266]. The presence of electron- hole puddles and quantum corrections also complicate the dependence of the electrical resistance on carrier density and temperature, especially at low temperature [101, 181, 184, 306]. For our graphene samples, in the whole range of gate voltage that we measured around the Dirac point, the current increases when the temperature increases.

B.3 Transmission property of ITO top gate for Mid-IR irradiation

The Mid-IR radiation actually delivered to the graphene is attenuated by the optical elements. Our ZnSe focusing lens has an anti-reflective (AR) coating, while the cryostat window has no AR coating and transmits 70% of the 10-μm wavelength laser beam. The other important source of attenuation is the Indium-Tin Oxide (ITO) material of the top gate in the experimental samples. Depending on growth conditions, post-treatment, and many other factors, the optical transmission of this material may vary significantly. Measured or theoretically expected values of Mid-IR transmission of ITO range from less than 10% to more than 50% for material thicknesses around 100 nm, depending on the electron concentrations [48, 106]. For an accurate estimation of attenuation in our case, we fabricated and tested ITO samples using the exact same growth conditions and thickness of the material as those we used in our experimental graphene devices. The infrared transmission spectra were measured using a Nicolet Nexus 8700 Fourier-Transform spectrometer

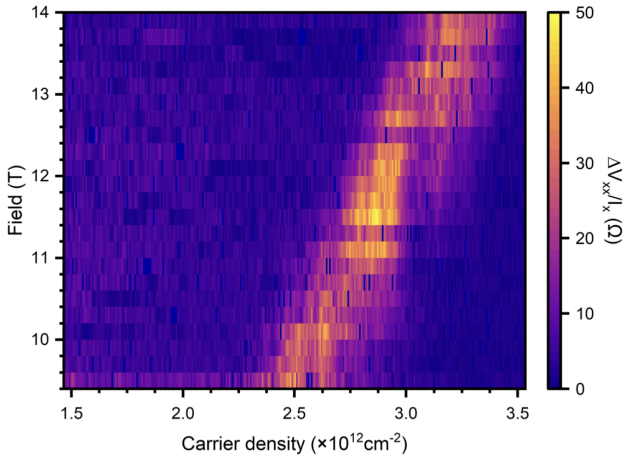

Figure B.5: Longitudinal photoresponse vs. carrier density at different B fields. Longitudinal voltage photoresponse as a function of magnetic field and carrier density, under chopper-modulated irradiation with circular polarization, at a laser intensity of 20 μW/μm^2 and photon energy $\hbar\Omega$ = 117 meV. The sample is biased at a fixed current I_x of 1 μA, and the photoinduced change in source-drain voltage ΔV_{xx} is measured with a lock-in amplifier.

equipped with a KBr beamsplitter and a DTGS photodetector. A typical transmission spectrum of a 110-nm-thick ITO layer is shown in Figure B.4. Transmission measurements were performed at multiple locations on two different samples, yielding an average transmission of 45%.

B.4 Cyclotron Resonance of the Top-Gated Epitaxial Graphene Samples

We performed cyclotron resonance measurements on an epitaxial graphene sample on SiC at 1.6 K using an 18/20 T general purpose superconducting magnet at NHMFL in Tallahassee, FL. We used a 1 MOhm resistor connected in series with the sample to keep the source-drain current at a constant value of about 1 μA throughout the measurements. The sample was illuminated by a CW CO_2 laser and a quarter waveplate, as described above. Unlike the zero-field measurement, the laser was delivered through a Mid-IR fiber and focused onto the sample with a ZnSe lens. As shown in Figure B.5, the magnetoresistance reveals a resonance magnetic field value of 11.5 ± 0.2 T that corresponds to a transition between the 0th and the 1st Landau levels, or

$$\Delta E = v_F\sqrt{2\hbar eB/c} = \hbar\Omega \tag{B.1}$$

where $\hbar\Omega$ = 117 meV and B = 11.5 ± 0.2 T. We can, therefore, extract the Fermi velocity in our epitaxial graphene as $v_F = (0.960 \pm 0.008) \times 10^6$ m/s. The cyclotron

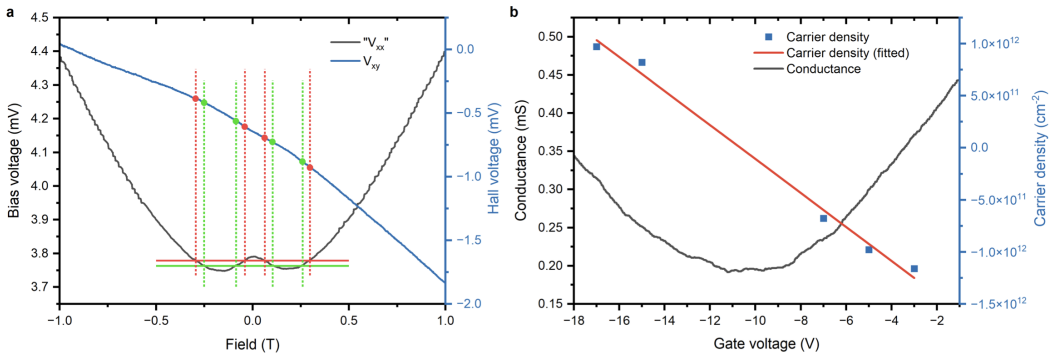

Figure B.6: Gate efficiency calibration. (a) (Black) Source-drain voltage and (blue) transverse voltage from the Hall effect measurements for $V_g = 7$ V and a constant bias (source-drain) current $I_{\mathrm{sd}} = 1\ \mu$A. The green and red lines are examples of the set of "4 points" used for extracting the actual transverse voltage. (b) (Black) Conductance at different gate voltages. (Blue) Carrier density at different V_g from Hall measurements. (Red) Linear fitting of carrier density at different V_g.

resonance peak is determined to have an FWHM of $\sim$ 8 meV, which is about two times broader than that reported in exfoliated graphene samples [46, 244]. Such broadening can be attributed to the charge puddles and traps in graphene introduced during the fabrication process. We can also extract the magnetic length at the resonance field $l_B \sim 7.6$ nm, which is smaller than our estimated mean free path (l_{MFP}) for carrier density $n_c \sim 2.9 \times 10^{12}$ cm^{-2}, about $l_{\mathrm{MFP}} \sim 30$ nm.

B.5 Gate Efficiency Calibration

The Hall effect measurements were performed on sample B at 4 K to determine the carrier density at different gate voltages using a Quantum Design PPMS® system. A 1 MOhm resistor was connected in series with the device to keep the current around 1 μA throughout the measurements. The typical Hall voltage and source-drain voltage curves as a function of the magnetic field at a fixed gate voltage are plotted in Figure B.6(a), where the Hall voltage revealed a non-linear behavior as well as an offset. We note that these source-drain voltages are two-terminal measurements. Unlike four-terminal measurements, two-terminal measurements yield curves that depend on the geometry of the samples [2]. In addition, a slight misalignment of the Hall terminals may lead to a purely geometric (not Hall-effect-related) contribution to the Hall voltage from the bias current that is proportional to the source-drain voltage. We estimated this misalignment as $\sim$ 300 nm along the source-drain current direction in the presented sample. To exclude the contribution from such misalignment, we used the "four-point" approach described below to extract the linear relationship between

the Hall voltage and the applied magnetic field: we randomly picked four data points around the bottom of the source-drain voltage curve at different fields, but with the same source-drain voltage value, so that the misalignment would contribute equally to the Hall voltages among these four points, and we extracted the carrier density from a linear fitting of those four points. For each gate voltage, three sets of the "four points" were randomly picked. Figure B.6(a) shows two sets of four points, in red and green, respectively, for measurements at a fixed gate voltage $V_g = -7$ V. For each set of 4 points the following linear fitting was performed:

$$V_{\text{Hall}}[\text{V}] = k[\text{VT}^{-1}]B[\text{T}] + V_{\text{Hall offset}}[\text{V}] \tag{B.2}$$

where the slope k links to the charge carrier density n_c with the following relationship:

$$n_c[\text{cm}^{-2}] = 10^{-4} \times \frac{I[\text{A}]}{ek[\text{VT}^{-1}]} \tag{B.3}$$

where I was kept around 1 μA as mentioned above and $e = 1.602 \times 10^{-19}$ C. Table B.1 summarizes the data obtained from the fittings and the carrier concentrations obtained at different gate voltages. The extracted values of carrier concentrations at different gate voltages are plotted in Figure B.6(b). From a linear fit of those points, we obtained the following "calibration curve" to relate the carrier density to the gate voltage:

$$n_c[\text{cm}^{-2}] = -k(V_g - V_d)[\text{V}] \tag{B.4}$$

where $k = 1.63 \times 10^{11} \pm \delta k$, $\delta k = 9 \times 10^9$, $V_d = kn_0 = 10.7$ V $\pm\, \delta V_d$, and $\delta V_d \approx V_d\sqrt{(\delta n_0/n_0)^2 + (\delta k/k)^2}$. Here, $n_0 = 1.74 \times 10^{12}$ and $\delta n_0 = 9.37 \times 10^{10}$, with the uncertainties estimated from the 68% confidence interval of the linear fit. The following relationship between the carrier density n_c and Fermi energy E_F in graphene was then applied to determine the corresponding V_g for $E_F = \hbar\Omega/2$:

$$E_F = \hbar v_F \sqrt{\pi n_c}, \tag{B.5}$$

where $\hbar$ is the reduced Plank constant, v_F is the Fermi velocity extracted from the cyclotron resonance measurements as 0.96×10^6 m/s is our top-gated epitaxial graphene samples. For the first crossings, the Fermi energy is half the photon energy, i.e., $E_F = \pm 58.5$ meV, and the corresponding gate voltage was calculated to be about 1.6 V from the charge neutrality point, as summarized in Table B.2.

B.6 Device Fabrication

The top-gated graphene FETs were fabricated using epitaxial graphene on SiC purchased from Graphene Waves. To prevent sample contamination from photoresists,

Table B.1: Fitting results of Hall measurements at different gate voltages

		Gate voltage (V)				
		-3 V	-5 V	-7 V	-15 V	-17 V
Slope ($\times 10^{-4}$)/VT^{-1}	Set 1	-5.290	-6.244	-9.074	7.458	6.294
	Set 2	-5.250	-6.247	-9.024	7.521	6.369
	Set 3	-5.283	-6.267	-9.029	7.412	6.281
Ave. slope ($\times 10^{-4}$)/VT^{-1}		-5.274	-6.252	-9.042	7.464	6.315

Table B.2: V_g corresponds to $E_F = \hbar\Omega/2$

	$-\hbar\Omega/2$	CNP	$+\hbar\Omega/2$
E_F/meV	-58.5	0	$+58.5$
n_c/cm^{-2}	-2.51×10^{11}	0	$+2.51 \times 10^{11}$
V_g/V	-12.2	-10.7	-9.1

a thin Pd/Au layer (5 nm Pd + 15 nm Au) was deposited on the graphene by electron-beam evaporation before further processing [73, 313]. The contacts were fabricated first to prevent the charging effect during the electron beam lithography (EBL) process. Contact patterns were written following a standard EBL process using a Zeiss SUPRA55-VP system on a methyl methacrylate/polymethyl methacrylate (MMA/PMMA) bilayer e-beam resist, followed by magnetron sputtering deposition of a total of 1.5 nm Ti and 400 nm Au. The graphene was then patterned into Hall bars following a process described in Figure B.7(a), where a layer of PMMA defined by EBL was used as the etch mask during dry etching (Ar plasma, 50 s.c.c.m., 150 W, Oxford Plasmalab 80), and the EBL pattern was designed in such a way that only the channel area shown in Figure B.7(b) remained unexposed. Prior to the top gate fabrication, diluted aqua regia (DAR, HNO3:HCl:H2O = 1:3:4) was used to remove the Pd/Au protection layer. The samples were annealed in vacuum afterwards to remove the residues from the DAR treatment as well as adsorbates from ambient exposure (H_2O, O_2, etc.).

Since the graphene grown on SiC is intrinsically n-doped due to the formation of the buffer layer during the graphene growth, before the atomic layer deposition (ALD) growth of an Al_2O_3 layer, we doped the samples with nitric acid vapors in a standard fume hood, following a procedure developed by Mhatre et al. [188]. to bring the Fermi level closer to the charge neutrality point. As shown in Figure B.7(c), a 90-nm Al_2O_3 dielectric layer was grown on top of graphene by atomic layer deposition (Beneq TFS 200). The Al_2O_3 masking of the contact pads was removed by buffered hydrofluoric acid using a layer of Shipley 1813 patterned by photolithography as

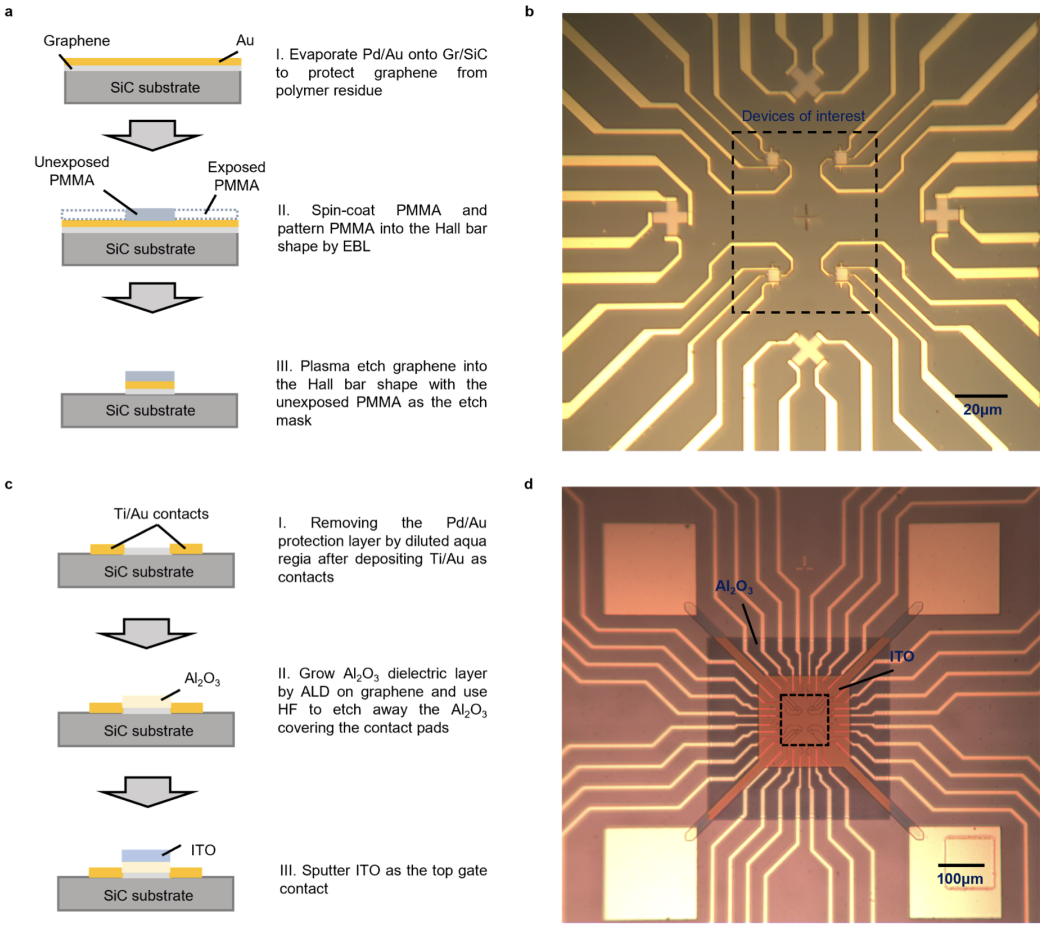

Figure B.7: Scheme of key steps in top-gated graphene device fabrication. (a) Patterning of graphene Hall bars with a thin Pd/Au protection layer. (b) Optical image of the graphene devices prior to removing the metal protection layer and the top gate fabrication. (c) Illustration of top gate fabrication using Al_2O_3 as the dielectric layer and ITO as the gate contact. (d) Optical image of the top-gated devices. The dashed line marks the area of devices shown in (b).

the etch mask. The top gate contact was patterned by photolithography, followed by sputtering of 110-nm indium tin oxide (ITO). Figure B.7(b) shows a cluster of four top-gated devices.

B.7 Characterization of Single-Particle Dynamics via Floquet States

We first derive the driven graphene Hamiltonian near the valleys $\xi = +1, -1$ corresponding to the K and K' valleys of graphene. The Dirac Hamiltonian in valley ξ is given by $H^{\xi}(\boldsymbol{k}) = \hbar v_F \boldsymbol{k} \cdot (\sigma_x, \xi\sigma_y)$ where $\boldsymbol{k} = (k_x, k_y)$ is the electronic momentum and σ_x and σ_y are the Pauli matrices. We include the irradiation by the circularly polarized laser of vector potential $\boldsymbol{A}(t) = A(\cos\Omega t, \sin\Omega t)$ via mini-

mal coupling: $H^{\xi}(\boldsymbol{k},t) = H^{\xi}(\boldsymbol{k} + e\boldsymbol{A}(t)/\hbar)$. The time evolution generated by $H^{\xi}(\boldsymbol{k},t)$ has a complete set of solutions of the form $|\psi^{\xi}_{\boldsymbol{k}\alpha}(t)\rangle = e^{-i\varepsilon_{\boldsymbol{k}\alpha}t/\hbar}|\Phi^{\xi}_{\boldsymbol{k}\alpha}(t)\rangle$, where $|\Phi^{\xi}_{\boldsymbol{k}\alpha}(t)\rangle = |\Phi^{\xi}_{\boldsymbol{k}\alpha}(t+T)\rangle$ is the Floquet-Bloch state, $\varepsilon_{\boldsymbol{k}\alpha}$ is the quasienergy, and $T = 2\pi/\Omega$ denotes the laser driving period. (Here, we drop the ξ index in $\varepsilon_{\boldsymbol{k}\alpha}$, because the quasienergy spectrum is identical in both valleys.) As a result of their time periodicity, the Floquet-Bloch states can be decomposed as $|\Phi^{\xi}_{\boldsymbol{k}\alpha}(t)\rangle = \sum_m e^{-im\Omega t}|\phi^{n\xi}_{\boldsymbol{k}\alpha}\rangle$, with $|\phi^{n\xi}_{\boldsymbol{k}\alpha}\rangle$ denoting the Floquet harmonics that can be found by solving the Floquet Schrodinger equation (see Ref. [241]). The Floquet-Bloch states form a complete basis of stationary solutions to the time-evolution generated by $H^{\xi}(\boldsymbol{k},t)$, which are taken onto themselves after each driving period, up to a phase controlled by the quasienergy $\varepsilon_{\boldsymbol{k}\alpha}$. Note that $\varepsilon_{\boldsymbol{k}\alpha}$ is only defined up to an integer multiple of the photon energy $\hbar\Omega$, compensated by a redefinition of $|\Phi^{\xi}_{\boldsymbol{k}\alpha}(t)\rangle$ via multiplication by factor(s) of $e^{i\Omega t}$. We use the convention where $\varepsilon_{\boldsymbol{k}\alpha}$ is chosen such that $\max_n |\langle\phi^{n\xi}_{\boldsymbol{k}\alpha}|\phi^{n\xi}_{\boldsymbol{k}\alpha}\rangle| = |\langle\phi^{0\xi}_{\boldsymbol{k}\alpha}|\phi^{0\xi}_{\boldsymbol{k}\alpha}\rangle|$.

Laser illumination with a circularly polarized laser opens dynamic gaps in the Floquet quasienergy spectrum. The gap opening at the resonance energies around $\varepsilon_{\boldsymbol{k}\alpha} = \pm\hbar\Omega/2$, with a size ΔE_1 linear in the laser field amplitude, controls the Rabi frequency of the resonant inter-band transitions induced by the laser drive. At the Dirac point ($\varepsilon_{\boldsymbol{k}\alpha} = 0$), the band degeneracy is lifted by a second-order resonance coupling between the conduction and valence bands, with a gap opening quadratic in the laser field amplitude [33, 140, 215]. In the low power regime, ΔE_1 is, therefore, larger than the bandgap at the Dirac point. Illustrating this, Figure B.8(a) shows the theoretical prediction for the quasienergy bandgap ΔE_1 as a function of laser power density and photon energy. For the photon energy and power density used in our experiment, ΔE_1 is predicted to be in the range of $\sim$ 1-10 meV, while the gap around the Dirac point, too small to be resolved in our measurements, cannot be clearly discerned in the numeric calculations.

B.8 Steady State Simulations of Laser-Illuminated Graphene

To determine the non-equilibrium steady state occupation $F^{\xi}_{\boldsymbol{k}\alpha}$ of the Floquet bands [3, 74, 257, 258], we consider the Floquet-Boltzmann equation (FBE) for electron-phonon collisions, which describes the flow of electronic occupations into Floquet states. The FBE is given by $\partial_t F^{\xi}_{\boldsymbol{k}\alpha} = I^{\text{el-ph},\xi}_{\boldsymbol{k}\alpha}[\{F^{\xi}_{\boldsymbol{k}\alpha}\}]$, where $I^{\text{el-ph},\xi}_{\boldsymbol{k}\alpha}[\{F^{\xi}_{\boldsymbol{k}\alpha}\}]$ is the electron-phonon collision integral. To estimate the collision integral, we consider electronic coupling to graphene-SiC surface acoustic phonons and graphene longitudinal acoustic phonons, indexed by $j = 0$ and 1, respectively. Assuming weak

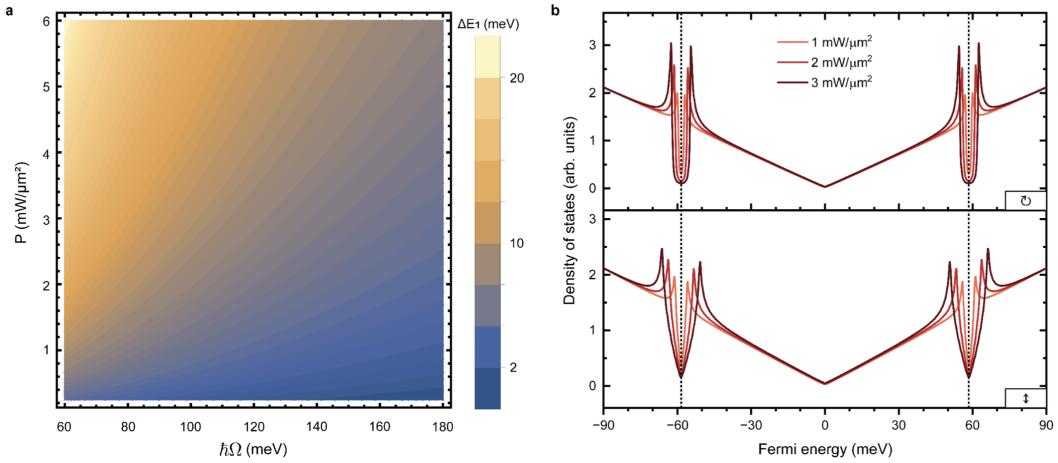

Figure B.8: Characteristics of the single-particle quasienergy spectrum. (a) Single-particle quasienergy bandgap ΔE_1 opening at $\varepsilon_{k\alpha} = \pm\hbar\Omega/2$, with $\varepsilon_{k\alpha} = 0$ corresponding to the Dirac point. The axes indicate the laser power density and photon energy. (b) Predicted light-induced modifications of the time-averaged density of states of graphene (see section J for definition) as a function of Fermi energy shift from the Dirac point for different power densities, with circular polarization (top) and linear polarization (bottom). Notice that the laser-induced gap at the Dirac point, which is a second-order process, is not resolved in the experiment for the chosen laser intensities. (See the main text for details.) The vertical dotted lines mark the E_F, value at $\pm\hbar\Omega/2$.

scattering rates relative to the Floquet gap ΔE_1, we use Fermi's golden rule to calculate the electron-phonon collision integral

$$
\begin{aligned}
I^{\text{el-ph},\xi}_{\boldsymbol{k}\alpha}[\{F_{\boldsymbol{k}\alpha}\}] \approx \frac{1}{N}\frac{2\pi}{\hbar} \sum_{\xi'=\pm1} \sum_{\boldsymbol{k}'\in \text{BZ}} \sum_{\alpha',j,n} |G^{\boldsymbol{k}'\alpha'\xi'}_{\boldsymbol{k}\alpha\xi}(n,j)|^2 \times \\
\times \left[\{F^{\xi'}_{\boldsymbol{k}'\alpha'}(1-F^{\xi}_{\boldsymbol{k}\alpha})\mathcal{N}(\hbar\omega_j(\boldsymbol{k}'-\boldsymbol{k})) - F^{\xi}_{\boldsymbol{k}\alpha}(1-F^{\xi'}_{\boldsymbol{k}'\alpha'})[1+\mathcal{N}(\hbar\omega_j(\boldsymbol{k}'-\boldsymbol{k}))]\right\} \\
\times p(\varepsilon_{\boldsymbol{k}'\alpha'} - \varepsilon_{\boldsymbol{k}\alpha} + \hbar\omega_j(\boldsymbol{k}'-\boldsymbol{k}) + n\hbar\Omega) \\
+ \{F^{\xi'}_{\boldsymbol{k}'\alpha'}(1-F^{\xi}_{\boldsymbol{k}\alpha})[1+\mathcal{N}(\hbar\omega_j(\boldsymbol{k}'-\boldsymbol{k}))] - F^{\xi}_{\boldsymbol{k}\alpha}(1-F^{\xi'}_{\boldsymbol{k}'\alpha'})\mathcal{N}(\hbar\omega_j(\boldsymbol{k}'-\boldsymbol{k}))\} \\
\times p(\varepsilon_{\boldsymbol{k}'\alpha'} - \varepsilon_{\boldsymbol{k}\alpha} - \hbar\omega_j(\boldsymbol{k}'-\boldsymbol{k}) + n\hbar\Omega)],
\end{aligned}
\tag{B.6}
$$

where $\omega_j(\boldsymbol{k}'-\boldsymbol{k}) = c^j_{\text{ph}}|\boldsymbol{k}'-\boldsymbol{k}|$ is the frequency dispersion of the phonon branch j, c^j_{ph} is the speed of sound, N is the number of discretized $\boldsymbol{k}$-points on the 2D grid, and $\mathcal{N}(\varepsilon) = (e^{-\varepsilon/k_BT} - 1)^{-1}$ is the occupation of a phonon mode with energy ε, evaluated at temperature T. The matrix element

$$
G^{\boldsymbol{k}'\alpha'\xi'}_{\boldsymbol{k}\alpha\xi}(n,j) = M_{j\boldsymbol{k}\boldsymbol{k}'} \sum_m \sum_{\nu\nu'} \langle \phi^{n+m,\xi}_{\boldsymbol{k}\alpha} | \phi^{m\xi}_{\boldsymbol{k}\alpha} \rangle \tag{B.7}
$$

describes the electronic coupling to the j-th phonon branch, where

$$M_{j\boldsymbol{k}\boldsymbol{k}'} = \frac{1}{\sqrt{A}} \frac{D^j}{\sqrt{2\rho c^j_{\text{ph}}}} \sqrt{\hbar\omega_j(\boldsymbol{k}' - \boldsymbol{k})}, \tag{B.8}$$

A is the unit cell size of graphene, ρ is the density of graphene, and D^j is the deformation potential corresponding to the phonon branch j. To impose energy conservation on electron-phonon scattering processes, we use the smeared Dirac-Delta function

$$p(\varepsilon) = 1.05 \frac{e^{-\varepsilon^2/2\sigma^2}}{2.51\sigma} \theta(2\sigma - |\varepsilon|) \tag{B.9}$$

where $\theta(x)$ is the Heaviside step function and the numerical prefactors ensure normalization ($\int_{-\infty}^{\infty} p(\varepsilon) d\varepsilon = 1$). Here, the phenomenological level broadening of $\sigma = 3$ meV describes the phonon and electronic spectral broadening due to disorder in the system. Our calculations assume that the speeds of the phonon branches are given by $c^0_{\text{ph}} = 1.3$ km/s and $c^1_{\text{ph}} = 11$ km/s and their deformation potentials satisfy $D^0/D^1 = 0.18$.

To obtain the steady state occupations, we solve for $I^{\text{el-ph},\xi}_{\boldsymbol{k}\alpha}[\{F_{\boldsymbol{k}\alpha}\}] = 0$ using the Newton-Raphson method. Our calculations are performed on a discretized square momentum grid covering the region $k_x, k_y \in [-0.17\ \text{nm}^{-1}, 0.17\ \text{nm}^{-1}]$ with 105 equally-spaced grid points in the k_x and k_y directions. We focus only on low-energy electronic states, where the Floquet occupations can be approximated as rotationally symmetric about the Dirac node, i.e., $F^{\xi}_{\boldsymbol{k}\alpha} \approx F_{k\alpha}$, with $F_{k\alpha}$ depending only on the momentum magnitude $k = |\boldsymbol{k}|$ and band index α. To impose the electronic particle number, we add a Lagrange multiplier term $\lambda(\sum_{\boldsymbol{k}\alpha} F_{\boldsymbol{k}\alpha} - gN)/N$ to the FBE with a large constant λ, and we vary the doping by changing g. The corresponding Fermi energies $E_F = \hbar v_F \sqrt{n/\pi}$ in equilibriu mcan be calculated from the electronic density $n = \int d^2\boldsymbol{k}/(2\pi)^2 F^{+1}_{\boldsymbol{k}+}$ as determined using the numerically-obtained steady state.

B.9 Transport in the Floquet Steady State

To calculate the longitudinal photocurrent ΔI from the steady state, we use linear response theory to estimate the longitudinal conductivity in the driven system:

$$\sigma_{xx} \approx e^2 \sum_{\alpha} \int \frac{dk}{2\pi} \int d\theta\ k\tau(k) v_x^2 \frac{dF_{k\alpha}}{d\varepsilon_{k\alpha}}, \tag{B.10}$$

where $v_x = |\nabla_{\boldsymbol{k}} \varepsilon_{\boldsymbol{k}\alpha}| \cos\theta$ and $\tau(k) \propto k$ for relaxation processes dominated by scattering from charge impurities [37]. The longitudinal photocurrent is given by

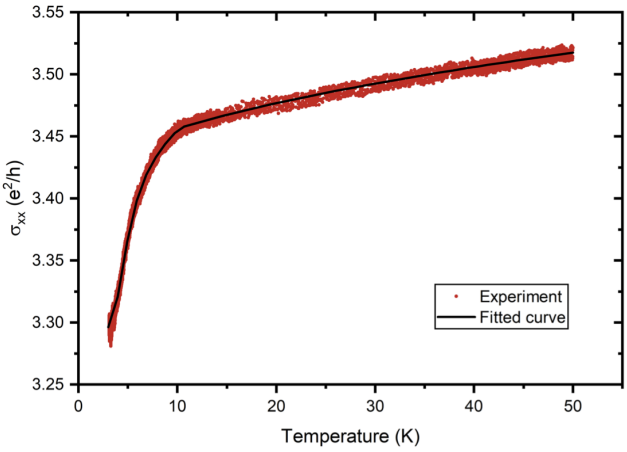

Figure B.9: Temperature dependence of the longitudinal conductivity at $E_F = 0$ without irradiation, which indicates charge puddle effects.

$\Delta I = (\sigma_{xx} - \sigma^0_{xx})V_{\text{sd}}$, where V_{sd} is the source-drain voltage and σ^0_{xx} is the longitudinal conductivity in the equilibrium system, obtained by replacing $v_x = v_F \cos\theta$ and $F_{k\alpha}$ with the Fermi-Dirac distribution.

In addition to the above-mentioned effects, charge puddles also modify the longitudinal conductivity. In particular, for doping near charge neutrality, where a clean graphene sheet normally exhibits low conductivity, the charge puddles introduce regions with larger chemical potential and greater mobility, thereby enhancing the conductivity [163]. To roughly capture this behavior, we employ a simple model to relate the conductivity σ in clean graphene to that with charge puddles, $\sigma_p = \sigma + c(T)$, similar to that used in Ref. [60]. Here, $c(T)$ is a function which captures the temperature-dependence of the experimentally-measured conductivity at charge neutrality, fit using $c(T) = \sum_{i=0}^{14} c_i T^i$ to the experimental data for $T < 10$ K, and fit using the function $c(T) = d_1 + d_2 T^{1/2}$ for $T > 10$ K, where c_i, d_1, and d_2 are fitting parameters (see Figure B.9). Due to heating effects from the drive, the temperature during the duty cycle of the chopper differs when the laser is blocked by the chopper T_{eq} and when the laser is unblocked T_{dr}. We account for the temperature mismatch and charge puddle effects by shifting the photocurrent by a magnitude $[c(T_{\text{dr}}) - c(T_{\text{eq}})]V_{\text{sd}}$ in our simulations. We find that this temperature mismatch accounts for the highly temperature and amplitude dependent photocurrent ΔI magnitude at charge neutrality $E_F = 0$ observed in the experiment. In particular, in our theory, we assume both $T_{\text{dr}} - T_{\text{eq}} \approx 7.3\ \text{K}/(\text{mW}/\mu\text{m}^2)P$ and $T_{\text{eq}} = 3.5\ \text{K} + 1.83\ \text{K}/(\text{mW}/\mu\text{m}^2)P$ increase linearly as a function of the laser power density P. The coefficients chosen allow our theory to roughly capture the

dependence of ΔI at charge neutrality as T_{eq} and P are varied in the experiment. We emphasize that the fitting procedures for the variables $c(T)$, $T_{\text{dr}} - T_{\text{eq}}$, and T_{eq} do not affect the width, depth, or shape of the photocurrent dip predicted in our theory; rather, it only shifts the ΔI by a constant independent of electronic doping.

B.10 Density of States and Berry Curvature Calculation

The time-averaged density of states (defined as the time-dependent spectral function averaged over one period) was calculated numerically through the formula

$$\text{DOS}(\varepsilon) = \sum_{k\alpha} \delta(\varepsilon_{k\alpha} - \varepsilon) \tag{B.11}$$

where the broadening parameter σ of the Gaussian function $\delta(\varepsilon)$ is chosen to be much smaller than the resonant Floquet gap.

The transverse conductivity was calculated from the anomalous conductivity in the steady state $\sigma_{xy} = \frac{2e^2}{\hbar} \sum_\alpha \int d^2\boldsymbol{k}\ B^{\xi}_{\boldsymbol{k}\alpha} F^{xi}_{\boldsymbol{k}\alpha}$, where $B^{\xi}_{\boldsymbol{k}\alpha}$ is the time-averaged Berry curvature, given by20

$$B^{\xi}_{\boldsymbol{k}\alpha} = \frac{1}{2\pi/\Omega} \int_0^{2\pi/\Omega} dt\ \frac{(2\pi)^2}{N_x N_y A} \arg\left[\frac{U_x(\boldsymbol{k},t) U_y(\boldsymbol{k}+\boldsymbol{e}_x,t)}{U_x(\boldsymbol{k}+\boldsymbol{e}_y,t) U_y(\boldsymbol{k},t)}\right], \tag{B.12}$$

where

$$U_\mu(\boldsymbol{k},t) = \frac{\langle u_{\boldsymbol{k}\alpha}(t) | u_{\boldsymbol{k}+\boldsymbol{e}_\mu,\alpha}(t)\rangle}{|\langle u_{\boldsymbol{k}\alpha}(t) | u_{\boldsymbol{k}+\boldsymbol{e}_\mu,\alpha}(t)\rangle|^2}, \tag{B.13}$$

$\boldsymbol{e}_\mu = \frac{G_\mu}{N_\mu}\hat{\mu}$, $\mu = x, y$, N_μ is the number of grid points in the μ-direction, G_μ is the length of the discretized momentum grid along the μ-direction, and $|u_{\boldsymbol{k}\alpha}(t)\rangle$ are the Bloch vectors, defined by $|\psi^{\xi}_{\boldsymbol{k}\alpha}(t)\rangle = e^{i\boldsymbol{k}\cdot\boldsymbol{r}} |u_{\boldsymbol{k}\alpha}(t)\rangle$.

B.11 Transverse Hall Voltage

An expected consequence of the Floquet states described above is the appearance of a Hall signal [3, 74, 215]. We measure the transverse voltage in samples under irradiation with both circular and linear polarization, as shown in Figures B.10-B.13. Floquet theory predicts that a nonzero transverse voltage originates only from nontrivial band topology, inconsistent with the observation of a transverse signal for linear polarization. However, the extraneous, helicity-independent transverse signal has been observed before under linearly polarized Mid-IR irradiation at zero source-drain bias in McIver et al. [185] and attributed to an effective extra bias voltage caused by band bending fields at the contacts, a possible result of asymmetries introduced by charge puddles. The helicity-independent component may also be a

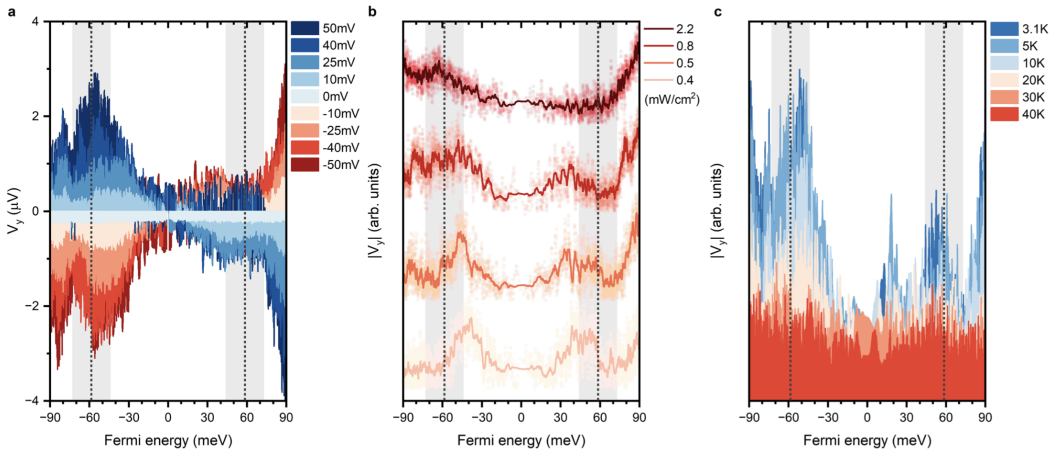

Figure B.10: Transverse voltage response under different conditions. Transverse voltage as a function of E_F, under light irradiation ($\hbar\Omega$ = 117 meV) with left-hand circular polarization. The dotted lines mark the values corresponding to $E_F = \pm\hbar\Omega/2$, with the related uncertainties indicated by the gray stripes. (a) Transverse voltage measured at different bias voltage values. The cryostat temperature is 3.1 K, and the laser beam is circularly polarized. (b) Transverse voltage measured under different irradiation power. The curves are vertically shifted for clarity. The cryostat temperature ranges from 3.0-3.3 K depending on laser intensity. The laser beam is circularly polarized. The circles represent data points, and the solid lines are obtained by adjacent point averaging. (c) Transverse voltage measured at different temperatures. For both (a) and (c), the laser intensity is 0.8 mW/μm^2 and for (b) and (c) the bias voltage is 50 mV. The measurements are from sample C.

product of photovoltaic effects generated by optical transitions in highly irradiated graphene [34, 70] or anisotropies in the Floquet band spectrum near the resonant Floquet gap [33], which may appear due to the distorted circular polarization near the metallic contacts (see Section B.1).

The weak polarization-dependent Hall voltage exhibits signs of a nontrivial E_F-dependence, shown in Figure B.11(b) for graphene sample A, displaying peaks starting to emerge around doping $E_F = \pm\hbar\Omega/2$. In Figure B.11(c), we show the corresponding Hall conductivity. Upon inverting the sign of the source-drain bias V_{sd}, the Hall voltage peaks reverse sign. Such a helicity-dependent Hall voltage contribution may be an indicator of the emergence of Floquet chiral edge states in our samples. The theoretically calculated Floquet Hall conductivity, see Figure B.11(d), also exhibits peaks near doping $E_F = \pm\hbar\Omega/2$. However, the magnitude of the Hall conductivity observed in the experiment is much weaker than the theory-predicted levels. There are several possible reasons for this discrepancy. One

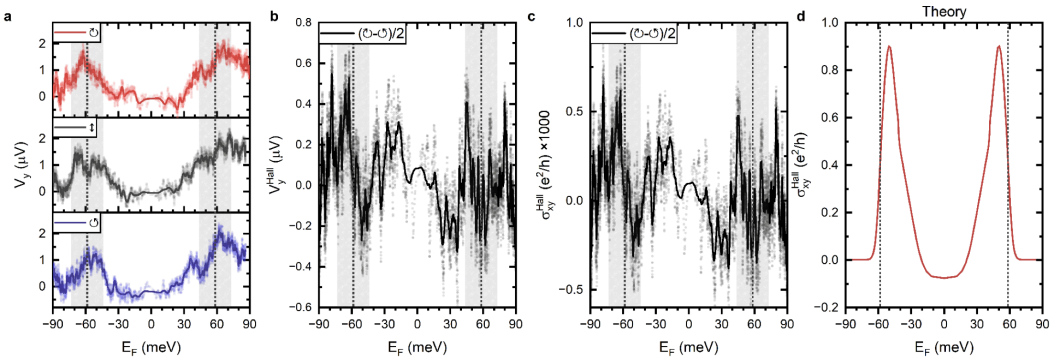

Figure B.11: Transverse voltage response under different conditions. (a) Transverse voltage as a function of E_F, under light irradiation ($\hbar\Omega$ = 117 meV) with different polarizations of the laser. (b) helicity-dependent Hall voltage in Sample A. (c) Hall conductivity in Sample A. Here, the laser intensity is 1.4 mW/μm^2, bias source-drain voltage is 6 mV, and cryostat temperature is 3.4 K. (d) Theoretically calculated Floquet Hall conductivity with nontrivial E_F-dependence arising from the tunable electronic steady state. The dotted lines in (a)-(d) mark the values corresponding to $E_F = \pm\hbar\Omega/2$, with the related uncertainties indicated by the gray stripes in (a)-(c). In (a)-(c), the circles represent data points, and the solid lines are obtained by adjacent point averaging.

possible contribution to the suppressed Hall voltage is the distorted polarization of the laser beam near the metallic contacts (see Section B.1 for details), which can create an anisotropic Floquet gap size in momentum space, as was already mentioned in the main text. Charge puddles could also play an important role in reducing the measured Hall response. The photocurrent ΔI flows through the most conducting puddles with larger chemical potential. Insulating regions with depleted photocurrent in this case would generate a much smaller Hall voltage than predicted, reducing the overall average Hall voltage.

B.12 Reproducibility of the Results

The photoresponse features and the signatures of Floquet-Bloch band formation are reproducible with multiple sweeps on the same device. As discussed in the main text and above, we characterized the transverse conductivity of the devices for different polarizations of laser irradiation. The results for samples A, B and C are shown in Figures B.11, B.12, and B.13. For all three samples, the longitudinal photocurrent ΔI showed dips around $E_F = \pm\hbar\Omega/2$ for circularly and linearly polarized light. Such symmetric dips around the Dirac point are consistent with the emergent non-equilibrium Floquet steady states in graphene.

B.13 Effect of Hall contact misalignment on the transverse signal measured under illumination

We made some estimates to quantify the contribution to the transverse voltage due to the geometric effect of the contact misalignment and compared it to the transverse voltage V_y measured under illumination. First, we measured the transverse voltage $V_{\text{Misalignment}}$ as a function of the source-drain voltage V_{sd} and the source-drain current I_{sd} in the zero magnetic field, with no laser illumination and at room temperature. The measured misalignment for sample A is plotted in Figure B.14(a). From this measurement we extracted the quantity $R_{\text{Misalignment}}/I_{\text{sd}} \sim 99.1\ \Omega$. Figure B.14(b) shows the estimated contribution to the transverse voltage from the photoinduced current change ΔI, $V_{\text{Misalignment}} = R_{\text{Misalignment}}\Delta I$, in the same graph with the measured transverse photoresponse. The comparison shows that this misalignment contribution is much smaller than the transverse signal measured under illumination. Similar misalignment contributions were determined in all the measured samples.

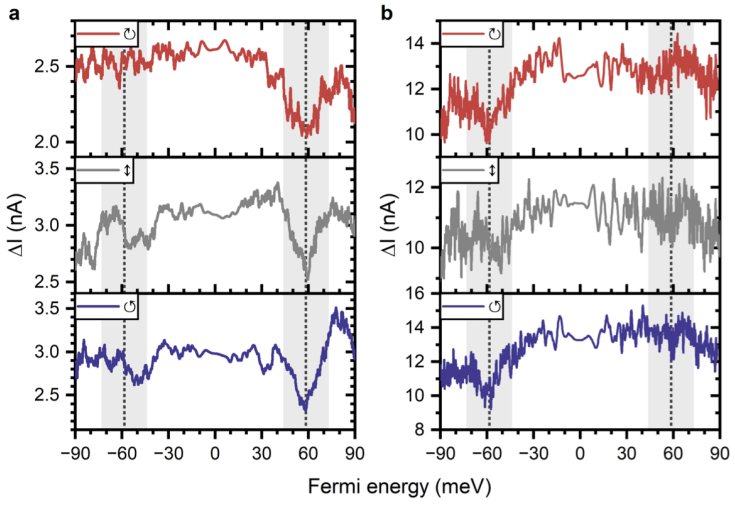

Figure B.12: Floquet signatures in the longitudinal photocurrent in additional devices. The dotted lines mark the E_F values corresponding to $\pm\hbar\Omega/2$, with the related uncertainty described by the gray stripes. (a) Longitudinal photocurrent as a function of E_F under different polarization illumination in sample B. Parameters: Laser power density 1.4 mW/μm^2 and bias voltage 6 mV. (b) Longitudinal photocurrent as a function of E_F, under different polarization illumination in sample C. Parameters: Laser power density 1.6 mW/μm^2, bias voltage 6 mV, and cryostat temperature 3.4 K.

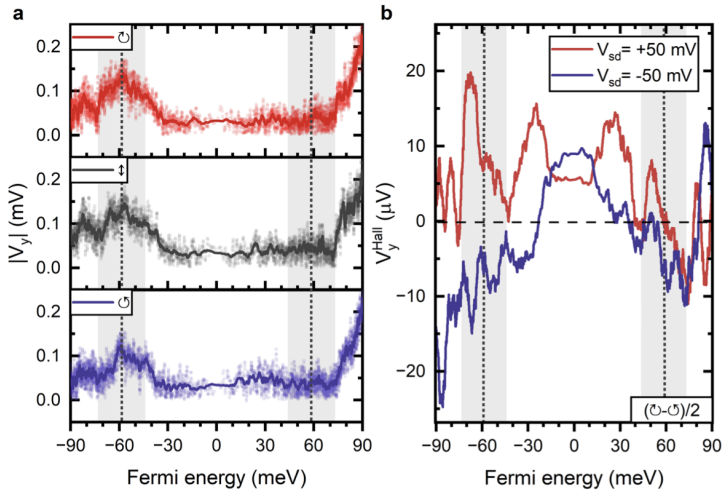

Figure B.13: Transverse voltage response in additional devices. Transverse voltage as a function of E_F, under irradiation with different polarizations in sample C [panel (a)] and the difference between the transverse voltage response from circular polarizations of the laser beam with opposite chirality extracted from the curves in panel (a) [see panel (b)], and upon reversing the source-drain bias V_{sd}. Laser power density 0.5 mW/μm^2, cryostat temperature 3.1 K. The dotted lines mark the E_F values corresponding to $\pm\hbar\Omega/2$, with the related uncertainty described by the gray stripes.

B.14 Linearity in the device response

The source-drain bias voltage dependence of the photoresponse is an important characteristic that can help determine its underlying physical mechanisms and separate intrinsic contributions from graphene or from the graphene-electrode boundaries. Figure B.15(a) shows a typical I-V curve (sample C). The clear linear relationship between the bias voltage and current indicates the ohmic contact nature of our graphene-electrode interface. Figure B.15(b) demonstrates the bias voltage dependence of the longitudinal photoresponse at a few different fixed V_g, which reveals a linear relationship between the sample response and the bias voltage. Moreover, no clear photoresponse signal was observed at $V_{sd} = 0$ for all measured gate voltages. Furthermore, as presented in Figure B.15(c), the normalized photoresponse curves collected at different V_{sd} as a function of Fermi energy further confirm the linearity of our sample's photoresponse.

B.15 Chopper frequency dependence of the photoresponse

To better understand our samples' photoresponse, we measured the longitudinal photoresponse as a function of the chopper modulation frequency. As one can see

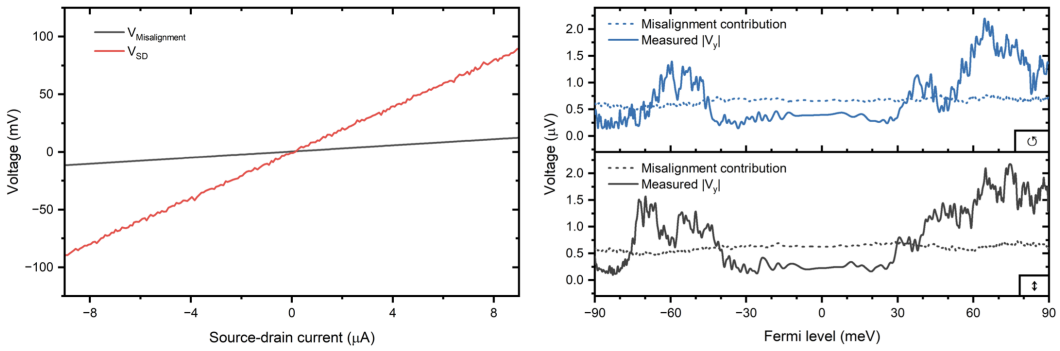

Figure B.14: Effect of Hall contacts misalignment. (a) (Red) $V_{\text{Misalignment}}$ and (black) V_{sd} measured at the same source-drain current. Room temperature. (b) Misalignment contribution to the measured transverse voltage for (top) circular and (bottom) linear irradiation. Solid lines represent the transverse voltages measured by the lock-in amplifier; dotted lines represent the contribution resulting from misalignment in the Hall contacts. The experimental data from Figure B.11 are shown for reference.

in Figure B.16, as the chopper frequency is increased, the signal first increases and then rapidly drops. Such non-monotonic behavior can be attributed to the heating and cooling processes of electrons that are associated with the chopping of the laser beam. At low frequencies, electrons are heated with a longer exposure time to the irradiation during each chopping cycle, while for high frequencies, although the exposure time is shorter, the electrons do not have enough time for cooling. As a result, for both too low and too high frequencies, a higher effective electron temperature is expected. Furthermore, as discussed in the main text, an elevated effective electron temperature will not only lead to the fading of Floquet features but will also suppress the overall signal strength. Therefore, for better detection of the Floquet features, one has to carefully control the chopper frequency and maintain the electron temperatures below the size of Floquet gaps. All results presented in this work were collected with a chopper frequency around 23 Hz.

B.16 Error Analysis

In this section, we provide details of the error estimates in Fermi level position, specifically for $E_F = \hbar\Omega/2$ as well as the full width at half maximum (FWHM) analysis for sample C, as presented in Figure 6.3(c)-(d) in the main text. The electronic carrier density in the sample was estimated using the relation

$$n = k(V_g - V_d) \tag{B.14}$$

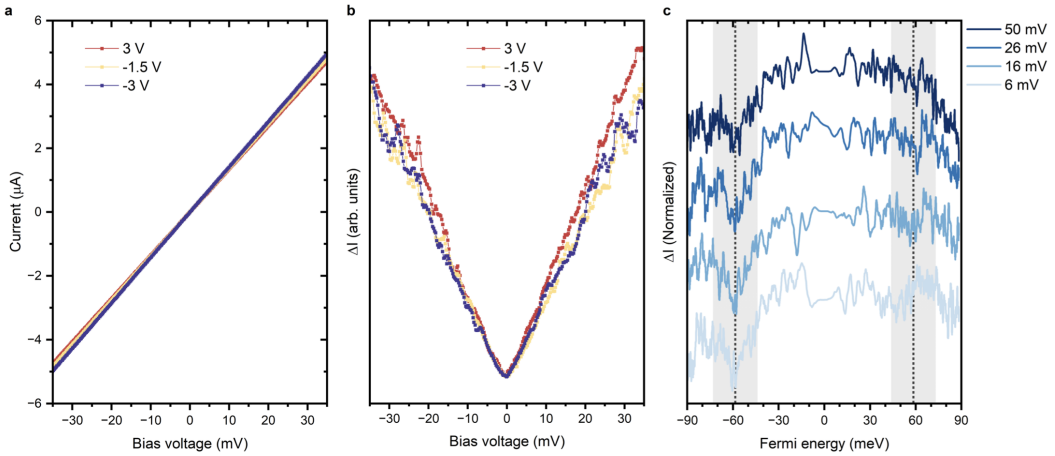

Figure B.15: Bias dependence of sample response. (a) I-V curve from sample C at different values of V_g. (b) Photo-induced current change ΔI as a function of bias voltage at different values of V_g. (c) Normalized longitudinal photoresponse ΔI as a function of E_F at different bias voltages, under circularly polarized irradiation, with a power density of 1.5 mW/μm^2. The curves are vertically shifted for clarity. The cryostat temperature is 3.4 K. The dotted lines mark the E_F values corresponding to $\pm\hbar\Omega/2$, with the related uncertainty described by the gray stripes.

where $k \approx 1.63\times10^{-15}$ m^{-2}/V $\pm\,\delta k$ and $\delta k = 9\times10^{13}$ m^{-2}/V were estiamted from the gate efficiency calibration. The voltage $V_d \approx 0.55$ V $\pm\,\delta V_d$ was estimated to be the gate voltage at which σ_{xx} is minimized, and the uncertainty $\delta V_d \approx 0.8$ V was estimated from the gate efficiency calibration. The corresponding uncertainties in the Fermi energy $E_F = \hbar v_F\sqrt{\pi n}$ are given by

$$\delta E_F \approx (E_F/2)\sqrt{(\delta k/k)^2 + [\delta V_d/(V_g - V_d)]^2}. \tag{B.15}$$

The FWHM of the conductivity dip [see Figure 6.3(d)] FWHM $= \Delta E_F = E_F(V_{g1}) - E_F(V_{g2})$, where $V_{g1} = B + \sqrt{2\ln 2}\sigma$ and $V_{g2} = B - \sqrt{2\ln 2}\sigma$, was estimated by performing a least squares fit of the experimental data to the function

$$\Delta I_{\text{fit}} = a_0 \exp\left[-(V_g - B)^2/2\sigma^2\right] + CV_g + D. \tag{B.16}$$

We estimated the uncertainty in the FWHM using the relationship

$$\delta\Delta E_F = \sqrt{\left[\frac{\partial\Delta E_F}{\partial v_F}\delta v_F\right]^2 + \left[\frac{\partial\Delta E_F}{\partial V_d}\delta V_d\right]^2 + \left[\frac{\partial\Delta E_F}{\partial k}\delta k\right]^2 + \left[\frac{\partial\Delta E_F}{\partial V_{g1}}\delta V_{g1}\right]^2 + \left[\frac{\partial\Delta E_F}{\partial V_{g2}}\delta V_{g2}\right]^2} \tag{B.17}$$

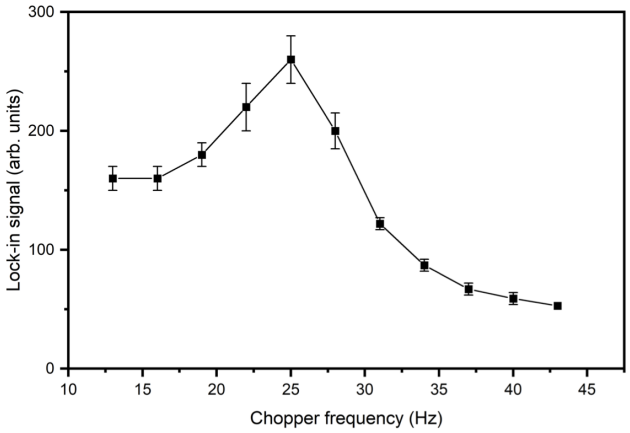

Figure B.16: Longitudinal photoresponse as a function of chopper frequency. Photo-induced current change measured in sample C under 1.5 mW/μm^2 of circularly polarized irradiation. The sample is biased at a fixed 6 mV. The cryostat temperature is 3.4 K. Error bars indicate the maximum deviation in the lock-in amplifier reading during the measurement.

where $\delta v_F \approx 0.008 \times 10^6$ m/s as determined by cyclotron resonance measurements. The uncertainties δV_{g1} and δV_{g2} were estimated using the relation

$$\delta V_{g1} \approx \delta V_{g2} \approx \sqrt{\delta B^2 + (\sqrt{2 \ln 2}\delta\sigma)^2} \tag{B.18}$$

where δB and $\delta\sigma$ are the uncertainties in the fitting parameters B and σ, respectively, as determined from the 68% confidence interval of the least squares fit.

Part III

Floquet Physics Beyond Optical Drives and Beyond Low-Dimensional Systems

Chapter 7

QUANTIZED ACOUSTOELECTRIC FLOQUET EFFECT IN QUANTUM NANOWIRES

External coherent fields can drive quantum materials into non-equilibrium states, revealing exotic properties that are unattainable under equilibrium conditions—an approach known as "Floquet engineering." While optical lasers have commonly been used as the driving fields, recent advancements have introduced nontraditional sources, such as coherent phonon drives. Building on this progress, we demonstrate that driving a metallic quantum nanowire with a coherent wave of terahertz phonons can induce an electronic steady state characterized by a persistent quantized current along the wire. The quantization of the current is achieved due to the coupling of electrons to the nanowire's vibrational modes, providing the low-temperature heat bath and energy relaxation mechanisms. Our findings underscore the potential of using non-optical drives, such as coherent phonon sources, to induce non-equilibrium phenomena in materials. Furthermore, our approach suggests a new method for the high-precision detection of coherent phonon oscillations via transport measurements.

7.1 Introduction

New phonon sources have recently enabled on-demand access to coherent phonon beams across a broad spectrum of frequencies [100, 103, 116, 123, 206, 226, 286, 297]. These phonon excitations in solids [18, 19, 89, 125, 162, 175, 179, 275] can induce new optical properties [135, 282], strong correlation physics [16, 134, 142, 164, 178, 192], tunable magnetic properties [18, 177, 206, 211], and acoustoelectric effects [126, 133, 154, 173, 221, 234, 262, 302]. The unique characteristics of coherent phonons—e.g., finite momentum, low energy, and electron coupling—enable Floquet engineering of non-equilibrium spatial-temporal electronic phenomena [40, 91, 114, 224]. Notably, terahertz (THz) phonons [20, 22, 35, 77] could become tools for the dynamic manipulation of narrow bandwidths materials, such as moiré systems [77, 131, 312]. Recent proposals demonstrated that coherent phonon beams can be used for Floquet engineering of nontrivial band topology [40, 224].

We demonstrate that a continuous propagating wave of coherent THz phonons can drive a quantum wire into a non-equilibrium Floquet steady state, resulting in a

persistent charge current [see Figure 5.1(a)]. Furthermore, under optimal conditions of doping and driving strength, this current can achieve a quantized value, $J = e\omega/\pi$, where ω represents the phonon driving angular frequency and e is the electron charge [see Figure 5.1(b)]. In the adiabatic limit, $\omega \to 0$, the quantization of current aligns with the principles of a topological pump [7, 29, 32, 47, 71, 82, 111, 159, 201, 201, 278, 279]. Remarkably, we find that quantized transport can be maintained over a wide range of THz frequencies, even beyond the adiabatic limit. This suggests a robust mechanism underpinning the quantization, stabilized by the non-equilibrium electronic steady state, which is set by the coupling to a bath of low-temperature thermal phonons and electron-electron interactions [28, 78, 200, 229, 298].

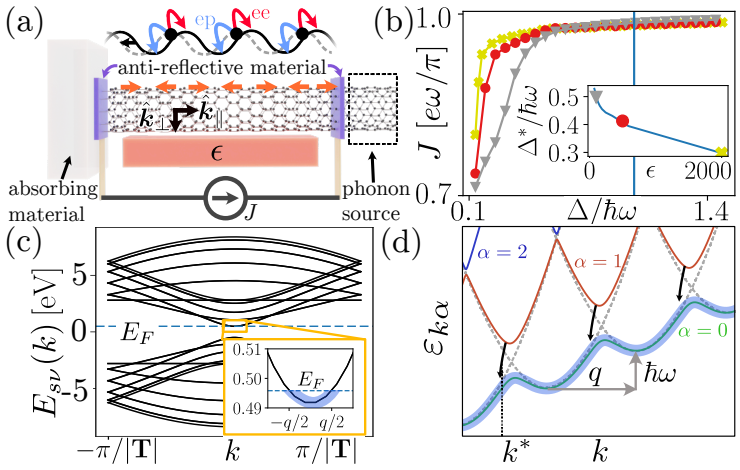

Figure 7.1: (a) Schematic experimental setup. A THz-frequency coherent phonon wave (with atomic displacements sketched by orange arrows) of momentum q and angular frequency ω propagates from the phonon source on the right to the absorbing material on the left. A screening material of dielectric constant ϵ is placed below the CNT. Black sinusoid represents the coherent phonon potential. Electrons (black dots) generate quantized current $J = e\omega/\pi$ when confined to the troughs of the potential, achieved when incoherent phonon relaxation (ep) is much faster than electron-electron heating (ee). (b) Current J vs. Floquet gap $\Delta/\hbar\omega$ for different ϵ (see inset). Vertical line denotes $\Delta = \hbar\omega$. Inset: Δ^* vs. ϵ, where Δ^* is the minimal Floquet gap at which J is nearly quantized, set as $0.96e\omega/\pi$. (c) Band structure of a $(10, 0)$ armchair CNT. Inset: Fermi energy lies near the band bottom of the lowest positive-energy band, and the electronic density n_e is chosen to be commensurate to q. (d) Quasienergy spectrum of the driven system. Blue shading on the $\alpha = 0$ band indicates the optimal filling resulting in quantized current. Incoherent phonon scattering transitions (black arrows) relax electrons into the $\alpha = 0$ band.

A device for robust generation of quantized current on demand through coherent phonon illumination has numerous potential applications in metrology [95, 129, 209,

222, 273, 326], electronics, and quantum computing [21, 57, 88, 316]. Furthermore, this device can be used to characterize and detect coherent phonons through transport measurement. Traditionally, the detection of coherent phonons has relied on optical methods such as reflectivity measurements [72, 96, 157, 314, 315]. Leveraging current quantization to probe the phonon field offers a more direct and sensitive method of coherent phonon detection.

In this work, we focus on an experimental setup of a single-walled carbon nanotube (CNT) [79, 105, 128, 191, 247, 249] coupled to a continuous source of coherent phonons. The phonon waves propagate from the right to the left end of the CNT, where they are absorbed by an absorbing material, see Figure 7.1(a). Anti-reflective material with appropriate thickness suppresses reflected phonon waves that destructively interfere with the coherent phonon mode. The electronic steady state in the CNT is formed from the balance between interactions with the coherent phonon wave, incoherent phonons of the CNT, and free electrons. Our model considers a detailed microscopic description of the phononic spectrum of the CNT that serves as the low-temperature heat bath for the phonons and the electron-electron interactions.

7.2 Phonon-Driven Carbon Nanotube.

To analyze the steady-state properties of this setup, we use an effective model of a single-walled CNT. We define $\hat{\boldsymbol{\psi}}^\dagger_{k,s} \equiv \begin{pmatrix} \hat{\psi}^\dagger_{k,A,s} & \hat{\psi}^\dagger_{k,B,s} \end{pmatrix}$ as the creation operator of a Bloch state on the CNT, where $\hat{\psi}^\dagger_{k,j,s}$ creates an electron of crystal momentum k on sublattice $j = A, B$, and k is the Bloch momentum in the direction $\hat{\boldsymbol{k}}_\parallel$ along the tube axis. The index $s = 0, \ldots, N-1$ enumerates the discrete electronic momenta along the direction $\hat{\boldsymbol{k}}_\perp$ around the circumference of the tube. Here, N is the number of graphene unit cells contained in a length $|\boldsymbol{T}|$ along the tube axis, and the CNT is periodic along the tube axis by translations of vector $\boldsymbol{T}$. The electronic momentum $k \in [-\pi/|\boldsymbol{T}|, \pi/|\boldsymbol{T}|]$ is approximately continuous for a long tube. Corresponding eigenenergies of the electronic states are given by $E_{sv}(k)$, where $v = +, -$ denote the conduction and valence bands, respectively, see Figure 7.1(c).

We focus on a semiconducting CNT whose Fermi surface in equilibrium lies near the bottom of the lowest conduction band [see inset of Figure 7.1(c)]. We omit the index s, considering only the lowest conduction and highest valence bands described by $v = +, -$ with eigenenergies $E_v(k)$ and eigenstates $|vk\rangle$. The two bands are described by the effective Hamiltonian $\hat{H}_\mathrm{e} = \int dk/2\pi\, \hat{\boldsymbol{\psi}}^\dagger_k H_\mathrm{e}(k) \hat{\boldsymbol{\psi}}_k$, where the x axis is aligned along a bond between carbon atoms. To describe electron-

phonon interactions in the CNT, we consider the Hamiltonian $\hat{H}_{\rm ep}(t) = \sum_\lambda \hat{H}_{\rm ep}^{(\lambda)}(t)$, where $\hat{H}_{\rm ep}^{(\lambda)}(t) = \int d^2\boldsymbol{r}\ \hat{\boldsymbol{\psi}}_{\boldsymbol{r}}^\dagger \hat{V}^{(\lambda)}(\boldsymbol{r},t)\hat{\boldsymbol{\psi}}_{\boldsymbol{r}}$ and $\hat{V}^{(\lambda)}(\boldsymbol{r},t)$ describe electronic coupling to a phonon mode indicated by λ, $\boldsymbol{r} = (x,y)$ is the spatial coordinate along the tube, $\hat{\boldsymbol{\psi}}_{\boldsymbol{r}}^\dagger = P^{-1}\int dk/(2\pi) e^{-i(\delta k \hat{\boldsymbol{k}}_\perp + k\hat{\boldsymbol{k}}_\parallel)\cdot\boldsymbol{r}}\hat{\boldsymbol{\psi}}_k^\dagger$, δk is the momentum along $\hat{\boldsymbol{k}}_\perp$, and P is the perimeter of the CNT [77, 296]. [See Appendix C for details.]

We assume that a phonon source [see Figure 7.1(a)] generates a coherent wave of phonons in one of the modes denoted by $\lambda = \lambda_0$ that propagates through the CNT, while other phonons are in low-temperature thermal equilibrium. The phonon mode λ_0 has momentum $\boldsymbol{q} = q\hat{\boldsymbol{k}}_\parallel$, angular frequency ω, and finite displacement expectation value $\langle \hat{\boldsymbol{u}}^{(\lambda_0)}(\boldsymbol{r},t)\rangle = u_0 \cos\big(\boldsymbol{q}\cdot\boldsymbol{r} - \omega t\big)\hat{\boldsymbol{k}}_\parallel$, where u_0 is the displacement amplitude and $\hat{\boldsymbol{u}}^{(\lambda_0)}(\boldsymbol{r},t)$ is the displacement operator of the mode. While we consider coherent longitudinal phonon modes, coherent transverse modes should induce similar behavior. We assume that the CNT is sufficiently short compared to the coherent phonon decay length such that u_0 is approximately constant [see Appendix C].

The electronic dynamics can be divided to coherent components described by the time- and spatially-periodic Hamiltonian $\hat{H}_0(t) = \hat{H}_{\rm e} + \hat{H}_{\rm ep}^{(\lambda_0)}(t)$ and incoherent components due to coupling to thermal phonon modes, $\hat{H}_{\rm b}(t) = \sum_{\lambda\neq\lambda_0}\hat{H}_{\rm ep}^{(\lambda)}(t)$. For simplicity, we assume that the wavelength of the coherent phonon mode is commensurate with the periodicity of the CNT along the tube axis. The single-particle Hamiltonian $\hat{H}_0(t)$ can be diagonalized by the Floquet-Bloch states, $|\psi_{k\alpha}(\boldsymbol{r},t)\rangle = e^{-i(\boldsymbol{k}\cdot\boldsymbol{r}+\varepsilon_{k\alpha}t/\hbar)}\sum_{n\in\mathbb{Z}} e^{-in(\boldsymbol{q}\cdot\boldsymbol{r}-\omega t)}|\phi_{k\alpha}^{(n)}\rangle$ [91, 114, 224, 241]. Here, $\varepsilon_{k\alpha}$ is the quasienergy satisfying

$$(\varepsilon_{k\alpha} + m\hbar\omega)|\phi_{k\alpha}^{(m)}\rangle = H_{\rm e}(k+mq) + \sum_{m'\neq 0} V_{m-m'}|\phi_{k\alpha}^{(m')}\rangle \tag{7.1}$$

where α enumerates the Floquet bands and V_n are the Fourier harmonics of $\langle\hat{V}^{(\lambda_0)}(\boldsymbol{r},t)\rangle$, i.e., $\langle\hat{V}^{(\lambda_0)}(\boldsymbol{r},t)\rangle = \sum_{n\neq 0} e^{-in(\boldsymbol{q}\cdot\boldsymbol{r}-\omega t)}V_n$. The quasienergy spectrum $\varepsilon_{k\alpha}$ arises from replicas of the original energy bands $E_\nu(k)$ shifted in energy and momentum by $m\hbar\omega$ and mq, respectively, where $m\in\mathbb{Z}$ [see light grey, dashed curves in Figure 7.1(d)]. At the crossings between the Floquet replicas corresponding to $k = k^* + mq$, the quasienergy spectrum exhibits Rabi-like gaps of size $\Delta \approx |V_1|$, see solid curves in Figure 7.1(d) [see Appendix C]. Remarkably, the quasienergy satisfies the periodicity condition $\varepsilon_{k\alpha} = \varepsilon_{k+q,\alpha} - \hbar\omega$, which is the basis for the quantized current

presented in this work. Specifically, the current is given by [74]

$$J = \frac{2e}{\hbar} \sum_{\alpha} \int_0^q \frac{dk}{2\pi} \frac{d\varepsilon_{k\alpha}}{dk} F_{k\alpha}. \tag{7.2}$$

Here, $F_{k\alpha}(t) = \langle \hat{f}^{\dagger}_{k\alpha}(t) \hat{f}_{k\alpha}(t) \rangle$ is the occupation of the Floquet-Bloch state $|\psi_{k\alpha}(\boldsymbol{r}, t)\rangle$ created by operator $\hat{f}^{\dagger}_{k\alpha}(t)$. The factor of two in Eq. (7.2) accounts for spin degeneracy. When only the $\alpha = 0$ band is fully-occupied, $J = e\omega/\pi$, resulting in quantized current. Our goal is to determine $F_{k\alpha}(t)$ in the steady state, which is set by incoherent electronic dynamics due to electron-phonon and electron-electron scattering.

7.3 Floquet-Boltzmann Equation.

To model the dynamics under electron-phonon scattering, we consider the microscopic Hamiltonian $\hat{H}_{\mathrm{b}}(t)$ for electronic coupling to incoherent bath phonons, as defined above. Our model considers only the longitudinal acoustic phonon mode of speed c_{ph}, momentum p, and energy $\hbar c_{\mathrm{ph}} p$, which dominates the electron-phonon scattering near the Fermi surface of the CNT. We assume that the CNT incoherent phonons are coupled to an external heat bath, remaining in thermal equilibrium at temperature T and thermalizing quickly with the heat bath phonons and environment.

Additionally, we consider scattering due to electron-electron interactions, given by the Hamiltonian

$$\hat{H}_{\mathrm{ee}} = \int \frac{dk_1 dk_2 dp}{(2\pi)^3} \mathcal{V}_{k_1,k_2}(p) \hat{c}^{\dagger}_{k_1+p,+} \hat{c}^{\dagger}_{k_2-p,+} \hat{c}_{k_2,+} \hat{c}_{k_1,+}, \tag{7.3}$$

where $\mathcal{V}_{k_1,k_2}(p) = U(p) \mathcal{W}_{k_1,p} \mathcal{W}_{k_2,-p} / (2\epsilon)$, $\mathcal{W}_{k,p} \equiv \langle +, k+p | +, k \rangle$ is the form-factor, $U(p)$ is the Coulomb potential, ϵ is the dielectric constant of the surrounding screening medium, and $\hat{c}^{\dagger}_{k\nu}$ creates an electron in the eigenstate $|\nu k\rangle$ of $\hat{H}_{\mathrm{e}}$. We consider scattering within the $\nu = +$ band only, because the Fermi level [see inset of Figure 7.1(c)] is energetically well-separated from other bands, restricting scattering to small momentum transfers $p \lesssim q$ near the Fermi surface. For small p, we approximate $U(p) \approx 1$ eV, consistent with estimates in Refs. [176, 325].

Under electron-phonon and electron-electron scattering, the electrons form a steady state distribution with occupations $F_{k\alpha}(t)$ determined by the Floquet-Boltzmann equation (FBE) [93, 110, 257, 258],

$$\dot{F}_{k\alpha}(t) = I^{\mathrm{b}}_{k\alpha}[\{F_{k\alpha}(t)\}] + I^{\mathrm{ee}}_{k\alpha}[\{F_{k\alpha}(t)\}] \tag{7.4}$$

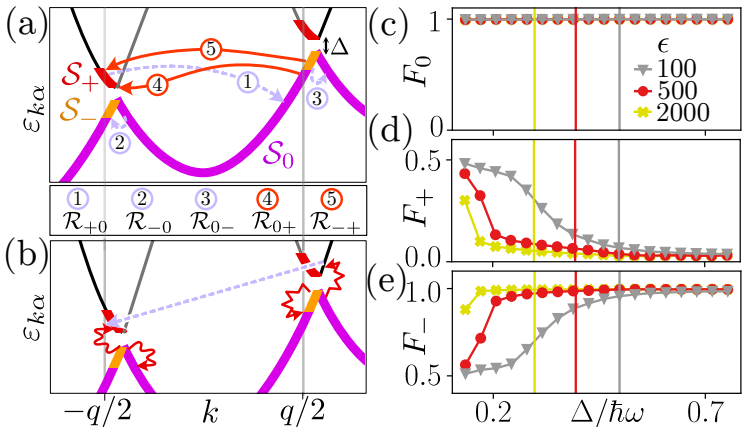

Figure 7.2: (a) Floquet bands upon driving by a coherent phonon wave. Dashed light purple arrows (1-3): dominant electron-phonon intraband and cooling processes relaxing electrons into the $\alpha = 0$ band. Solid red arrows (4-5): electron-phonon heating processes exciting electrons into the $\alpha = 1$ band, which are kinematically suppressed when $\Delta \gg \delta\varepsilon$. (b) Pairs of zigzag and squiggly red arrows: electron-electron scattering exciting electrons into the $\alpha = 1$ band. Dashed light purple arrow: electron-phonon process relaxing excited electrons into $\mathcal{S}_+$. (c)-(e) Occupation F_i of the patch $\mathcal{S}_i$ for $i = +, -, 0$ [see panel (a)] vs Δ for various dielectric constants ϵ. Vertical lines: $\Delta = \Delta^*(\epsilon)$. Note $F_+ \to 0, F_- \to 1$ as $\Delta \to \Delta^*$, resulting in quantized current.

with $\dot{F}_{k\alpha}(t) = 0$. The FBE is valid when $\hat{H}_{\rm ee}$ and $\hat{H}_{\rm b}$ weakly scatter electrons between single-particle Floquet eigenstates. Here, we use the Fermi golden rule modified for transitions between Floquet states [257, 258] to calculate the electron-phonon and electron-electron collision integrals $I^{\rm b}_{k\alpha}[\{F_{k\alpha}(t)\}]$ and $I^{\rm ee}_{k\alpha}[\{F_{k\alpha}(t)\}]$, respectively (see Appendix C). We note that the analysis in terms of the occupations, $F_{k\alpha}(t)$, diagonal in the Floquet basis neglects the coherences $\langle \hat{f}^\dagger_{k\alpha}(t)\hat{f}_{k\alpha'}(t)\rangle$ for $\alpha \neq \alpha'$. These coherences are suppressed when $1/\tau^{\rm ph}_{k\alpha\alpha'} + 1/\tau^{\rm el}_{k\alpha\alpha'} \ll |\varepsilon_{k\alpha} - \varepsilon_{k\alpha'}|/\hbar$, where $1/\tau^{\rm ph}_{k\alpha\alpha'}$ and $1/\tau^{\rm el}_{k\alpha\alpha'}$ are respectively the electron-phonon and electron-electron interband scattering rates between bands α and $\alpha' \neq \alpha$ [145, 257, 258]. Interband scattering transitions also broaden the electronic spectral function by an energy of roughly $\delta\varepsilon \approx \hbar/\tau^{\rm tot}_{k\alpha\alpha'}$, relaxing energy conservation in the FBE.

7.4 Phenomenological Rate Equation

Before discussing the numerical solution to the FBE, we present a simplified phenomenological analysis. Our goal is to estimate the conditions on the scattering rates leading to $F_{k\alpha} \approx F^{\rm opt}_{k\alpha}$ in the steady state. Here, $F^{\rm opt}_{k\alpha}$ is the optimal steady state distribution, defined as $F^{\rm opt}_{k0} = 1$, and $F^{\rm opt}_{k,\alpha\neq 0} = 0$, in which the current is quan-

tized. To this end, we identify the key scattering processes that contribute to the steady state, indicated by arrows in Figure 7.2(a)-(b). These processes connect three patches of Floquet states denoted by $\mathcal{S}_+$, $\mathcal{S}_-$, and $\mathcal{S}_0$, with approximately uniform electronic occupation F_+, F_-, and F_0 respectively. The patch $\mathcal{S}_0$ includes Floquet states with momentum $k^* \leq k < q/2$ in the $\alpha = 0$ band, while $\mathcal{S}_+$ and $\mathcal{S}_-$ encloses those with momentum $-q/2 \leq k < k^*$ in the $\alpha = 1$ and $\alpha = 0$ bands, respectively [see Figure 7.2(a)].

To estimate the electronic occupations of the patches, let us first consider the limit $\epsilon \to \infty$ and $I^{\text{ee}}_{k\alpha} \to 0$ in which scattering is mediated by acoustic phonons only. Averaging the FBE over the patches, we obtain rate equations for their occupations,

$$\dot{F}_i = \sum_j [\mathcal{R}_{ji} F_j (1 - F_i) - \mathcal{R}_{ij} F_i (1 - F_j)], \tag{7.5}$$

where $i, j = +, -, 0$ and $\mathcal{R}_{ij}$ denotes the average scattering rate of an electron from patch $\mathcal{S}_i$ to $\mathcal{S}_j$. We begin by assuming that the system is optimally doped, i.e., $n_e = q$, where n_e is the density of the electrons. The optimal steady state $F^{\text{opt}}_{k\alpha}$ is obtained when the "Floquet-cooling" processes $\mathcal{R}_{+0}$, $\mathcal{R}_{0-}$ and $\mathcal{R}_{-0}$ [dashed, light purple arrows numbered 1-3 in Figure 7.2(a)] dominate the scattering rates. The rest of the scattering rates $\mathcal{R}_{ij}$ create excitations in $\mathcal{S}_+$, leading to deviations from $F^{\text{opt}}_{k\alpha}$ and therefore are dubbed "Floquet-heating" rates [solid red arrows numbered 4-5 in Figure 7.2(a)].

When the incoherent phonons remain at temperature $T = 0$, all "Floquet-heating" processes mediated by acoustic phonons require a small energy and large momentum transfer. This kinematically constrains the rates $\mathcal{R}_{+-}$ and $\mathcal{R}_{0+}$ at high drive intensities, i.e., when $\Delta > \delta\varepsilon$, disabling all "Floquet-heating" processes. Simultaneously, the processes described by the rates $\mathcal{R}_{0-}$ and $\mathcal{R}_{-0}$ are kinematically allowed. These processes are of the Floquet-Umklapp (FU) type and therefore increase with the drive intensity as $(\Delta/\hbar\omega)^2$ yielding $F_{k\alpha} \to F^{\text{opt}}_{k\alpha}$ [76, 241, 257]. This is a remarkable result that shows that the coupling to acoustic phonons can stabilize a quantized current in the non-adiabatic regime $\delta\varepsilon < \Delta < \hbar\omega$. In contrast, in the low intensity limit ($\Delta \to 0$) of the drive, the rates $\mathcal{R}_{0-}$ and $\mathcal{R}_{-0}$ vanish, whereas the rates $\mathcal{R}_{-+}$ and $\mathcal{R}_{0+}$ become kinematically enabled. This situation leads to $F_+ = F_0 = 1$ and $F_- = 0$, recovering the equilibrium Fermi-Dirac distribution.

A finite incoherent phonon temperature $k_B T < \hbar\omega$ and electron-electron interactions (finite ϵ) cause deviations of the steady state from $F^{\text{opt}}_{k\alpha}$ when $\Delta > \delta\varepsilon$. Absorption of incoherent phonons yields a finite but weak electron-phonon heating rate $\mathcal{R}_{0+}$,

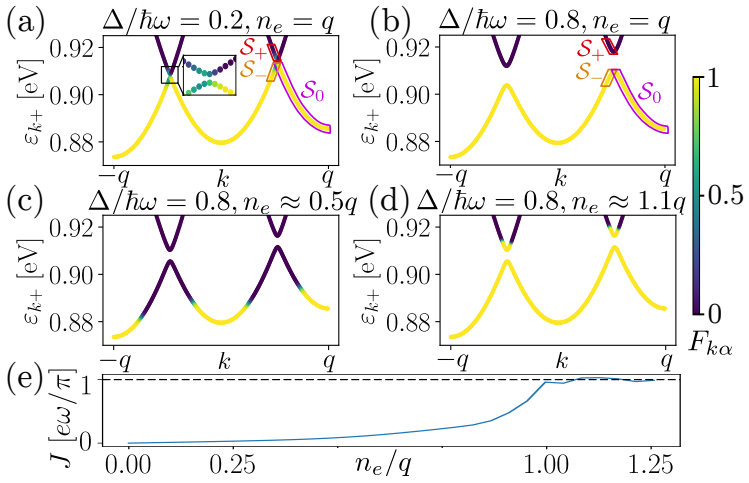

Figure 7.3: (a) Steady state occupation of the phonon-driven CNT for a weak phonon drive ($\Delta < \Delta^*$), dielectric constant $\epsilon = 80$, and optimal doping $n_e = q$. Inset shows excitations in the $\alpha = 1$ band near the Floquet gap. (b) Same as (a) but for a strong drive amplitude ($\Delta > \Delta^*$) where the occupation of the $\alpha = 1$ band is negligible, and the $\alpha = 0$ band is fully occupied. (c)-(d) Same as (b), but with two different electronic densities n_e away from optimal doping. (e) Steady state current vs n_e evaluated at $\Delta = 0.8\hbar\omega > \Delta^*$ for $\epsilon = 80$.

generating small electron and hole densities in $\mathcal{S}_+$ and $\mathcal{S}_-$ respectively. Heating processes due to electron-electron interactions excite electrons into the patch $\mathcal{S}_+$ in the $\alpha = 1$ band [pairs of squiggly red arrows in Figure 7.2(b)]. Other electron-electron scattering processes [pairs of zigzag arrows in Figure 7.2(b)] excite electrons to states elsewhere in the $\alpha = 1$ band, which are relaxed to $\mathcal{S}_+$ by electron-phonon cooling [dashed, light purple arrow in Figure 7.2(b)]. These processes result in a net increase in F_+ and reduced current response. Electron-electron heating can be suppressed by increasing the drive intensity, since the phase space for such scattering processes is constrained to small energy and momentum transfers near the Floquet gap [see Figure 7.2(b)] and is reduced as Δ is increased. In Figure 7.2(c)-(e), we show the average occupations of the patches as a function of Δ for various dielectric constants ϵ. We define Δ^* as the minimal Floquet gap at which $J = 0.96e\omega/\pi$. The equilibrium Fermi-Dirac distribution ($F_+ = F_0 = 1 - F_- = 1$) transitions to $F^{\text{opt}}_{k\alpha}$ as $\Delta \to \Delta^*$.

7.5 Numerical Analysis

To test our prediction of the steady state current, we solve the FBE numerically in the steady state. We consider a coherent acoustic phonon mode of angular frequency $\omega = 6$ meV$/\hbar$ with speed of sound $c_{\text{ph}} = 20$ km/s, incoherent phonon modes

at temperature $T = 7$ K, and optimal electronic density $n_e = q$. Figure 7.3(a)-(b) compares the steady state distributions for weak ($\delta\varepsilon < \Delta < \Delta^*$) and strong ($\Delta^* < \Delta < \hbar\omega$) non-adiabatic drives. As predicted using the phenomenological model, the density of excitations in the $\alpha = 1$ band is suppressed in the strong drive limit, approaching the optimal distribution $F^{\text{opt}}_{k\alpha}$.

Figure 7.1(b) shows the current J as a function of $\Delta/\hbar\omega$ for different dielectric constants ϵ. The vertical line indicates $\Delta = \hbar\omega$, the boundary between the non-adiabatic and adiabatic drive regimes. The current approaches quantization in the non-adiabatic regime $\Delta < \hbar\omega$ when ϵ is sufficiently large, verifying the phenomenological model. The inset of Figure 7.1(b) shows that the optimal Floquet gap Δ^* decreases as a function of ϵ.

Finally, we study the current as a function of the doping. The optimal distribution, $F^{\text{opt}}_{k\alpha}$, is obtained at optimal doping $n_e = q$. Figure 7.3(c)-(d) compares the steady state distributions for electronic densities below ($n_e < q$) and above ($n_e > q$) optimal doping, where the steady state deviates significantly from $F^{\text{opt}}_{k\alpha}$. Figure 7.3(e) shows J as a function of n_e for $\Delta \approx 0.8\hbar\omega > \Delta^*$ and $\epsilon = 80$. The quantized current is reached at optimal doping.

Experimental realization.—In Figure 7.1(a), we show a CNT suspended above a material of high relative permittivity ϵ, such as $SrTiO_3$ with $\epsilon \sim 10^3$ at THz frequencies [69, 243, 295]. The CNT is enclosed by a conducting anti-reflective material (ARM) with thickness tuned for destructive interference of reflected phonon waves [231]. Gold leads attached to the ARM measure the current. On the right, a segment of the CNT extends beyond the ARM. Phonon generation could be achieved by placing the segment under an intense laser pulse [67, 68, 85, 92, 246, 249, 250, 274, 317] or in contact with a material hosting coherent phonons, such as a phonon laser [22, 77, 151, 182, 213, 327] (see the Appendix C for details of potential coherent phonon sources.) The CNT must also be shorter than the coherent phonon decay length, which we estimate by $c_{\text{ph}}\tau \sim 1$ μm, where $\tau \sim 100$ ps is the approximate coherent phonon lifetime, set by FU and phonon-phonon scattering [18, 27, 94] (see Appendix C). Additionally, the phonon drive amplitude u_0 must be much weaker than that which causes melting, i.e., $u_0 \ll 0.1q^{-1}$, predicted by the Lindemann criterion [136, 166]. Indeed, the inset of Figure 7.1(b) shows that nearly quantized current is realized for experimentally-accessible values of ϵ when the Floquet gap satisfies $\Delta^*/\hbar\omega \sim 0.5$, corresponding to sufficiently weak driving amplitudes of $u_0 \sim 0.001a \ll 0.1q^{-1}$.

Conclusion.—Our work shows that coherent phonons can induce Floquet bands with quantized transport in screened quantum wires, where the steady state electronic population is stabilized by interactions with low-temperature incoherent phonons [see Figure 7.1(c)]. Furthermore, our device can serve as a detector of coherent phonons, where the measured current indicates the intensity and degree of coherence of the incoming acoustic waves. We anticipate sensitive detection even to weak fields because adiabaticity is not required [see Figs. 7.1(a)-(b)], in contrast to conventional methods utilizing optical reflectivity [72, 96, 157, 315].

A stronger signal, also sensitive to the direction of phonon propagation, could be obtained in higher-dimensional materials and heterostructures. Exploration of these systems is left for future work. While our work specialized on a phonon-driven CNT, the effect is general to various fermionic models with spatio-temoral modulation and energy-relaxing heat bath coupling (see Appendix C for a general model), including solid state and AMO systems [111, 201, 201].

7.6 Acknowledgements

We thank Yang Peng, Michael Kolodrubetz, and Erez Berg for valuable discussions. C.Y. gratefully acknowledges support from the DOE NNSA Stewardship Science Graduate Fellowship program, which is provided under cooperative agreement number DE-NA0003960. W.H. gratefully acknowledges support from the Caltech Cambridge Scholars Exchange Program. G.R. and I.E. are grateful for support from the Simons Foundation and the Institute of Quantum Information and Matter, as well as support from the NSF DMR grant number 1839271. This work is supported by ARO MURI Grant No. W911NF-16-1-0361, and was performed in part at Aspen Center for Physics, which is supported by National Science Foundation grant PHY-1607611.

Appendix C

APPENDIX

C.1 Microscopic Details of the Carbon Nanotube

In this section, we discuss in detail the microscopic model for the phonon-driven carbon nanotube, including the single particle electronic physics and electronic coupling to coherent and incoherent phonons.

The Carbon Nanotube Hamiltonian

The carbon nanotube (CNT) structure is described by the chirality indices (m, n) [79, 105, 128, 191, 247, 249]. Along the axis of the CNT, the lattice is periodic under translations by $\boldsymbol{T} = t_1\boldsymbol{a}_1 + t_2\boldsymbol{a}_2$, where $t_1 = (2m+n)/d_R$, $t_2 = -(2n+m)/d_R$, and $d_R = \gcd(2n+m, 2m+n)$, resulting in enlarged CNT unit cells that each contain $N = 2(n^2 + nm + m^2)/d_R$ graphene unit cells. Here, $\boldsymbol{a}_1 = \boldsymbol{\delta}_1 - \boldsymbol{\delta}_3$ and $\boldsymbol{a}_2 = \boldsymbol{\delta}_2 - \boldsymbol{\delta}_3$ are the primitive lattice vectors the graphene layer, where $\boldsymbol{\delta}_j = a/\sqrt{3}(\sin(2\pi j/3), \cos(2\pi j/3))$ and $a = 0.246$ nm. Along the circumference of the tube, the electron and phonon momenta acquire discrete values, while the momenta remain approximately continuous along the tube axis for a long CNT. The possible momenta can be expressed as $\boldsymbol{k} = s\boldsymbol{k}_\perp + k\hat{\boldsymbol{k}}_\parallel$, where $s = 0, 1, \ldots, N$ and $k \in [-\pi/|\boldsymbol{T}|, \pi/|\boldsymbol{T}|]$, with momentum vectors $\boldsymbol{k}_\perp = (-t_2\boldsymbol{b}_1 + t_1\boldsymbol{b}_2)$ and $\boldsymbol{k}_\parallel = (m\boldsymbol{b}_1 - n\boldsymbol{b}_2)/N$, and unit vectors $\hat{\boldsymbol{k}}_\perp = \boldsymbol{k}_\perp/|\boldsymbol{k}_\perp|$ and $\hat{\boldsymbol{k}}_\parallel = \boldsymbol{k}_\parallel/|\boldsymbol{k}_\parallel|$. We use $\boldsymbol{b}_1$ and $\boldsymbol{b}_2$ to denote the reciprocal lattice vectors of the graphene layer ($\boldsymbol{a}_i \cdot \boldsymbol{b}_j = 2\pi\delta_{ij}$). The family of possible momenta for each value of s represents a linear path, or 'cut,' along the Brillouin zone of the monolayer graphene. Now, the Hamiltonian for the CNT is of a block-diagonal form, with N blocks each corresponding to the Hamiltonian $\hat{H}_s(\boldsymbol{k}) = \hat{H}_{\mathrm{g}}(s\boldsymbol{k}_\perp + k\hat{\boldsymbol{k}}_\parallel)$ along a cut $s = 0, \ldots N$, where the single-particle tight-binding Hamiltonian for a monolayer graphene sheet with nearest-neighbor hopping is given by

$$\hat{H}_{\mathrm{g}} = \sum_{\boldsymbol{k}} \hat{\boldsymbol{\psi}}_{\boldsymbol{k}}^\dagger \begin{pmatrix} 0 & h^*(\boldsymbol{k}) \\ h(\boldsymbol{k}) & 0 \end{pmatrix} \hat{\boldsymbol{\psi}}_{\boldsymbol{k}}. \tag{C.1}$$

Here, $\hat{\boldsymbol{\psi}}_{\boldsymbol{k}} \equiv \begin{pmatrix} \hat{\psi}_{\boldsymbol{k},A} & \hat{\psi}_{\boldsymbol{k},B} \end{pmatrix}$ where $\hat{\psi}_{\boldsymbol{k},x}^\dagger$ creates a fermion of crystal momentum $\boldsymbol{k}$ on sublattice $x = A, B$ of the graphene sheet, $h(\boldsymbol{k}) = h\sum_j e^{i\boldsymbol{k}\cdot\boldsymbol{\delta}_j}$, and $h = 2.8$ eV.

The lowest-energy conduction and highest-energy valence bands are indexed by

$s_{\mathrm{m}} = \mathrm{argmin}_s \min_k |s\boldsymbol{k}_\perp + k\hat{\boldsymbol{k}}_\parallel - \boldsymbol{K}|$, where $\boldsymbol{K}$ is the momentum of the Dirac K point in the monolayer graphene Brillouin zone. The lowest energy electronic state along the cut s_m has momentum $k_m = \mathrm{argmin}_k |s_m\boldsymbol{k}_\perp + k\hat{\boldsymbol{k}}_\parallel - \boldsymbol{K}|$.

The Electron-Phonon Hamiltonian

In this section, we detail the CNT Hamiltonian and electron-phonon coupling Hamiltonian used in the main text. The lowest conduction and highest valence bands [see Figure 1(c) in the main text] of the CNT are described by the effective Hamiltonian $\hat{H}_{\mathrm{e}} = \int dk/2\pi\, \hat{\boldsymbol{\psi}}_k^\dagger H_{\mathrm{e}}(k)\hat{\boldsymbol{\psi}}_k$, where

$$H_{\mathrm{e}}(k) = \hbar v_F(\delta k\hat{\boldsymbol{k}}_\perp + k\hat{\boldsymbol{k}}_\parallel)\cdot\boldsymbol{\sigma}, \tag{C.2}$$

v_F is the Fermi velocity of graphene, $\boldsymbol{\sigma} = (\sigma_x, \sigma_y)$ is a vector of Pauli matrices acting in the graphene sublattice basis, the x axis is aligned along a bond between carbon atoms, and $\delta k = |s_m\boldsymbol{k}_\perp + k_m\hat{\boldsymbol{k}}_\parallel - \boldsymbol{K}|$.

To describe electron-phonon interactions in the CNT, we consider the Hamiltonian $\hat{H}_{\mathrm{ep}}(t) = \sum_\lambda \hat{H}_{\mathrm{ep}}^{(\lambda)}(t)$, where $\hat{H}_{\mathrm{ep}}^{(\lambda)}(t) = \int d^2\boldsymbol{r}\, \hat{\boldsymbol{\psi}}_{\boldsymbol{r}}^\dagger \hat{V}^{(\lambda)}(\boldsymbol{r},t)\hat{\boldsymbol{\psi}}_{\boldsymbol{r}}$ and

$$\hat{V}^{(\lambda)}(\boldsymbol{r},t) = \hbar v_F \hat{\boldsymbol{\mathcal{A}}}_{\mathrm{ph}}^{(\lambda)}(\boldsymbol{r},t)\cdot\boldsymbol{\sigma} + \hat{\phi}_{\mathrm{ph}}^{(\lambda)}(\boldsymbol{r},t) \tag{C.3}$$

describe electronic coupling to a phonon mode indicated by λ, $\boldsymbol{r} = (x, y)$ is the spatial coordinate along the tube, and $\hat{\boldsymbol{\psi}}_{\boldsymbol{r}}^\dagger = P^{-1}\int dk/(2\pi) e^{-i(\delta k\hat{\boldsymbol{k}}_\perp + k\hat{\boldsymbol{k}}_\parallel)\cdot\boldsymbol{r}}\hat{\boldsymbol{\psi}}_k^\dagger$. The electrons interact with the phonons through the effective vector potential

$$\hat{\boldsymbol{\mathcal{A}}}_{\mathrm{ph}}^{(\lambda)}(\boldsymbol{r},t) = \sqrt{3}\beta/(2a)(\hat{u}_{xx}^{(\lambda)}(\boldsymbol{r},t) - \hat{u}_{yy}^{(\lambda)}(\boldsymbol{r},t), 2\hat{u}_{xy}^{(\lambda)}(\boldsymbol{r},t)) \tag{C.4}$$

and through the local scalar potential

$$\hat{\phi}_{\mathrm{ph}}^{(\lambda)}(\boldsymbol{r},t) = D[\hat{u}_{xx}^{(\lambda)}(\boldsymbol{r},t) + \hat{u}_{yy}^{(\lambda)}(\boldsymbol{r},t)]I, \tag{C.5}$$

where $a = 0.246$ nm, $\beta \approx 3.14$, and deformation potential $D = 15$ eV [77, 296]. Here, $\hat{\boldsymbol{u}}^{(\lambda)}(\boldsymbol{r},t)$ is the displacement operator of the phonon mode, $\hat{u}_b^{(\lambda)}(\boldsymbol{r},t)$ is its b-th component, and $\hat{u}_{bc}^{(\lambda)}(\boldsymbol{r},t) = [\partial_b\hat{u}_c^{(\lambda)}(\boldsymbol{r},t) + \partial_c\hat{u}_b^{(\lambda)}(\boldsymbol{r},t)]/2$.

Hamiltonian for Interactions Between Electrons and Incoherent Phonons

In this section, we provide the full expression for the microscopic Hamiltonian $\hat{H}_{\mathrm{b}}(t)$ accounting for electronic coupling to incoherent bath phonon modes. The low-energy longitudinal acoustic phonons dominate the electron-phonon scattering near the Fermi surface of the lightly-doped CNT. Upon writing the displacement

operators $\hat{\boldsymbol{u}}^{(\lambda)}(\boldsymbol{r},t)$ for such phonon modes in terms of bath acoustic phonon creation operators $\hat{b}_p^\dagger$, we derive the effective Hamiltonian [246]:

$$\hat{H}_{\rm b} = \int \frac{dkdq}{(2\pi)^2} M_{k,p} \hat{c}^\dagger_{k+p,+} \hat{c}_{k,+} (\hat{b}^\dagger_p + \hat{b}_{-p}) + \text{h.c.} \tag{C.6}$$

where $M_{k,p} = D\sqrt{\hbar c_{\rm ph} p}/(\sqrt{2A\rho} c_{\rm ph}) \mathcal{W}_{k,p}$ with unit cell area $A = \sqrt{3}Na^2/2$, and graphene density ρ.

C.2 Details of the coherent phonon drive

In this section, we analyze the coherent phonon drive in detail and propose possible coherent phonon sources.

Analytic Expression for the Floquet Gap

In this section, we derive the expression for the Floquet gap

$$\Delta \approx q u_0 [D + \hat{k}^y_{\parallel} \hbar v_F \sqrt{3}\beta/2a] \tag{C.7}$$

used in the main text.

We begin by constructing an effective drive Hamiltonian by working in the eigenbasis of the electronic Hamiltonian

$$H_{\rm e}(k) = \hbar v_F \boldsymbol{k} \cdot \sigma, \tag{C.8}$$

where $\boldsymbol{k} = \delta k \hat{\boldsymbol{k}}_\perp + k \hat{\boldsymbol{k}}_\parallel$ [see the full definition in the main text]. Let U be the matrix that diagonalizes $H_{\rm e}(k)$, where

$$U^{-1} H_{\rm e}(k) U = \begin{pmatrix} -\hbar v_F |\boldsymbol{k}| & 0 \\ 0 & \hbar v_F |\boldsymbol{k}| \end{pmatrix}. \tag{C.9}$$

In the limit near $k = 0$, one can show that

$$U^{-1} H_{\rm e}(k) U \approx \begin{pmatrix} E_-(k) & 0 \\ 0 & E_+(k) \end{pmatrix} \tag{C.10}$$

where $E_\pm(k) = \hbar^2 k^2/(2m) \pm \hbar v_F \delta k$. The electronic coupling to a coherent phonon mode is described by the Hamiltonian

$$V(\boldsymbol{r},t) = \hbar v_F \langle \hat{\boldsymbol{\mathcal{A}}}^{(\lambda_0)}_{\rm ph}(\boldsymbol{r},t) \rangle \cdot \boldsymbol{\sigma} + \langle \hat{\phi}^{(\lambda_0)}_{\rm ph}(\boldsymbol{r},t) \rangle. \tag{C.11}$$

Note that

$$[\langle \hat{\boldsymbol{\mathcal{A}}}^{(\lambda_0)}_{\rm ph}(\boldsymbol{r},t) \rangle]_x = \frac{\sqrt{3}\beta}{2a} [(\hat{k}^y_{\parallel})^2 - (\hat{k}^x_{\parallel})^2] q u \sin\big(qr - \omega t\big) \tag{C.12}$$

$$[\langle \hat{\mathcal{A}}_{\mathrm{ph}}^{(\lambda_0)}(\boldsymbol{r},t)\rangle]_y = \frac{\sqrt{3}\beta}{2a}(-2\hat{k}_{\parallel}^{x}\hat{k}_{\parallel}^{y})qu\sin\big(qr-\omega t\big) \tag{C.13}$$

and

$$\langle \hat{\phi}_{\mathrm{ph}}^{(\lambda_0)}(\boldsymbol{r},t)\rangle = Dqu\sin\big(qr-\omega t\big)I. \tag{C.14}$$

To transform $V(\boldsymbol{r},t)$ into the diagonal basis of $H_{\mathrm{e}}(k)$, first note that

$$\begin{aligned} &U^{-1}[\hbar v_F\langle \hat{\mathcal{A}}_{\mathrm{ph}}^{(\lambda_0)}(r,t)\rangle\cdot\boldsymbol{\sigma}]U \\ &= \begin{pmatrix} -\langle \hat{\mathcal{A}}_{\mathrm{ph}}^{(\lambda_0)}(\boldsymbol{r},t)\rangle\cdot\boldsymbol{k}/|\boldsymbol{k}| & -i\langle \hat{\mathcal{A}}_{\mathrm{ph}}^{(\lambda_0)}(\boldsymbol{r},t)\rangle\times\boldsymbol{k}/|\boldsymbol{k}| \\ i\langle \hat{\mathcal{A}}_{\mathrm{ph}}^{(\lambda_0)}(\boldsymbol{r},t)\rangle\times\boldsymbol{k}/|\boldsymbol{k}| & \langle \hat{\mathcal{A}}_{\mathrm{ph}}^{(\lambda_0)}(\boldsymbol{r},t)\rangle\cdot\boldsymbol{k}/|\boldsymbol{k}| \end{pmatrix}. \end{aligned} \tag{C.15}$$

In a semiconducting nanotube, near the band extrema, $k \ll \delta k$, so $\boldsymbol{k}$ and $\hat{\boldsymbol{k}}_{\perp}$ are roughly parallel and

$$\langle \hat{\mathcal{A}}_{\mathrm{ph}}^{(\lambda_0)}(r,t)\rangle\cdot\boldsymbol{k}/|\boldsymbol{k}| \approx \hat{k}_{\parallel}^{y}\hbar v_F\frac{\sqrt{3}\beta}{2a}qu\sin\big(qr-\omega t\big). \tag{C.16}$$

When $\hbar v_F\beta a^{-1} \ll \hbar v_F\delta k$, the off-diagonal components of Eq. (C.15) are negligible. In this limit, we finally obtain an effective Hamiltonian for the lowest conduction band of the CNT,

$$\begin{aligned} &[U^{-1}H_0(k,t)U]_{00} \\ &\approx E_+(k) + \left[\hat{k}_{\parallel}^{y}\hbar v_F\frac{\sqrt{3}\beta}{2a} + D\right]qu\sin\big(qr-\omega t\big). \end{aligned} \tag{C.17}$$

From Eq. (C.17), we read the Floquet gap $\Delta \approx qu_0[D + \hat{k}_{\parallel}^{y}\hbar v_F\sqrt{3}\beta/2a]$ from the amplitude of the spatially- and time-periodic component of the Hamiltonian.

Coherent Phonon Occupancy

The Floquet theory used in the main text assumes that the coherent phonon occupancy n is large. In this section, we show that the assumption is true for the phonon displacement amplitudes required to observe quantized acoustelectric Floquet effect. The coherent phonon amplitude, expressed in terms of the phonon occupation n, is given by

$$u_0 = 2\sqrt{\frac{(n+1/2)\hbar}{2NM_C\omega}}, \tag{C.18}$$

where M_C is the mass of a carbon atom and N is the total number of graphene unit cells in the carbon nanotube. For a $(10,0)$ carbon nanotube of length on the order of 1 μm, we estimate $N \approx 10^5$. To estimate the minimum phonon occupancy necessary to achieve nearly-quantized currents, we refer to the inset of Figure 1(b)

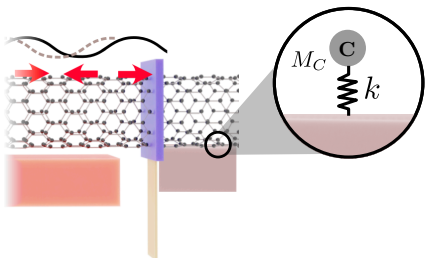

Figure C.1: Phonon transfer mechanism when a phonon source (grey block) is placed under the right end of the carbon nanotube [see Figure 1(a) in the main text for the complete, proposed experimental setup]. A carbon atom of mass M_c (grey circle in magnified picture) experiences a Van der Waals force across the interface, with effective spring constant k.

in the main text, which indicates that the Floquet gap at current saturation is given by $\Delta^* \approx 0.5\hbar\omega$, corresponding to the phonon amplitude [141]

$$u_0^* \approx 0.5\hbar c_{\text{ph}}/[D + 0.866\hbar v_F\sqrt{3}\pi/(2a)]. \tag{C.19}$$

(See Section C.2 for a derivation.) Here, D is the deformation potential, c_{ph} is the speed of sound, $v_F = 10^6$ m/s is the Fermi velocity, and $a = 0.246$ nm is the graphene lattice constant. As an example, assuming $D \approx 10$ eV, $\hbar\omega \approx 10$ meV, and $c_{\text{ph}} = 25$ km/s, we arrive at the phonon occupancy $n \sim 36$. Given $n \gg 1$, this occupation can provide multi-phonon absorption processes with an approximately constant amplitude.

Coherent Phonon Lifetime

To estimate the coherent phonon lifetime τ, which limits the total length of the CNT, we note that the Floquet scattering rates shown in Figure C.2 saturate on the order $\tau^{\text{tot}}_{k\alpha\alpha'} \sim 10$ ps for relative permittivities $\epsilon > 500$. The Floquet-Umklapp scattering rates contribute to coherent phonon absorption and emission and are suppressed by a factor of $(\Delta/\hbar\omega)^2$, occuring on timescales of ~ 100 ps. Phonon-phonon and phonon-impurity interactions in graphene materials are also estimated to occur on timescales of ~ 100 ps [18, 27, 94]. Thus, we estimate $\tau \sim 100$ ps.

Proposals for Experimental Realizations of the Quantized Acoustoelectric Floquet Effect

In this section, we investigate possible coherent phonon sources and their coupling to the CNT. There are several potential sources of coherent THz-frequency phonons in materials. Conventionally, THz-frequency phonons have been generated optically,

by a direct driving of an IR-active phonon mode [68], or by excitation of electrons that generate phonons through electron-phonon coupling [22, 67, 85, 109, 182, 274, 317].

Alternatively, acoustic phonons can be generated in strongly biased metals through the acoustic Cerenkov [10, 151, 213, 327], Klein-Zehner effects [5, 103], and through the phaser effect [35], which has been theoretically demonstrated in twisted bilayer graphene-based devices.

These methods have been demonstrated to induce intense phonon waves. In particular, a medium with a positive phonon gain in an acoustic resonator is predicted to induce acoustic waves with amplitudes of the order of ~ 0.01 nm, when reaching saturation [77].

In Figure 1(a) of the main text, we show a potential experimental setup, where a segment of the carbon nanotube extends to the right of the anti-reflective material. The coherent phonons can be directly generated by an optical illumination of the segment of CNT [92, 249, 250]. Alternatively, they can be generated in a different system, outside the CNT, and then coupled to the CNT. The latter is a more versatile approach that allows for on-demand coherent phonon generation by various methods. We estimate that the coherent phonon amplitudes in the CNT can reach the order of ~ 0.01 nm when an acoustic resonator like the phaser is placed in contact with the CNT, provided that the phonon angular frequency does not exceed the natural resonance frequency set by the coupling between the source and the CNT. To estimate the resonance frequency, we consider the Van der Waals forces between the source and CNT, which can be modeled by a forced oscillation problem (see Figure C.1). For efficient transmission of the phonon wave into the CNT, the angular frequency ω of the coherent phonon should satisfy $\omega < \omega_r$, where the resonance frequency $\omega_r = \sqrt{k/M_C}$ is set by the effective spring constant k and the mass M_C of the carbon atom. We estimate $k \approx 2$ N/m and $\hbar\omega_r = 7$ meV by utilizing the Lennard-Jones potential function calculated from first principles for Van der Waals forces between graphene layers [56]. The angular frequency presented in the main text satisfies $\omega < \omega_r$.

Let us finally discuss the necessary conditions on the placement of the dielectric material. Because the characteristic separation between electrons in the tube, $2\pi/q \sim 100$, is much larger than the diameter of the CNT, the dielectric screens the entire CNT. To avoid interference with the coherent phonon wave, one can minimize phonon transfer between the dielectric and CNT by suspending the CNT above the dielectric a distance much larger than the equilibrium interatomic distance ~ 3 set

by Van der Waals (VdW) potential between the materials [56].

C.3 Details on the Steady State Calculation

We start by presenting the full expression for the Floquet-Boltzmann equation (FBE) discussed in main text and show that the FBE is valid under the conditions considered in our work.

Floquet Boltzmann Equation

In this section, we present the full expressions for the electron-phonon and electron-electron collision integrals, discretized on a 1D momentum grid of N points. The electron-phonon collision integral is given by

$$
\begin{aligned}
I^{\mathrm{b}}_{k\alpha}[\{F_{k\alpha}\}] = \frac{2\pi}{\hbar}\frac{1}{N}\sum_{k'\in\mathrm{BZ}}\sum_{\alpha'}\sum_{s}\sum_{n}|\mathcal{G}^{k'\alpha'}_{k\alpha}(n)|^2\frac{1}{\hbar c_{\mathrm{ph}}}\times \\
\times\big(\{-\mathcal{N}(\varepsilon_{k'\alpha'}-\varepsilon_{k\alpha})F_{k\alpha}(1-F_{k'\alpha'})\delta(k'-k+nq+k_s) \\
+[1+\mathcal{N}(\varepsilon_{k'\alpha'}-\varepsilon_{k\alpha})](1-F_{k\alpha})F_{k'\alpha'}\delta(k'-k+nq-k_s)\}\theta(\varepsilon_{k'\alpha'}-\varepsilon_{k\alpha}) \\
+\{-[1+\mathcal{N}(\varepsilon_{k'\alpha'}-\varepsilon_{k\alpha})]F_{k\alpha}(1-F_{k'\alpha'})\delta(k'-k+nq-k_s) \\
+\mathcal{N}(\varepsilon_{k'\alpha'}-\varepsilon_{k\alpha})(1-F_{k\alpha})F_{k'\alpha'}\delta(k'-k+nq+k_s)\}\theta(\varepsilon_{k'\alpha'}-\varepsilon_{k\alpha})
\end{aligned}
\tag{C.20}
$$

$$
\mathcal{G}^{k'\alpha'}_{k\alpha}(n) = \frac{1}{\sqrt{A}}\frac{D\hbar k_s}{\sqrt{2\rho\hbar|\varepsilon_{k'\alpha'}-\varepsilon_{k\alpha}|}}\sum_{m}\langle\phi^{n+m}_{k'\alpha'}|+,k'\rangle\mathcal{W}_{k,k'-k}\langle+,k|\phi^{m}_{k\alpha}\rangle \tag{C.21}
$$

where $\rho = 1.52\times10^{-6}$ kg/m^2 is the 2D density of the graphene layers, D is the deformation potential, k_s satisfies $\hbar c_{\mathrm{ph}}|s\boldsymbol{k}_\perp + k_s\hat{\boldsymbol{k}}_\parallel| = \varepsilon_{k'\alpha'}-\varepsilon_{k\alpha}$, and $\mathcal{N}(\varepsilon) = 1/(e^{\varepsilon/k_BT}-1)$ is the Bose-Einstein distribution for incoherent phonons maintained in thermal equilibrium at temperature T. The electron-electron collision integral is given by

$$
\begin{aligned}
I^{\mathrm{ee}}_{k\alpha}[\{F_{k\alpha}\}] = \frac{4\pi}{\hbar}\frac{1}{N^2}\sum_{k_2\in\mathrm{BZ}}\sum_{k_3\in\mathrm{BZ}}\sum_{\alpha_2,\alpha_3,\alpha_4}\sum_{n}|\mathcal{V}^{(k_3,\alpha_3),(k_1+k_2-k_3,\alpha_4)}_{(k,\alpha),(k_2,\alpha_2)}(n)|^2\times \\
\times\delta(\varepsilon_{k\alpha}+\varepsilon_{k_2\alpha_2}-\varepsilon_{k_3\alpha_3}-\varepsilon_{k+k_2-k_3,\alpha_4}+n\hbar\Omega)\times \\
\times\left[(1-F_{k\alpha})(1-F_{k_2\alpha_2})F_{k_3\alpha_3}F_{k_1+k_2-k_3,\alpha_4}-F_{k\alpha}F_{k_2\alpha_2}(1-F_{k_3\alpha_3})(1-F_{k_1+k_2-k_3,\alpha_4})\right]
\end{aligned}
\tag{C.22}
$$

$$\mathcal{V}^{(k_3,\alpha_3),(k_1+k_2-k_3,\alpha_4)}_{(k,\alpha),(k_2,\alpha_2)}(n) = \sum_{n_2,n_3,n_4} V(k_2-k_3)\mathcal{W}_{k_1,k_3-k_2}\mathcal{W}_{k_2,-(k_3-k_2)}\langle\phi^{n-n_2+n_3+n_4}_{k\alpha}|+,k\rangle\langle\phi^{n_2}_{k_2\alpha_2}|+,k_2\rangle\times \times\langle+,k_3|\phi^{n_3}_{k_3\alpha_3}\rangle\langle+,k_4|\phi^{n_4}_{k+k_2-k_3,\alpha_4}\rangle. \tag{C.23}$$

To solve for the steady-state, we use the Newton-Raphson algorithm to find the roots $\partial_t F_{k\alpha} = 0$ of the FBE. We set the doping of the system by adding the Lagrange multiplier term $\lambda(\sum_{k\alpha} F_{k\alpha} - Nk_F/q)$ with large constant λ to the FBE.

Validity of Floquet Boltzmann Equation and Steady State Scattering Times

The interband scattering rates $1/\tau^{\text{ph}}_{k\alpha\alpha'}$ and $1/\tau^{\text{el}}_{k\alpha\alpha'}$ are given by

$$\begin{aligned}\frac{1}{\tau^{\text{ph}}_{k\alpha\alpha'}} = \frac{2\pi}{\hbar}\frac{1}{N}\sum_{k'\in\text{BZ}}\sum_{s}\sum_{n}|\mathcal{G}^{k'\alpha'}_{k\alpha}(n)|^2\frac{1}{\hbar c_{\text{ph}}}\times \\ \times\{\mathcal{N}(\varepsilon_{k'\alpha'}-\varepsilon_{k\alpha})(1-F_{k'\alpha'})\delta(k'-k+nq+k_s)+ \\ +[1+\mathcal{N}(\varepsilon_{k'\alpha'}-\varepsilon_{k\alpha})](1-F_{k'\alpha'})\delta(k'-k+nq-k_s)\}\end{aligned} \tag{C.24}$$

and

$$\begin{aligned}\frac{1}{\tau^{\text{el}}_{k\alpha\alpha'}} = \frac{4\pi}{\hbar}\frac{1}{N^2}\sum_{k_2\in\text{BZ}}\sum_{k_3\in\text{BZ}}\sum_{\substack{\alpha_2,\alpha_3,\alpha_4 \\ \alpha_3=\alpha' \text{ or } \alpha_4=\alpha'}}\sum_{n}\sum_{G} \\ |\mathcal{V}^{(k_3,\alpha_3),(k_1+k_2-k_3,\alpha_4)}_{(k,\alpha),(k_2,\alpha_2)}(n,G)|^2\times \\ \times\delta(\varepsilon_{k\alpha}+\varepsilon_{k_2\alpha_2}-\varepsilon_{k_3\alpha_3}-\varepsilon_{k+k_2-k_3,\alpha_4}+n\hbar\Omega)\times \\ \times F_{k_2\alpha_2}(1-F_{k_3\alpha_3})(1-F_{k_1+k_2-k_3,\alpha_4}).\end{aligned} \tag{C.25}$$

To verify that the steady state coherences are suppressed and that the Floquet Boltzmann equation is valid, we check that $\zeta \ll 1$, where $\zeta \equiv \max_{k,\alpha,\alpha'} \hbar/(\tau^{\text{tot}}_{k\alpha\alpha'}|\varepsilon_{k\alpha} - \varepsilon_{k\alpha'}|)$, where $1/\tau^{\text{tot}}_{k\alpha\alpha'} \equiv 1/\tau^{\text{ph}}_{k\alpha\alpha'} + 1/\tau^{\text{el}}_{k\alpha\alpha'}$ [see full definition in the main text]. Figure C.2 verifies that $\zeta \ll 1$ as a function of drive amplitude.

C.4 Effective Description Using Lindblad Master Equation

In the present and following sections, we analyze the quantized acoustoelectric Floquet effect using a toy model that can be analytically solved. The purpose of the toy model is to provide an intuitive and simple picture of the key conditions required to observe the quantized acoustoelectric Floquet effect. We demonstrate that the effect is analogous to a Thouless pump driven non-adiabatically, i.e. $\Delta < \hbar\omega$, with quantized transport stabilized by an incoherent energy relaxation mechanism, which in the microscopic model arises from phonon cooling [see Figure C.3]. In

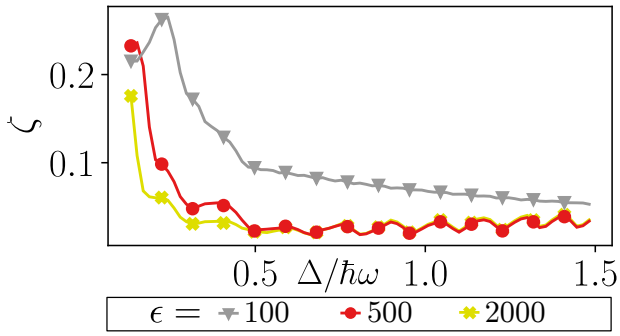

Figure C.2: The ratio ζ of the maximum interband scattering rate to the Floquet band energy separation vs. Floquet gap Δ for various dielectric constants ϵ. Note that $\zeta \ll 1$, so steady state coherences are suppressed.

particular, incoherent phonons relax electrons into the troughs of the moving periodic potential $V(x,t)$, which is induced by the coherent phonon wave. This process is dominant when the relaxation time of incoherent phonon scattering, τ_{ep}, is much faster than that of heating processes, τ_h. Importantly, we stress that the Lindblad master equation analysis used in this section is distinct from the full Floquet theory and Floquet-Boltzmann equation approach presented in the main text and previous supplementary materials sections.

Effective Hamiltonian

Let us first derive an effective Hamiltonian for the driven carbon nanotube. In the limit where coupling strength of the coherent electrons via the vector potential $\hat{\mathcal{A}}_{\text{ph}}^{(\lambda)}(\boldsymbol{r},t)$ is much smaller than the separation between the lowest conduction and highest valence bands, i.e., $\hbar v_F \beta a^{-1} \ll \hbar v_F \delta k$ (see definitions of δk and β in Section C.1) we can approximate $V(\hat{\boldsymbol{r}},t) \approx \Delta\cos\big(q\hat{x} - \omega t\big)$, where $V(\hat{\boldsymbol{r}},t) \equiv \langle \hat{V}^{(\lambda_0)}(\hat{\boldsymbol{r}},t)\rangle$, and $\hat{\boldsymbol{r}} = \hat{x}\hat{\boldsymbol{k}}_{\parallel}$ is the spatial position along the tube axis of the CNT (see Section C.2 for the derivation). We also approximate $E_+(k) \approx \hbar^2 k^2/(2m) + \hbar v_F \delta k$ where m is the effective mass at the band bottom [see Figure 1(c) in the main text]. Up to a constant energy offset, the resulting effective Hamiltonian is given by

$$\hat{H}(t) = \hat{H}_0 + \Delta\cos\big(q\hat{x} - \omega t\big), \tag{C.26}$$

where $\hat{H}_0 = \hbar^2\hat{k}^2/2m$, $\hat{x} = -i\partial_{\hat{k}}$ is the position operator, and $\hat{k}$ is the momentum operator. To analyze the problem analytically, we work in the eigenbasis $|k\rangle$ of the free-propagation Hamiltonian $\hat{H}_0$. Using the relation $e^{iq\hat{x}}|k\rangle = |k+q\rangle$, and considering the limit $\hbar^2 q^2/(2m) \gg \Delta$, we obtain the approximate matrix form of

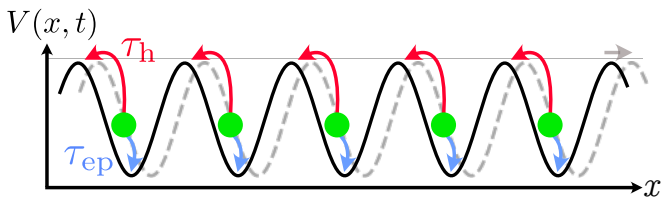

Figure C.3: Simplified model of the quantized acoustoelectric Floquet effect. The black curve represents the moving coherent phonon potential $V(x,t)$, and the grey dashed curve sketches the potential at a slightly later time. Electrons (green dots) generate quantized current when confined to the troughs of the potential, which is achieved when the incoherent phonon relaxation time τ_{ep} is much faster than the heating time τ_h.

$\hat{H}(t)$,

$$H(t) \approx \bar{\varepsilon}_k + \begin{pmatrix} \delta_k & \Delta e^{i\omega t}/2 \\ \Delta e^{-i\omega t}/2 & -\delta_k \end{pmatrix}, \tag{C.27}$$

where $\bar{\varepsilon}_k = (\varepsilon_k + \varepsilon_{k-q})/2$, $\delta_k = (\varepsilon_k - \varepsilon_{k-q})/2$, and $\varepsilon_k = \hbar^2 k^2/(2m)$.

Lindblad Master Equation

Our goal is to compute the time-averaged current, given by

$$J = \frac{2e}{\hbar}\frac{1}{T}\int_0^T dt \int_0^q \frac{dk}{2\pi}\mathrm{Tr}\left[\frac{\partial H(t)}{\partial k}\rho(k,t)\right] \tag{C.28}$$

where the factor of two accounts for spin degeneracy, $T = 2\pi/\omega$, and $\rho(k,t)$ is the density matrix for an electron with crystal momentum k. The actual value of $\rho(k,t)$ is controlled by the Hamiltonian $H(t)$, collisions with incoherent phonon modes, and electron-electron interactions. We approximate the relaxation dynamics of the electrons in the CNT due to scattering processes by the Lindbladian

$$\mathcal{L}\{\rho(k,t)\} \equiv -\frac{\rho(k,t) - \rho^{\mathrm{eq}}(k,t)}{\tau_h} - \frac{\rho(k,t) - \rho^{F}(k,t)}{\tau_{ep}} \tag{C.29}$$

with two characteristic relaxation times τ_h and τ_{ep}. Here, heating processes, such as electron-electron interactions, relax electrons into a thermal equilibrium state in the instantaneous basis of $H(t)$, denoted by $\rho^{\mathrm{eq}}(k,t)$. Separately, incoherent phonon scattering processes relax electrons into the Floquet ground state $\rho^{F}(k,t)$, representing a fully-occupied lowest-energy band of the Floquet Hamiltonian $H_F \equiv H(t) - i\hbar\partial_t$. Eq. (C.29) captures the key microscopic scattering processes analyzed in the main text. Under these approximations, the time evolution of the density

matrix can be described by the master equation [186, 253]

$$\dot{\rho}(k,t) = \frac{i}{\hbar}[\rho(k,t), H(t)] + \mathcal{L}\{\rho(k,t)\}. \tag{C.30}$$

To solve the Lindblad master equation analytically, we utilize the time-independent basis, where the Hamiltonian is given by

$$\tilde{H} = R(t)H(t)R(t)^\dagger = \bar{\varepsilon}_k + \begin{pmatrix} \delta_k & \Delta/2 \\ \Delta/2 & -\delta_k \end{pmatrix}. \tag{C.31}$$

Here,

$$R(t) = \begin{pmatrix} e^{-i\omega t/2} & 0 \\ 0 & e^{i\omega t/2} \end{pmatrix} \tag{C.32}$$

is the transformation matrix. In the time-independent basis, the master equation is given by

$$\dot{\tilde{\rho}}(k,t) = \frac{i}{\hbar}[\tilde{\rho}(k,t), \tilde{H} + B] + \tilde{\mathcal{L}}\{\tilde{\rho}(k,t)\} \tag{C.33}$$

where $B = i\dot{R}(t)R(t)^\dagger = (\hbar\omega/2)\sigma_z$, $\tilde{\rho}(k,t) = R(t)\rho(k,t)R(t)^\dagger$, and $\tilde{\mathcal{L}}\{\tilde{\rho}(k,t)\} = R(t)\mathcal{L}\{\rho(k,t)\}R(t)^\dagger$. In the instantaneous basis, we also define

$$\tilde{\rho}^{\mathrm{eq}}(k) \equiv R(t)\rho^{\mathrm{eq}}(k,t)R(t)^\dagger, \tag{C.34}$$

and

$$\tilde{\rho}^{F}(k) \equiv R(t)\rho^{F}(k,t)R(t)^\dagger. \tag{C.35}$$

Thermal Distribution in the Instantaneous Eigenbasis

The instantaneous thermal distribution $\rho^{\mathrm{eq}}(k,t)$ is diagonal in the instantaneous eigenbasis. In this section, we transfer $\rho^{\mathrm{eq}}(k,t)$ into the time-independent basis to determine $\tilde{\rho}^{\mathrm{eq}}(k)$. We use the operator U to transform into the instantaneous eigenbasis of $H(t)$, where

$$\mathcal{H} = U\tilde{H}U^\dagger = \begin{pmatrix} \varepsilon^I_-(k) & 0 \\ 0 & \varepsilon^I_+(k) \end{pmatrix} \tag{C.36}$$

and $\varepsilon^I_\pm(k) \equiv \bar{\varepsilon}_k \pm \sqrt{\delta_k^2 + (\Delta/2)^2}$ are the instantaneous eigenenergies. It follows that the density matrix corresponding to the thermal distribution in the instantaneous basis is given by

$$\begin{aligned} \tilde{\rho}^{\mathrm{eq}}(k) &= U^\dagger \begin{pmatrix} 1 - f^I_k & 0 \\ 0 & f^I_k \end{pmatrix} U \\ &= \frac{1}{2} + \frac{1 - 2f^I_k}{2\sqrt{\delta_k + (\Delta/2)^2}} \left[\frac{\Delta}{2}\sigma_x + \delta_k \sigma_z \right]. \end{aligned} \tag{C.37}$$

where f^I_k is the Fermi-Dirac occupation of the electronic state with energy $\varepsilon^I_-(k)$.

Floquet Ground State

The Floquet ground state distribution $\rho^F(k,t)$ is diagonal in the Floquet basis. In this section, we transfer $\rho^F(k,t)$ into the time-independent basis by determining $\tilde{\rho}^F(k)$. To find the Floquet eigenenergies, we consider the diagonal basis of the Floquet Hamiltonian $\tilde{H}_F = R(t)H_F R(t)^\dagger = \tilde{H} + B$, which can be obtained using the transformation operator U_F, where

$$\mathcal{H}_F = U_F \tilde{H}_F U_F^\dagger = \begin{pmatrix} \varepsilon_-^F(k) & 0 \\ 0 & \varepsilon_+^F(k) \end{pmatrix} \tag{C.38}$$

and $\varepsilon_\pm^F(k) = \bar{\varepsilon}_k \pm \sqrt{(\delta_k + \hbar\omega/2)^2 + (\Delta/2)^2}$ are the quasienergies. The density matrix corresponding to a fully-occupied Floquet ground state is given by

$$\begin{aligned} \tilde{\rho}^F(k) &= U_F^\dagger \begin{pmatrix} 1 - f_k^F & 0 \\ 0 & f_k^F \end{pmatrix} U \\ &= \frac{1}{2} + \frac{1 - 2f_k^F}{2\sqrt{(\delta_k + \hbar\omega/2)^2 + (\Delta/2)^2}} \left[\left(\frac{\Delta + \hbar\omega}{2} \right) \sigma_x + \delta_k \sigma_z \right]. \end{aligned} \tag{C.39}$$

where f_k^F is the occupation function of the electronic state with quasienergy $\varepsilon_-^F(k)$.

Steady State Solution

To calculate the current in the steady state, we solve for the steady state density matrix in the time-independent basis, denoted $\tilde{\rho}(k)$, which satisfies the steady state condition

$$\frac{i}{\hbar}[\tilde{\rho}(k), \tilde{H} + B] + \tilde{\mathcal{L}}\{\tilde{\rho}(k)\} = 0 \tag{C.40}$$

[see Eq. (C.33)]. It can be shown that the steady state solution is given by

$$\tilde{\rho}(k) = \frac{1}{2} I + \frac{1}{2}(\tilde{\rho}_x \sigma_x + \tilde{\rho}_y \sigma_y + \tilde{\rho}_z \sigma_z), \tag{C.41}$$

where

$$\rho_x = \frac{\eta + 4\eta\beta^2 - 4\zeta\beta^2[\alpha\gamma(x - 1/2) + 1/2]}{1 + 4\beta^2\{1 + [\gamma(x - 1/2) + \alpha^{-1}/2]\}}, \tag{C.42}$$

$$\rho_y = \frac{2\beta\{\eta[\gamma(x - 1/2) + \alpha^{-1}/2] - \zeta\}}{1 + 4\beta^2\{1 + [\gamma(x - 1/2) - \alpha^{-1}/2]\}}, \tag{C.43}$$

$$\rho_z = \frac{4\eta^2[\gamma(x - 1/2) + \alpha^{-1}/2] + \zeta\{1 + 4\beta^2[\gamma(x - 1/2) + \alpha^{-1}/2]^2\}}{1 + 4\beta^2\{1 + [\gamma(x - 1/2) + \alpha^{-1}/2]^2\}}, \tag{C.44}$$

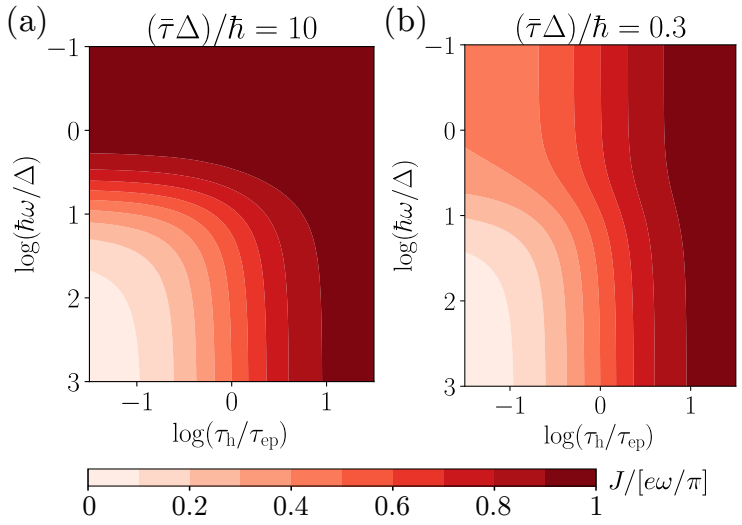

Figure C.4: Steady state current J as calculated from the Lindblad master equation [Eq. (C.33)]. (a) Steady state current in the regime $\hbar/(\bar{\tau}\Delta) \ll 1$ analyzed in the main text using the Floquet Boltzmann equation. The current is quantized when the system is driven adiabatically, i.e., $\log(\hbar\omega/\Delta) < 0$. In the non-adiabatic regime $\log(\hbar\omega/\Delta) > 0$, the current attains a quantized value in the regime where incoherent phonon relaxation dominates $\tau_{ep} \ll \tau_h$. (b) Steady state current for a weak driving potential amplitude Δ satisfying $(\bar{\tau}\Delta)/\hbar = 0.3$. In contrast to panel (a), the current deviates from quantization in the adiabatic regime $\log(\hbar\omega/\Delta) < 0$, and instead only attains a quantized value when $\tau_{ep} \ll \tau_h$.

$$\eta = \nu \frac{(1-2f_k^I)}{\sqrt{1+\gamma^{-2}(x-1/2)^{-2}}}\text{sign}(x-1/2) + \nu\chi\frac{(1-2f_k^F)[\gamma(x-1/2)+1/2]}{\sqrt{[\gamma(x-1/2)\alpha+1/2]^2+\alpha^2}}, \tag{C.45}$$

and

$$\zeta = \nu \frac{(1-2f_k^I)}{\sqrt{1+\gamma^{2}(x-1/2)^{2}}} + \nu\chi\frac{(1-2f_k^F)[\gamma(x-1/2)+1/2]}{\sqrt{[\gamma(x-1/2)+\alpha^{-1}/2]^2+1}}. \tag{C.46}$$

Here, $x = k/q$, $\alpha = \Delta/(2\hbar\omega)$, $\beta = \bar{\tau}\Delta/(2\hbar)$, $\gamma = 2[q^2/(2m)]/\Delta$, $\nu = \bar{\tau}/\tau_h$, $\chi = \tau_h/\tau_{ep}$, and $\bar{\tau} = (1/\tau_{ep} + 1/\tau_h)^{-1}$.

Using Eq. (C.28), we find that the time averaged current is given by

$$J = \int_0^q \frac{dk}{\pi}(\partial_k\delta_k)\rho_z = \frac{e\omega}{\pi}\gamma\alpha\int_0^1 dx\ \rho_z. \tag{C.47}$$

The integral in Eq. (C.47) can be calculated numerically.

Figure C.4 shows the steady state current at several representative values of $\hbar/(\bar{\tau}\Delta)$. We choose a large $\gamma = 10^4$ to ensure the approximation used in Eq. (C.27) is accurate,

and we assume that the system relaxes to zero-temperature thermal distributions in the Floquet and instantaneous bases, i.e., $f_k^I = f_k^F = 1$. In Figure C.4(a), we analyze the regime $\hbar/(\bar{\tau}\Delta) \ll 1$ considered in the main text. Consistent with the analysis of the Floquet-Boltzmann equation, the current is quantized in the non-adiabatic regime $\log(\hbar\omega/\Delta) > 0$ when incoherent phonon relaxation dominates $\tau_{\text{ep}} \ll \tau_{\text{h}}$. When the system is driven adiabatically, i.e., $\log(\hbar\omega/\Delta) < 0$, the current is quantized regardless of the strength of incoherent phonon coupling, consistent with the picture of a Thouless pump. In Figure C.4(b), we show the current for a weak driving potential Δ satisfying $(\bar{\tau}\Delta)/\hbar = 0.3$. In contrast to panel (a), the system only exhibits quantized quantized current in the adiabatic regime when incoherent phonon relaxation dominates $\tau_{\text{ep}} \ll \tau_{\text{h}}$.

In conclusion, our effective description reproduces both the quantized acousto-electric Floquet effect for non-adiabatic phonon drives and the Thouless pumping regime for adiabatic phonon drives. In the the adiabatic regime, given by $\hbar\omega \ll \Delta$ and $\hbar/\tau \ll \Delta$, the current is quantized regardless of the rate of incoherent phonon relaxation [see Figure C.4(a)]. Such a regime has been realized experimentally using GHz-frequency surface acoustic phonon waves, which have been observed to host a quantized acousto-electric current response [7, 29, 71, 82, 159, 278]. In contrast, the quantized acoustoelectric Floquet effect relies on incoherent phonon relaxation to realize quantized transport in the non-adiabatic regime where $\hbar\omega > \Delta$ or $\hbar/\tau \gtrsim \Delta$ [see Figs. C.4(a-b)].

Chapter 8

CHIRAL PLASMONS AND TOPOLOGICAL PHOTOCURRENT IN WEYL SEMIMETALS

We analyze a realizaton of Thouless' adiabatic charge pump in a Weyl semimetal (WSM) irradiated by circularly polarized light, first reported in Ref. [55]. We show the effect can lead to a strong and highly nonlinear topological photocurrent along the light propagation axis, which is insensitive to anisotropy, lattice orientation, and interactions. The effect can emerge in non-centrosymmetric WSMs where Weyl nodes of opposite chiralities are isolated and offset in energy, such as, potentially, $SrSi_2$. We estimate the current can reach 10 A/mm^2 for THz frequencies at 10^6 V/m amplitudes. We discuss the possibility of further amplification due to coinciding plasmonic resonances in the THz-low infrared regime. We also report that WSMs with broken time reversal and inversion symmetry may support two nontrivial response phenomena: namely, a helicity-independent photocurrent, and a mechanism for chiral plasmon modes, whose frequencies depend on their helicities relative to an anisotropy axis of the material. The phenomena we uncover may find uses in sensing, photovoltaics, and electronics.

8.1 Introduction

The linear dispersion and unique band topology of Weyl semimetals (WSMs) translates to exotic electronic responses [12, 14, 31, 38, 43, 58, 102, 121, 121, 150, 170–172, 197, 199, 205, 207, 218, 230, 237, 285, 310, 319, 323, 328], with promising applications in optics [9, 44, 122, 150, 156, 194, 198, 219, 283, 305, 311], magnetism [11, 66, 161, 202, 207, 208, 252, 267, 268, 276, 299, 324], and electronics [13, 30, 98, 107, 112, 168, 190, 217, 227, 228, 265, 269, 272, 288, 300, 309, 318, 321]. These effects can arise both from interband photoabsorption, such as the circular photogalvanic effect [58, 102, 121, 121, 172, 197, 218, 230, 237, 323], and from *i*ntraband dynamics, such as topological frequency conversion [205], quantum nonlinear Hall effects [264], photovoltaic chiral magnetic effects [51, 132, 277], and shift current-induced bulk photovoltaic effects [218].

Here we study the intra-band dynamics of WSMs driven by circularly-polarized light in the near-adiabatic regime, with frequency in the THz range, and less than the momentum-dependent gap [see Figure 8.1(a)]. In noncentrosymmetric WSMs,

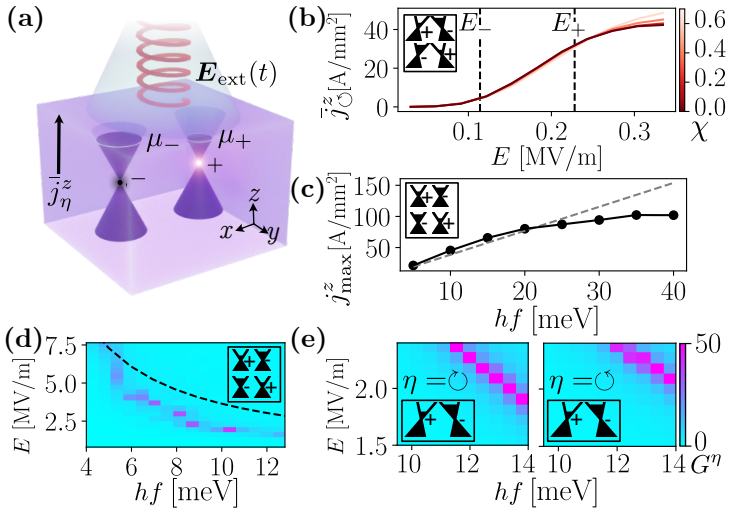

Figure 8.1: Light-induced charge pumping and chiral plasmons. (a) We consider the optical response of a noncentrosymmetric WSMs, where opposite-chirality Weyl nodes (WNs) can have distinct effective chemical potentials ($\mu_\pm$) and tilts ($\chi_\pm$). We show that circularly polarized driving in the near-adiabiatic regime can induce a topological charge pumping effect leading to a strong photocurrent $\bar{j}^z_\eta$ along the beam axis, where $\eta = \circlearrowleft, \circlearrowright$ denotes the helicity of the laser. (b) Numerically computed photocurrent, $\bar{j}^z_{\circlearrowleft}$, for $\mu_- = 15\,meV$, $\mu_+ = 30\ meV$, and $hf = 5$ meV, with $\chi_\pm = \pm\chi$. (c) Maximal $\bar{j}^z_\eta$, denoted $j^z_{\rm max}$, attained numerically (scatter points) and predicted semiclassically (dashed line) [Eq. (8.7)]. Discrepancies arise as hf is raised beyond the adiabatic limit. (d) Plasmon enhancement factor $G^\eta \equiv E/E_{\rm ext}$ vs hf and E, where $E_{\rm ext}$ (E) denotes the drive-field amplitude outside (inside) the WSM. Dashed curve indicates plasmon resonance predicted semiclassically. (e) Same as (d), but for a WSM with broken TRS and a pair of WNs with opposite chirality and tilt. Here, the chiral plasmon resonance differs for left (left panel) and right (right panel) circular polarizations.

we show these conditions induce Thouless' topological charge pumping that generates a strong topological photocurrent along the propagation of light [47, 279]. The photocurrent is insensitive to lattice orientation or anisotropy in the WSM [see Figure 8.1(b)] and can therefore arise even in systems with many domains of crystal orientation. It is pronounced in WSMs where Weyl nodes (WNs) of opposite chiralities are isolated and well-separated in energy [see Eq. (8.7)], such as, potentially, $SrSi_2$ [113]. When the WNs are tilted and time-reversal symmetry (TRS) is broken, the WSM can further support a photocurrent component independent of laser helicity. Interestingly, the THz driving coincides with the plasma resonance frequency range of WSMs [43, 322], enabling significant amplification of the photocurrents at moderate driving intensities [Figure 8.1(c)]. As a second result, when TRS is bro-

ken, we show the plasmon frequency becomes *c*hiral, dependent on the alignment of the laser chirality with the anisotropy axis.

8.2 System

Let us start with the photoresponse of electrons near a single Weyl node (WN). Focusing on the conduction and valence band, the Hamiltonian near a WN reads $H(\boldsymbol{k}) = \xi\hbar v_F \boldsymbol{k}\cdot\boldsymbol{\sigma} + \hbar\boldsymbol{V}\cdot\boldsymbol{k}$ [12]. Here, $\boldsymbol{\sigma} = (\sigma_x, \sigma_y, \sigma_z)$ denotes the vector of Pauli matrices acting in the orbital basis, and the crystal momentum $\boldsymbol{k} = (k_x, k_y, k_z)$ is measured from the WN located at $\boldsymbol{k} = 0$. The Fermi velocity v_F controls the gap size of the energy dispersion away from the WN, while $\boldsymbol{V}$ parameterizes a tilt in the WN dispersion. Finally, $\xi = +, -$ defines the *chirality* of the WN. Below, $\varepsilon_{\boldsymbol{k}\nu}$ and $|\psi_{\boldsymbol{k}\nu}\rangle$ respectively denote the single-particle energies and eigenstates of $H(\boldsymbol{k})$, where $\nu = 0$ ($\nu = 1$) indicate the conduction (valence) band. The WN provides a point source of the Berry curvature of the bands, defined as $\backslash\Omega_\nu(\boldsymbol{k}) \equiv (2\pi)^{-1}\nabla_{\boldsymbol{k}} \times \langle\psi_{\boldsymbol{k}\nu}|i\nabla_{\boldsymbol{k}}|\psi_{\boldsymbol{k}\nu}\rangle$, where $\nabla_{\boldsymbol{k}}$ indicates the gradient with respect to $\boldsymbol{k}$. Specifically, $\nabla\cdot\backslash\Omega_\nu(\boldsymbol{k}) = 2\pi\xi(-1)^\nu\delta(\boldsymbol{k})$, where $\delta(\boldsymbol{k})$ denotes the Dirac delta function. Nonzero Berry-curvature divergence is the hallmark of WSMs.

The system is illuminated by coherent circularly-polarized light traveling along the z-direction with frequency f and polarization η, which can take value $\circlearrowleft$ or $\circlearrowright$, corresponding to left or right polarization, respectively. The time-dependent vector potential inside the material is then $\boldsymbol{A}(t) = A(\cos(2\pi f t), c_\eta \sin(2\pi f t), 0)$, where $c_{\circlearrowleft} = +1$ and $c_{\circlearrowright} = -1$, with the corresponding internal electric field given by $\boldsymbol{E}(t) = \partial_t \boldsymbol{A}(t)$. The electrons couple to the light via $\boldsymbol{k} \to \boldsymbol{k} + e\boldsymbol{A}(t)/\hbar$, where e is the electron charge, resulting in the time-periodic Hamiltonian $H(\boldsymbol{k}, t) = H(\boldsymbol{k}+e\boldsymbol{A}(t)/\hbar)$. We are interested in the *p*hotocurrent density in the system, denoted $\boldsymbol{j}_\eta(t)$, and its time-averaged value $\bar{\boldsymbol{j}}_\eta \equiv \lim_{t\to\infty}\frac{1}{t}\int_0^t dt'\,\boldsymbol{j}_\eta(t')$ in the adiabatic regime given by $hf \ll v_F eA/\hbar$. This expression is derived from the adiabatic conditions $\hbar||\partial_t\hat{H}(\boldsymbol{k}, t)|| \ll \delta\varepsilon^2(\boldsymbol{k}, t)$ and $\hbar\omega \ll \delta\varepsilon^2(\boldsymbol{k}, t)$, where $||\cdot||$ denotes the operator spectral norm and $\delta\varepsilon(\boldsymbol{k}, t) \equiv \varepsilon_1(\boldsymbol{k}, t) - \varepsilon_0(\boldsymbol{k}, t)$ denotes the spectral gap.

8.3 Origin of Topological Response

To elucidate the photoresponse of an isolated WN in the adiabatic regime [55], we concentrate on the subset of electron modes with xy-plane momentum $\boldsymbol{k}_\perp = (k_x, k_y)$, represented by the vertical yellow line in Figure 8.2(a). These modes can be viewed as a 1D Fermionic chain aligned in the z-direction, whose Bloch Hamiltonian $H(\boldsymbol{k}, t)$ is controlled by $\boldsymbol{k}_\perp$. For now, we fix $\mu = 0$, and assume that the bands of this chain

are fully gapped over a full driving cycle, such that they do not intersect the WN. The light's vector potential drives the Fermionic chain along a closed loop, indicated by the yellow arrow in Figure 8.2(a). This adiabatic trajectory produces a Thouless charge pump [201], which transports one electron per cycle in the z-direction: $\mathcal{I}_\eta^z(\boldsymbol{k}_\perp) = -c_\eta \xi C_{\boldsymbol{k}_\perp} e f$. Here $C_{\boldsymbol{k}_\perp} \equiv (2\pi)^{-1} \int_{\mathcal{S}} d\boldsymbol{S} \cdot \boldsymbol{\Omega}_0(\boldsymbol{k})$, where $\int_{\mathcal{S}} d\boldsymbol{S}$ denotes the oriented surface integral on the closed cylinder $\mathcal{S}$ defined by $\boldsymbol{k}'(t) \equiv \boldsymbol{k} + e\boldsymbol{A}(t)/\hbar$ for $t \in [0, T]$ and $\boldsymbol{k}_\perp$ fixed [see Figure 8.2(a)]. Stoke's theorem implies that $C_{\boldsymbol{k}_\perp}$ is given by the net charge of WNs inside $\mathcal{S}$, leading to $C_{\boldsymbol{k}_\perp} = \xi\theta(|eA/\hbar| - |\boldsymbol{k}_\perp|)$, with θ the step function. We verify this quantization in simulations, see Figure 8.2(b). Summing all cylindrical trajectories that enclose the WN, the average current density is the quantized current $-ef$ times the reciprocal space area formed by the disk of radius $eA/\hbar$. This results in $\bar{j}_\eta^z = c_\eta \xi j_{top}$, where

$$j_{top} = -\frac{ef}{4\pi}\left(\frac{eA}{\hbar}\right)^2. \tag{8.1}$$

This topological photoresponse is unique to WSMs.

8.4 Nonzero Filling

Realistically, we must consider a nonzero chemical potential. To this end, we consider the reduced density operator of the electronic many-body state, $\hat{\rho}(\boldsymbol{k}, t)$, obtained by tracing over all electronic modes with crystal momenta distinct from $\boldsymbol{k}$. This operator acts on a 4-dimensional Fock space of the 2 Bloch space orbitals $s = \downarrow, \uparrow$, spanned by the states $|n_\uparrow, n_\downarrow\rangle$ where $n_s = 0, 1$ gives the occupation number in Bloch state $|s\rangle$. The photocurrent is found from $\hat{\rho}(\boldsymbol{k}, t)$ via

$$\boldsymbol{j}_\eta(t) = e \int \frac{d^3\boldsymbol{k}}{(2\pi)^3} \mathrm{Tr}[\hat{\rho}(\boldsymbol{k}, t)\hbar^{-1}\nabla_k \hat{H}(\boldsymbol{k}, t)], \tag{8.2}$$

where $\hat{H}(\boldsymbol{k}, t) = (\hat{c}_\uparrow^\dagger, \hat{c}_\downarrow^\dagger) H(\boldsymbol{k}, t) (\hat{c}_\uparrow, \hat{c}_\downarrow)^T$ denotes the Hamiltonian acting on the Fock space, with $\hat{c}_s^\dagger$ creating a fermion in the orbital s. In addition to the coherent evolution generated by $\hat{H}(\boldsymbol{k}, t)$, $\hat{\rho}(\boldsymbol{k}, t)$ is affected by incoherent processes such as electron-electron and electron-phonon collisions. We model these phenomenologically, through the master equation

$$\partial_t \hat{\rho}(\boldsymbol{k}, t) = \frac{i}{\hbar}[\hat{\rho}(\boldsymbol{k}, t), \hat{H}(\boldsymbol{k}, t)] - \frac{1}{\tau}[\hat{\rho}(\boldsymbol{k}, t) - \hat{\rho}^{\mathrm{eq}}(\boldsymbol{k}, t)]. \tag{8.3}$$

Here, we assume that electrons relax to a thermal state in the instantaneous eigenbasis of $\hat{H}(\boldsymbol{k}, t)$ (this is physically justified when the correlation time of the environment

is fast relative to the driving frequency [203]),

$$\hat{\rho}^{\mathrm{eq}}(\boldsymbol{k},t) = e^{-[\hat{H}(\boldsymbol{k},t)-\mu\sum_s \hat{c}_s^\dagger \hat{c}_s]/k_BT}/\mathcal{N} \tag{8.4}$$

where $\mathcal{N} = \mathrm{Tr}[e^{-[\hat{H}(\boldsymbol{k},t)-\mu\sum_s \hat{c}_s^\dagger \hat{c}_s]/k_BT}]$, μ is the chemical potential, and T the lattice temperature. We assume a uniform phenomenonlogical relaxation time τ. The explicit dissipator form is not essential, and chosen for simplicity.

In the adiabatic regime, $hf \ll v_F eA/\hbar$ [1], $\boldsymbol{j}_\eta(t)$ can be approximated semiclassically [205] via $\mathrm{Tr}[\hat{\rho}(\boldsymbol{k},t)\hbar^{-1}\nabla_{\boldsymbol{k}}\hat{H}(\boldsymbol{k},t)] \approx \sum_\nu g_\nu(\boldsymbol{k},t)\boldsymbol{v}_\nu(\boldsymbol{k},t)$, where

$$\boldsymbol{v}_\nu(\boldsymbol{k},t) \equiv \frac{\nabla_{\boldsymbol{k}}}{\hbar}\varepsilon_{\boldsymbol{k}\nu}(t) + e\boldsymbol{\Omega}_\nu\left(\boldsymbol{k}+\frac{e}{\hbar}\boldsymbol{A}(t)\right)\times\frac{\boldsymbol{E}(t)}{\hbar}, \tag{8.5}$$

$g_\nu(\boldsymbol{k},t) = \mathrm{Tr}[\hat{\rho}(\boldsymbol{k},t)\hat{\psi}^\dagger_{\boldsymbol{k}\nu}(t)\hat{\psi}_{\boldsymbol{k}\nu}(t)]$ denotes the instantaneous occupation of band ν, and $\hat{\psi}^\dagger_{\boldsymbol{k}\nu}(t) = \sum_s \langle s|\psi_{[\boldsymbol{k}+e\boldsymbol{A}(t)/\hbar]\nu}\rangle c_s^\dagger$ creates an electron in the instantaneous eigenstate in band ν. The first and second term in Eq. (8.5) are the group velocity and the anomalous velocity generated by the Berry curvature $\boldsymbol{\Omega}_\nu$, respectively. Near the WN, $\boldsymbol{\Omega}_\nu(\boldsymbol{k}) = \xi(-1)^\nu\boldsymbol{k}/2|\boldsymbol{k}|^3$.

For a circularly polarized field $\boldsymbol{E}(t)$, the z-component of the anomalous velocity is oriented in the same direction inside a radius $eA/\hbar$ from the origin (i.e., where $C_{\boldsymbol{k}_\perp} \neq 0$). This generates a topological photocurrent which is always normal to the electric field plane.

8.5 Photoresponse of a Single WN

Let us now consider the photoresponse of a WN with finite μ. We focus on the experimentally-relevant regime of slow relaxation $\tau f \gg 1$, realized for THz or above in typical WSMs, where $\tau \sim 1-100$ ps [38, 320]. In this limit and at $k_BT \ll \mu$, the photocurrent in Eq. (8.2) can be approximated by

$$\bar{j}^z_\eta \approx c_\eta \xi j_{top}\left(1-\gamma(\mu)\left[\frac{|\mu|}{v_F eA}\right]^{\varphi(\mu)}\right) + \chi\frac{e\mu(eA/\hbar)^2}{12\pi^2\hbar}, \tag{8.6}$$

[see Supplementary Material (SM) for details], where we assumed anisotropy along the z-axis, $\boldsymbol{V}_i = (0,0,\pm v_F\chi)$, with χ parameterizing the tilt of the WN. The tilt gives rise to the second term in Eq. (8.6), which describes a helicity-independent photocurrent originating from the group velocity term in Eq. (8.5). The first term

[1] This expression is derived from the adiabatic conditions $\hbar||\partial_t\hat{H}(\boldsymbol{k},t)|| \ll \delta\varepsilon^2(\boldsymbol{k},t)$ and $\hbar\omega \ll \delta\varepsilon^2(\boldsymbol{k},t)$, where $||\cdot||$ denotes the operator spectral norm and $\delta\varepsilon(\boldsymbol{k},t) \equiv \varepsilon_1(\boldsymbol{k},t) - \varepsilon_0(\boldsymbol{k},t)$ denotes the spectral gap.

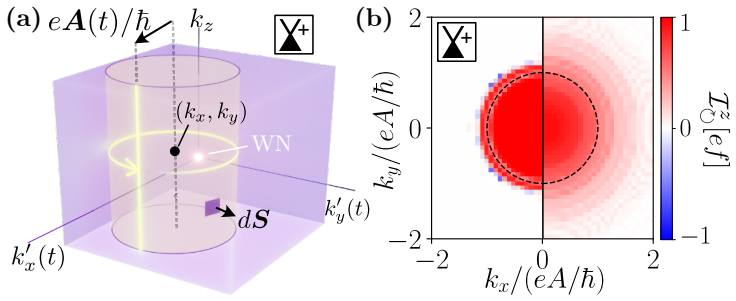

Figure 8.2: Topological photocurrent as quantized charge pumping. (a) Brillouin zone region (purple) surrounding a single WN (bright yellow) at $\mu = 0$. Under illumination by circularly polarized light, all electronic states with a given k_x and k_y (yellow vertical line) traces out a cylinder (pink) in momentum space during a period of the drive. This generates a quantized charge transfer per cycle along the z direction, given by $-e$ times the total flux of Berry curvature through the surface of the cylinder (differential area element indicated by dark purple). When the cylinder encloses the WN, this integral is nonzero and given by ± 1. (b) Total time-averaged current $\mathcal{I}^z_{\circlearrowleft}(\boldsymbol{k}_\perp)$ in the system generated by electrons with a fixed in-plane momentum $\boldsymbol{k}_\perp = (k_x, k_y)$. Left and right panels depict $v_F eA/\hbar \approx 5hf$ and $v_F eA/\hbar \approx 0.2hf$, respectively, corresponding to adiabatic and nonadiabatic driving. The dashed curve indicates the trajectory of the WN.

is the topological photocurrent originating from the anomalous velocity term in Eq. (8.5), and generates the charge pumping effect described above. This term is insensitive to the tilt, but controlled by the drive helicity.

The topological current is set by $\gamma(\mu)$ and $\varphi(\mu)$, which cross over from $\gamma \approx 0.4$ and $\varphi = 3$ for $|\mu| \ll eAv_{\mathrm{F}}$ to $\gamma \approx 0.2$ and $\varphi = 2$ for $eAv_F < |\mu| < 2eAv_F$. The topological current scales with the number of carriers ($\propto \mu^3$) near the WN in the light-doping regime $|\mu|/(\hbar v_F) \ll eA/\hbar$, and with the area of charge-pumping fermionic chains intersecting the Fermi sea ($\propto \mu^2$) at higher μ. It decreases monotonically with $|\mu|$, and plateaus in the regime $|\mu|/(\hbar v_F) \gg 2eA/\hbar$, at a value given by $Bc_\eta \xi j_{top}$, where B depends on the Fermi volume geometry. The residual topological current in this regime originates from the finite height of the cylinder $\mathcal{S}$ depicted in Figure 8.2(a), which terminates at the Fermi surface. The Berry flux through the top and bottom ends of $\mathcal{S}$ leads to a reduction of $\mathcal{I}^z_\eta(\boldsymbol{k}_\perp)$ from the quantized value $c_\eta \xi ef$ derived above Eq. (8.1). A semiclassical analysis (see SM) yields $B = 1/3$ for spherical Fermi volumes in the $|\mu|/(\hbar v_F) \gg 2eA/\hbar$ limit. When the Fermi volume extends beyond the periodic Brillouin zone boundaries, $\mathcal{S}$ is no longer closed in the k_z-direction, resulting in $B = 0$.

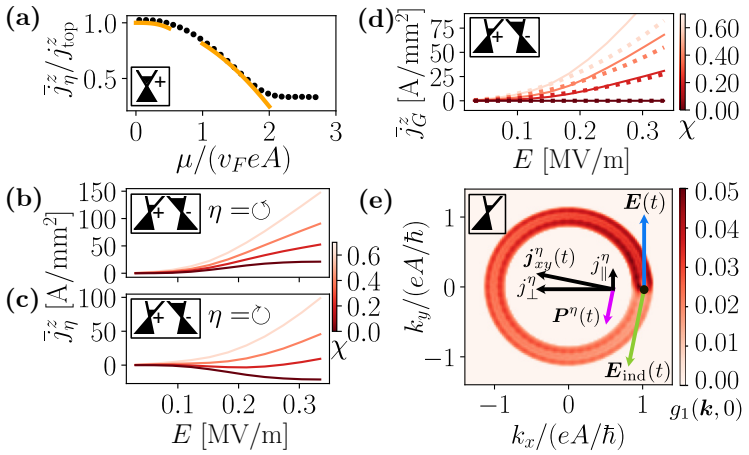

Figure 8.3: Photoresponse from doped and tilted WNs, with parameters $E = 1.5$ MV/m, $hf = 5$ meV and $\tau = 5$ ps, corresponding to $\tau f \approx 6$. (a) Photocurrent $\bar{j}^z_\eta$ vs. μ for an isolated, untilted WN. The orange curve indicates semiclassical prediction [see discussion below Eq. (8.6)]. (b)-(c) Photocurrent $\bar{j}^z_\eta$ from a pair of opposite-chirality WNs with opposite tilts, $\chi \equiv \chi_+ = -\chi_-$ under left (b) and right (c) laser polarization. In the limit $\chi \to 0$, the photoresponse is dominated by the chirality-dependent component generated by the anomalous velocity. (d) Chirality-independent component $\bar{j}^z_G = (\bar{j}^z_{\circlearrowleft} + \bar{j}^z_{\circlearrowright})/2$ of $\bar{j}^z_\eta$. Dashed line indicates prediction from semiclassical analysis [Eq. (8.6)]. (e) Steady state occupation function $g_1(\boldsymbol{k}, 0)$ at time $t = 0$ in the $\nu = 1$ band, for the same parameters as panel (a). Black dot indicates the position of the WN, and vectors indicate the oscillating current components generated parallel $j_\parallel$ and perpendicular $j_\perp$ to the internal electric field $\boldsymbol{E}(t)$ and the resulting polarization $\boldsymbol{P}^\eta(t)$, along with induced field $\boldsymbol{E}_{\rm ind}(t)$.

8.6 Symmetry Constraints

The total photocurrent $\bar{j}^z_\eta$ of a WSM is obtained by adding contributions from all WNs, whose chemical potentials, tilts, and chiralities are related by the symmetries of the system. WSMs must break either TRS, inversion symmetry (IS), or both.

Noncentrosymmetric WSMs with TRS are characterized by chemical potential imbalance between nodes of opposite chiralities ξ, allowing for a nonzero net topological photocurrent. TRS relates each node to another at opposite crystal momentum with identical chirality and opposite tilt [see Figure 8.1(a)], implying a minimum of four WNs, two $\xi = +1$ nodes with chemical potential μ_+ and two $\xi = -1$ nodes with chemical potential μ_- [208]. TRS also implies that each pair of equal-chirality WNs have opposite tilt, resulting in no net helicity-independent photocurrent [see Eq. (8.6)]. Without loss of generality, we let $\mu_- \leq \mu_+$. The photocurrent $\bar{j}^z_\eta$ sharply changes as the electric field amplitude E approaches two critical values set by the chemical potentials, $E_\pm \equiv hf\mu_\pm/(2\hbar v_F e)$ [Figure 8.1(b)]. While for

$E < E_-$ none of the WNs exhibit photocurrents [see discussion below Eq. (8.6)], for $E_- < E < E_+$, the $\xi = -$ WNs contribute a nonzero topological current and the $\xi = +$ WNs remain inactive. Finally, for $E > E_+$ both $\xi = +, -$ WNs contribute. The sharp changes of $\bar{j}^z_\eta$ imply a highly nonlinear nature of the topological photocurrent, and can not be captured perturbing about $E = 0$ [205]. Eq. (8.6) implies that $\bar{j}^z_\eta$ attains its maximum when $E > E_+, E_-$,

$$j^z_{\max} \approx 0.016 ef[(\mu_+)^2 - (\mu_-)^2]/(\hbar v_F)^2. \tag{8.7}$$

Hence the topological photocurrent is most pronounced when μ_+ differs significantly from μ_-, such as, potentially, in $SrSi_2$ [113].

If inversion *a*nd TRS are broken, the WSM hosts a minimum of two WNs with opposite ξ and different chemical potentials, but generically different tilts. The lack of symmetry constraints on the tilts enables a photocurrent with both helicity-dependent and independent components. Finally, WSMs with broken TRS but preserved inversion symmetry do not support a photocurrent.

8.7 Numerical Verification

To numerically verify our results, we first use Eq. (D.1) to compute $\bar{j}^z_\eta$ from an isolated WN with no tilt, using parameters $v_F = 5 \times 10^5$ m/s, $\tau = 5$ ps, $T = 20$ K, $hf = 5$ meV, and $E = 5 \times 10^5$ V/m, reflecting experimentally achievable conditions [38]. Note that our simulation is agnostic to the estimates in Eqs. (8.5)-(8.6). Figure 8.2(b) shows the in-plane momentum-resolved photocurrent, $\mathcal{I}^z_{\circlearrowleft}(\boldsymbol{k}_\perp)$ for $\mu = 0$. For adiabatic driving (left panel), $eA/\hbar \approx 5hf$, we see a clear quantized plateau with $\mathcal{I}^z_{\circlearrowleft}(\boldsymbol{k}_\perp) \approx ef$, of disk shape and radius $eA/\hbar$, as the semiclassical analysis above Eq. (8.1) predicts. Illustrating the role of adiabaticity, the right half of Figure 8.2(b) depicts the same data for non-adiabatic driving, $eA \approx 0.2hf$. Here, non-adiabatic heating reduces the photocurrent of electronic states with momentum close to the trajectory (black dashed curve) of the WN [205]. Figure 8.3(a) plots $\bar{j}^z_\eta$ vs. μ. The dashed line is the analytical result, Eq. (8.6). For $\mu/(v_F eA) \gg 2$, the current plateaus near $\bar{j}^z_\eta = j^z_{\text{top}}/3$, as semiclassically predicted.

To calculate $\bar{j}^z_\eta$ in a noncentrosymmetric WSM with TRS, we take $\mu_- = 15$ meV and $\mu_+ = 30$ meV. Time-reversal conjugate nodes have opposite tilt, and, for simplicity, we assume that non-conjugate pairs of opposite-chirality WNs have opposite tilts, $\pm\chi$. Figure 8.1(b) plots $\bar{j}^z_{\circlearrowleft}$ for various values of χ. As we expect, $\bar{j}^z_{\circlearrowleft}$ exhibits sharp changes at the predicted field amplitudes $E_\pm$ [defined above Eq. (8.7)], and is moreover insensitive to χ. Figure 8.1(c), shows j^z_{max} calculated numerically and

as predicted by Eq. (8.7). We expect the discrepancy for $hf \gtrsim eA/\hbar$ are due to non-adiabatic effects.

Lastly, Figure 8.3(b)-(c) compares $\bar{j}^z_{\circlearrowleft}$ and $\bar{j}^z_{\circlearrowright}$ for a WSM with broken TRS. When $\chi \to 0$, $\bar{j}^z_\eta$ exhibits a sign flip upon reversing the laser helicity η, as expected. The sign flip does not persist for finite tilts $\chi > 0$, where the helicity-independent photocurrent emerges. Figure 8.3(d) shows that the helicity-independent component $\bar{j}^z_G = (\bar{j}^z_{\circlearrowleft} + \bar{j}^z_{\circlearrowright})/2$ scales quadratically with the field amplitude in agreement with Eq. (8.6) (dashed lines) for $\chi \ll 1$.

8.8 Plasmon Enhancement

We now discuss how the plasmonic response of WSMs may enhance the topological photocurrent. We assume that the size of the WSM sample is smaller than the skin depth, estimated to be 0.1-1 μm for THz frequencies [183]. The light-induced plasma oscillations of the WSMs induce a surface charge oscillation on the sample. This in turn induces an electric field $\boldsymbol{E}_{\rm ind}(t)$ that modifies the internal electric field $\boldsymbol{E}(t)$ relative to the external field provided by the light outside the WSM, $\boldsymbol{E}_{\rm ext}(t)$, via $\boldsymbol{E}(t) = \boldsymbol{E}_{\rm ind}(t) + \boldsymbol{E}_{\rm ext}(t)$. The modification can induce either damping or amplification, depending on whether the gain ratio $G_\eta \equiv |\boldsymbol{E}(t)|/|\boldsymbol{E}_{\rm ext}(t)|$ is smaller or larger than 1. The induced field $\boldsymbol{E}_{\rm ind}(t)$ is appreciable in 3D geometries, but may be negligble in quasi-2D settings such as thin films.

To estimate $\boldsymbol{E}_{\rm ind}(t)$ in a 3D configuration, we consider a spherical geometry. The drive-induced in-plane current, $\boldsymbol{j}^\eta(t)$, creates surface charge corresponding to a uniform internal polarization density $\boldsymbol{P}^\eta(t)$ such that $\partial_t \boldsymbol{P}^\eta(t) = \boldsymbol{j}^\eta(t)$. With spherical geometry, $\boldsymbol{E}_{\rm ind}(t) = \boldsymbol{P}^\eta(t)/(3\epsilon_0)$. Writing $\boldsymbol{j}^\eta(t) = j^\eta_z(t)\hat{z} + j^\eta_P \hat{\boldsymbol{e}}(t) + j^\eta_N \hat{z} \times \hat{\boldsymbol{e}}(t)$, where $\hat{\boldsymbol{e}}(t) \equiv \boldsymbol{E}(t)/E$ and $E = |\boldsymbol{E}(t)|$, we find

$$G^\eta = E\{[E + c_\eta j^\eta_N/(6\pi\epsilon_0 f)]^2 + [j^\eta_P/(6\pi\epsilon_0 f)]^2\}^{-1/2}. \tag{8.8}$$

In noncentrosymmetric WSMs with TRS, the instantaneous population distribution for $\tau f \gg 1$ [see color plot in Figure 8.3(e)] is anisotropic about the WN, yielding $j^\eta_P \approx 0$, and $j^\eta_N \approx c_\eta e v_F \sum_{\xi=\pm}[\mu_\xi/(\hbar v_F)]^3/(3\pi^3)$ in the limit $\mu_\xi \ll \hbar v_F eA/\hbar$. This result is derived from Eq. (8.5) [see SM], and implies a plasma resonance (divergent G^η) which takes the internal field amplitude inside system towards the critical value

$$E_p(f) \approx e v_F[(\mu_+)^3 + (\mu_-)^3]/[(\hbar v_F)^3(18\pi^4\epsilon_0 f)]. \tag{8.9}$$

The existence of a characteristic internal field amplitude is a consequence of the linear dispersion of the WSM, which gives rise to an inherently nonlinear response.

Figure 8.1(d) plots the numerically obtained value of G^{η}, along with $E_p(f)$ as predicted above.

8.9 Chiral Plasmons in WSMs with broken TRS

When TRS is broken, noncentrosymmetric WSMs support a chiral plasmonic resonance, where plasma modes with opposite helicities have different frequencies. To illustrate this, we again consider the minimal example of a pair of WNs of opposite chirality, with unequal chemical potentials $\mu_{\pm}$ and tilts $\chi_{\pm}$. The tilt reshapes the Fermi surface in the $\nu = 1$ band of each WN, creating an imbalance of electronic carriers with positive and negative k_z. In this regime, an additional, in-plane topological current emerges, given by $\delta \boldsymbol{j}_N^{\eta}(t) \approx -\sum_{\xi=\pm} \xi \chi_{\xi} e f (\mu_{\xi}/\hbar v_F)^2 \hat{z} \times \hat{\boldsymbol{e}}(t)/(4\pi^2)$ in the slow relaxation limit $\tau f \gg 1$. The topological current arises from the in-plane, oscillating component of the anomalous velocity $e\boldsymbol{\Omega}_{\nu} \times \boldsymbol{E}(t)/\hbar$ which is nonzero after integration over k_z for a tilted WN. The resonant electric field amplitude is modified as a result, and, in the limit $\chi_{\pm} \ll 1$, is now given by

$$E_p(f) \approx \frac{1}{6\pi\epsilon_0 f} \sum_{\{\xi\}} \left[\frac{e v_F}{3\pi^3} \frac{\mu_{\xi}^3}{(\hbar v_F)^3} - \xi c_{\eta} \chi_{\xi} \frac{\mu_{\xi}^2}{(\hbar v_F)^2} \frac{e f}{4\pi^2} \right]. \tag{8.10}$$

This chirality-dependent plasma resonance is verified numerically in Figure 8.1(e) for the case where the WNs of positive and negative chirality exhibit opposite tilts, $\chi_{\pm} = \pm\chi$. Notably, the plasma resonance amplitudes and frequencies depend on the helicity of the laser drive.

8.10 Conclusions

Here we analyzed the generation of robust topological photocurrent induced by circularly polarized light in noncentrosymmetric WSMs, first reported in Ref. [55]. We showed that the effect is insensitive to anisotropy and electronic interactions. The effect may be observed in noncentrosymmetric WSMs where nodes of opposite chiralities are well-separated in energy, such as, possibly, $SrSi_2$ [113]. When time-reversal symmetry is broken and the WNs are tilted, the transport further exhibits a giant helicity-independent photocurrent and a helicity-dependent plasmon resonance. These exotic topological electronic and plasmonic responses constitute a new class of highly nonlinear photoresponses in Weyl semimetals with low symmetry constraints.

Multiple works have investigated the light-induced current responses of WSMs [38, 58, 102, 117, 118, 121, 121, 147, 172, 197, 218, 230, 237, 264, 323]. The pho-

tocurrent we analyze here (first reported in Ref. [55]) is different from these works, since it is of intra-band origin and of strongly nonlinear nature, beyond the paradigm of conventional nonlinear response theory [55, 205]. The topological photocurrent moreover does not require any explicit band structure anisotropy, and can be orders of magnitude stronger than in Refs. [117, 118].

8.11 Acknowledgments

We thank Ivar Martin, Cyprian Lewandowski, Elio König, Tobias Hölder, Takahiro Morimoto, Alexander Tyner, and Hiro Ishizuka for insightful discussions. C.Y. gratefully acknowledges support from the DOE NNSA Stewardship Science Graduate Fellowship program, which is provided under cooperative agreement number DE-NA0003960. G.R. is grateful for support from the Simons Foundation and the Institute of Quantum Information and Matter, as well as support from the NSF DMR grant number 1839271. This work is supported by ARO MURI Grant No. W911NF-16-1-0361, and was performed in part at Aspen Center for Physics, which is supported by National Science Foundation grant PHY-1607611. F.N. was supported by the U.S. Department of Energy, Office of Science, Basic Energy Sciences under award DE-SC0019166, the Simons Foundation under award 623768, and the Carlsberg Foundation, grant CF22-0727.

Appendix D

APPENDIX

Here we provide the semiclassical calculation of the photocurrent $\boldsymbol{j}(t)$ quoted in the main text. Before we proceed to the technical details of the derivation, which are provided in the following sections, we begin by outlining the structure of the calculation.

Our calculation of $\boldsymbol{j}(t)$ is based on solving the Lindblad master equation in Eq. (D.1) of the main text,

$$\partial_t \hat{\rho}(\boldsymbol{k},t) = \frac{i}{\hbar}[\hat{\rho}(\boldsymbol{k},t), \hat{H}(\boldsymbol{k},t)] - \frac{1}{\tau}[\hat{\rho}(\boldsymbol{k},t) - \hat{\rho}^{\mathrm{eq}}(\boldsymbol{k},t)], \tag{D.1}$$

with $\hat{H}(\boldsymbol{k},t)$, $\hat{\rho}(\boldsymbol{k},t)$, and $\hat{\rho}_{eq}(\boldsymbol{k},t)$ denoting the second-quantized Bloch Hamiltonian, density matrix and equilibrium density matrix, respectively, while τ is the phenomenological relaxation time of the system (see main text for more details). The photocurrent is obtained from the steady-state solution to Eq. (D.1), $\hat{\rho}_{\mathrm{s}}(\boldsymbol{k},t)$ via $\boldsymbol{j}(t) = \frac{1}{(2\pi)^3}\int d^3\boldsymbol{k}\mathrm{Tr}[\hat{\rho}_{\mathrm{s}}(\boldsymbol{k},t)\hbar^{-1}\nabla_{\boldsymbol{k}}\hat{H}(\boldsymbol{k},t)]$. In the quasi-adiabatic limit we consider, this integral can be approximated by [205]

$$\boldsymbol{j}(t) \approx \sum_{\nu} g_{\nu}(\boldsymbol{k},t)\boldsymbol{v}_{\nu}(\boldsymbol{k},t). \tag{D.2}$$

Here $g_{\nu}(\boldsymbol{k},t) = \mathrm{Tr}[\hat{\rho}_{\mathrm{s}}(\boldsymbol{k},t)\hat{\psi}^{\dagger}_{\boldsymbol{k}\nu}(t)\hat{\psi}_{\boldsymbol{k}\nu}(t)]$ denotes the steady-state occupation of the instantaneous electronic bands, with $\hat{\psi}_{\boldsymbol{k}\nu}(t)$ denoting the creation operator of an electron with crystal momentum $\boldsymbol{k}$ in the instantaneous eigenstate in band ν [see full definition below Eq. (8.5) in the main text]. Moreover,

$$\boldsymbol{v}_{\nu}(\boldsymbol{k},t) \equiv \frac{\nabla_{\boldsymbol{k}}}{\hbar}\varepsilon_{\boldsymbol{k}\nu}(t) + e\boldsymbol{\Omega}_{\nu}\left(\boldsymbol{k} + \frac{e}{\hbar}\boldsymbol{A}(t)\right) \times \frac{\boldsymbol{E}(t)}{\hbar} \tag{D.3}$$

denotes the phase velocity of the electrons in band ν. Here, $\boldsymbol{\Omega}_{\nu}(\boldsymbol{k} + e\boldsymbol{A}(t)/\hbar)$ and $\varepsilon_{\boldsymbol{k}\nu}(t)$ are respectively the Berry curvature and eigenenergies of the bands of the Bloch Hamiltonian $H(\boldsymbol{k},t)$, $\boldsymbol{A}(t)$ is the drive-induced magnetic vector potential, and $\boldsymbol{E}(t) = \partial_t \boldsymbol{A}(t)$ the corresponding electric field. We provide more details on the quantities above in the main text.

The remainder of this supplement is devoted to calculating the photocurrent $\boldsymbol{j}(t)$ using the results above. The calculation is structured as follows: in Section D.1,

we derive approximate steady state solutions for $g_\nu(\boldsymbol{k}, t)$. In Section D.2, we use this solution along with Eqs. (D.2)-(D.3) to compute $\boldsymbol{j}(t)$ for an isolated Weyl node with no tilt, focusing on the out-of-plane (Section D.2) and in-plane (Section D.2) components separately. In Section D.3, we extend the calculation to the case of a finite Weyl node tilt to demonstrate the emergence of the helicity-independent photocurrent and chiral plasmons.

D.1 Steady State Electronic Distribution

We first derive an approximate analytic expression for the steady state occupation function of the electronic bands, $g_\nu(\boldsymbol{k}, t)$. By explicitly solving the master equation [see Eq. (D.1)] [205], we obtain the solution

$$g_\nu(\boldsymbol{k}, t) = \frac{1}{\tau} \int_{-\infty}^{t} ds\, e^{-(t-s)/\tau} f_\nu^{\mathrm{eq}}(\boldsymbol{k}, s), \tag{D.4}$$

where $f_\nu^{\mathrm{eq}}(\boldsymbol{k}, t)$ defines the electronic occupation function of band ν in thermal equilibrium, and is given by

$$f_\nu^{\mathrm{eq}}(\boldsymbol{k}, t) = \frac{1}{e^{[\varepsilon_{\boldsymbol{k}\nu}(t)-\mu]/k_B T} + 1}, \tag{D.5}$$

where μ is the chemical potential, k_B is the Boltzmann constant, and T is the lattice temperature. As discussed in the main text, we focus on the slow-relaxation limit $\tau f \gg 1$, which is realized for picosecond-scale relaxation times and terahertz or higher frequency drives [38, 320]. In this limit, using Eq. (D.4) and exploiting the time-periodicity of $f_\nu^{\mathrm{eq}}(\boldsymbol{k}, t)$, we find that

$$g_\nu(\boldsymbol{k}, t) \approx \frac{1}{T_{\mathrm{dr}}} \int_0^{T_{\mathrm{dr}}} du\, f_\nu^{\mathrm{eq}}(\boldsymbol{k}, u), \tag{D.6}$$

where $T_{\mathrm{dr}} = 1/f$ is the period of the drive. Thus, the steady-state distribution $g_\nu(\boldsymbol{k}, t)$ approaches a distribution obtained from "smearing" the equilibrium distribution $f_\nu(\boldsymbol{k}, t)$ along the circular trajectory $\boldsymbol{k} + e\boldsymbol{A}(t)/\hbar$ defined by the drive-induced vector potential.

D.2 Photoresponse of an Isolated, Untilted Weyl Node

Here, we use the results above to compute $\boldsymbol{j}_\eta(t)$ for an isolated, untilted Weyl node driven by circularly polarized light in the slow relaxation limit $\tau f \gg 1$. The Hamiltonian we consider is given by

$$H(\boldsymbol{k}) = \xi \hbar v_F \boldsymbol{k} \cdot \boldsymbol{\sigma}, \tag{D.7}$$

where v_F is the Fermi velocity. We first consider the photocurrent component in the z-direction (Section D.2), and finally in the x-y plane (Section D.2).

Photocurrent along the z-axis

We compute the photocurrent in the z-direction by analyzing the contribution from each electronic band separately. To this end, we define $\bar{j}^z_\eta = \sum_\nu \bar{j}^z_{\nu,\eta}$, where $\bar{j}^z_{\nu,\eta}$ is the time-averaged contribution to the current from the ν-th band. Using the semiclassical equations of motion [Eqs. (D.2)-(D.3)], we find

$$\bar{j}^z_{\nu,\eta} = \frac{1}{T_{\rm dr}} \int_0^{T_{\rm dr}} dt \int \frac{d^3\boldsymbol{k}}{(2\pi)^3} \left[\frac{1}{\hbar} \partial_{k_z} \varepsilon_{\boldsymbol{k}\nu}(t) + \left\{ e\boldsymbol{\Omega}_\nu \left(\boldsymbol{k} + \frac{e}{\hbar}\boldsymbol{A}(t) \right) \times \frac{\boldsymbol{E}(t)}{\hbar} \right\} \cdot \hat{z} \right] g_\nu(\boldsymbol{k}, t). \tag{D.8}$$

In untilted Weyl nodes, the occupation function $g_\nu(\boldsymbol{k}, t)$ is symmetric upon inversion along k_z ($k_z \to -k_z$), and $\partial_{k_z}\varepsilon_{\boldsymbol{k}\nu}(t)$ is an odd function of k_z. Therefore, the group velocity contribution vanishes. The remaining anomalous velocity is the origin of the topological current. For the positive-chirality Weyl node we consider in Eq. (D.7), the Berry curvature is given by $\boldsymbol{\Omega}_\nu(\boldsymbol{k}) = \xi(-1)^\nu \boldsymbol{k}/2|\boldsymbol{k}|^3$. Moreover using that $\boldsymbol{E}(t) = -2\pi f c_\eta \hat{z} \times \boldsymbol{A}(t)$ for circularly polarized light, we obtain the photocurrent

$$\bar{j}^z_{\nu,\eta} = -c_\eta \xi (-1)^\nu \frac{e^2}{2\hbar} \frac{f}{2\pi} \int \frac{d^3\boldsymbol{k}}{(2\pi)^3} \int_0^{T_{\rm dr}} dt \frac{\boldsymbol{k} \cdot \boldsymbol{A}(t) + eA^2/\hbar}{|\boldsymbol{k} + e\boldsymbol{A}(t)/\hbar|^3} g_\nu(\boldsymbol{k}, t). \tag{D.9}$$

We now compute the contributions from the $\nu = 0$ and $\nu = 1$ bands separately. In our analysis, we focus on the case $\mu \geq 0$, noting that the results can be easily generalized to $\mu < 0$.

Computing $\bar{j}^z_{0,\eta}$

To compute the photocurrent from electronic states in the fully-occupied $\nu = 0$ valence band, we note that the inner integral over t in Eq. (D.9) is symmetric under rotation around the z-axis. We can therefore set $k_x = k_\perp$ and $k_y = 0$ to evaluate it, where $\boldsymbol{k}_\perp = (k_x, k_y)$ denotes the in-plane momentum and $k_\perp = |\boldsymbol{k}_\perp|$ denotes its magnitude. Introducing the unitless parameters $x_\perp = k_\perp/(eA/\hbar)$, $x_F \equiv k_F/(eA/\hbar)$, $x_z \equiv k_z/(eA/\hbar)$, and $\phi = 2\pi t$, where $k_F = \mu/(\hbar v_F)$, the net current produced by electrons in the $\nu = 0$ band is given by

$$\bar{j}^z_{0,\eta} = -c_\eta \xi \frac{ef}{8\pi^2} \left(\frac{eA}{\hbar} \right)^2 \int_0^\infty dx \int_0^{2\pi} d\phi \int_{-\infty}^\infty dx_z \frac{x_\perp \cos\phi + 1}{(x_\perp^2 + 2x_\perp \cos\phi + 1 + x_z^2)^{3/2}}. \tag{D.10}$$

Here, we have used $g_0(\boldsymbol{k}, t) = 1$ because the valence band is fully occupied. We first perform integration over x_z, which yields

$$\bar{j}^z_{0,\eta} = -c_\eta \xi \frac{ef}{8\pi^2} \left(\frac{eA}{\hbar} \right)^2 \int_0^\infty dx \int_0^{2\pi} d\phi \frac{x_\perp \cos\phi + 1}{x_\perp^2 + 1 + 2x_\perp \cos\phi}. \tag{D.11}$$

Using the identity

$$\int_0^{2\pi} d\phi \frac{\cos\phi + x_\perp^{-1}}{\cos\phi + (x_\perp^{-1} + x_\perp)/2} = 4\pi\theta(1 - x_\perp), \tag{D.12}$$

it follows that $\bar{j}^z_{0,\eta} = c_\eta \xi j_{\text{top}}$, where

$$j_{\text{top}} = -\frac{ef}{4\pi}\left(\frac{eA}{\hbar}\right)^2. \tag{D.13}$$

Thus, we have reproduced the quantized current result in Eq. (1) of the main text, which was obtained using the charge pump picture [see discussion above Eq. (1)].

Computing $j^z_{1,\eta}$

We next calculate the current $j^z_{1,\eta}$ generated by electronic states in the partially-filled $\nu = 1$ conduction band, which hosts a spherical Fermi volume with radius $k_F = \mu/(\hbar v_F)$. We again exploit that the inner integral in Eq. (D.9) is symmetric under rotation around the z-axis, and, without loss of generality, set $k_x = k_\perp$ and $k_y = 0$. Using the approximate expression for the occupation function in Eq. (D.6), and the same unitless paramters as in Section D.2, we find that

$$\begin{aligned} j^z_{1,\eta} = c_\eta \xi \frac{ef}{8\pi^2}\left(\frac{eA}{\hbar}\right)^2 \int_{\max(0,1-x_F)}^{1+x_F} dx_\perp \int_{-\sqrt{x_F^2-(x_\perp-1)^2}}^{\sqrt{x_F^2-(x_\perp-1)^2}} dx_z \\ \times \int_0^{2\pi} d\phi \frac{x_\perp \cos\phi + 1}{(x_\perp^2 + 2x_\perp\cos\phi + 1 + x_z^2)^{3/2}} \mathcal{G}_1(x_\perp, x_z, t). \end{aligned} \tag{D.14}$$

Here, $\mathcal{G}_1(x_\perp, x_z, t) = g_1[eA/\hbar(x_\perp, 0, x_z), t]$. Eq. (D.14) can be integrated numerically for different values of x_F. We show the numerical result in Figure D.1(a). We fit $j^z_{1,\eta}$ to the function

$$j^z_{1,\eta} = -c_\eta \xi j_{top} \gamma(\mu) x_F^{\varphi(\mu)}, \tag{D.15}$$

where $j_{\text{top}} = -ef\left(eA/\hbar\right)^2/(4\pi)$. In Figure D.1(b), we plot $\log[-j^z_{1,\eta}/(c_\eta \xi j_{\text{top}})]$ vs. $\log(x_F)$ and we perform fits to the numerically-calculated data using $\varphi = 3$ in the regime $0.05 < x_F < 0.3$ and $\varphi = 2$ in the regime $1.0 < x_F < 1.7$ to arrive at the values of $\gamma(\mu)$ provided in the main text. For $x_F \gg 2$, the coefficients saturate to $\gamma = 2/3$, and $\varphi = 0$, as we show below.

Saturation value of $j^z_{1,\eta}$ for $k_F \gg 2eA/\hbar$. We can analytically compute the saturation value of $j^z_{1,\eta}$ in the limit $k_F \gg 2eA/\hbar$. To this end, we first consider

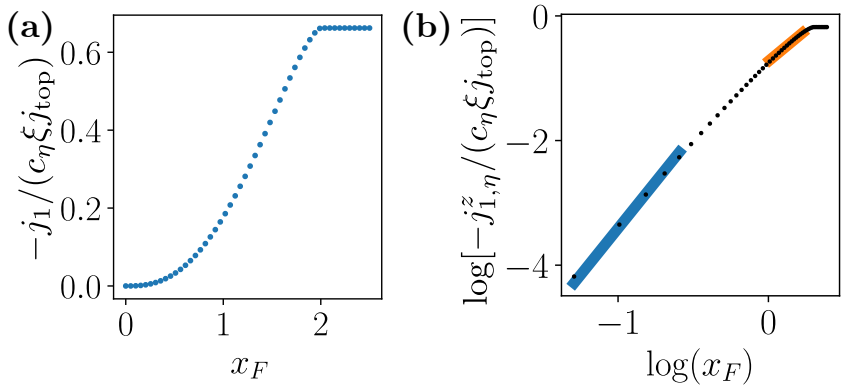

Figure D.1: (a) Topological current produced by conduction band ($\nu = 1$) states in an isolated Weyl node, calculated by numerically integrating the semiclassical equations of motion [see Eq. (D.14)]. Here, $j_{\rm top} = -ef(eA/\hbar)^2/(4\pi)$ denotes the topological current magnitude produced by a fully-occupied valence band [see Eq. (1) in the main text], and $x_F = \hbar k_F/(eA)$. (b) Log-scale plot of panel (a), with fits (solid lines) to the numerical data.

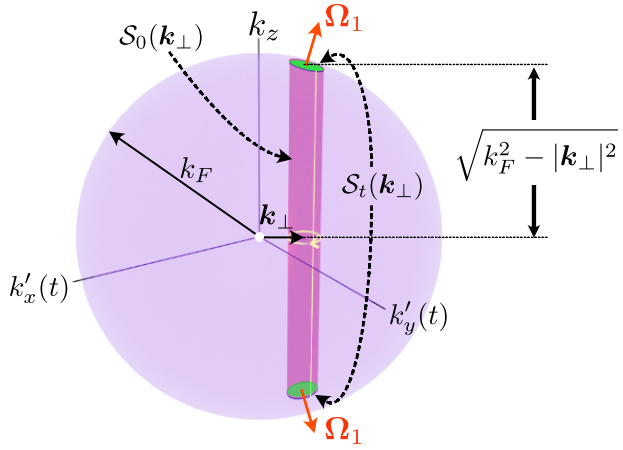

Figure D.2: Illustration of the coordinate system used to calculate the saturation value of $j^z_{1,\eta}$ for $k_F \gg 2eA/\hbar$. Here, $\boldsymbol{k}' = \boldsymbol{k} + e\boldsymbol{A}(t)/\hbar$ is the shifted coordinate system, which fixes the WN at the origin. Purple sphere indicates the Fermi volume in the conduction band, which is centered at the WN (center white dot). Under illumination by circularly polarized light, populated electronic states with a given $\boldsymbol{k}_\perp = (k_x, k_y)$ traces out a cylinder $\mathcal{S}_t(\boldsymbol{k}_\perp)$ (dark purple) in momentum space during a period of the drive. Due to the finite Fermi momentum k_F, finite Berry curvature $\boldsymbol{\Omega}_1$ penetrates the "caps" $\mathcal{S}_t(\boldsymbol{k}_\perp)$ (light green) of the cylinder located at $k_z = \pm\sqrt{k_F^2 - |\boldsymbol{k}_\perp|^2}$. The Berry flux through the caps $\mathcal{S}_t(\boldsymbol{k}_\perp)$ produces a saturation value of $j^z_{1,\eta}$ in the limit $k_F \gg 2eA/\hbar$.

the current produced by a single Fermionic chain of states with fixed in-plane momentum $\boldsymbol{k}_\perp$, given by

$$\mathcal{I}(\boldsymbol{k}_\perp) = \frac{1}{T_{\rm dr}} \int_0^{T_{\rm dr}} dt \int_{-\infty}^{\infty} \frac{dk_z}{2\pi} \left[\frac{1}{\hbar} \partial_{k_z} \varepsilon_{\boldsymbol{k}1}(t) + \left\{ e\boldsymbol{\Omega}_1 \left(\boldsymbol{k} + \frac{e}{\hbar}\boldsymbol{A}(t) \right) \times \frac{\boldsymbol{E}(t)}{\hbar} \right\} \cdot \hat{z} \right] g_1(\boldsymbol{k}, t). \tag{D.16}$$

This in-plane-momentum-resolved current determines $j^z_{1,\eta}$ via

$$j^z_{1,\eta} = \int \frac{d^2\boldsymbol{k}_\perp}{(2\pi)^2} \mathcal{I}(\boldsymbol{k}_\perp). \tag{D.17}$$

Noting again that the group velocity term in Eq. (D.16) vanishes by symmetry, it follows that

$$\mathcal{I}(\boldsymbol{k}_\perp) = \frac{ef}{2\pi} \int_{-\infty}^{\infty} dk_z \int_0^{T_{\rm dr}} dt\, \frac{e}{\hbar} [\boldsymbol{\Omega}_1(\boldsymbol{k} + e\boldsymbol{A}(t)/\hbar) \times \boldsymbol{E}(t)] \cdot \hat{z}\, g_1(\boldsymbol{k}, t). \tag{D.18}$$

To further simplify the expression, we note that the magnetic vector potential $\boldsymbol{A}(t)$ is always perpendicular to the electric field $\boldsymbol{E}(t)$, and, therefore,

$$\mathcal{I}(\boldsymbol{k}_\perp) = c_\eta \frac{ef}{2\pi} \int_{-\infty}^{\infty} \int_0^{T_{\rm dr}} \boldsymbol{\Omega}_1(\boldsymbol{k} + e\boldsymbol{A}(t)/\hbar) \cdot \left[\frac{e}{\hbar} E \hat{\boldsymbol{A}}(t) dt dk_z \right] g_1(\boldsymbol{k}, t), \tag{D.19}$$

where $E = |\boldsymbol{E}(t)|$ and $\hat{\boldsymbol{A}} = \boldsymbol{A}(t)/|\boldsymbol{A}(t)|$. We identify

$$\boldsymbol{\Omega}_1(\boldsymbol{k} + e\boldsymbol{A}(t)/\hbar) \cdot (e/\hbar) E \hat{\boldsymbol{A}}(t) dt dk_z \tag{D.20}$$

[see Figure 2(a) in the main text] as the flux of Berry curvature through an infinitesimal surface area element for a cylinder $\mathcal{S}_0(\boldsymbol{k}_\perp)$ of radius $eA/\hbar$ oriented along the z axis and with center located at $\boldsymbol{k}_\perp = (k_x, k_y)$. Next, we note that $g_1(\boldsymbol{k}, t) \approx \theta(k_F - |\boldsymbol{k}|)$ for $k_F \gg eA/\hbar$. Thus $\mathcal{I}(\boldsymbol{k}_\perp)$ is given by the total Berry flux through the open surface (or "ribbon") defined by the segment of $\mathcal{S}_0(\boldsymbol{k}_\perp)$ with $|k_z| < \sqrt{k_F^2 - |\boldsymbol{k}_\perp|^2}$:

$$\mathcal{I}(\boldsymbol{k}_\perp) = c_\eta \frac{ef}{2\pi} \int_{\mathcal{S}_0(\boldsymbol{k}_\perp)} \boldsymbol{\Omega}_1 \cdot d\boldsymbol{S}. \tag{D.21}$$

To compute this, we consider the closed surface $\mathcal{S}(\boldsymbol{k}_\perp)$ formed by closing the ends of $\mathcal{S}_0(\boldsymbol{k})$ by adding the disk-shaped "caps" $\mathcal{S}_t(\boldsymbol{k}_\perp)$, consisting of points $\boldsymbol{k}' = (k_x, k_y, \pm\sqrt{k_F^2 - |\boldsymbol{k}_\perp|^2})$, see Figure D.2 for an illustration. The surface integral over $\mathcal{S}_0(\boldsymbol{k}_\perp)$ is given by the surface integral over $\mathcal{S}(\boldsymbol{k}_\perp)$ minus the oriented surface integral over $\mathcal{S}_t(\boldsymbol{k}_\perp)$:

$$\mathcal{I}(\boldsymbol{k}_\perp) = c_\eta \frac{ef}{2\pi} \left(\int_{\mathcal{S}(\boldsymbol{k}_\perp)} \boldsymbol{\Omega}_1 \cdot d\boldsymbol{S} - \int_{\mathcal{S}_t(\boldsymbol{k}_\perp)} \boldsymbol{\Omega}_1 \cdot d\boldsymbol{S} \right). \tag{D.22}$$

The first integral evaluates to j_{top} following the analysis presented before Eq. (8.1) in the main text. To evaluate the second integral, we recall that $\boldsymbol{\Omega}_1(\boldsymbol{k}) = \xi \boldsymbol{k}/|\boldsymbol{k}|^3$. When $k_F \gg 2eA/\hbar$, we can effectively set $k_z = \sqrt{k_F^2 - |\boldsymbol{k}_\perp|^2}$ on the surface $\mathcal{S}_t(\boldsymbol{k}_\perp)$, implying that the Berry flux density through $\mathcal{S}_t(\boldsymbol{k}_\perp)$ is uniform and given by $\xi\sqrt{k_F^2 - |\boldsymbol{k}|^2}/k_F^3$. Noting that $\mathcal{S}_t(\boldsymbol{k}_\perp)$ has area $2\pi(eA/\hbar)^2$, this leads us to

$$\int_{\mathcal{S}_t(\boldsymbol{k}_\perp)} \boldsymbol{\Omega}_1(\boldsymbol{k}) \cdot d\boldsymbol{S} \approx 2\pi\xi \left(\frac{eA}{\hbar}\right)^2 \frac{\sqrt{k_F^2 - |\boldsymbol{k}|^2}}{k_F^3}. \tag{D.23}$$

Using Eq. (D.17) and Eq. (D.22) to compute the total current produced all Fermionic chains in the conduction band, we find that

$$j^z_{1,\eta} = c_\eta \xi \frac{2}{3}\frac{ef}{4\pi}\left(\frac{eA}{\hbar}\right)^2 \quad for \quad k_F \gg 2eA/\hbar. \tag{D.24}$$

Photocurrent in the x-y plane for $k_F \ll eA/\hbar$

We next calculate the (oscillating) photocurrent in the x-y plane induced by the circularly polarized laser. We focus on the low temperature regime $T \ll \mu/k_B$ and for small Fermi momenta $k_F \ll eA/\hbar$. This current gives rise to the plasma resonances described in the main text [see Eq. (8.8)]. For concreteness, we set $t = 0$, noting that the results for later times are related to this case through trivial rotation. Using the semiclassical equations in Eqs. (D.2) and (D.3), we find that the total current is given by

$$\boldsymbol{j}^\eta(t) = e\sum_\nu \int \frac{d^3\boldsymbol{k}}{(2\pi)^3}\left[\frac{\nabla_{\boldsymbol{k}}}{\hbar}\varepsilon_{\boldsymbol{k}\nu}(t) + \left\{e\boldsymbol{\Omega}_\nu\left(\boldsymbol{k} + \frac{e}{\hbar}\boldsymbol{A}(0)\right) \times \frac{\boldsymbol{E}(0)}{\hbar}\right\}\right]_\perp g_\nu(\boldsymbol{k}, t), \tag{D.25}$$

To evaluate the in-plane component of $\boldsymbol{j}^\eta(t)$, we first note that the anomalous velocity term does not contribute to the in-plane photocurrent for untilted Weyl nodes, because the in-plane component of the anomalous velocity reverses direction upon inversion along the k_z axis ($k_z \to -k_z$), and the Fermi volume (and hence also $g_\nu(\boldsymbol{k}, t)$) is symmetric upon the same transformation. We also note that the $\nu = 0$ band does not contribute, because $g_0(\boldsymbol{k}, t) = 1$ and $\nabla_{\boldsymbol{k}}\varepsilon_{\boldsymbol{k}0}(0)$ is odd under momentum inversion about the Weyl node ($\boldsymbol{k} + e\boldsymbol{A}(0)/\hbar \to -\boldsymbol{k} + e\boldsymbol{A}(0)/\hbar$) and the Fermi volume is also symmetric about the same transformation. Thus,

$$j^\eta_{x,y}(t) = e\int \frac{d^3\boldsymbol{k}}{(2\pi)^3}\nabla_{k_x,k_y}\varepsilon_{\boldsymbol{k}1}(0)g_1(\boldsymbol{k}, t). \tag{D.26}$$

We next decompose the in-plane photocurrent into its components j^η_P and j^η_N parallel and normal to the direction of the instantaneous electric field, $\hat{\boldsymbol{e}}(t) \equiv \boldsymbol{E}(t)/E$,

respectively, such that

$$\boldsymbol{j}^{\eta}(t) = j_z^{\eta}(t)\hat{z} + j_P^{\eta}\hat{\boldsymbol{e}}(t) + j_N^{\eta}\hat{z}\times\hat{\boldsymbol{e}}(t). \tag{D.27}$$

The combination of rotation and time translation symmetry of the problem implies that j_z^{η}, j_N^{η}, and j_P^{η} are all time-independent in the steady-state. We moreover identify $j_N^{\eta} = c_\eta j_x(0)$, $j_P^{\eta} = c_\eta j_y(0)$. Also using the expression for the energies $\varepsilon_{\boldsymbol{k}1}(t)$, we find

$$j_N^{\eta} = c_\eta e v_F \int \frac{d^3\boldsymbol{k}}{(2\pi)^3} \frac{k_x - eA/\hbar}{\sqrt{[k_x + eA/\hbar]^2 + k_y^2 + k_z^2}} g_1(\boldsymbol{k}, 0), \tag{D.28}$$

$$j_P^{\eta} = c_\eta e v_F \int \frac{d^3\boldsymbol{k}}{(2\pi)^3} \frac{k_y}{\sqrt{[k_x + eA/\hbar]^2 + k_y^2 + k_z^2}} g_1(\boldsymbol{k}, 0). \tag{D.29}$$

To evaluate the above, we need to find an approximate expression for the occupation function $g_1(\boldsymbol{k}, t) = {T_{\rm dr}}^{-1} \int_0^{T_{\rm dr}} dt' f_1^{eq}(\boldsymbol{k}, t')$ [See Eq. (D.6)]. We transform into the cylindrical coordinates $\boldsymbol{k} = (k_\perp \cos\varphi, k_\perp \sin\varphi, k_z)$ and first find an approximate expression for the zero-temperature instantaneous equilibrium occupation function $f_1^{\rm eq}(\boldsymbol{k}, t) = \theta(k_F - |\boldsymbol{k} + e\boldsymbol{A}(t)/\hbar|)$, where θ is the Heaviside step function. In the regime $k_F \ll eA/\hbar$, it can be approximated by

$$f_1^{\rm eq}(\boldsymbol{k}, t) \approx \theta(\min_{n\in\mathbb{Z}} |\varphi - 2\pi f t + 2\pi n| - \delta\varphi(k_\perp, k_z))\theta(k_F^2 - k_z^2 - (k_\perp - eA/\hbar)^2), \tag{D.30}$$

where $\delta\varphi(k_\perp, k_z)$ measures the azimuthal angle taken up by the Fermi volume at fixed $k_\perp$ and k_z [see Figure D.3(a)]. The second step function in Eq. (D.30) requires that the in-plane momentum magnitude $k_\perp$ of occupied states lies between the two dashed blue circles in Figure D.3(a), while the first step function in Eq. (D.30) requires that the azimuthal angle φ of the in-plane momentum lies between the two angles indicated by green dashed lines in Figure D.3(a). The angle between the two green dashed lines can be estimated by $\delta\varphi(k_\perp, k_z) = \varphi_+(k_\perp, k_z) - \varphi_-(k_\perp, k_z)$, where $\varphi_\pm(k_\perp, k_z)$ are defined via the relation

$$\hbar v_F |(k_\perp \cos[\varphi_\pm(k_\perp, k_z)] - eA/\hbar, k_\perp \sin[\varphi_\pm(k_\perp, k_z)], k_z)| = \hbar v_F k_F, \tag{D.31}$$

which parameterizes the boundary of the Fermi volume. Expanding $\cos[\varphi_\pm(k_\perp, k_z)] \approx 1 - [\varphi_\pm(k_\perp, k_z)]^2/2$ in the limit $k_F \ll eA/\hbar$, solving for $\varphi_\pm(k_\perp, k_z)$ yields

$$\delta\varphi(k_\perp, k_z) \approx (\hbar/eA)\sqrt{k_F^2 - k_z^2 - (k_\perp - eA/\hbar)^2}. \tag{D.32}$$

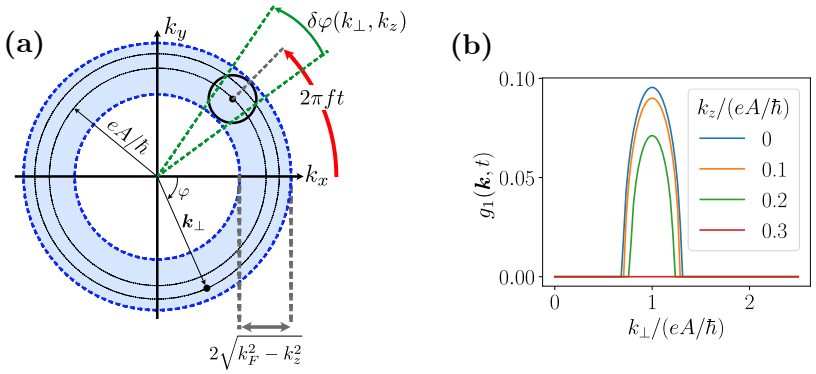

Figure D.3: (a) Illustration of the characteristic in-plane momentum dynamics relevant for analyzing the photocurrent. Solid black circle indicates the edge of the instantaneous equilibrium Fermi volume of $H(\boldsymbol{k}, t)$ as a function of in-plane momentum, $\boldsymbol{k}_\perp = (k_x, k_y)$, for an arbitrary, fixed value of k_z. Black dot indicates the instantaneous location of the Weyl node, which is located at an azimuthal angle of $2\pi ft$ from the k_x axis (red arrow). We approximate the instantaneous equilibrium occupation $f_1^{\text{eq}}(\boldsymbol{k}, t)$ [Eq. (D.30)] to be given by 1 if $\boldsymbol{k}_\perp$ is located within the annulus segment (shaded blue) and between the two angles indicated by green lines, and 0 otherwise. (For the choice of $\boldsymbol{k}_\perp$ sketched in the figure, $\boldsymbol{k}_\perp$ is positioned such that $f_1^{\text{eq}}(\boldsymbol{k}, t) = 0$.) Such an approximation is accurate in the limit where the Fermi momentum k_F is much less than the vector potential $eA/\hbar$. (b) Occupation function $g_1(\boldsymbol{k}, t)$ as a function of the in-plane momentum magnitude $k_\perp = \sqrt{k_x^2 + k_y^2}$ in the slow relaxation time limit $\tau f \gg 1$, plotted for several values of the z-momentum k_z.

The steady state occupation function [see Eq. (D.6)] in the $\tau f \gg 1$ limit is the time-average of Eq. (D.30), which is time-independent and given by

$$g_1(\boldsymbol{k}, t) \approx \frac{1}{\pi}\left(\frac{\hbar}{eA}\right)\sqrt{k_F^2 - k_z^2 - (k_\perp - eA/\hbar)^2}\,\theta(k_F^2 - k_z^2 - (k_\perp - eA/\hbar)^2). \quad \text{(D.33)}$$

We plot $g_1(\boldsymbol{k}, t)$ as a function of $k_\perp$ for several values of k_z in Figure D.3(b). We finally exploit the rotational symmetry of $g_1(\boldsymbol{k}, t)$ to express it in terms of the dimensionless cylindrical coordinates $x_\perp, x_z, \phi$, defined via

$$(k_x, k_y, k_z) = eA/\hbar(x_\perp \cos\phi, x_\perp \sin\phi, x_z), \quad \text{(D.34)}$$

giving

$$\mathcal{G}(x_\perp, x_z, \phi) \equiv g_1[eA/\hbar(x_\perp \cos\phi, x_\perp \sin\phi, x_z), 0]. \quad \text{(D.35)}$$

In terms of this function, the in-plane components of the current read, for $\alpha = N, P$,

$$j_\alpha^\eta = c_\eta \frac{e v_F}{(2\pi)^3}\left(\frac{eA}{\hbar}\right)^3 \int_0^\infty dx_\perp\, x_\perp \int_0^{2\pi} d\phi \int_{-\infty}^{\infty} dx_z \frac{h_\alpha(\phi)}{\sqrt{x_\perp^2 + x_z^2 + 1 - 2x_\perp \cos\phi}} \mathcal{G}(x_\perp, x_z, \phi), \tag{D.36}$$

where $h_N(\phi) = 1 - x_\perp \cos\phi$ and $h_P(\phi) = -x_\perp \sin\phi$. Because $\mathcal{G}(x_\perp, x_z, \phi)$ is only nonzero when $|x_z| \leq k_F/(eA/\hbar)$ and we assume $k_F \ll eA/\hbar$, we have $x_z \ll 1$. As a result, we can approximate

$$j_\alpha^\eta \approx c_\eta \frac{e v_F}{(2\pi)^3}\left(\frac{eA}{\hbar}\right)^3 \int_0^\infty dx_\perp\, x_\perp \int_0^{2\pi} d\phi \frac{h_\alpha(\phi)}{\sqrt{x_\perp^2 + 1 - 2x_\perp \cos\phi}} \int_{-\infty}^{\infty} dx_z\, \mathcal{G}(x_\perp, x_z, \phi). \tag{D.37}$$

Converting the expression for $g_1(\boldsymbol{k}, 0)$ in Eq. (D.33) to the cylindrical coordinates, we find

$$\mathcal{G}(x_\perp, x_z, \phi) \approx \frac{1}{\pi}\sqrt{x_F^2 - x_z^2 - (x_\perp - 1)^2}\,\theta(x_F^2 - x_z^2 - (x_\perp - 1)^2). \tag{D.38}$$

We next perform the integral over x_z, finding

$$\int_{-\sqrt{x_F^2-(x_\perp-1)^2}}^{\sqrt{x_F^2-(x_\perp-1)^2}} dx_z\, \mathcal{G}(x_\perp, x_z, \phi) = \frac{1}{2}[x_F^2 - (x_\perp - 1)^2]. \tag{D.39}$$

Furthermore, in the $x_F \ll 1$ limit, we approximate

$$j_\alpha^\eta \approx c_\eta \frac{e v_F}{(2\pi)^3}\frac{1}{2\sqrt{2}}\left(\frac{eA}{\hbar}\right)^3 \left(\int_{1-x_F}^{1+x_F} dx\, x[x_F^2 - (x_\perp - 1)^2]\right) \int_0^{2\pi} d\phi \frac{h_\alpha(\phi)}{\sqrt{1 - \cos\phi}}. \tag{D.40}$$

Integration over x and ϕ yields

$$j_P^\eta = 0 \quad and \quad j_N^\eta \approx c_\eta \frac{e v_F}{3\pi^3} x_F^3 \left(\frac{eA}{\hbar}\right)^3 \quad for \quad k_F \ll eA/\hbar \tag{D.41}$$

for the components parallel and perpendicular to the electric field $\boldsymbol{E}(t)$, respectively, where we have used that $h_N(\phi) \approx 1 - \cos\phi$ throughout the integration range and $\int_0^{2\pi} d\phi\, \sqrt{1 - \cos\phi} = 4\sqrt{2}$.

D.3 Consequences of Finite tilt

In this section, we finally consider the photocurrent produced by Weyl node with finite tilt. We focus on an isolated Weyl node with anisotropy along the z-direction, described by the Hamiltonian

$$H(\boldsymbol{k}) = \hbar v_F \boldsymbol{k} \cdot \boldsymbol{\sigma} + \hbar V_z \sigma_z. \tag{D.42}$$

In what follows, we use the unitless tilt parameter $\chi \equiv V_z/v_F$ and focus on the slow relaxation limit $\tau f \gg 1$ at temperature $T \ll \mu/k_B, v_F eA/k_B$. The anisotropy gives rise to a laser helicity-independent photocurrent in the z-direction, which we analyze semiclassically in Section D.3. In Section D.3, we show that the anistropy contributes an anomalous velocity component to the oscillating current in the plane of the electric field, giving rise to a laser helicity-dependent plasmon resonance frequency. We semiclassically estimate the additional topological current perpendicular to the electric field, denoted $j_N^H(\chi)$, and the modifications to $j_{N,G}^\eta$ and $j_{P,G}^\eta$ in leading order of χ. These calculations allow us to calculate the total photocurrent in the presence of a tilt, given by

$$\boldsymbol{j}^\eta(t) = j_z^\eta(t)\hat{z} + j_{P,G}^\eta \hat{\boldsymbol{e}}(t) + [j_{N,G}^\eta + j_N^H(\chi)]\hat{z} \times \hat{\boldsymbol{e}}(t). \tag{D.43}$$

Photocurrent along the z-axis in the weak field limit $eA/\hbar \ll k_F$

When the Weyl node exhibits a tilt $\chi \neq 0$ along the z-axis, the topological photocurrent is insensitive to weak anisotropy $\chi \ll 1$, as demonstrated numerically in Figure 1(b) in the main text. However, the anisotropy allows for the group velocity term in the semiclassical equations of motion [see Eq. (4)] to contribute a nonzero, laser helicity-independent photocurrent [see Figure 3(d) in the main text], given by

$$\bar{j}_G^z = \frac{1}{T_{\rm dr}} \int_0^{T_{\rm dr}} dt \int \frac{d^3\boldsymbol{k}}{(2\pi)^3} \left[\frac{1}{\hbar}\frac{\partial \varepsilon_{\boldsymbol{k}1}(t)}{\partial k_z}\right] g_1(\boldsymbol{k}, t). \tag{D.44}$$

In the slow relaxation limit $\tau f \gg 1$, we can rewrite

$$g_1(\boldsymbol{k}, t) \approx \frac{1}{T_{\rm dr}} \int_0^{T_{\rm dr}} dt'\, f_1^{\rm eq}(\boldsymbol{k}, t') \tag{D.45}$$

[see Eq. (D.6)] and express the instantaneous equilibrium occupation function in terms of the instantaneous eigenenergies

$$f_1^{\rm eq}(\boldsymbol{k}, t) = \theta(\varepsilon_{\boldsymbol{k}1}(t) - \mu). \tag{D.46}$$

To provide intuition for the emergence of the helicity-independent photocurrent, we note that the tilt produces an asymmetric $f_1^{\rm eq}(\boldsymbol{k}, t)$ that preferentially populates electronic states with z-momentum k_z antiparallel to the direction of anisotropy, i.e., $\text{sign}(k_z) = -\text{sign}(\chi)$. The steady state occupation $g_1(\boldsymbol{k}, t)$, which time-averages the instantaneous electronic occupation, therefore acquires larger values for electronic states whose z-momentum has sign $-\text{sign}(\chi)$, leading to a net group velocity in the same direction.

To estimate the helicity-independent photocurrent, we rewrite Eq. (D.44) as

$$\bar{j}_G^z = ef \int \frac{dk_x dk_y}{(2\pi)^2} \int_0^{T_{\rm dr}} dt' \mathcal{J}_z(k_x, k_y, t, t'), \tag{D.47}$$

where

$$\mathcal{J}_z(k_x, k_y, t, t') \equiv \int \frac{dk_z}{2\pi} \frac{1}{\hbar} \frac{\partial \varepsilon_{\boldsymbol{k}1}(t)}{\partial k_z} \theta(\varepsilon_{\boldsymbol{k}1}(t') - \mu). \tag{D.48}$$

As discussed previously, the slow relaxation time τ gives rise to a lagging of the Fermi volume along the trajectory of the Weyl node traced out by the vector potential. This is captured in Eq. (D.47) because the current at time t is given by the average of the occupation-weighted group velocity $\mathcal{J}_z(k_x, k_y, t, t')$ set by the instantaneous thermal equilibrium distribution at all other times t'. Crucially, $\mathcal{J}_z(k_x, k_y, t, t')$ is nonzero with sign given by $\text{sign}(\chi)$ only when $\chi \neq 0$ and $t \neq t'$, as illustrated in Figure D.4(a), which is the origin of the helicity-independent photocurrent. When $\chi < 0$, the electronic momenta with nonzero instantaneous equilibrium occupation $\theta(\varepsilon_{\boldsymbol{k}1}(t') - \mu)$ (thick orange line) at previous time $t' < t$ preferentially populates electronic states with negative z-group velocity $\partial \varepsilon_{\boldsymbol{k}1}(t)/\partial k_z < 0$ at time t, allowing the integral in Eq. (D.48) to attain a nonzero negative value. Eq. (D.48) can be solved by integration by parts, yielding

$$\mathcal{J}_z(k_x, k_y, t, t') = \frac{1}{2\pi\hbar} \left[\varepsilon_{\boldsymbol{k}1}(t)|_{k_z = k_z^+(t')} - \varepsilon_{\boldsymbol{k}1}(t)|_{k_z = k_z^-(t')} \right], \tag{D.49}$$

where $\varepsilon_{\boldsymbol{k}1}(t')|_{k_z = k_z^\pm(t')} = \mu$. To compute the values of $k_z^\pm(t')$, we consider the instantaneous eigenenergy at time t', given by

$$\varepsilon_{\boldsymbol{k}1}(t') = \hbar v_F |\boldsymbol{k} + e\boldsymbol{A}(t')/\hbar| + \hbar v_F \chi k_z. \tag{D.50}$$

Defining $k_F \equiv \mu/(\hbar v_F)$ and solving for the instantaneous Fermi surface $\varepsilon_{\boldsymbol{k}1}(t') = \hbar v_F k_F$ gives rise to two roots

$$k_z^\pm(t') \equiv \frac{\chi k_F \mp \sqrt{(\chi^2 - 1)[\tilde{\boldsymbol{k}}_\perp(t')]^2 + k_F^2}}{\chi^2 - 1}, \tag{D.51}$$

where

$$\tilde{\boldsymbol{k}}_\perp(t') \equiv (k_x + eA_x(t')/\hbar, k_y + eA_y(t')/\hbar) \tag{D.52}$$

denotes the in-plane momentum shifted by the drive-induced vector potential via minimal coupling. Therefore, using Eq. (D.49), we find that

$$\begin{aligned} \mathcal{J}_z(k_x, k_y, t, t') &= \frac{v_F}{\pi} \sqrt{-[\tilde{\boldsymbol{k}}_\perp(t)]^2 + k_F^2} \\ &\times \left(1 - \frac{k_F}{\sqrt{-[\tilde{\boldsymbol{k}}_\perp(t)]^2 + [\tilde{\boldsymbol{k}}_\perp(t')]^2 + k_F^2}} \right) \theta(k_F^2 - [\tilde{\boldsymbol{k}}_\perp(t)]^2) \chi + O(\chi^3). \end{aligned} \tag{D.53}$$

To make further progress, we take the limit of weak fields, given by $eA/\hbar \ll k_F$, in which case we can take the limit $|[\boldsymbol{k}_\perp(t')]^2 - [\boldsymbol{k}_\perp(t)]^2| \ll k_F$ and obtain

$$\mathcal{J}_z(k_x, k_y, t, t') \approx \frac{v_F}{2\pi}\sqrt{-[\tilde{\boldsymbol{k}}_\perp(t)]^2 + k_F^2}\,\frac{[\tilde{\boldsymbol{k}}_\perp(t')]^2 - [\tilde{\boldsymbol{k}}_\perp(t)]^2}{k_F^2}\theta(k_F^2 - |\tilde{\boldsymbol{k}}_\perp(t)|^2)\chi. \tag{D.54}$$

Note that after integration over t', the photocurrent $\bar{j}_G^z$ is time-independent. Therefore, without loss of generality, we set $t = 0$. To estimate $|\boldsymbol{k}_\perp(t)|$ and $|\boldsymbol{k}_\perp(t')|$, we transform to the polar coordinates $k_x = k_\perp \cos\varphi$ and $k_y = k_\perp \sin\varphi$, where

$$[\boldsymbol{k}_\perp(t')]^2 - [\boldsymbol{k}_\perp(t)]^2 = \frac{eA}{\hbar}\left[\frac{eA}{\hbar} - 2\frac{eA}{\hbar}\cos\big(2\pi f t'\big) + 2k_\perp \sin\big(\varphi + 2\pi f t'\big)\right]. \tag{D.55}$$

Furthermore, in the limit $eA/\hbar \ll k_F$, $k_F^2 - [\boldsymbol{k}_\perp(t)]^2 \approx k_F^2 - k_\perp^2$. Using these approximations,

$$\begin{aligned}\bar{j}_G^z = \frac{ef}{(2\pi)^2}\int_0^{k_F} dk_\perp\, k_\perp \int_0^{T_{\rm dr}} dt' \int_0^{2\pi} d\varphi \frac{v_F}{2\pi k_F^2}\sqrt{k_F^2 - k_\perp^2}\left(\frac{eA}{\hbar}\right)^2 \\ \times\left[1 - 2\cos\big(2\pi f t'\big) + 2\frac{k_\perp}{eA/\hbar}\sin\big(\varphi + 2\pi f t'\big)\right].\end{aligned} \tag{D.56}$$

Upon integration over φ, k, and t', we find that

$$\bar{j}_G^z = \frac{e\mu}{12\pi^2\hbar}\left(\frac{eA}{\hbar}\right)^2 \chi \quad for \quad k_F \gg eA/\hbar. \tag{D.57}$$

Photocurrent in the x-y plane

We finally discuss how band anisotropy modifies the photocurrent induced by the circularly polarized laser in the x-y plane. In Section D.3, we discuss the effect of weak band anisotropy ($\chi \ll 1$) on the occupation function. In Section D.3, we use the occupation function to understand the emergence of an additional topological current $j_N^H(\chi)$ in the direction perpendicular to the laser electric field, produced by the anomalous velocity of electrons. This mechanism gives rise to the chiral plasmons discussed in the main text [see Figure 8.1(e)]. In Section D.3, we demonstrate that the nonzero Weyl node tilt does not modify the group velocity contribution to the in-plane current to first order in χ. As in Section D.2, we analyze the photocurrent in the small Fermi volume limit $k_F \ll eA/\hbar$.

Occupation function for $\chi \ll 1$ and $k_F \ll eA/\hbar$

The tilt along the z-axis reshapes the instantaneous equilibrium occupation function $f_1^{\rm eq}(\boldsymbol{k}, t)$ in the conduction band of the Weyl node, which in turn modifies the steady

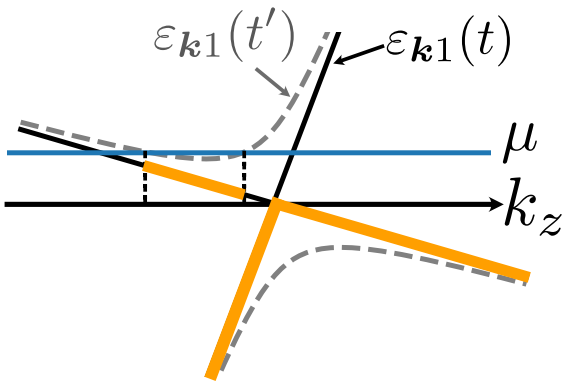

Figure D.4: Origin of the laser helicity-independent photocurrent in a tilted WN. In the limit $\tau f \gg 1$, the steady state occupation of bands at any given time t is the time average of the instantaneous equilibrium occupation function $\theta(\varepsilon_{\boldsymbol{k}1}(t') - \mu)$ at all other times t'. The black solid and dashed gray curves represent the electronic bands at representative times t and t', respectively. The instantaneous equilibrium distribution at time t' (orange) preferentially fills states with $\partial\varepsilon_{\boldsymbol{k}1}(t)/\partial k_z < 0$, producing a net helicity-independent current.

state ocupation function $g_1(\boldsymbol{k}, t)$. To recalculate $g_1(\boldsymbol{k}, t)$, we revisit the derivation in Section D.2, using the approximate expression for the occupation function in the slow relaxation limit $\tau f \gg 1$ given by

$$g_1(\boldsymbol{k}, t) \approx \frac{1}{T_{\rm dr}} \int_0^{T_{\rm dr}} du\ f_1^{\rm eq}(\boldsymbol{k}, u). \tag{D.58}$$

In the presence of a tilt, we again have

$$f_1^{\rm eq}(\boldsymbol{k}, t) \approx \theta(\min_{n\in\mathbb{Z}} |\varphi - 2\pi f t + 2\pi n| - \delta\varphi_\chi(k_\perp, k_z))\theta(k_F^2 - k_z^2 - (k_\perp - eA/\hbar)^2) \tag{D.59}$$

[see Eq. (D.30)], but with a modified $\delta\varphi_\chi(k_\perp, k_z)$ defined by $\delta\varphi_\chi(k_\perp, k_z) = \varphi_{\chi,+}(k_\perp, k_z) - \varphi_{\chi,-}(k_\perp, k_z)$, where

$$\hbar v_F |(k_\perp \cos[\varphi_{\chi,\pm}(k_\perp, k_z)] - eA/\hbar, k_\perp \sin[\varphi_{\chi,\pm}(k_\perp, k_z)]| + \hbar\chi k_z = \hbar v_F k_F \tag{D.60}$$

parameterizes the edge of the Fermi volume [see Eq. (D.31)] which may be rewritten in the form

$$\begin{aligned}(1+\chi^2)k_F^2 = k_\perp^2 - 2\frac{eA}{\hbar}k_\perp \cos[\varphi_{\chi,\pm}(k_\perp, k_z)] + \frac{e^2A^2}{\hbar} \\ + (\sqrt{1-\chi^2}k_z + \chi k_F)^2 + 2(1-\sqrt{1-\chi^2})\chi k_F k_z.\end{aligned} \tag{D.61}$$

Expanding $\cos[\varphi_{\chi,\pm}(k_\perp, k_z)] \approx 1 - [\varphi_{\chi,\pm}(k_\perp, k_z)]^2/2$ in the limit $k_F \ll eA/\hbar$ and evaluating $\delta\varphi_\chi(k_\perp, k_z) = \varphi_{\chi,+}(k_\perp, k_z) - \varphi_{\chi,-}(k_\perp, k_z)$, we find that

$$[\delta\varphi_\chi(k_\perp, k_z)]^2 \approx (\hbar/eA)^2[k_F^2 - (k_z + \chi k_F)^2 - (k_\perp - eA/\hbar)^2], \tag{D.62}$$

where we have discarded terms of $O(\chi^2)$ or higher.

Using Eq. (D.58), we time-average the equilibrium occupation function, Eq. (D.59), to find

$$g_1(\boldsymbol{k},t) \approx \frac{1}{\pi}\left(\frac{\hbar}{eA}\right)\sqrt{k_F^2-(k_z+\chi k_F)^2-(k_\perp-eA/\hbar)^2}\,\theta(k_F^2-(k_z+\chi k_F)^2-(k_\perp-eA/\hbar)^2). \tag{D.63}$$

Note that $g_1(\boldsymbol{k},t)$ is time-independent. We see that the primary effect of the tilt in the limit of weak anisotropy $\chi \ll 1$ is the shift of the Fermi volume along the k_z axis by χk_F.

Topological current $j_N^H(\chi)$ for $\chi \ll 1$ and $k_F \ll eA/\hbar$

Due to the asymmetry of the electronic occupation function along the k_z-axis, and the combination of rotation and time-translation symmetry of the problem, the anomalous velocity in Eq. (D.25) contributes a photocurrent given by

$$\boldsymbol{j}_\perp^a = e\int\frac{d^3\boldsymbol{k}}{(2\pi)^3}\left[e\boldsymbol{\Omega}_1\left(\boldsymbol{k}+\frac{e}{\hbar}\boldsymbol{A}(0)\right)\cdot\hat{z}\right]\left[\hat{z}\times\frac{\boldsymbol{E}(0)}{\hbar}\right]g_1(\boldsymbol{k},0). \tag{D.64}$$

The current flows perpendicular to $\boldsymbol{E}(0)$ and is given by $\boldsymbol{j}_\perp^a = j_N^H(\chi)\hat{z}\times\boldsymbol{E}(0)$, where

$$j_N^H(\chi) = \xi\frac{e^2}{2\hbar}E\int\frac{d^3\boldsymbol{k}}{(2\pi)^3}\frac{k_z}{\{[k_x+eA/\hbar]^2+k_y^2+k_z^2\}^{3/2}}g_1(\boldsymbol{k},0). \tag{D.65}$$

To evaluate the integral, we again transform to the dimensionless coordinates given by $x_F = k_F/(eA/\hbar)$, $x_\perp = k_\perp/(eA/\hbar)$, and $x_z = k_z/(eA/\hbar)$, such that $\mathcal{G}(x_\perp,x_z,\phi) \equiv g_1[eA/\hbar(x_\perp\cos\phi, x_\perp\sin\phi, x_z),0]$. This leads to

$$j_N^H(\chi) = \xi\frac{ef}{8\pi^2}\left(\frac{eA}{\hbar}\right)^2\int_0^\infty dx_\perp\, x_\perp\int_0^{2\pi}d\phi\int_{-\infty}^{\infty}dx_z\frac{x_z}{(x_\perp^2+1-2x_\perp\cos\phi+x_z^2)^{3/2}}\mathcal{G}(x_\perp,x_z,\phi). \tag{D.66}$$

Next we caluclate $\mathcal{G}(x_\perp,x_z,\phi)$ using Eq. (D.63):

$$\mathcal{G}(x_\perp,x_z,\phi) \approx \frac{1}{\pi}\sqrt{x_F^2-(x_z+\delta)^2-(x_\perp-1)^2}\,\theta(x_F^2-(x_z+\delta)^2-(x_\perp-1)^2), \tag{D.67}$$

where $\delta \equiv \chi x_F$. This leads to

$$\begin{aligned} j_N^H(\chi) \approx \xi\frac{ef}{8\pi^3}\left(\frac{eA}{\hbar}\right)^2&\int_{-x_F-\delta}^{x_F-\delta}dx_z\int_{1-\sqrt{x_F^2-(x_z+\delta)^2}}^{1+\sqrt{x_F^2-(x_z+\delta)^2}}dx_\perp\, x_\perp\times \\ &\int_0^{2\pi}d\phi\frac{\sqrt{x_F^2-(x_z+\delta)^2-(x_\perp-1)^2}}{[x_\perp^2+1-2x_\perp\cos\phi+x_z^2]^{3/2}}x_z. \end{aligned} \tag{D.68}$$

We first perform integration over ϕ by expanding the integrand around $\phi \sim \pi$, where the integrand is largest

$$\int_0^{2\pi} d\phi \frac{1}{[x_\perp^2 + 1 - 2x_\perp \cos\phi + x_z^2]^{3/2}} \approx \frac{1}{x_\perp^{3/2}} \frac{2}{x_z^2 + \delta x_\perp^2}, \tag{D.69}$$

where $\delta x_\perp \equiv x_\perp - 1$. Therefore,

$$j_N^H(\chi) \approx \xi \frac{ef}{4\pi^3} \left(\frac{eA}{\hbar}\right)^2 \int_{-x_F-\delta}^{x_F-\delta} dx_z \int_{-\sqrt{x_F^2-(x_z+\delta)^2}}^{\sqrt{x_F^2-(x_z+\delta)^2}} d\delta x \frac{\sqrt{x_F^2 - (x_z+\delta)^2 - \delta x_\perp^2}}{x_z^2 + \delta x_\perp^2} x_z. \tag{D.70}$$

Transforming to the shifted coordinates $x_z' = x_z + \delta$, we find

$$j_N^H(\chi) \approx \xi \frac{ef}{4\pi^3} \left(\frac{eA}{\hbar}\right)^2 \int_{-x_F}^{x_F} dx_z' \int_{-\sqrt{x_F^2-(x_z')^2}}^{\sqrt{x_F^2-(x_z')^2}} d\delta x \frac{\sqrt{x_F^2 - (x_z')^2 - \delta x_\perp^2}}{(x_z'-\delta)^2 + \delta x_\perp^2} (x_z' - \delta). \tag{D.71}$$

We now use the integral identity

$$\int_{-a}^{a} dx \frac{\sqrt{a^2 - x^2}}{b^2 + x^2} = \pi \left[\sqrt{1 + \frac{a^2}{b^2}} - 1\right] \tag{D.72}$$

to obtain

$$\int_{-\sqrt{x_F^2-(x_z')^2}}^{\sqrt{x_F^2-(x_z')^2}} d\delta x \frac{\sqrt{x_F^2 - (x_z')^2 - \delta x_\perp^2}}{(x_z'-\delta)^2 + \delta x_\perp^2} = \pi \sqrt{1 + \frac{x_F^2 - (x_z')^2}{(x_z'-\delta)^2}} - \pi. \tag{D.73}$$

Therefore,

$$j_N^H(\chi) = \xi \frac{ef}{4\pi^2} \left(\frac{eA}{\hbar}\right)^2 \int_{-x_F}^{x_F} dx_z' \left[\mathrm{sign}(x_z'-\delta)\sqrt{x_F^2 - (x_z')^2 + (x_z'-\delta)^2} - (x_z'-\delta)\right]. \tag{D.74}$$

Finally, upon integrating over x_z' and expanding in χ, we find

$$j_N^H(\chi) \approx -\xi \frac{ef}{4\pi^2} \left(\frac{eA}{\hbar}\right)^2 x_F^2 \chi \quad for \quad k_F \ll eA/\hbar. \tag{D.75}$$

Current $j_{N,G}^\eta$ and $j_{P,G}^\eta$ for $\chi \ll 1$ and $k_F \ll eA/\hbar$

Lastly, we consider the effect of the tilt on the in-plane current components produced by the group velocity of electrons. The group velocity contribution to the currents perpendicular and parallel to the electric field $\boldsymbol{E}(t)$ are respectively given by

$$j_{N,G}^\eta = c_\eta e v_F \int \frac{d^3\boldsymbol{k}}{(2\pi)^3} \frac{k_x - eA/\hbar}{\sqrt{[k_x + eA/\hbar]^2 + k_y^2 + k_z^2}} g_1(\boldsymbol{k}, 0), \tag{D.76}$$

$$j_{P,G}^\eta = c_\eta e v_F \int \frac{d^3\boldsymbol{k}}{(2\pi)^3} \frac{k_y}{\sqrt{[k_x + eA/\hbar]^2 + k_y^2 + k_z^2}} g_1(\boldsymbol{k}, 0), \tag{D.77}$$

as predicted by the semiclassical equations of motion [see Section D.2 for details].

Transforming Eq. (D.76) into the dimensionless cylindrical coordinates parameterized by $x_\perp, x_z$, and ϕ, we obtain, for $\alpha = N, P$,

$$j^\eta_{\alpha,G} \approx c_\eta \frac{e v_F}{(2\pi)^3}\left(\frac{eA}{\hbar}\right)^3 \int_0^\infty dx_\perp\, x_\perp \int_0^{2\pi} d\phi \int_{-\infty}^{\infty} dx_z \frac{h_\alpha(\phi)}{\sqrt{x_\perp^2 + 1 - 2x_\perp \cos\phi + x_z^2}}\, \mathcal{G}(x_\perp, x_z, \phi), \tag{D.78}$$

where $h_N(\phi) = 1 - x_\perp \cos\phi$ and $h_P(\phi) = -x_\perp \sin\phi$. Because $\mathcal{G}(x_\perp, x_z, \phi)$ is only nonzero when $|x_z| \lesssim k_F$ and we assume $k_F \ll eA/\hbar$, we have $x_z \ll 1$. As a result, we can approximate

$$j^\eta_{\alpha,G} \approx c_\eta \frac{e v_F}{(2\pi)^3}\left(\frac{eA}{\hbar}\right)^3 \int_0^\infty dx_\perp\, x_\perp \int_0^{2\pi} d\phi \frac{h_\alpha(\phi)}{\sqrt{x_\perp^2 + 1 - 2x_\perp \cos\phi}} \int_{-\infty}^{\infty} dx_z\, \mathcal{G}(x_\perp, x_z, \phi). \tag{D.79}$$

We now use the occupation function $\mathcal{G}(x_\perp, x_z, \phi)$ in the presence of a tilt in Eq. (D.67) to evaluate the integral above. The integral over x_z reads

$$\int_{-\infty}^{\infty} dx_z\, \mathcal{G}(x_\perp, x_z, \phi) = \int_{-\sqrt{x_F^2-(x_\perp-1)^2}-\delta}^{\sqrt{x_F^2-(x_\perp-1)^2}-\delta} dx_z\, \frac{1}{\pi}\sqrt{x_F^2 - (x_z+\delta)^2 - (x_\perp - 1)^2}, \tag{D.80}$$

which evaluates to

$$\int_{-\sqrt{x_F^2-(x_\perp-1)^2}-\delta}^{\sqrt{x_F^2-(x_\perp-1)^2}-\delta} dx_z\, \frac{1}{\pi}\sqrt{x_F^2 - (x_z+\delta)^2 - (x_\perp - 1)^2} = \frac{1}{2}[x_F^2 - (x_\perp - 1)^2], \tag{D.81}$$

which is identical to the result without a tilt, see Eq. (D.39). Thus, to first order in χ, the group velocity contribution to the in-plane currents $j^\eta_{N,G}$ and $j^\eta_{P,G}$ are unmodified relative to the isotropic case, and given by

$$j^\eta_{P,G} = 0 \quad \textit{and} \quad j^\eta_{N,G} \approx c_\eta \frac{e v_F}{3\pi^3} x_F^3 \left(\frac{eA}{\hbar}\right)^3 \quad \textit{for} \quad k_F \ll eA/\hbar, \tag{D.82}$$

for the components parallel and perpendicular to the electric field $\boldsymbol{E}(t)$, respectively.

Bibliography

[1] Dmitry Abanin, Wojciech De Roeck, Wen Wei Ho, and François Huveneers. A rigorous theory of many-body prethermalization for periodically driven and closed quantum systems. *Communications in Mathematical Physics*, 354(3): 809–827, June 2017. ISSN 1432-0916. doi: 10.1007/s00220-017-2930-x. URL http://dx.doi.org/10.1007/s00220-017-2930-x.

[2] Dmitry A. Abanin and Leonid S. Levitov. Conformal invariance and shape-dependent conductance of graphene samples. *Phys. Rev. B*, 78:035416, Jul 2008. doi: 10.1103/PhysRevB.78.035416. URL https://link.aps.org/doi/10.1103/PhysRevB.78.035416.

[3] Dmitry A. Abanin, Wojciech De Roeck, and Fran çois Huveneers. Exponentially slow heating in periodically driven many-body systems. *Phys. Rev. Lett.*, 115:256803, Dec 2015. doi: 10.1103/PhysRevLett.115.256803. URL https://link.aps.org/doi/10.1103/PhysRevLett.115.256803.

[4] Dmitry A. Abanin, Wojciech De Roeck, Wen Wei Ho, and Fran çois Huveneers. Effective hamiltonians, prethermalization, and slow energy absorption in periodically driven many-body systems. *Phys. Rev. B*, 95: 014112, Jan 2017. doi: 10.1103/PhysRevB.95.014112. URL https://link.aps.org/doi/10.1103/PhysRevB.95.014112.

[5] L. Abou-Hamdan, A. Schmitt, R. Bretel, S. Rossetti, M. Tharrault, D. Mele, A. Pierret, M. Rosticher, T. Taniguchi, K. Watanabe, C. Maestre, C. Journet, B. Toury, V. Garnier, P. Steyer, J. H. Edgar, E. Janzen, J-M. Berroir, G. Fève, G. Ménard, B. Plaçais, C. Voisin, J-P. Hugonin, E. Bailly, B. Vest, J-J. Greffet, P. Bouchon, Y. De Wilde, and E. Baudin. Electroluminescence and energy transfer mediated by hyperbolic polaritons, 2023. URL https://arxiv.org/abs/2310.08351.

[6] Sven Aeschlimann, Shunsuke A. Sato, Razvan Krause, Mariana Chávez-Cervantes, Umberto De Giovannini, Hannes Hübener, Stiven Forti, Camilla Coletti, Kerstin Hanff, Kai Rossnagel, Angel Rubio, and Isabella Gierz. Survival of floquet–bloch states in the presence of scattering. *Nano Letters*, 21(12):5028–5035, 2021. doi: 10.1021/acs.nanolett.1c00801. URL https://doi.org/10.1021/acs.nanolett.1c00801. PMID: 34082532.

[7] F.J. Ahlers, N.E. Fletcher, J. Ebbecke, and T.J.B.M. Janssen. Surface acoustic wave driven quantized current transport. *Current Applied Physics*, 4(5): 529–533, August 2004. ISSN 1567-1739. doi: 10.1016/j.cap.2004.01.012. URL http://dx.doi.org/10.1016/j.cap.2004.01.012.

[8] Iman Ahmadabadi, Hossein Dehghani, and Mohammad Hafezi. Optical conductivity and orbital magnetization of floquet vortex states. *Communications Physics*, 6(1), June 2023. ISSN 2399-3650. doi: 10.1038/s42005-023-01267-0. URL http://dx.doi.org/10.1038/s42005-023-01267-0.

[9] Sultan Almutairi, Qianfan Chen, Mikhail Tokman, and Alexey Belyanin. Four-wave mixing in weyl semimetals. *Physical Review B*, 101(23), June 2020. ISSN 2469-9969. doi: 10.1103/physrevb.101.235156. URL http://dx.doi.org/10.1103/PhysRevB.101.235156.

[10] Trond I. Andersen, Bo L. Dwyer, Javier D. Sanchez-Yamagishi, Joaquin F. Rodriguez-Nieva, Kartiek Agarwal, Kenji Watanabe, Takashi Taniguchi, Eugene A. Demler, Philip Kim, Hongkun Park, and Mikhail D. Lukin. Electron-phonon instability in graphene revealed by global and local noise probes. *Science*, 364(6436):154–157, April 2019. ISSN 1095-9203. doi: 10.1126/science.aaw2104. URL http://dx.doi.org/10.1126/science.aaw2104.

[11] Yasufumi Araki. Magnetic textures and dynamics in magnetic weyl semimetals. *Annalen der Physik*, 532(2), October 2019. ISSN 1521-3889. doi: 10.1002/andp.201900287. URL http://dx.doi.org/10.1002/andp.201900287.

[12] N. P. Armitage, E. J. Mele, and Ashvin Vishwanath. Weyl and dirac semimetals in three-dimensional solids. *Rev. Mod. Phys.*, 90:015001, Jan 2018. doi: 10.1103/RevModPhys.90.015001. URL https://link.aps.org/doi/10.1103/RevModPhys.90.015001.

[13] Phillip E. C. Ashby and J. P. Carbotte. Magneto-optical conductivity of weyl semimetals. *Phys. Rev. B*, 87:245131, Jun 2013. doi: 10.1103/PhysRevB.87.245131. URL https://link.aps.org/doi/10.1103/PhysRevB.87.245131.

[14] Phillip E. C. Ashby and J. P. Carbotte. Chiral anomaly and optical absorption in weyl semimetals. *Phys. Rev. B*, 89:245121, Jun 2014. doi: 10.1103/PhysRevB.89.245121. URL https://link.aps.org/doi/10.1103/PhysRevB.89.245121.

[15] I. A. Assi, J. P. F. LeBlanc, Martin Rodriguez-Vega, Hocine Bahlouli, and Michael Vogl. Floquet engineering and nonequilibrium topological maps in twisted trilayer graphene. *Phys. Rev. B*, 104:195429, Nov 2021. doi: 10.1103/PhysRevB.104.195429. URL https://link.aps.org/doi/10.1103/PhysRevB.104.195429.

[16] Mehrtash Babadi, Michael Knap, Ivar Martin, Gil Refael, and Eugene Demler. Theory of parametrically amplified electron-phonon superconductivity. *Phys. Rev. B*, 96:014512, Jul 2017. doi: 10.1103/PhysRevB.96.014512. URL https://link.aps.org/doi/10.1103/PhysRevB.96.014512.

[17] Utkarsh Bajpai, Mark J. H. Ku, and Branislav K. Nikolić. Robustness of quantized transport through edge states of finite length: Imaging current density in floquet topological versus quantum spin and anomalous hall insulators. *Phys. Rev. Res.*, 2:033438, Sep 2020. doi: 10.

1103/PhysRevResearch.2.033438. URL https://link.aps.org/doi/10.1103/PhysRevResearch.2.033438.

[18] Alexander A. Balandin. Phononics of graphene and related materials. *ACS Nano*, 14(5):5170–5178, April 2020. ISSN 1936-086X. doi: 10.1021/acsnano.0c02718. URL http://dx.doi.org/10.1021/acsnano.0c02718.

[19] Alexander A. Balandin and Denis L. Nika. Phononics in low-dimensional materials. *Materials Today*, 15(6):266–275, 2012. ISSN 1369-7021. doi: https://doi.org/10.1016/S1369-7021(12)70117-7. URL https://www.sciencedirect.com/science/article/pii/S1369702112701177.

[20] Aaron H. Barajas-Aguilar, Jasen Zion, Ian Sequeira, Andrew Z. Barabas, Takashi Taniguchi, Kenji Watanabe, Eric Barrett, Thomas Scaffidi, and Javier D. Sanchez-Yamagishi. Electrically-driven amplification of terahertz acoustic waves in graphene, 2023. URL https://arxiv.org/abs/2310.12225.

[21] Christopher Bäuerle, D Christian Glattli, Tristan Meunier, Fabien Portier, Patrice Roche, Preden Roulleau, Shintaro Takada, and Xavier Waintal. Coherent control of single electrons: a review of current progress. *Reports on Progress in Physics*, 81(5):056503, April 2018. ISSN 1361-6633. doi: 10.1088/1361-6633/aaa98a. URL http://dx.doi.org/10.1088/1361-6633/aaa98a.

[22] R. P. Beardsley, A. V. Akimov, M. Henini, and A. J. Kent. Coherent terahertz sound amplification and spectral line narrowing in a stark ladder superlattice. *Phys. Rev. Lett.*, 104:085501, Feb 2010. doi: 10.1103/PhysRevLett.104.085501. URL https://link.aps.org/doi/10.1103/PhysRevLett.104.085501.

[23] B. Andrei Bernevig, Zhi-Da Song, Nicolas Regnault, and Biao Lian. Twisted bilayer graphene. iii. interacting hamiltonian and exact symmetries. *Phys. Rev. B*, 103:205413, May 2021. doi: 10.1103/PhysRevB.103.205413. URL https://link.aps.org/doi/10.1103/PhysRevB.103.205413.

[24] P. Biagioni, J. S. Huang, L. Duò, M. Finazzi, and B. Hecht. Cross resonant optical antenna. *Phys. Rev. Lett.*, 102:256801, Jun 2009. doi: 10.1103/PhysRevLett.102.256801. URL https://link.aps.org/doi/10.1103/PhysRevLett.102.256801.

[25] Rafi Bistritzer and A. Macdonald. Moire bands in twisted double-layer graphene. *Proceedings of the National Academy of Sciences of the United States of America*, 108, 09 2010. doi: 10.1073/pnas.1108174108.

[26] K. I. Bolotin, K. J. Sikes, J. Hone, H. L. Stormer, and P. Kim. Temperature-dependent transport in suspended graphene. *Phys. Rev. Lett.*, 101:096802,

Aug 2008. doi: 10.1103/PhysRevLett.101.096802. URL https://link.aps.org/doi/10.1103/PhysRevLett.101.096802.

[27] Nicola Bonini, Jivtesh Garg, and Nicola Marzari. Acoustic phonon lifetimes and thermal transport in free-standing and strained graphene. *Nano Letters*, 12(6):2673–2678, May 2012. doi: 10.1021/nl202694m. URL https://doi.org/10.1021/nl202694m.

[28] Anton Bruch, Silvia Viola Kusminskiy, Gil Refael, and Felix von Oppen. Interacting adiabatic quantum motor. *Phys. Rev. B*, 97:195411, May 2018. doi: 10.1103/PhysRevB.97.195411. URL https://link.aps.org/doi/10.1103/PhysRevB.97.195411.

[29] M R Buitelaar, P J Leek, V I Talyanskii, C G Smith, D Anderson, G A C Jones, J Wei, and D H Cobden. Charge pumping and current quantization in surface acoustic-wave-driven carbon nanotube devices. *Semiconductor Science and Technology*, 21(11):S69–S77, October 2006. ISSN 1361-6641. doi: 10.1088/0268-1242/21/11/s10. URL http://dx.doi.org/10.1088/0268-1242/21/11/S10.

[30] A A Burkov. Chiral anomaly and transport in weyl metals. *Journal of Physics: Condensed Matter*, 27(11):113201, February 2015. ISSN 1361-648X. doi: 10.1088/0953-8984/27/11/113201. URL http://dx.doi.org/10.1088/0953-8984/27/11/113201.

[31] A. A. Burkov and Leon Balents. Weyl semimetal in a topological insulator multilayer. *Phys. Rev. Lett.*, 107:127205, Sep 2011. doi: 10.1103/PhysRevLett.107.127205. URL https://link.aps.org/doi/10.1103/PhysRevLett.107.127205.

[32] Raúl Bustos-Marún, Gil Refael, and Felix von Oppen. Adiabatic quantum motors. *Phys. Rev. Lett.*, 111:060802, Aug 2013. doi: 10.1103/PhysRevLett.111.060802. URL https://link.aps.org/doi/10.1103/PhysRevLett.111.060802.

[33] Hernán L. Calvo, Horacio M. Pastawski, Stephan Roche, and Luis E. F. Foa Torres. Tuning laser-induced band gaps in graphene. *Applied Physics Letters*, 98(23), June 2011. ISSN 1077-3118. doi: 10.1063/1.3597412. URL http://dx.doi.org/10.1063/1.3597412.

[34] S. Candussio, S. Bernreuter, T. Rockinger, K. Watanabe, T. Taniguchi, J. Eroms, I. A. Dmitriev, D. Weiss, and S. D. Ganichev. Terahertz radiation induced circular hall effect in graphene. *Phys. Rev. B*, 105:155416, Apr 2022. doi: 10.1103/PhysRevB.105.155416. URL https://link.aps.org/doi/10.1103/PhysRevB.105.155416.

[35] Andrea Cartella, Tobia Nova, M. Fechner, Roberto Merlin, and Andrea Cavalleri. Parametric amplification of optical phonons. *Proceedings of the National Academy of Sciences*, 115, 08 2017. doi: 10.1073/pnas.1809725115.

[36] Alberto Castro, Umberto De Giovannini, Shunsuke A. Sato, Hannes Hübener, and Angel Rubio. Floquet engineering the band structure of materials with optimal control theory. *Phys. Rev. Res.*, 4:033213, Sep 2022. doi: 10.1103/PhysRevResearch.4.033213. URL https://link.aps.org/doi/10.1103/PhysRevResearch.4.033213.

[37] A. H. Castro Neto, F. Guinea, N. M. R. Peres, K. S. Novoselov, and A. K. Geim. The electronic properties of graphene. *Rev. Mod. Phys.*, 81:109–162, Jan 2009. doi: 10.1103/RevModPhys.81.109. URL https://link.aps.org/doi/10.1103/RevModPhys.81.109.

[38] Ching-Kit Chan, Netanel H. Lindner, Gil Refael, and Patrick A. Lee. Photocurrents in weyl semimetals. *Phys. Rev. B*, 95:041104, Jan 2017. doi: 10.1103/PhysRevB.95.041104. URL https://link.aps.org/doi/10.1103/PhysRevB.95.041104.

[39] Anushya Chandran and S. L. Sondhi. Interaction-stabilized steady states in the driven $o(n)$ model. *Phys. Rev. B*, 93:174305, May 2016. doi: 10.1103/PhysRevB.93.174305. URL https://link.aps.org/doi/10.1103/PhysRevB.93.174305.

[40] Swati Chaudhary, Arbel Haim, Yang Peng, and Gil Refael. Phonon-induced floquet topological phases protected by space-time symmetries. *Phys. Rev. Res.*, 2:043431, Dec 2020. doi: 10.1103/PhysRevResearch.2.043431. URL https://link.aps.org/doi/10.1103/PhysRevResearch.2.043431.

[41] J.-H. Chen, C. Jang, S. Adam, M. S. Fuhrer, E. D. Williams, and M. Ishigami. Charged-impurity scattering in graphene. *Nature Physics*, 4(5):377–381, April 2008. ISSN 1745-2481. doi: 10.1038/nphys935. URL http://dx.doi.org/10.1038/nphys935.

[42] Qi Chen, Liang Du, and Gregory A. Fiete. Floquet band structure of a semi-dirac system. *Phys. Rev. B*, 97:035422, Jan 2018. doi: 10.1103/PhysRevB.97.035422. URL https://link.aps.org/doi/10.1103/PhysRevB.97.035422.

[43] Qianfan Chen, A. Ryan Kutayiah, Ivan Oladyshkin, Mikhail Tokman, and Alexey Belyanin. Optical properties and electromagnetic modes of weyl semimetals. *Phys. Rev. B*, 99:075137, Feb 2019. doi: 10.1103/PhysRevB.99.075137. URL https://link.aps.org/doi/10.1103/PhysRevB.99.075137.

[44] J. L. Cheng, J. E. Sipe, and S. W. Wu. Third-order optical nonlinearity of three-dimensional massless dirac fermions. *ACS Photonics*, 7(9):2515–2526, July 2020. ISSN 2330-4022. doi: 10.1021/acsphotonics.0c00836. URL http://dx.doi.org/10.1021/acsphotonics.0c00836.

[45] Hiroomi Chono, Kazuaki Takasan, and Youichi Yanase. Laser-induced topological *s*-wave superconductivity in bilayer transition metal dichalcogenides. *Phys. Rev. B*, 102:174508, Nov 2020. doi: 10.1103/PhysRevB.102.174508. URL https://link.aps.org/doi/10.1103/PhysRevB.102.174508.

[46] Kai-Chieh Chuang, Russell S Deacon, Robin J Nicholas, Kostya S Novoselov, and Andre K Geim. Cyclotron resonance of electrons and holes in graphene monolayers. *Philosophical Transactions of the Royal Society A: Mathematical, Physical and Engineering Sciences*, 366(1863):237–243, November 2007. ISSN 1471-2962. doi: 10.1098/rsta.2007.2158. URL http://dx.doi.org/10.1098/rsta.2007.2158.

[47] Roberta Citro and Monika Aidelsburger. Thouless pumping and topology. *Nature Reviews Physics*, 5(2):87–101, January 2023. ISSN 2522-5820. doi: 10.1038/s42254-022-00545-0. URL http://dx.doi.org/10.1038/s42254-022-00545-0.

[48] Justin W. Cleary, Evan M. Smith, Kevin D. Leedy, Gordon Grzybowski, and Junpeng Guo. Optical and electrical properties of ultra-thin indium tin oxide nanofilms on silicon for infrared photonics. *Optical Materials Express*, 8 (5):1231, April 2018. ISSN 2159-3930. doi: 10.1364/ome.8.001231. URL http://dx.doi.org/10.1364/ome.8.001231.

[49] Alexis Coissard, David Wander, Hadrien Vignaud, Adolfo G. Grushin, Cécile Repellin, Kenji Watanabe, Takashi Taniguchi, Frédéric Gay, Clemens B. Winkelmann, Hervé Courtois, Hermann Sellier, and Benjamin Sacépé. Imaging tunable quantum Hall broken-symmetry orders in graphene. *Nature*, 605 (7908):51–56, May 2022. ISSN 1476-4687. doi: 10.1038/s41586-022-04513-7. URL https://doi.org/10.1038/s41586-022-04513-7.

[50] Xin Cong, Qiao-Qiao Li, Xin Zhang, Miao-Ling Lin, Jiang-Bin Wu, Xue-Lu Liu, P. Venezuela, and Ping-Heng Tan. Probing the acoustic phonon dispersion and sound velocity of graphene by raman spectroscopy. *Carbon*, 149:19–24, August 2019. ISSN 0008-6223. doi: 10.1016/j.carbon.2019.04.006. URL http://dx.doi.org/10.1016/j.carbon.2019.04.006.

[51] Alberto Cortijo. Magnetic-field-induced nonlinear optical responses in inversion symmetric dirac semimetals. *Phys. Rev. B*, 94:235123, Dec 2016. doi: 10.1103/PhysRevB.94.235123. URL https://link.aps.org/doi/10.1103/PhysRevB.94.235123.

[52] J. Costello, S. O'Hara, Qile Wu, D. Valovcin, L. Pfeiffer, K. West, and M. Sherwin. Reconstruction of bloch wavefunctions of holes in a semiconductor. *Nature*, 599:57–61, 11 2021. doi: 10.1038/s41586-021-03940-2.

[53] S. Dai, Q. Ma, M. K. Liu, T. Andersen, Z. Fei, M. D. Goldflam, M. Wagner, K. Watanabe, T. Taniguchi, M. Thiemens, F. Keilmann, G. C. A. M. Janssen, S-E. Zhu, P. Jarillo-Herrero, M. M. Fogler, and D. N. Basov. Graphene

on hexagonal boron nitride as a tunable hyperbolic metamaterial. *Nature Nanotechnology*, 10(8):682–686, June 2015. ISSN 1748-3395. doi: 10.1038/nnano.2015.131. URL http://dx.doi.org/10.1038/nnano.2015.131.

[54] Luca D'Alessio and Marcos Rigol. Long-time behavior of isolated periodically driven interacting lattice systems. *Phys. Rev. X*, 4:041048, Dec 2014. doi: 10.1103/PhysRevX.4.041048. URL https://link.aps.org/doi/10.1103/PhysRevX.4.041048.

[55] Renato M. A. Dantas, Zhe Wang, Piotr Surówka, and Takashi Oka. Nonperturbative topological current in weyl and dirac semimetals in laser fields. *Phys. Rev. B*, 103:L201105, May 2021. doi: 10.1103/PhysRevB.103.L201105. URL https://link.aps.org/doi/10.1103/PhysRevB.103.L201105.

[56] Y. J. Dappe, M. A. Basanta, F. Flores, and J. Ortega. Weak chemical interaction and van der waals forces between graphene layers: A combined density functional and intermolecular perturbation theory approach. *Phys. Rev. B*, 74:205434, Nov 2006. doi: 10.1103/PhysRevB.74.205434. URL https://link.aps.org/doi/10.1103/PhysRevB.74.205434.

[57] Kunal K. Das, Sungjun Kim, and Ari Mizel. Controlled flow of spin-entangled electrons via adiabatic quantum pumping. *Phys. Rev. Lett.*, 97:096602, Aug 2006. doi: 10.1103/PhysRevLett.97.096602. URL https://link.aps.org/doi/10.1103/PhysRevLett.97.096602.

[58] Fernando de Juan, Adolfo G. Grushin, Takahiro Morimoto, and Joel E Moore. Quantized circular photogalvanic effect in weyl semimetals. *Nature Communications*, 8(1), July 2017. ISSN 2041-1723. doi: 10.1038/ncomms15995. URL http://dx.doi.org/10.1038/ncomms15995.

[59] Alberto de la Torre, Dante M. Kennes, Martin Claassen, Simon Gerber, James W. McIver, and Michael A. Sentef. Colloquium: Nonthermal pathways to ultrafast control in quantum materials. *Rev. Mod. Phys.*, 93:041002, Oct 2021. doi: 10.1103/RevModPhys.93.041002. URL https://link.aps.org/doi/10.1103/RevModPhys.93.041002.

[60] C. R. Dean, A. F. Young, I. Meric, C. Lee, L. Wang, S. Sorgenfrei, K. Watanabe, T. Taniguchi, P. Kim, K. L. Shepard, and J. Hone. Boron nitride substrates for high-quality graphene electronics. *Nature Nanotechnology*, 5(10): 722–726, August 2010. ISSN 1748-3395. doi: 10.1038/nnano.2010.172. URL http://dx.doi.org/10.1038/nnano.2010.172.

[61] Hossein Dehghani and Aditi Mitra. Floquet topological systems in the vicinity of band crossings: Reservoir-induced coherence and steady-state entropy production. *Phys. Rev. B*, 93:245416, Jun 2016. doi: 10.1103/PhysRevB.93.245416. URL https://link.aps.org/doi/10.1103/PhysRevB.93.245416.

[62] Hossein Dehghani, Takashi Oka, and Aditi Mitra. Dissipative floquet topological systems. *Phys. Rev. B*, 90:195429, Nov 2014. doi: 10.1103/PhysRevB.90.195429. URL https://link.aps.org/doi/10.1103/PhysRevB.90.195429.

[63] Hossein Dehghani, Takashi Oka, and Aditi Mitra. Out-of-equilibrium electrons and the hall conductance of a floquet topological insulator. *Phys. Rev. B*, 91:155422, Apr 2015. doi: 10.1103/PhysRevB.91.155422. URL https://link.aps.org/doi/10.1103/PhysRevB.91.155422.

[64] Hossein Dehghani, Mohammad Hafezi, and Pouyan Ghaemi. Light-induced topological superconductivity via floquet interaction engineering. *Phys. Rev. Res.*, 3:023039(R), Apr 2021. doi: 10.1103/PhysRevResearch.3.023039. URL https://link.aps.org/doi/10.1103/PhysRevResearch.3.023039.

[65] Rémi Desbuquois, Michael Messer, Frederik Görg, Kilian Sandholzer, Gregor Jotzu, and Tilman Esslinger. Controlling the floquet state population and observing micromotion in a periodically driven two-body quantum system. *Phys. Rev. A*, 96:053602, Nov 2017. doi: 10.1103/PhysRevA.96.053602. URL https://link.aps.org/doi/10.1103/PhysRevA.96.053602.

[66] Daniel Destraz, Lakshmi Das, Stepan S. Tsirkin, Yang Xu, Titus Neupert, J. Chang, A. Schilling, Adolfo G. Grushin, Joachim Kohlbrecher, Lukas Keller, Pascal Puphal, Ekaterina Pomjakushina, and Jonathan S. White. Magnetism and anomalous transport in the weyl semimetal pralge: possible route to axial gauge fields. *npj Quantum Materials*, 5(1), January 2020. ISSN 2397-4648. doi: 10.1038/s41535-019-0207-7. URL http://dx.doi.org/10.1038/s41535-019-0207-7.

[67] Shaina Dhamija, Garima Bhutani, Ajay Jayachandran, and Arijit K. De. A revisit on impulsive stimulated raman spectroscopy: Importance of spectral dispersion of chirped broadband probe. *The Journal of Physical Chemistry A*, 126(7):1019–1032, February 2022. ISSN 1520-5215. doi: 10.1021/acs.jpca.1c10566. URL http://dx.doi.org/10.1021/acs.jpca.1c10566.

[68] Ankit S. Disa, Tobia F. Nova, and Andrea Cavalleri. Engineering crystal structures with light. *Nature Physics*, 17(10):1087–1092, October 2021. ISSN 1745-2481. doi: 10.1038/s41567-021-01366-1. URL http://dx.doi.org/10.1038/s41567-021-01366-1.

[69] P. Dore, A. Paolone, and R. Trippetti. Mid-infrared and near-infrared properties of srtio3 from transmission and reflection measurements. *Journal of Applied Physics*, 80(9):5270–5274, 1996. doi: 10.1063/1.363513. URL https://doi.org/10.1063/1.363513.

[70] M. V. Durnev. Photovoltaic hall effect in the two-dimensional electron gas: Kinetic theory. *Phys. Rev. B*, 104:085306, Aug 2021. doi:

10.1103/PhysRevB.104.085306. URL https://link.aps.org/doi/10.1103/PhysRevB.104.085306.

[71] J. Ebbecke, C. J. Strobl, and A. Wixforth. Acoustoelectric current transport through single-walled carbon nanotubes. *Phys. Rev. B*, 70:233401, Dec 2004. doi: 10.1103/PhysRevB.70.233401. URL https://link.aps.org/doi/10.1103/PhysRevB.70.233401.

[72] W. Eisfeld and K. F. Renk. Tunable optical detection and generation of terahertz phonons in CaF2 and SrF2. *Applied Physics Letters*, 34(8):481–483, April 1979. doi: 10.1063/1.90855. URL https://doi.org/10.1063/1.90855.

[73] Abdel El Fatimy, Rachael L. Myers-Ward, Anthony K. Boyd, Kevin M. Daniels, D. Kurt Gaskill, and Paola Barbara. Epitaxial graphene quantum dots for high-performance terahertz bolometers. *Nature Nanotechnology*, 11 (4):335–338, January 2016. ISSN 1748-3395. doi: 10.1038/nnano.2015.303. URL http://dx.doi.org/10.1038/nnano.2015.303.

[74] Iliya Esin, Mark S. Rudner, Gil Refael, and Netanel H. Lindner. Quantized transport and steady states of floquet topological insulators. *Phys. Rev. B*, 97:245401, Jun 2018. doi: 10.1103/PhysRevB.97.245401. URL https://link.aps.org/doi/10.1103/PhysRevB.97.245401.

[75] Iliya Esin, Mark S. Rudner, and Netanel H. Lindner. Floquet metal-to-insulator phase transitions in semiconductor nanowires. *Science Advances*, 6(35):eaay4922, 2020. doi: 10.1126/sciadv.aay4922. URL https://www.science.org/doi/abs/10.1126/sciadv.aay4922.

[76] Iliya Esin, Gaurav Gupta, Erez Berg, Mark Rudner, and Netanel Lindner. Electronic floquet gyro-liquid crystal. *Nature Communications*, 12, 09 2021. doi: 10.1038/s41467-021-25511-9.

[77] Iliya Esin, Ilya Esterlis, Eugene Demler, and Gil Refael. Generating coherent phonon waves in narrow-band materials: A twisted bilayer graphene phaser. *Phys. Rev. Lett.*, 130:147001, Apr 2023. doi: 10.1103/PhysRevLett.130.147001. URL https://link.aps.org/doi/10.1103/PhysRevLett.130.147001.

[78] Iliya Esin, Clemens Kuhlenkamp, Gil Refael, Erez Berg, Mark S. Rudner, and Netanel H. Lindner. Universal transport in periodically driven systems without long-lived quasiparticles. *Phys. Rev. Res.*, 6:013094, Jan 2024. doi: 10.1103/PhysRevResearch.6.013094. URL https://link.aps.org/doi/10.1103/PhysRevResearch.6.013094.

[79] Davood Fathi. A review of electronic band structure of graphene and carbon nanotubes using tight binding. *Journal of Nanotechnology*, 2011, 01 2011. doi: 10.1155/2011/471241.

[80] D. Fausti, R. I. Tobey, N. Dean, S. Kaiser, A. Dienst, M. C. Hoffmann, S. Pyon, T. Takayama, H. Takagi, and A. Cavalleri. Light-induced superconductivity in a stripe-ordered cuprate. *Science*, 331(6014):189–191, 2011. doi: 10.1126/science.1197294. URL https://www.science.org/doi/abs/10.1126/science.1197294.

[81] Serena Fazzini, Piotr Chudzinski, Christoph Dauer, Imke Schneider, and Sebastian Eggert. Nonequilibrium floquet steady states of time-periodic driven luttinger liquids. *Phys. Rev. Lett.*, 126:243401, Jun 2021. doi: 10.1103/PhysRevLett.126.243401. URL https://link.aps.org/doi/10.1103/PhysRevLett.126.243401.

[82] N. E. Fletcher, J. Ebbecke, T. J. B. M. Janssen, F. J. Ahlers, M. Pepper, H. E. Beere, and D. A. Ritchie. Quantized acoustoelectric current transport through a static quantum dot using a surface acoustic wave. *Phys. Rev. B*, 68:245310, Dec 2003. doi: 10.1103/PhysRevB.68.245310. URL https://link.aps.org/doi/10.1103/PhysRevB.68.245310.

[83] N. Fläschner, B. S. Rem, M. Tarnowski, D. Vogel, D.-S. Lühmann, K. Sengstock, and C. Weitenberg. Experimental reconstruction of the berry curvature in a floquet bloch band. *Science*, 352(6289):1091–1094, 2016. doi: 10.1126/science.aad4568. URL https://www.science.org/doi/abs/10.1126/science.aad4568.

[84] L. E. F. Foa Torres, P. M. Perez-Piskunow, C. A. Balseiro, and Gonzalo Usaj. Multiterminal conductance of a floquet topological insulator. *Phys. Rev. Lett.*, 113:266801, Dec 2014. doi: 10.1103/PhysRevLett.113.266801. URL https://link.aps.org/doi/10.1103/PhysRevLett.113.266801.

[85] M. Först, C. Manzoni, S. Kaiser, Y. Tomioka, Y. Tokura, R. Merlin, and A. Cavalleri. Nonlinear phononics as an ultrafast route to lattice control. *Nature Physics*, 7(11):854–856, August 2011. ISSN 1745-2481. doi: 10.1038/nphys2055. URL http://dx.doi.org/10.1038/nphys2055.

[86] Kazuyuki Fujii. Introduction to the rotating wave approximation (rwa): Two coherent oscillations. *Journal of Modern Physics*, 08(12):2042–2058, 2017. ISSN 2153-120X. doi: 10.4236/jmp.2017.812124. URL http://dx.doi.org/10.4236/jmp.2017.812124.

[87] Takahiro Fukui, Yasuhiro Hatsugai, and Hiroshi Suzuki. Chern numbers in discretized brillouin zone: Efficient method of computing (spin) hall conductances. *Journal of the Physical Society of Japan*, 74(6):1674–1677, 2005. doi: 10.1143/JPSJ.74.1674. URL https://doi.org/10.1143/JPSJ.74.1674.

[88] G. Fève, A. Mahé, J.-M. Berroir, T. Kontos, B. Plaçais, D. C. Glattli, A. Cavanna, B. Etienne, and Y. Jin. An on-demand coherent single-electron source. *Science*, 316(5828):1169–1172, May 2007. ISSN 1095-

9203. doi: 10.1126/science.1141243. URL http://dx.doi.org/10.1126/science.1141243.

[89] Michael Först, Cristian Manzoni, Stefan Kaiser, Yasuhide Tomioka, Yoshinori Tokura, Roberto Merlin, and Andrea Cavalleri. Nonlinear phononics: A new ultrafast route to lattice control. *Nature Physics*, 7, 01 2011. doi: 10.1038/NPHYS2055.

[90] V M Galitskii and V F Elesin. Electric and Magnetic Properties of a Semiconductor in the Field of a Strong Electromagnetic Wave. *Journal of Experimental and Theoretical Physics*, 30(1), 1970.

[91] Qiang Gao and Qian Niu. Semiclassical dynamics of electrons in a spacetime crystal: Magnetization, polarization, and current response. *Phys. Rev. B*, 106:224311, Dec 2022. doi: 10.1103/PhysRevB.106.224311. URL https://link.aps.org/doi/10.1103/PhysRevB.106.224311.

[92] M.E. Garcia, T. Dumitrică, and H.O. Jeschke. Laser-induced coherent phonons in graphite and carbon nanotubes: model and simulations. *Applied Physics A*, 79(4–6):855–857, September 2004. ISSN 1432-0630. doi: 10.1007/s00339-004-2690-2. URL http://dx.doi.org/10.1007/s00339-004-2690-2.

[93] Maximilian Genske and Achim Rosch. Floquet-boltzmann equation for periodically driven fermi systems. *Phys. Rev. A*, 92:062108, Dec 2015. doi: 10.1103/PhysRevA.92.062108. URL https://link.aps.org/doi/10.1103/PhysRevA.92.062108.

[94] S. Ghosh, I. Calizo, D. Teweldebrhan, E. P. Pokatilov, D. L. Nika, A. A. Balandin, W. Bao, F. Miao, and C. N. Lau. Extremely high thermal conductivity of graphene: Prospects for thermal management applications in nanoelectronic circuits. *Applied Physics Letters*, 92(15), April 2008. ISSN 1077-3118. doi: 10.1063/1.2907977. URL http://dx.doi.org/10.1063/1.2907977.

[95] Stephen P Giblin, Akira Fujiwara, Gento Yamahata, Myung-Ho Bae, Nam Kim, Alessandro Rossi, Mikko Möttönen, and Masaya Kataoka. Evidence for universality of tunable-barrier electron pumps. *Metrologia*, 56(4):044004, July 2019. ISSN 1681-7575. doi: 10.1088/1681-7575/ab29a5. URL http://dx.doi.org/10.1088/1681-7575/ab29a5.

[96] Flavio Giorgianni, Mattia Udina, Tommaso Cea, Eugenio Paris, Marco Caputo, Milan Radovic, Larissa Boie, Joe Sakai, Christof W. Schneider, and Steven Lee Johnson. Terahertz displacive excitation of a coherent raman-active phonon in v2o3. *Communications Physics*, 5(1), April 2022. doi: 10.1038/s42005-022-00882-7. URL https://doi.org/10.1038/s42005-022-00882-7.

[97] Steven M. Girvin and Kun Yang. *Modern Condensed Matter Physics*. Cambridge University Press, February 2019. ISBN 9781107137394. doi: 10.1017/9781316480649. URL http://dx.doi.org/10.1017/9781316480649.

[98] E. V. Gorbar, V. A. Miransky, I. A. Shovkovy, and P. O. Sukhachov. Anomalous transport properties of dirac and weyl semimetals (review article). *Low Temperature Physics*, 44(6):487–505, June 2018. ISSN 1090-6517. doi: 10.1063/1.5037551. URL http://dx.doi.org/10.1063/1.5037551.

[99] A. X. Gray, M. C. Hoffmann, J. Jeong, N. P. Aetukuri, D. Zhu, H. Y. Hwang, N. C. Brandt, H. Wen, A. J. Sternbach, S. Bonetti, A. H. Reid, R. Kukreja, C. Graves, T. Wang, P. Granitzka, Z. Chen, D. J. Higley, T. Chase, E. Jal, E. Abreu, M. K. Liu, T.-C. Weng, D. Sokaras, D. Nordlund, M. Chollet, R. Alonso-Mori, H. Lemke, J. M. Glownia, M. Trigo, Y. Zhu, H. Ohldag, J. W. Freeland, M. G. Samant, J. Berakdar, R. D. Averitt, K. A. Nelson, S. S. P. Parkin, and H. A. Dürr. Ultrafast terahertz field control of electronic and structural interactions in vanadium dioxide. *Phys. Rev. B*, 98:045104, Jul 2018. doi: 10.1103/PhysRevB.98.045104. URL https://link.aps.org/doi/10.1103/PhysRevB.98.045104.

[100] Ivan S. Grudinin, Hansuek Lee, O. Painter, and Kerry J. Vahala. Phonon laser action in a tunable two-level system. *Phys. Rev. Lett.*, 104:083901, Feb 2010. doi: 10.1103/PhysRevLett.104.083901. URL https://link.aps.org/doi/10.1103/PhysRevLett.104.083901.

[101] F. Guinea, M. I. Katsnelson, and M. A. H. Vozmediano. Midgap states and charge inhomogeneities in corrugated graphene. *Phys. Rev. B*, 77:075422, Feb 2008. doi: 10.1103/PhysRevB.77.075422. URL https://link.aps.org/doi/10.1103/PhysRevB.77.075422.

[102] Cheng Guo, Viktar S. Asadchy, Bo Zhao, and Shanhui Fan. Light control with weyl semimetals. *eLight*, 3(1), January 2023. ISSN 2662-8643. doi: 10.1186/s43593-022-00036-w. URL http://dx.doi.org/10.1186/s43593-022-00036-w.

[103] Qiushi Guo, Iliya Esin, Cheng Li, Chen Chen, Song Liu, James H. Edgar, Selina Zhou, Eugene Demler, Gil Refael, and Fengnian Xia. Hyperbolic phonon-polariton electroluminescence in graphene-hbn van der waals heterostructures, 2023. URL https://arxiv.org/abs/2310.03926.

[104] Qiushi Guo, Iliya Esin, Cheng Li, Chen Chen, Guanyu Han, Song Liu, James H. Edgar, Selina Zhou, Eugene Demler, Gil Refael, and Fengnian Xia. Hyperbolic phonon-polariton electroluminescence in 2d heterostructures. *Nature*, 639(8056):915–921, March 2025. ISSN 1476-4687. doi: 10.1038/s41586-025-08686-9. URL http://dx.doi.org/10.1038/s41586-025-08686-9.

[105] Noriaki Hamada, S.I. Sawada, and Atsushi Oshiyama. New one-dimensional conductors: Graphitic microtubules. *Phys. Rev. Lett.*, 68:1579–1581, Mar 1992. doi: 10.1103/PhysRevLett.68.1579. URL https://link.aps.org/doi/10.1103/PhysRevLett.68.1579.

[106] S Ould Saad Hamady and A Karsaklian dal Bosco. Low temperature transparent ito-based contacts for mid-ir applications. *MRS Online Proceedings Library (OPL)*, 1327:mrss11–1327, 2011.

[107] Xingyue Han, Anastasios Markou, Jonathan Stensberg, Yan Sun, Claudia Felser, and Liang Wu. Giant intrinsic anomalous terahertz faraday rotation in the magnetic weyl semimetal co_2MnGa at room temperature. *Phys. Rev. B*, 105:174406, May 2022. doi: 10.1103/PhysRevB.105.174406. URL https://link.aps.org/doi/10.1103/PhysRevB.105.174406.

[108] Daniel Z. Haxell, Marco Coraiola, Deividas Sabonis, Manuel Hinderling, Sofieke C. ten Kate, Erik Cheah, Filip Krizek, Rüdiger Schott, Werner Wegscheider, Wolfgang Belzig, Juan Carlos Cuevas, and Fabrizio Nichele. Microwave-induced conductance replicas in hybrid josephson junctions without floquet—andreev states. *Nature Communications*, 14(1), October 2023. ISSN 2041-1723. doi: 10.1038/s41467-023-42357-5. URL http://dx.doi.org/10.1038/s41467-023-42357-5.

[109] M. Henstridge, M. Först, E. Rowe, M. Fechner, and A. Cavalleri. Nonlocal nonlinear phononics. *Nature Physics*, 18(4):457–461, March 2022. ISSN 1745-2481. doi: 10.1038/s41567-022-01512-3. URL http://dx.doi.org/10.1038/s41567-022-01512-3.

[110] Daniel W. Hone, Roland Ketzmerick, and Walter Kohn. Statistical mechanics of floquet systems: The pervasive problem of near degeneracies. *Phys. Rev. E*, 79:051129, May 2009. doi: 10.1103/PhysRevE.79.051129. URL https://link.aps.org/doi/10.1103/PhysRevE.79.051129.

[111] Inbar Hotzen Grinberg, Mao Lin, Cameron Harris, Wladimir Benalcazar, Christopher Peterson, Taylor Hughes, and Gaurav Bahl. Robust temporal pumping in a magneto-mechanical topological insulator. *Nature Communications*, 11, 02 2020. doi: 10.1038/s41467-020-14804-0.

[112] Jin Hu, Su-Yang Xu, Ni Ni, and Zhiqiang Mao. Transport of topological semimetals. *Annual Review of Materials Research*, 49(1):207–252, July 2019. ISSN 1545-4118. doi: 10.1146/annurev-matsci-070218-010023. URL http://dx.doi.org/10.1146/annurev-matsci-070218-010023.

[113] Shin-Ming Huang, Su-Yang Xu, Ilya Belopolski, Chi-Cheng Lee, Guoqing Chang, Tay-Rong Chang, BaoKai Wang, Nasser Alidoust, Guang Bian, Madhab Neupane, Daniel Sanchez, Hao Zheng, Horng-Tay Jeng, Arun Bansil, Titus Neupert, Hsin Lin, and M. Zahid Hasan. New type of weyl semimetal with quadratic double weyl fermions. *Proceedings of the National Academy*

of Sciences, 113(5):1180–1185, January 2016. ISSN 1091-6490. doi: 10.1073/pnas.1514581113. URL http://dx.doi.org/10.1073/pnas.1514581113.

[114] Hannes Hübener, Umberto De Giovannini, and Angel Rubio. Phonon driven floquet matter. *Nano Letters*, 18, 01 2018. doi: 10.1021/acs.nanolett.7b05391.

[115] S. Ibáñez, A. Peralta Conde, D. Guéry-Odelin, and J. G. Muga. Interaction of strongly chirped pulses with two-level atoms. *Phys. Rev. A*, 84:013428, Jul 2011. doi: 10.1103/PhysRevA.84.013428. URL https://link.aps.org/doi/10.1103/PhysRevA.84.013428.

[116] Michael Ip, Anthony Ransford, Andrew M. Jayich, Xueping Long, Conrad Roman, and Wesley C. Campbell. Phonon lasing from optical frequency comb illumination of trapped ions. *Phys. Rev. Lett.*, 121:043201, Jul 2018. doi: 10.1103/PhysRevLett.121.043201. URL https://link.aps.org/doi/10.1103/PhysRevLett.121.043201.

[117] Hiroaki Ishizuka, Tomoya Hayata, Masahito Ueda, and Naoto Nagaosa. Emergent electromagnetic induction and adiabatic charge pumping in noncentrosymmetric weyl semimetals. *Phys. Rev. Lett.*, 117:216601, Nov 2016. doi: 10.1103/PhysRevLett.117.216601. URL https://link.aps.org/doi/10.1103/PhysRevLett.117.216601.

[118] Hiroaki Ishizuka, Tomoya Hayata, Masahito Ueda, and Naoto Nagaosa. Momentum-space electromagnetic induction in weyl semimetals. *Phys. Rev. B*, 95:245211, Jun 2017. doi: 10.1103/PhysRevB.95.245211. URL https://link.aps.org/doi/10.1103/PhysRevB.95.245211.

[119] Hiroaki Ishizuka, Ali Fahimniya, Francisco Guinea, and Leonid Levitov. Purcell-like enhancement of electron–phonon interactions in long-period superlattices: Linear-temperature resistivity and cooling power. *Nano Letters*, 21(18):7465–7471, 2021. doi: 10.1021/acs.nanolett.1c00565. URL https://doi.org/10.1021/acs.nanolett.1c00565. PMID: 34515488.

[120] S. Ito, M. Schüler, M. Meierhofer, S. Schlauderer, J. Freudenstein, J. Reimann, D. Afanasiev, K. A. Kokh, O. E. Tereshchenko, J. Güdde, M. A. Sentef, U. Höfer, and R. Huber. Build-up and dephasing of floquet–bloch bands on subcycle timescales. *Nature*, 616(7958):696–701, April 2023. ISSN 1476-4687. doi: 10.1038/s41586-023-05850-x. URL http://dx.doi.org/10.1038/s41586-023-05850-x.

[121] Zhurun Ji, Gerui Liu, Zachariah Addison, Wenjing Liu, Peng Yu, Heng Gao, Zheng Liu, Andrew M. Rappe, Charles L. Kane, Eugene J. Mele, and Ritesh Agarwal. Spatially dispersive circular photogalvanic effect in a weyl semimetal. *Nature Materials*, 18(9):955–962, July 2019. ISSN 1476-4660.

doi: 10.1038/s41563-019-0421-5. URL http://dx.doi.org/10.1038/s41563-019-0421-5.

[122] Zhurun Ji, Wenjing Liu, Sergiy Krylyuk, Xiaopeng Fan, Zhifeng Zhang, Anlian Pan, Liang Feng, Albert Davydov, and Ritesh Agarwal. Photocurrent detection of the orbital angular momentum of light. *Science*, 368(6492): 763–767, May 2020. ISSN 1095-9203. doi: 10.1126/science.aba9192. URL http://dx.doi.org/10.1126/science.aba9192.

[123] Hui Jing, S. K. Özdemir, Xin-You Lü, Jing Zhang, Lan Yang, and Franco Nori. $\mathcal{PT}$-symmetric phonon laser. *Phys. Rev. Lett.*, 113:053604, Jul 2014. doi: 10.1103/PhysRevLett.113.053604. URL https://link.aps.org/doi/10.1103/PhysRevLett.113.053604.

[124] Gregor Jotzu, Michael Messer, Rémi Desbuquois, Martin Lebrat, Thomas Uehlinger, Daniel Greif, and Tilman Esslinger. Experimental realization of the topological haldane model with ultracold fermions. *Nature*, 515(7526): 237–240, November 2014. ISSN 1476-4687. doi: 10.1038/nature13915. URL http://dx.doi.org/10.1038/nature13915.

[125] D. M. Juraschek, M. Fechner, and N. A. Spaldin. Ultrafast structure switching through nonlinear phononics. *Phys. Rev. Lett.*, 118:054101, Jan 2017. doi: 10.1103/PhysRevLett.118.054101. URL https://link.aps.org/doi/10.1103/PhysRevLett.118.054101.

[126] A. V. Kalameitsev, V. M. Kovalev, and I. G. Savenko. Valley acousto-electric effect. *Phys. Rev. Lett.*, 122:256801, Jun 2019. doi: 10.1103/PhysRevLett.122.256801. URL https://link.aps.org/doi/10.1103/PhysRevLett.122.256801.

[127] Nikolai G Kalugin, Lei Jing, Eric Suarez Morell, Gregory C Dyer, Lee Wickey, Mekan Ovezmyradov, Albert D Grine, Michael C Wanke, Eric A Shaner, Chun Ning Lau, Luis E F Foa Torres, Mikhail V Fistul, and Konstantin B Efetov. Photoelectric polarization-sensitive broadband photoresponse from interface junction states in graphene. *2D Materials*, 4(1):015002, October 2016. ISSN 2053-1583. doi: 10.1088/2053-1583/4/1/015002. URL http://dx.doi.org/10.1088/2053-1583/4/1/015002.

[128] C. L. Kane and E. J. Mele. Size, shape, and low energy electronic structure of carbon nanotubes. *Phys. Rev. Lett.*, 78:1932–1935, Mar 1997. doi: 10.1103/PhysRevLett.78.1932. URL https://link.aps.org/doi/10.1103/PhysRevLett.78.1932.

[129] Nobu-Hisa Kaneko, Shuji Nakamura, and Yuma Okazaki. A review of the quantum current standard. *Measurement Science and Technology*, 27(3):032001, February 2016. ISSN 1361-6501. doi: 10.1088/0957-0233/27/3/032001. URL http://dx.doi.org/10.1088/0957-0233/27/3/032001.

[130] Ouri Karni, Iliya Esin, and Keshav M. Dani. Through the lens of a momentum microscope: Viewing light-induced quantum phenomena in 2d materials. *Advanced Materials*, 35(27):2204120, 2023. doi: https://doi.org/10.1002/adma.202204120. URL https://onlinelibrary.wiley.com/doi/abs/10.1002/adma.202204120.

[131] Or Katz, Gil Refael, and Netanel H. Lindner. Optically induced flat bands in twisted bilayer graphene. *Phys. Rev. B*, 102:155123, Oct 2020. doi: 10.1103/PhysRevB.102.155123. URL https://link.aps.org/doi/10.1103/PhysRevB.102.155123.

[132] Sahal Kaushik, Dmitri E. Kharzeev, and Evan John Philip. Chiral magnetic photocurrent in dirac and weyl materials. *Phys. Rev. B*, 99:075150, Feb 2019. doi: 10.1103/PhysRevB.99.075150. URL https://link.aps.org/doi/10.1103/PhysRevB.99.075150.

[133] Takuya Kawada, Masashi Kawaguchi, Takumi Funato, Hiroshi Kohno, and Masamitsu Hayashi. Acoustic spin hall effect in strong spin-orbit metals. *Science Advances*, 7(2), January 2021. ISSN 2375-2548. doi: 10.1126/sciadv.abd9697. URL http://dx.doi.org/10.1126/sciadv.abd9697.

[134] Dante Kennes, Eli Wilner, David Reichman, and Andrew Millis. Transient superconductivity from electronic squeezing of optically pumped phonons. *Nature Physics*, 13, 01 2017. doi: 10.1038/nphys4024.

[135] Guru Khalsa, Nicole A. Benedek, and Jeffrey Moses. Ultrafast control of material optical properties via the infrared resonant raman effect. *Phys. Rev. X*, 11:021067, Jun 2021. doi: 10.1103/PhysRevX.11.021067. URL https://link.aps.org/doi/10.1103/PhysRevX.11.021067.

[136] Sergey A. Khrapak. Lindemann melting criterion in two dimensions. *Phys. Rev. Res.*, 2:012040(R), Feb 2020. doi: 10.1103/PhysRevResearch.2.012040. URL https://link.aps.org/doi/10.1103/PhysRevResearch.2.012040.

[137] Hwanmun Kim, Hossein Dehghani, Iman Ahmadabadi, Ivar Martin, and Mohammad Hafezi. Floquet vortex states induced by light carrying an orbital angular momentum. *Phys. Rev. B*, 105:L081301, Feb 2022. doi: 10.1103/PhysRevB.105.L081301. URL https://link.aps.org/doi/10.1103/PhysRevB.105.L081301.

[138] Hyungwon Kim, Tatsuhiko N. Ikeda, and David A. Huse. Testing whether all eigenstates obey the eigenstate thermalization hypothesis. *Phys. Rev. E*, 90:052105, Nov 2014. doi: 10.1103/PhysRevE.90.052105. URL https://link.aps.org/doi/10.1103/PhysRevE.90.052105.

[139] Takuya Kitagawa, Erez Berg, Mark Rudner, and Eugene Demler. Topological characterization of periodically driven quantum systems. *Phys. Rev. B*, 82:

235114, Dec 2010. doi: 10.1103/PhysRevB.82.235114. URL https://link.aps.org/doi/10.1103/PhysRevB.82.235114.

[140] Takuya Kitagawa, Takashi Oka, Arne Brataas, Liang Fu, and Eugene Demler. Transport properties of nonequilibrium systems under the application of light: Photoinduced quantum hall insulators without landau levels. *Phys. Rev. B*, 84:235108, Dec 2011. doi: 10.1103/PhysRevB.84.235108. URL https://link.aps.org/doi/10.1103/PhysRevB.84.235108.

[141] Charles Kittel. *Introduction to solid state physics*. John Wiley & Sons, Nashville, TN, 8 edition, October 2004.

[142] Michael Knap, Mehrtash Babadi, Gil Refael, Ivar Martin, and Eugene Demler. Dynamical cooper pairing in nonequilibrium electron-phonon systems. *Phys. Rev. B*, 94:214504, Dec 2016. doi: 10.1103/PhysRevB.94.214504. URL https://link.aps.org/doi/10.1103/PhysRevB.94.214504.

[143] Yuki Kobayashi, Christian Heide, Amalya C. Johnson, Vishal Tiwari, Fang Liu, David A. Reis, Tony F. Heinz, and Shambhu Ghimire. Floquet engineering of strongly driven excitons in monolayer tungsten disulfide. *Nature Physics*, January 2023. ISSN 1745-2481. doi: 10.1038/s41567-022-01849-9. URL http://dx.doi.org/10.1038/s41567-022-01849-9.

[144] Walter Kohn. *Journal of Statistical Physics*, 103(3/4):417–423, 2001. ISSN 0022-4715. doi: 10.1023/a:1010327828445. URL http://dx.doi.org/10.1023/A:1010327828445.

[145] Walter Kohn. Periodic thermodynamics. *Journal of Statistical Physics*, 103: 417–423, 05 2001. doi: 10.1023/A:1010327828445.

[146] M. Kominami, D. Pozar, and D. Schaubert. Dipole and slot elements and arrays on semi-infinite substrates. *IEEE Transactions on Antennas and Propagation*, 33(6):600–607, 1985. doi: 10.1109/TAP.1985.1143638.

[147] E. J. König, H.-Y. Xie, D. A. Pesin, and A. Levchenko. Photogalvanic effect in weyl semimetals. *Phys. Rev. B*, 96:075123, Aug 2017. doi: 10.1103/PhysRevB.96.075123. URL https://link.aps.org/doi/10.1103/PhysRevB.96.075123.

[148] Mikito Koshino and Young-Woo Son. Moiré phonons in twisted bilayer graphene. *Phys. Rev. B*, 100:075416, Aug 2019. doi: 10.1103/PhysRevB.100.075416. URL https://link.aps.org/doi/10.1103/PhysRevB.100.075416.

[149] Mikito Koshino, Noah F. Q. Yuan, Takashi Koretsune, Masayuki Ochi, Kazuhiko Kuroki, and Liang Fu. Maximally localized wannier orbitals and the extended hubbard model for twisted bilayer graphene. *Phys. Rev. X*, 8:031087, Sep 2018. doi: 10.1103/PhysRevX.8.031087. URL https://link.aps.org/doi/10.1103/PhysRevX.8.031087.

[150] O. V. Kotov and Yu. E. Lozovik. Giant tunable nonreciprocity of light in weyl semimetals. *Phys. Rev. B*, 98:195446, Nov 2018. doi: 10.1103/PhysRevB.98.195446. URL https://link.aps.org/doi/10.1103/PhysRevB.98.195446.

[151] S. S. Kubakaddi. Cerenkov emission of acoustic phonons electrically generated from three-dimensional dirac semimetals. *Journal of Applied Physics*, 119(19), May 2016. ISSN 1089-7550. doi: 10.1063/1.4949753. URL http://dx.doi.org/10.1063/1.4949753.

[152] Abhishek Kumar, M. Rodriguez-Vega, T. Pereg-Barnea, and B. Seradjeh. Linear response theory and optical conductivity of floquet topological insulators. *Phys. Rev. B*, 101:174314, May 2020. doi: 10.1103/PhysRevB.101.174314. URL https://link.aps.org/doi/10.1103/PhysRevB.101.174314.

[153] Arijit Kundu, H. A. Fertig, and Babak Seradjeh. Effective theory of floquet topological transitions. *Phys. Rev. Lett.*, 113:236803, Dec 2014. doi: 10.1103/PhysRevLett.113.236803. URL https://link.aps.org/doi/10.1103/PhysRevLett.113.236803.

[154] Arijit Kundu, Mark Rudner, Erez Berg, and Netanel H. Lindner. Quantized large-bias current in the anomalous floquet-anderson insulator. *Phys. Rev. B*, 101:041403(R), Jan 2020. doi: 10.1103/PhysRevB.101.041403. URL https://link.aps.org/doi/10.1103/PhysRevB.101.041403.

[155] Tomotaka Kuwahara, Takashi Mori, and Keiji Saito. Floquet–magnus theory and generic transient dynamics in periodically driven many-body quantum systems. *Annals of Physics*, 367:96–124, April 2016. ISSN 0003-4916. doi: 10.1016/j.aop.2016.01.012. URL http://dx.doi.org/10.1016/j.aop.2016.01.012.

[156] Jiawei Lai, Junchao Ma, Zipu Fan, Xiaoming Song, Peng Yu, Zheng Liu, Pei Zhang, Yi Shi, Jinluo Cheng, and Dong Sun. Direct light orbital angular momentum detection in mid-infrared based on the type-ii weyl semimetal tairte4. *Advanced Materials*, 34(29), June 2022. ISSN 1521-4095. doi: 10.1002/adma.202201229. URL http://dx.doi.org/10.1002/adma.202201229.

[157] N. D. Lanzillotti-Kimura, A. Fainstein, B. Perrin, and B. Jusserand. Theory of coherent generation and detection of thz acoustic phonons using optical microcavities. *Phys. Rev. B*, 84:064307, Aug 2011. doi: 10.1103/PhysRevB.84.064307. URL https://link.aps.org/doi/10.1103/PhysRevB.84.064307.

[158] Achilleas Lazarides, Arnab Das, and Roderich Moessner. Equilibrium states of generic quantum systems subject to periodic driving. *Phys. Rev. E*, 90:012110, Jul 2014. doi: 10.1103/PhysRevE.90.012110. URL https://link.aps.org/doi/10.1103/PhysRevE.90.012110.

[159] P. J. Leek, M. R. Buitelaar, V. I. Talyanskii, C. G. Smith, D. Anderson, G. A. C. Jones, J. Wei, and D. H. Cobden. Charge pumping in carbon nanotubes. *Phys. Rev. Lett.*, 95:256802, Dec 2005. doi: 10.1103/PhysRevLett.95.256802. URL https://link.aps.org/doi/10.1103/PhysRevLett.95.256802.

[160] R A Lewis. A review of terahertz sources. *Journal of Physics D: Applied Physics*, 47(37):374001, aug 2014. doi: 10.1088/0022-3727/47/37/374001. URL https://dx.doi.org/10.1088/0022-3727/47/37/374001.

[161] Cong Li, Jianfeng Zhang, Yang Wang, Hongxiong Liu, Qinda Guo, Emile Rienks, Wanyu Chen, Francois Bertran, Huancheng Yang, Dibya Phuyal, Hanna Fedderwitz, Balasubramanian Thiagarajan, Maciej Dendzik, Magnus H. Berntsen, Youguo Shi, Tao Xiang, and Oscar Tjernberg. Emergence of weyl fermions by ferrimagnetism in a noncentrosymmetric magnetic weyl semimetal. *Nature Communications*, 14(1), November 2023. ISSN 2041-1723. doi: 10.1038/s41467-023-42996-8. URL http://dx.doi.org/10.1038/s41467-023-42996-8.

[162] Nianbei Li, Jie Ren, Lei Wang, Gang Zhang, Peter Hänggi, and Baowen Li. Colloquium: Phononics: Manipulating heat flow with electronic analogs and beyond. *Rev. Mod. Phys.*, 84:1045–1066, Jul 2012. doi: 10.1103/RevModPhys.84.1045. URL https://link.aps.org/doi/10.1103/RevModPhys.84.1045.

[163] Qiuzi Li, E. H. Hwang, and S. Das Sarma. Disorder-induced temperature-dependent transport in graphene: Puddles, impurities, activation, and diffusion. *Phys. Rev. B*, 84:115442, Sep 2011. doi: 10.1103/PhysRevB.84.115442. URL https://link.aps.org/doi/10.1103/PhysRevB.84.115442.

[164] Xian Li, Tian Qiu, Jiahao Zhang, Edoardo Baldini, Jian Lu, Andrew M. Rappe, and Keith A. Nelson. Terahertz field–induced ferroelectricity in quantum paraelectric srtio 3. *Science*, 364(6445):1079–1082, June 2019. ISSN 1095-9203. doi: 10.1126/science.aaw4913. URL http://dx.doi.org/10.1126/science.aaw4913.

[165] Yantao Li, H. A. Fertig, and Babak Seradjeh. Floquet-engineered topological flat bands in irradiated twisted bilayer graphene. *Phys. Rev. Res.*, 2:043275, Nov 2020. doi: 10.1103/PhysRevResearch.2.043275. URL https://link.aps.org/doi/10.1103/PhysRevResearch.2.043275.

[166] F. Lindemann. *Z. Phys.*, 11:609, 1910.

[167] Netanel H. Lindner, Gil Refael, and Victor Galitski. Floquet topological insulator in semiconductor quantum wells. *Nat. Phys.*, 7(6):490–495, mar 2011. ISSN 1745-2473. doi: 10.1038/nphys1926. URL http://dx.doi.org/10.1038/nphys1926.

[168] D. F. Liu, A. J. Liang, E. K. Liu, Q. N. Xu, Y. W. Li, C. Chen, D. Pei, W. J. Shi, S. K. Mo, P. Dudin, T. Kim, C. Cacho, G. Li, Y. Sun, L. X. Yang, Z. K. Liu, S. S. P. Parkin, C. Felser, and Y. L. Chen. Magnetic weyl semimetal phase in a kagomé crystal. *Science*, 365(6459):1282–1285, September 2019. ISSN 1095-9203. doi: 10.1126/science.aav2873. URL http://dx.doi.org/10.1126/science.aav2873.

[169] Mengkun Liu, Harold Y. Hwang, Hu Tao, Andrew C. Strikwerda, Kebin Fan, George R. Keiser, Aaron J. Sternbach, Kevin G. West, Salinporn Kittiwatanakul, Jiwei Lu, Stuart A. Wolf, Fiorenzo G. Omenetto, Xin Zhang, Keith A. Nelson, and Richard D. Averitt. Terahertz-field-induced insulator-to-metal transition in vanadium dioxide metamaterial. *Nature*, 487(7407): 345–348, July 2012. ISSN 1476-4687. doi: 10.1038/nature11231. URL https://doi.org/10.1038/nature11231.

[170] Ling Lu, Zhiyu Wang, Dexin Ye, Lixin Ran, Liang Fu, John D. Joannopoulos, and Marin Soljačić. Experimental observation of weyl points. *Science*, 349 (6248):622–624, August 2015. ISSN 1095-9203. doi: 10.1126/science.aaa9273. URL http://dx.doi.org/10.1126/science.aaa9273.

[171] B. Q. Lv, H. M. Weng, B. B. Fu, X. P. Wang, H. Miao, J. Ma, P. Richard, X. C. Huang, L. X. Zhao, G. F. Chen, Z. Fang, X. Dai, T. Qian, and H. Ding. Experimental discovery of weyl semimetal taas. *Phys. Rev. X*, 5:031013, Jul 2015. doi: 10.1103/PhysRevX.5.031013. URL https://link.aps.org/doi/10.1103/PhysRevX.5.031013.

[172] Qiong Ma, Su-Yang Xu, Ching-Kit Chan, Cheng-Long Zhang, Guoqing Chang, Yuxuan Lin, Weiwei Xie, Tomás Palacios, Hsin Lin, Shuang Jia, Patrick A. Lee, Pablo Jarillo-Herrero, and Nuh Gedik. Direct optical detection of weyl fermion chirality in a topological semimetal. *Nature Physics*, 13 (9):842–847, May 2017. ISSN 1745-2481. doi: 10.1038/nphys4146. URL http://dx.doi.org/10.1038/nphys4146.

[173] Farzad Mahfouzi and Nicholas Kioussis. Elastodynamically induced spin and charge pumping in bulk heavy metals. *Phys. Rev. Lett.*, 128:215902, May 2022. doi: 10.1103/PhysRevLett.128.215902. URL https://link.aps.org/doi/10.1103/PhysRevLett.128.215902.

[174] Fahad Mahmood, Ching-Kit Chan, Zhanybek Alpichshev, Dillon Gardner, Young Lee, Patrick A. Lee, and Nuh Gedik. Selective scattering between floquet–bloch and volkov states in a topological insulator. *Nature Physics*, 12(4):306–310, January 2016. ISSN 1745-2481. doi: 10.1038/nphys3609. URL http://dx.doi.org/10.1038/nphys3609.

[175] Martin Maldovan. Sound and heat revolutions in phononics. *Nature*, 503: 209–17, 11 2013. doi: 10.1038/nature12608.

[176] Ermin Malic, Matthias Hirtschulz, Frank Milde, Marten Richter, Janina Maultzsch, Stephanie Reich, and Andreas Knorr. Coulomb effects in single-walled carbon nanotubes. *physica status solidi (b)*, 245:2155 – 2158, 10 2008. doi: 10.1002/pssb.200879612.

[177] R. Mankowsky, A. von Hoegen, M. Först, and A. Cavalleri. Ultrafast reversal of the ferroelectric polarization. *Phys. Rev. Lett.*, 118:197601, May 2017. doi: 10.1103/PhysRevLett.118.197601. URL https://link.aps.org/doi/10.1103/PhysRevLett.118.197601.

[178] Roman Mankowsky, A Subedi, M Först, S Mariager, Matthieu Chollet, Hilmar Lemke, J Robinson, J Glownia, Michael Minitti, Alex Frano, M. Fechner, N Spaldin, T Loew, B Keimer, A Georges, and Andrea Cavalleri. Nonlinear lattice dynamics as a basis for enhanced superconductivity in yba2cu3o6.5. *Nature*, 516:71–3, 12 2014. doi: 10.1038/nature13875.

[179] Roman Mankowsky, Michael Först, and Andrea Cavalleri. Non-equilibrium control of complex solids by nonlinear phononics. *Reports on Progress in Physics*, 79:064503, 06 2016. doi: 10.1088/0034-4885/79/6/064503.

[180] Ivar Martin, Gil Refael, and Bertrand Halperin. Topological frequency conversion in strongly driven quantum systems. *Phys. Rev. X*, 7:041008, Oct 2017. doi: 10.1103/PhysRevX.7.041008. URL https://link.aps.org/doi/10.1103/PhysRevX.7.041008.

[181] J. Martin, N. Akerman, G. Ulbricht, T. Lohmann, J. H. Smet, K. von Klitzing, and A. Yacoby. Observation of electron–hole puddles in graphene using a scanning single-electron transistor. *Nature Physics*, 4(2):144–148, November 2007. ISSN 1745-2481. doi: 10.1038/nphys781. URL http://dx.doi.org/10.1038/nphys781.

[182] W. Maryam, A. V. Akimov, R. P. Campion, and A. J. Kent. Dynamics of a vertical cavity quantum cascade phonon laser structure. *Nature Communications*, 4(1), July 2013. ISSN 2041-1723. doi: 10.1038/ncomms3184. URL http://dx.doi.org/10.1038/ncomms3184.

[183] Paweł Matus, Renato M. A. Dantas, Roderich Moessner, and Piotr Surówka. Skin effect as a probe of transport regimes in weyl semimetals. *Proceedings of the National Academy of Sciences*, 119(12), March 2022. ISSN 1091-6490. doi: 10.1073/pnas.2200367119. URL http://dx.doi.org/10.1073/pnas.2200367119.

[184] E. McCann, K. Kechedzhi, Vladimir I. Fal'ko, H. Suzuura, T. Ando, and B. L. Altshuler. Weak-localization magnetoresistance and valley symmetry in graphene. *Phys. Rev. Lett.*, 97:146805, Oct 2006. doi: 10.1103/PhysRevLett.97.146805. URL https://link.aps.org/doi/10.1103/PhysRevLett.97.146805.

[185] James McIver, B. Schulte, F.-U Stein, Toru Matsuyama, Gregor Jotzu, Guido Meier, and A. Cavalleri. Light-induced anomalous hall effect in graphene. *Nature Physics*, 16:1–4, 01 2020. doi: 10.1038/s41567-019-0698-y.

[186] T. Meier, G. von Plessen, P. Thomas, and S. W. Koch. Coherent electric-field effects in semiconductors. *Phys. Rev. Lett.*, 73:902–905, Aug 1994. doi: 10.1103/PhysRevLett.73.902. URL https://link.aps.org/doi/10.1103/PhysRevLett.73.902.

[187] Marco Merboldt, Michael Schüler, David Schmitt, Jan Philipp Bange, Wiebke Bennecke, Karun Gadge, Klaus Pierz, Hans Werner Schumacher, Davood Momeni, Daniel Steil, Salvatore R. Manmana, Michael Sentef, Marcel Reutzel, and Stefan Mathias. Observation of floquet states in graphene, 2024. URL https://arxiv.org/abs/2404.12791.

[188] Swapnil M. Mhatre, Ngoc Thanh Mai Tran, Heather M. Hill, Dipanjan Saha, Angela R. Hight Walker, Chi-Te Liang, Randolph E. Elmquist, David B. Newell, and Albert F. Rigosi. Dynamics of transient hole doping in epitaxial graphene. *Phys. Rev. B*, 105:205423, May 2022. doi: 10.1103/PhysRevB.105.205423. URL https://link.aps.org/doi/10.1103/PhysRevB.105.205423.

[189] Marios H. Michael, Michael Först, Daniele Nicoletti, Sheikh Rubaiat Ul Haque, Yuan Zhang, Andrea Cavalleri, Richard D. Averitt, Daniel Podolsky, and Eugene Demler. Generalized fresnel-floquet equations for driven quantum materials. *Phys. Rev. B*, 105:174301, May 2022. doi: 10.1103/PhysRevB.105.174301. URL https://link.aps.org/doi/10.1103/PhysRevB.105.174301.

[190] G. P. Mikitik and Yu. V. Sharlai. Magnetic susceptibility of topological semimetals. *Journal of Low Temperature Physics*, 197(3–4):272–309, August 2019. ISSN 1573-7357. doi: 10.1007/s10909-019-02225-3. URL http://dx.doi.org/10.1007/s10909-019-02225-3.

[191] J. W. Mintmire, B. I. Dunlap, and C. T. White. Are fullerene tubules metallic? *Phys. Rev. Lett.*, 68:631–634, Feb 1992. doi: 10.1103/PhysRevLett.68.631. URL https://link.aps.org/doi/10.1103/PhysRevLett.68.631.

[192] M. Mitrano, A. Cantaluppi, D. Nicoletti, S. Kaiser, A. Perucchi, S. Lupi, P. Di Pietro, D. Pontiroli, M. Riccò, S. R. Clark, D. Jaksch, and A. Cavalleri. Possible light-induced superconductivity in k3c60 at high temperature. *Nature*, 530(7591):461–464, February 2016. ISSN 1476-4687. doi: 10.1038/nature16522. URL http://dx.doi.org/10.1038/nature16522.

[193] Hendrik J. Monkhorst and James D. Pack. Special points for brillouin-zone integrations. *Phys. Rev. B*, 13:5188–5192, Jun 1976. doi: 10.1103/PhysRevB.13.5188. URL https://link.aps.org/doi/10.1103/PhysRevB.13.5188.

[194] Joel E Moore. Optical properties of weyl semimetals. *National Science Review*, 6(2):206–208, December 2018. ISSN 2053-714X. doi: 10.1093/nsr/nwy164. URL http://dx.doi.org/10.1093/nsr/nwy164.

[195] Takashi Mori. Heating rates under fast periodic driving beyond linear response. *Phys. Rev. Lett.*, 128:050604, Feb 2022. doi: 10.1103/PhysRevLett.128.050604. URL https://link.aps.org/doi/10.1103/PhysRevLett.128.050604.

[196] Takashi Mori. Floquet states in open quantum systems. *Annual Review of Condensed Matter Physics*, 14(1):35–56, March 2023. ISSN 1947-5462. doi: 10.1146/annurev-conmatphys-040721-015537. URL http://dx.doi.org/10.1146/annurev-conmatphys-040721-015537.

[197] Takahiro Morimoto, Shudan Zhong, Joseph Orenstein, and Joel E. Moore. Semiclassical theory of nonlinear magneto-optical responses with applications to topological dirac/weyl semimetals. *Phys. Rev. B*, 94:245121, Dec 2016. doi: 10.1103/PhysRevB.94.245121. URL https://link.aps.org/doi/10.1103/PhysRevB.94.245121.

[198] S. P. Mukherjee and J. P. Carbotte. Absorption of circular polarized light in tilted type-i and type-ii weyl semimetals. *Phys. Rev. B*, 96:085114, Aug 2017. doi: 10.1103/PhysRevB.96.085114. URL https://link.aps.org/doi/10.1103/PhysRevB.96.085114.

[199] Naoto Nagaosa, Takahiro Morimoto, and Yoshinori Tokura. Transport, magnetic and optical properties of weyl materials. *Nature Reviews Materials*, 5(8):621–636, June 2020. ISSN 2058-8437. doi: 10.1038/s41578-020-0208-y. URL http://dx.doi.org/10.1038/s41578-020-0208-y.

[200] Masaya Nakagawa, Tsuneya Yoshida, Robert Peters, and Norio Kawakami. Breakdown of topological thouless pumping in the strongly interacting regime. *Phys. Rev. B*, 98:115147, Sep 2018. doi: 10.1103/PhysRevB.98.115147. URL https://link.aps.org/doi/10.1103/PhysRevB.98.115147.

[201] Shuta Nakajima, Takafumi Tomita, Shintaro Taie, Tomohiro Ichinose, Hideki Ozawa, Lei Wang, Matthias Troyer, and Yoshiro Takahashi. Topological thouless pumping of ultracold fermions. *Nature Physics*, 12, 07 2015. doi: 10.1038/nphys3622.

[202] Ayano Nakamura, Shinichi Nishihaya, Hiroaki Ishizuka, Markus Kriener, Mizuki Ohno, Yuto Watanabe, Masashi Kawasaki, and Masaki Uchida. Berry curvature derived negative magnetoconductivity observed in type-ii magnetic weyl semimetal films. *Phys. Rev. B*, 109:L121108, Mar 2024. doi: 10.1103/PhysRevB.109.L121108. URL https://link.aps.org/doi/10.1103/PhysRevB.109.L121108.

[203] Frederik Nathan and Mark S. Rudner. Universal lindblad equation for open quantum systems. *Phys. Rev. B*, 102:115109, Sep 2020. doi: 10.1103/PhysRevB.102.115109. URL https://link.aps.org/doi/10.1103/PhysRevB.102.115109.

[204] Frederik Nathan, Mark S. Rudner, Netanel H. Lindner, Erez Berg, and Gil Refael. Quantized magnetization density in periodically driven systems. *Phys. Rev. Lett.*, 119:186801, Oct 2017. doi: 10.1103/PhysRevLett.119.186801. URL https://link.aps.org/doi/10.1103/PhysRevLett.119.186801.

[205] Frederik Nathan, Ivar Martin, and Gil Refael. Topological frequency conversion in weyl semimetals. *Phys. Rev. Res.*, 4:043060, Oct 2022. doi: 10.1103/PhysRevResearch.4.043060. URL https://link.aps.org/doi/10.1103/PhysRevResearch.4.043060.

[206] Ryan C. Ng, Alexandros El Sachat, Francisco Cespedes, Martin Poblet, Guilhem Madiot, Juliana Jaramillo-Fernandez, Omar Florez, Peng Xiao, Marianna Sledzinska, Clivia M. Sotomayor-Torres, and Emigdio Chavez-Angel. Excitation and detection of acoustic phonons in nanoscale systems. *Nanoscale*, 14:13428–13451, 2022. doi: 10.1039/D2NR04100F. URL http://dx.doi.org/10.1039/D2NR04100F.

[207] Simin Nie, Tatsuki Hashimoto, and Fritz B. Prinz. Magnetic weyl semimetal in $k_2mn_3(aso_4)_3$ with the minimum number of weyl points. *Phys. Rev. Lett.*, 128:176401, Apr 2022. doi: 10.1103/PhysRevLett.128.176401. URL https://link.aps.org/doi/10.1103/PhysRevLett.128.176401.

[208] H.B. Nielsen and Masao Ninomiya. The adler-bell-jackiw anomaly and weyl fermions in a crystal. *Physics Letters B*, 130(6):389–396, November 1983. ISSN 0370-2693. doi: 10.1016/0370-2693(83)91529-0. URL http://dx.doi.org/10.1016/0370-2693(83)91529-0.

[209] Q. Niu. Towards a quantum pump of electric charges. *Phys. Rev. Lett.*, 64:1812–1815, Apr 1990. doi: 10.1103/PhysRevLett.64.1812. URL https://link.aps.org/doi/10.1103/PhysRevLett.64.1812.

[210] Even Marius Nordhagen, Henrik Andersen Sveinsson, and Anders Malthe-Sørenssen. Diffusion-driven frictional aging in silicon carbide. *Tribology Letters*, 71(3), July 2023. ISSN 1573-2711. doi: 10.1007/s11249-023-01762-z. URL http://dx.doi.org/10.1007/s11249-023-01762-z.

[211] T. Nova, Ankit Disa, M. Fechner, and A. Cavalleri. Metastable ferroelectricity in optically strained srtio 3. *Science*, 364:1075–1079, 06 2019. doi: 10.1126/science.aaw4911.

[212] Kevin Nuckolls, Myungchul Oh, Dillon Wong, Biao Lian, Kenji Watanabe, Takashi Taniguchi, B. Bernevig, and Ali Yazdani. Strongly correlated chern

insulators in magic-angle twisted bilayer graphene. *Nature*, 588:1–6, 12 2020. doi: 10.1038/s41586-020-3028-8.

[213] O. A. C. Nunes and A. L. A. Fonseca. Amplification of hippersound in graphene under external direct current electric field. *Journal of Applied Physics*, 112(4), August 2012. ISSN 1089-7550. doi: 10.1063/1.4748174. URL http://dx.doi.org/10.1063/1.4748174.

[214] M. Nuske, L. Broers, B. Schulte, G. Jotzu, S. A. Sato, A. Cavalleri, A. Rubio, J. W. McIver, and L. Mathey. Floquet dynamics in light-driven solids. *Phys. Rev. Res.*, 2:043408, Dec 2020. doi: 10.1103/PhysRevResearch.2.043408. URL https://link.aps.org/doi/10.1103/PhysRevResearch.2.043408.

[215] Takashi Oka and Hideo Aoki. Photovoltaic hall effect in graphene. *Phys. Rev. B*, 79:081406(R), Feb 2009. doi: 10.1103/PhysRevB.79.081406. URL https://link.aps.org/doi/10.1103/PhysRevB.79.081406.

[216] Takashi Oka and Sota Kitamura. Floquet engineering of quantum materials. *Annual Review of Condensed Matter Physics*, 10(1):387–408, March 2019. ISSN 1947-5462. doi: 10.1146/annurev-conmatphys-031218-013423. URL http://dx.doi.org/10.1146/annurev-conmatphys-031218-013423.

[217] N. P. Ong and Sihang Liang. Experimental signatures of the chiral anomaly in dirac–weyl semimetals. *Nature Reviews Physics*, 3(6):394–404, May 2021. ISSN 2522-5820. doi: 10.1038/s42254-021-00310-9. URL http://dx.doi.org/10.1038/s42254-021-00310-9.

[218] Gavin B. Osterhoudt, Laura K. Diebel, Mason J. Gray, Xu Yang, John Stanco, Xiangwei Huang, Bing Shen, Ni Ni, Philip J. W. Moll, Ying Ran, and Kenneth S. Burch. Colossal mid-infrared bulk photovoltaic effect in a type-i weyl semimetal. *Nature Materials*, 18(5):471–475, March 2019. ISSN 1476-4660. doi: 10.1038/s41563-019-0297-4. URL http://dx.doi.org/10.1038/s41563-019-0297-4.

[219] Simo Pajovic, Yoichiro Tsurimaki, Xin Qian, and Gang Chen. Intrinsic nonreciprocal reflection and violation of kirchhoff's law of radiation in planar type-i magnetic weyl semimetal surfaces. *Phys. Rev. B*, 102:165417, Oct 2020. doi: 10.1103/PhysRevB.102.165417. URL https://link.aps.org/doi/10.1103/PhysRevB.102.165417.

[220] Sein Park, Wonjun Lee, Seong Jang, Yong-Bin Choi, Jinho Park, Woochan Jung, Kenji Watanabe, Takashi Taniguchi, Gil Young Cho, and Gil-Ho Lee. Steady floquet–andreev states in graphene josephson junctions. *Nature*, 603 (7901):421–426, March 2022. ISSN 1476-4687. doi: 10.1038/s41586-021-04364-8. URL http://dx.doi.org/10.1038/s41586-021-04364-8.

[221] R. H. Parmenter. The acousto-electric effect. *Phys. Rev.*, 89:990–998, Mar 1953. doi: 10.1103/PhysRev.89.990. URL https://link.aps.org/doi/10.1103/PhysRev.89.990.

[222] Jukka P. Pekola, Olli-Pentti Saira, Ville F. Maisi, Antti Kemppinen, Mikko Möttönen, Yuri A. Pashkin, and Dmitri V. Averin. Single-electron current sources: Toward a refined definition of the ampere. *Rev. Mod. Phys.*, 85: 1421–1472, Oct 2013. doi: 10.1103/RevModPhys.85.1421. URL https://link.aps.org/doi/10.1103/RevModPhys.85.1421.

[223] Pai Peng, Chao Yin, Xiaoyang Huang, Chandrasekhar Ramanathan, and Paola Cappellaro. Floquet prethermalization in dipolar spin chains. *Nature Physics*, 17(4):444–447, January 2021. ISSN 1745-2481. doi: 10.1038/s41567-020-01120-z. URL http://dx.doi.org/10.1038/s41567-020-01120-z.

[224] Yang Peng. Topological space-time crystal. *Phys. Rev. Lett.*, 128:186802, May 2022. doi: 10.1103/PhysRevLett.128.186802. URL https://link.aps.org/doi/10.1103/PhysRevLett.128.186802.

[225] P. M. Perez-Piskunow, Gonzalo Usaj, C. A. Balseiro, and L. E. F. Foa Torres. Floquet chiral edge states in graphene. *Phys. Rev. B*, 89:121401, Mar 2014. doi: 10.1103/PhysRevB.89.121401. URL https://link.aps.org/doi/10.1103/PhysRevB.89.121401.

[226] Robert Pettit, Wenchao Ge, Pardeep Kumar, Danika Luntz-Martin, Justin Schultz, Levi Neukirch, Mishkat Bhattacharya, and A. Vamivakas. An optical tweezer phonon laser. *Nature Photonics*, 13:1, 06 2019. doi: 10.1038/s41566-019-0395-5.

[227] D. I. Pikulin, Anffany Chen, and M. Franz. Chiral anomaly from strain-induced gauge fields in dirac and weyl semimetals. *Phys. Rev. X*, 6:041021, Oct 2016. doi: 10.1103/PhysRevX.6.041021. URL https://link.aps.org/doi/10.1103/PhysRevX.6.041021.

[228] S. Polatkan, M. O. Goerbig, J. Wyzula, R. Kemmler, L. Z. Maulana, B. A. Piot, I. Crassee, A. Akrap, C. Shekhar, C. Felser, M. Dressel, A. V. Pronin, and M. Orlita. Magneto-optics of a weyl semimetal beyond the conical band approximation: Case study of tap. *Phys. Rev. Lett.*, 124:176402, Apr 2020. doi: 10.1103/PhysRevLett.124.176402. URL https://link.aps.org/doi/10.1103/PhysRevLett.124.176402.

[229] Lorenzo Privitera, Angelo Russomanno, Roberta Citro, and Giuseppe E. Santoro. Nonadiabatic breaking of topological pumping. *Phys. Rev. Lett.*, 120: 106601, Mar 2018. doi: 10.1103/PhysRevLett.120.106601. URL https://link.aps.org/doi/10.1103/PhysRevLett.120.106601.

[230] Arpit Raj, Swati Chaudhary, and Gregory A. Fiete. Photogalvanic response in multi-weyl semimetals. *Phys. Rev. Res.*, 6:013048, Jan 2024.

doi: 10.1103/PhysRevResearch.6.013048. URL https://link.aps.org/doi/10.1103/PhysRevResearch.6.013048.

[231] Hemant Kumar Raut, V. Anand Ganesh, A. Sreekumaran Nair, and Seeram Ramakrishna. Anti-reflective coatings: A critical, in-depth review. *Energy & Environmental Science*, 4(10):3779, 2011. ISSN 1754-5706. doi: 10.1039/c1ee01297e. URL http://dx.doi.org/10.1039/C1EE01297E.

[232] Gil Refael. Ph 135 lecture notes. 2018. URL http://gilrefael.org/wp-content/uploads/2018/10/BerryThouless.pdf.

[233] Cécile Repellin and T. Senthil. Chern bands of twisted bilayer graphene: Fractional chern insulators and spin phase transition. *Phys. Rev. Res.*, 2: 023238, May 2020. doi: 10.1103/PhysRevResearch.2.023238. URL https://link.aps.org/doi/10.1103/PhysRevResearch.2.023238.

[234] B. Reulet, A. Yu. Kasumov, M. Kociak, R. Deblock, I. I. Khodos, Yu. B. Gorbatov, V. T. Volkov, C. Journet, and H. Bouchiat. Acoustoelectric effects in carbon nanotubes. *Phys. Rev. Lett.*, 85:2829–2832, Sep 2000. doi: 10.1103/PhysRevLett.85.2829. URL https://link.aps.org/doi/10.1103/PhysRevLett.85.2829.

[235] Martin Rodriguez-Vega, Michael Vogl, and Gregory A. Fiete. Floquet engineering of twisted double bilayer graphene. *Phys. Rev. Res.*, 2:033494, Sep 2020. doi: 10.1103/PhysRevResearch.2.033494. URL https://link.aps.org/doi/10.1103/PhysRevResearch.2.033494.

[236] Martin Rodriguez-Vega, Michael Vogl, and Gregory Fiete. Low-frequency and moiré floquet engineering: A review. *Annals of Physics*, 435:168434, 03 2021. doi: 10.1016/j.aop.2021.168434.

[237] Habib Rostami and Marco Polini. Nonlinear anomalous photocurrents in weyl semimetals. *Phys. Rev. B*, 97:195151, May 2018. doi: 10.1103/PhysRevB.97.195151. URL https://link.aps.org/doi/10.1103/PhysRevB.97.195151.

[238] Antonio Rubio-Abadal, Matteo Ippoliti, Simon Hollerith, David Wei, Jun Rui, S. L. Sondhi, Vedika Khemani, Christian Gross, and Immanuel Bloch. Floquet prethermalization in a bose-hubbard system. *Phys. Rev. X*, 10:021044, May 2020. doi: 10.1103/PhysRevX.10.021044. URL https://link.aps.org/doi/10.1103/PhysRevX.10.021044.

[239] Mark Rudner and Netanel Lindner. Band structure engineering and non-equilibrium dynamics in floquet topological insulators. *Nature Reviews Physics*, 2:1–16, 05 2020. doi: 10.1038/s42254-020-0170-z.

[240] Mark S. Rudner. Driving toward hot new phases. *Nature Physics*, 16(10): 1008–1009, July 2020. ISSN 1745-2481. doi: 10.1038/s41567-020-0963-0. URL http://dx.doi.org/10.1038/s41567-020-0963-0.

[241] Mark S. Rudner and Netanel H. Lindner. The floquet engineer's handbook, 2020. URL https://arxiv.org/abs/2003.08252.

[242] Mark S. Rudner and Justin C. W. Song. Self-induced berry flux and spontaneous non-equilibrium magnetism. *Nature Physics*, 15(10):1017–1021, July 2019. ISSN 1745-2481. doi: 10.1038/s41567-019-0578-5. URL http://dx.doi.org/10.1038/s41567-019-0578-5.

[243] Jonathan Ruhman and Patrick A. Lee. Superconductivity at very low density: The case of strontium titanate. *Phys. Rev. B*, 94:224515, Dec 2016. doi: 10.1103/PhysRevB.94.224515. URL https://link.aps.org/doi/10.1103/PhysRevB.94.224515.

[244] B. Jordan Russell, Boyi Zhou, T. Taniguchi, K. Watanabe, and Erik A. Henriksen. Many-particle effects in the cyclotron resonance of encapsulated monolayer graphene. *Phys. Rev. Lett.*, 120:047401, Jan 2018. doi: 10.1103/PhysRevLett.120.047401. URL https://link.aps.org/doi/10.1103/PhysRevLett.120.047401.

[245] Surajit Saha, Orhan Kahya, Manu Jaiswal, Amar Srivastava, A. Annadi, Jayakumar Balakrishnan, Alexandre Pachoud, Chee-Tat Toh, Byung-Hee Hong, Jong-Hyun Ahn, T. Venkatesan, and Barbaros Ozyilmaz. Unconventional transport through graphene on srtio3: A plausible effect of srtio3 phase-transitions. *Scientific reports*, 4:6173, 08 2014. doi: 10.1038/srep06173.

[246] R. Saito, T. Takeya, T. Kimura, G. Dresselhaus, and M. S. Dresselhaus. Raman intensity of single-wall carbon nanotubes. *Phys. Rev. B*, 57:4145–4153, Feb 1998. doi: 10.1103/PhysRevB.57.4145. URL https://link.aps.org/doi/10.1103/PhysRevB.57.4145.

[247] Riichiro Saito, Mitsutaka Fujita, G. Dresselhaus, and M. S. Dresselhaus. Electronic structure of graphene tubules based on c_{60}. *Phys. Rev. B*, 46:1804–1811, Jul 1992. doi: 10.1103/PhysRevB.46.1804. URL https://link.aps.org/doi/10.1103/PhysRevB.46.1804.

[248] T. Sakudo and H. Unoki. Dielectric properties of $srtio_3$ at low temperatures. *Phys. Rev. Lett.*, 26:851–853, Apr 1971. doi: 10.1103/PhysRevLett.26.851. URL https://link.aps.org/doi/10.1103/PhysRevLett.26.851.

[249] G. D. Sanders, C. J. Stanton, J.-H. Kim, K.-J. Yee, Y.-S. Lim, E. H. Hároz, L. G. Booshehri, J. Kono, and R. Saito. Resonant coherent phonon spectroscopy of single-walled carbon nanotubes. *Phys. Rev. B*, 79:205434, May 2009. doi: 10.1103/PhysRevB.79.205434. URL https://link.aps.org/doi/10.1103/PhysRevB.79.205434.

[250] G D Sanders, A R T Nugraha, K Sato, J-H Kim, J Kono, R Saito, and C J Stanton. Theory of coherent phonons in carbon nanotubes and graphene nanoribbons. *Journal of Physics: Condensed Matter*, 25(14):144201, March

2013. ISSN 1361-648X. doi: 10.1088/0953-8984/25/14/144201. URL http://dx.doi.org/10.1088/0953-8984/25/14/144201.

[251] Giuseppe E Santoro. Introduction to floquet. *Lecture Notes*, 2019.

[252] D. Santos-Cottin, I. Mohelský, J. Wyzula, F. Le Mardelé, I. Kapon, S. Nasrallah, N. Barišić, I. Živković, J. R. Soh, F. Guo, K. Rigaux, M. Puppin, J. H. Dil, B. Gudac, Z. Rukelj, M. Novak, A. B. Kuzmenko, C. C. Homes, Tomasz Dietl, M. Orlita, and Ana Akrap. $eucd_2as_2$: A magnetic semiconductor. *Phys. Rev. Lett.*, 131:186704, Nov 2023. doi: 10.1103/PhysRevLett.131.186704. URL https://link.aps.org/doi/10.1103/PhysRevLett.131.186704.

[253] S. A. Sato, J. W. McIver, M. Nuske, P. Tang, G. Jotzu, B. Schulte, H. Hübener, U. De Giovannini, L. Mathey, M. A. Sentef, A. Cavalleri, and A. Rubio. Microscopic theory for the light-induced anomalous hall effect in graphene. *Phys. Rev. B*, 99:214302, Jun 2019. doi: 10.1103/PhysRevB.99.214302. URL https://link.aps.org/doi/10.1103/PhysRevB.99.214302.

[254] S A Sato, P Tang, M A Sentef, U De Giovannini, H Hübener, and A Rubio. Light-induced anomalous hall effect in massless dirac fermion systems and topological insulators with dissipation. *New Journal of Physics*, 21(9):093005, sep 2019. doi: 10.1088/1367-2630/ab3acf. URL https://dx.doi.org/10.1088/1367-2630/ab3acf.

[255] Stella T. Schindler and Hanan Herzig Sheinfux. Floquet engineering with spatially non-uniform driving fields. 2023. doi: 10.48550/ARXIV.2311.00845. URL https://arxiv.org/abs/2311.00845.

[256] Karthik Seetharam, Paraj Titum, Michael Kolodrubetz, and Gil Refael. Absence of thermalization in finite isolated interacting floquet systems. *Phys. Rev. B*, 97:014311, Jan 2018. doi: 10.1103/PhysRevB.97.014311. URL https://link.aps.org/doi/10.1103/PhysRevB.97.014311.

[257] Karthik I. Seetharam, Charles-Edouard Bardyn, Netanel H. Lindner, Mark S. Rudner, and Gil Refael. Controlled population of floquet-bloch states via coupling to bose and fermi baths. *Phys. Rev. X*, 5:041050, Dec 2015. doi: 10.1103/PhysRevX.5.041050. URL https://link.aps.org/doi/10.1103/PhysRevX.5.041050.

[258] Karthik I. Seetharam, Charles-Edouard Bardyn, Netanel H. Lindner, Mark S. Rudner, and Gil Refael. Steady states of interacting floquet insulators. *Phys. Rev. B*, 99:014307, Jan 2019. doi: 10.1103/PhysRevB.99.014307. URL https://link.aps.org/doi/10.1103/PhysRevB.99.014307.

[259] Karthik Iyengar Seetharam. *Thermalization in Periodically-Driven Interacting Quantum Systems*. PhD thesis, California Institute of Technology, Pasadena, 5 2018.

[260] Junyi Shan, M. Ye, H. Chu, Sungmin Lee, Je-Geun Park, L. Balents, and D. Hsieh. Giant modulation of optical nonlinearity by floquet engineering. *Nature*, 600:235–239, 12 2021. doi: 10.1038/s41586-021-04051-8.

[261] Girish Sharma, Indra Yudhistira, Nilotpal Chakraborty, Derek Ho, Mohammed Al Ezzi, Michael Fuhrer, Giovanni Vignale, and Shaffique Adam. Carrier transport theory for twisted bilayer graphene in the metallic regime. *Nature Communications*, 12, 09 2021. doi: 10.1038/s41467-021-25864-1.

[262] Chang Shu, Kai Zhang, and Kai Sun. Loss-induced universal one-way transport in periodically driven systems, 2023. URL https://arxiv.org/abs/2306.10000.

[263] Edbert J. Sie, James W. McIver, Yi-Hsien Lee, Liang Fu, Jing Kong, and Nuh Gedik. Valley-selective optical stark effect in monolayer ws2. *Nature Materials*, 14(3):290–294, December 2014. ISSN 1476-4660. doi: 10.1038/nmat4156. URL http://dx.doi.org/10.1038/nmat4156.

[264] Inti Sodemann and Liang Fu. Quantum nonlinear hall effect induced by berry curvature dipole in time-reversal invariant materials. *Phys. Rev. Lett.*, 115:216806, Nov 2015. doi: 10.1103/PhysRevLett.115.216806. URL https://link.aps.org/doi/10.1103/PhysRevLett.115.216806.

[265] J.-R. Soh, F. de Juan, M. G. Vergniory, N. B. M. Schröter, M. C. Rahn, D. Y. Yan, J. Jiang, M. Bristow, P. Reiss, J. N. Blandy, Y. F. Guo, Y. G. Shi, T. K. Kim, A. McCollam, S. H. Simon, Y. Chen, A. I. Coldea, and A. T. Boothroyd. Ideal weyl semimetal induced by magnetic exchange. *Phys. Rev. B*, 100:201102, Nov 2019. doi: 10.1103/PhysRevB.100.201102. URL https://link.aps.org/doi/10.1103/PhysRevB.100.201102.

[266] R. Somphonsane, H. Ramamoorthy, G. He, J. Nathawat, C.-P. Kwan, N. Arabchigavkani, Y.-H. Lee, J. Fransson, and J. P. Bird. Evaluating the sources of graphene's resistivity using differential conductance. *Scientific Reports*, 7(1), September 2017. ISSN 2045-2322. doi: 10.1038/s41598-017-10367-1. URL http://dx.doi.org/10.1038/s41598-017-10367-1.

[267] D. T. Son and B. Z. Spivak. Chiral anomaly and classical negative magnetoresistance of weyl metals. *Phys. Rev. B*, 88:104412, Sep 2013. doi: 10.1103/PhysRevB.88.104412. URL https://link.aps.org/doi/10.1103/PhysRevB.88.104412.

[268] Dam Thanh Son and Naoki Yamamoto. Berry curvature, triangle anomalies, and the chiral magnetic effect in fermi liquids. *Phys. Rev. Lett.*, 109:181602, Nov 2012. doi: 10.1103/PhysRevLett.109.181602. URL https://link.aps.org/doi/10.1103/PhysRevLett.109.181602.

[269] Justin C. W. Song and Mark S. Rudner. Fermi arc plasmons in weyl semimetals. *Phys. Rev. B*, 96:205443, Nov 2017. doi: 10.1103/PhysRevB.96.205443. URL https://link.aps.org/doi/10.1103/PhysRevB.96.205443.

[270] Zhi-Da Song, Biao Lian, Nicolas Regnault, and B. Andrei Bernevig. Twisted bilayer graphene. ii. stable symmetry anomaly. *Phys. Rev. B*, 103:205412, May 2021. doi: 10.1103/PhysRevB.103.205412. URL https://link.aps.org/doi/10.1103/PhysRevB.103.205412.

[271] Zhida Song, Zhijun Wang, Wujun Shi, Gang Li, Chen Fang, and B. Andrei Bernevig. All magic angles in twisted bilayer graphene are topological. *Phys. Rev. Lett.*, 123:036401, Jul 2019. doi: 10.1103/PhysRevLett.123.036401. URL https://link.aps.org/doi/10.1103/PhysRevLett.123.036401.

[272] Marcus Stålhammar, Jorge Larana-Aragon, Johannes Knolle, and Emil J. Bergholtz. Magneto-optical conductivity in generic weyl semimetals. *Phys. Rev. B*, 102:235134, Dec 2020. doi: 10.1103/PhysRevB.102.235134. URL https://link.aps.org/doi/10.1103/PhysRevB.102.235134.

[273] Friederike Stein, Dietmar Drung, Lukas Fricke, Hansjörg Scherer, Frank Hohls, Christoph Leicht, Martin Götz, Christian Krause, Ralf Behr, Eckart Pesel, Klaus Pierz, Uwe Siegner, Franz J. Ahlers, and Hans W. Schumacher. Validation of a quantized-current source with 0.2ppm uncertainty. *Applied Physics Letters*, 107(10), September 2015. ISSN 1077-3118. doi: 10.1063/1.4930142. URL http://dx.doi.org/10.1063/1.4930142.

[274] T. E. Stevens, J. Kuhl, and R. Merlin. Coherent phonon generation and the two stimulated raman tensors. *Phys. Rev. B*, 65:144304, Mar 2002. doi: 10.1103/PhysRevB.65.144304. URL https://link.aps.org/doi/10.1103/PhysRevB.65.144304.

[275] Alaska Subedi, Andrea Cavalleri, and Antoine Georges. Theory of nonlinear phononics for coherent light control of solids. *Phys. Rev. B*, 89:220301(R), Jun 2014. doi: 10.1103/PhysRevB.89.220301. URL https://link.aps.org/doi/10.1103/PhysRevB.89.220301.

[276] Peter Swekis, Aleksandr S. Sukhanov, Yi-Cheng Chen, Andrei Gloskovskii, Gerhard H. Fecher, Ioannis Panagiotopoulos, Jörg Sichelschmidt, Victor Ukleev, Anton Devishvili, Alexei Vorobiev, Dmytro S. Inosov, Sebastian T. B. Goennenwein, Claudia Felser, and Anastasios Markou. Magnetic and electronic properties of weyl semimetal co2mnga thin films. *Nanomaterials*, 11 (1):251, January 2021. ISSN 2079-4991. doi: 10.3390/nano11010251. URL http://dx.doi.org/10.3390/nano11010251.

[277] Katsuhisa Taguchi, Tatsushi Imaeda, Masatoshi Sato, and Yukio Tanaka. Photovoltaic chiral magnetic effect in weyl semimetals. *Phys. Rev. B*, 93: 201202, May 2016. doi: 10.1103/PhysRevB.93.201202. URL https://link.aps.org/doi/10.1103/PhysRevB.93.201202.

[278] V. I. Talyanskii, D. S. Novikov, B. D. Simons, and L. S. Levitov. Quantized adiabatic charge transport in a carbon nanotube. *Phys. Rev. Lett.*, 87:276802,

Dec 2001. doi: 10.1103/PhysRevLett.87.276802. URL https://link.aps.org/doi/10.1103/PhysRevLett.87.276802.

[279] D. J. Thouless. Quantization of particle transport. *Phys. Rev. B*, 27:6083–6087, May 1983. doi: 10.1103/PhysRevB.27.6083. URL https://link.aps.org/doi/10.1103/PhysRevB.27.6083.

[280] Andrea Tomadin, Sebastian Diehl, and Peter Zoller. Nonequilibrium phase diagram of a driven and dissipative many-body system. *Phys. Rev. A*, 83: 013611, Jan 2011. doi: 10.1103/PhysRevA.83.013611. URL https://link.aps.org/doi/10.1103/PhysRevA.83.013611.

[281] Gabriel E. Topp, Gregor Jotzu, James W. McIver, Lede Xian, Angel Rubio, and Michael A. Sentef. Topological floquet engineering of twisted bilayer graphene. *Phys. Rev. Res.*, 1:023031, Sep 2019. doi: 10.1103/PhysRevResearch.1.023031. URL https://link.aps.org/doi/10.1103/PhysRevResearch.1.023031.

[282] Chiara Trovatello, Henrique P. C. Miranda, Alejandro Molina-Sánchez, Rocío Borrego-Varillas, Cristian Manzoni, Luca Moretti, Lucia Ganzer, Margherita Maiuri, Junjia Wang, Dumitru Dumcenco, Andras Kis, Ludger Wirtz, Andrea Marini, Giancarlo Soavi, Andrea C. Ferrari, Giulio Cerullo, Davide Sangalli, and Stefano Dal Conte. Strongly coupled coherent phonons in single-layer MoSsub2/sub. *ACS Nano*, 14(5):5700–5710, April 2020. doi: 10.1021/acsnano.0c00309. URL https://doi.org/10.1021/acsnano.0c00309.

[283] Yoichiro Tsurimaki, Xin Qian, Simo Pajovic, Fei Han, Mingda Li, and Gang Chen. Large nonreciprocal absorption and emission of radiation in type-i weyl semimetals with time reversal symmetry breaking. *Phys. Rev. B*, 101: 165426, Apr 2020. doi: 10.1103/PhysRevB.101.165426. URL https://link.aps.org/doi/10.1103/PhysRevB.101.165426.

[284] Gonzalo Usaj, P. M. Perez-Piskunow, L. E. F. Foa Torres, and C. A. Balseiro. Irradiated graphene as a tunable floquet topological insulator. *Phys. Rev. B*, 90:115423, Sep 2014. doi: 10.1103/PhysRevB.90.115423. URL https://link.aps.org/doi/10.1103/PhysRevB.90.115423.

[285] Oskar Vafek and Ashvin Vishwanath. Dirac fermions in solids: From high-tc cuprates and graphene to topological insulators and weyl semimetals. *Annual Review of Condensed Matter Physics*, 5(1):83–112, March 2014. ISSN 1947-5462. doi: 10.1146/annurev-conmatphys-031113-133841. URL http://dx.doi.org/10.1146/annurev-conmatphys-031113-133841.

[286] K. Vahala, M. Herrmann, S. Knünz, V. Batteiger, G. Saathoff, T. W. Hänsch, and Th. Udem. A phonon laser. *Nature Physics*, 5(9):682–686, August 2009. ISSN 1745-2481. doi: 10.1038/nphys1367. URL http://dx.doi.org/10.1038/nphys1367.

[287] David Vanderbilt. *Berry Phases in Electronic Structure Theory*, page 75–140. Cambridge University Press. doi: 10.1017/9781316662205.005. URL http://dx.doi.org/10.1017/9781316662205.005.

[288] M. M. Vazifeh and M. Franz. Electromagnetic response of weyl semimetals. *Phys. Rev. Lett.*, 111:027201, Jul 2013. doi: 10.1103/PhysRevLett.111.027201. URL https://link.aps.org/doi/10.1103/PhysRevLett.111.027201.

[289] Louis Veyrat, Déprez Corentin, Alexis Coissard, Xiaoxi Li, Frédéric Gay, Kenji Watanabe, Takashi Taniguchi, Zheng Han, B. Piot, Hermann Sellier, and Benjamin Sacépé. Helical quantum hall phase in graphene on srtio3. *Science*, 367:781–786, 02 2020. doi: 10.1126/science.aax8201.

[290] Konrad Viebahn. Introduction to floquet theory. *Institute for Quantum Electronics, ETH Zurich*, 8093, 2020.

[291] Michael Vogl, Martin Rodriguez-Vega, and Gregory A. Fiete. Effective floquet hamiltonians for periodically driven twisted bilayer graphene. *Phys. Rev. B*, 101:235411, Jun 2020. doi: 10.1103/PhysRevB.101.235411. URL https://link.aps.org/doi/10.1103/PhysRevB.101.235411.

[292] Michael Vogl, Martin Rodriguez-Vega, and Gregory A. Fiete. Floquet engineering of interlayer couplings: Tuning the magic angle of twisted bilayer graphene at the exit of a waveguide. *Phys. Rev. B*, 101:241408(R), Jun 2020. doi: 10.1103/PhysRevB.101.241408. URL https://link.aps.org/doi/10.1103/PhysRevB.101.241408.

[293] Michael Vogl, Martin Rodriguez-Vega, Benedetta Flebus, Allan H. MacDonald, and Gregory A. Fiete. Floquet engineering of topological transitions in a twisted transition metal dichalcogenide homobilayer. *Phys. Rev. B*, 103:014310, Jan 2021. doi: 10.1103/PhysRevB.103.014310. URL https://link.aps.org/doi/10.1103/PhysRevB.103.014310.

[294] Michael Vogl, Swati Chaudhary, and Gregory A Fiete. Light driven magnetic transitions in transition metal dichalcogenide heterobilayers. *Journal of Physics: Condensed Matter*, 35(9):095801, dec 2022. doi: 10.1088/1361-648X/acab49. URL https://dx.doi.org/10.1088/1361-648X/acab49.

[295] H. Vogt and G. Rossbroich. Accurate determination of the far-infrared dispersion in $srtio_3$ by hyper-raman spectroscopy. *Phys. Rev. B*, 24:3086–3091, Sep 1981. doi: 10.1103/PhysRevB.24.3086. URL https://link.aps.org/doi/10.1103/PhysRevB.24.3086.

[296] Felix von Oppen, Francisco Guinea, and Eros Mariani. Synthetic electric fields and phonon damping in carbon nanotubes and graphene. *Phys. Rev. B*, 80:075420, Aug 2009. doi: 10.1103/PhysRevB.80.075420. URL https://link.aps.org/doi/10.1103/PhysRevB.80.075420.

[297] S. Wallentowitz, W. Vogel, I. Siemers, and P. E. Toschek. Vibrational amplification by stimulated emission of radiation. *Phys. Rev. A*, 54:943–946, Jul 1996. doi: 10.1103/PhysRevA.54.943. URL https://link.aps.org/doi/10.1103/PhysRevA.54.943.

[298] Anne-Sophie Walter, Zijie Zhu, Marius Gächter, Joaquín Minguzzi, Stephan Roschinski, Kilian Sandholzer, Konrad Viebahn, and Tilman Esslinger. Quantization and its breakdown in a hubbard–thouless pump. *Nature Physics*, 19 (10):1471–1475, July 2023. ISSN 1745-2481. doi: 10.1038/s41567-023-02145-w. URL http://dx.doi.org/10.1038/s41567-023-02145-w.

[299] Jin-Feng Wang, Qing-Xin Dong, Zhao-Peng Guo, Meng Lv, Yi-Fei Huang, Jun-Sen Xiang, Zhi-An Ren, Zhi-Jun Wang, Pei-Jie Sun, Gang Li, and Gen-Fu Chen. Ndalsi: A magnetic weyl semimetal candidate with rich magnetic phases and atypical transport properties. *Phys. Rev. B*, 105:144435, Apr 2022. doi: 10.1103/PhysRevB.105.144435. URL https://link.aps.org/doi/10.1103/PhysRevB.105.144435.

[300] Shuo Wang, Ben-Chuan Lin, An-Qi Wang, Da-Peng Yu, and Zhi-Min Liao. Quantum transport in dirac and weyl semimetals: a review. *Advances in Physics: X*, 2(3):518–544, May 2017. ISSN 2374-6149. doi: 10.1080/23746149.2017.1327329. URL http://dx.doi.org/10.1080/23746149.2017.1327329.

[301] Y. H. Wang, H. Steinberg, P. Jarillo-Herrero, and N. Gedik. Observation of floquet-bloch states on the surface of a topological insulator. *Science*, 342 (6157):453–457, October 2013. ISSN 1095-9203. doi: 10.1126/science.1239834. URL http://dx.doi.org/10.1126/science.1239834.

[302] Gabriel Weinreich and Harry G. White. Observation of the acoustoelectric effect. *Phys. Rev.*, 106:1104–1106, Jun 1957. doi: 10.1103/PhysRev.106.1104. URL https://link.aps.org/doi/10.1103/PhysRev.106.1104.

[303] Achim Woessner, Mark B. Lundeberg, Yuanda Gao, Alessandro Principi, Pablo Alonso-González, Matteo Carrega, Kenji Watanabe, Takashi Taniguchi, Giovanni Vignale, Marco Polini, James Hone, Rainer Hillenbrand, and Frank H. L. Koppens. Highly confined low-loss plasmons in graphene–boron nitride heterostructures. *Nature Materials*, 14(4):421–425, December 2014. ISSN 1476-4660. doi: 10.1038/nmat4169. URL http://dx.doi.org/10.1038/nmat4169.

[304] E Laine Wong, Andrew J. Winchester, Vivek Pareek, Julien Madéo, Michael K. L. Man, and Keshav M. Dani. Pulling apart photoexcited electrons by photoinducing an in-plane surface electric field. *Science Advances*, 4 (9):eaat9722, 2018. doi: 10.1126/sciadv.aat9722. URL https://www.science.org/doi/abs/10.1126/sciadv.aat9722.

[305] Liang Wu, S. Patankar, T. Morimoto, N. L. Nair, E. Thewalt, A. Little, J. G. Analytis, J. E. Moore, and J. Orenstein. Giant anisotropic nonlinear optical response in transition metal monopnictide weyl semimetals. *Nature Physics*, 13(4):350–355, December 2016. ISSN 1745-2481. doi: 10.1038/nphys3969. URL http://dx.doi.org/10.1038/nphys3969.

[306] Xiaosong Wu, Xuebin Li, Zhimin Song, Claire Berger, and Walt A. de Heer. Weak antilocalization in epitaxial graphene: Evidence for chiral electrons. *Phys. Rev. Lett.*, 98:136801, Mar 2007. doi: 10.1103/PhysRevLett.98.136801. URL https://link.aps.org/doi/10.1103/PhysRevLett.98.136801.

[307] Di Xiao, Ming-Che Chang, and Qian Niu. Berry phase effects on electronic properties. *Rev. Mod. Phys.*, 82:1959–2007, Jul 2010. doi: 10.1103/RevModPhys.82.1959. URL https://link.aps.org/doi/10.1103/RevModPhys.82.1959.

[308] Yonglong Xie, Andrew Pierce, Jeong Park, Daniel Parker, Eslam Khalaf, Patrick Ledwith, Yuan Cao, Seung Lee, Shaowen Chen, Patrick Forrester, Kenji Watanabe, Takashi Taniguchi, Ashvin Vishwanath, Pablo Jarillo-Herrero, and Amir Yacoby. Fractional chern insulators in magic-angle twisted bilayer graphene. *Nature*, 600:439–443, 12 2021. doi: 10.1038/s41586-021-04002-3.

[309] Jun Xiong, Satya K. Kushwaha, Tian Liang, Jason W. Krizan, Max Hirschberger, Wudi Wang, R. J. Cava, and N. P. Ong. Evidence for the chiral anomaly in the dirac semimetal na 3 bi. *Science*, 350(6259):413–416, October 2015. ISSN 1095-9203. doi: 10.1126/science.aac6089. URL http://dx.doi.org/10.1126/science.aac6089.

[310] Su-Yang Xu, Ilya Belopolski, Nasser Alidoust, Madhab Neupane, Guang Bian, Chenglong Zhang, Raman Sankar, Guoqing Chang, Zhujun Yuan, Chi-Cheng Lee, Shin-Ming Huang, Hao Zheng, Jie Ma, Daniel S. Sanchez, BaoKai Wang, Arun Bansil, Fangcheng Chou, Pavel P. Shibayev, Hsin Lin, Shuang Jia, and M. Zahid Hasan. Discovery of a weyl fermion semimetal and topological fermi arcs. *Science*, 349(6248):613–617, August 2015. ISSN 1095-9203. doi: 10.1126/science.aaa9297. URL http://dx.doi.org/10.1126/science.aaa9297.

[311] Chiyu Yang, Bo Zhao, Wenshan Cai, and Zhuomin M. Zhang. Mid-infrared broadband circular polarizer based on weyl semimetals. *Optics Express*, 30(2):3035, January 2022. ISSN 1094-4087. doi: 10.1364/oe.445803. URL http://dx.doi.org/10.1364/OE.445803.

[312] Christopher Yang, Iliya Esin, Cyprian Lewandowski, and Gil Refael. Optical control of slow topological electrons in moiré systems. *Phys. Rev. Lett.*, 131:026901, Jul 2023. doi: 10.1103/PhysRevLett.131.026901. URL https://link.aps.org/doi/10.1103/PhysRevLett.131.026901.

[313] Yanfei Yang, Lung-I. Huang, Yasuhiro Fukuyama, Fan-Hung Liu, Mariano A. Real, Paola Barbara, Chi-Te Liang, David B. Newell, and Randolph E. Elmquist. Low carrier density epitaxial graphene devices on sic. *Small*, 11 (1):90–95, August 2014. ISSN 1613-6829. doi: 10.1002/smll.201400989. URL http://dx.doi.org/10.1002/smll.201400989.

[314] Yoseob Yoon, Zheyu Lu, Can Uzundal, Ruishi Qi, Wenyu Zhao, Sudi Chen, Qixin Feng, Kenji Watanabe, Takashi Taniguchi, Michael F. Crommie, and Feng Wang. Terahertz phonon engineering and spectroscopy with van der waals heterostructures, 2023. URL https://arxiv.org/abs/2310.04939.

[315] Yoseob Yoon, Zheyu Lu, Can Uzundal, Ruishi Qi, Wenyu Zhao, Sudi Chen, Qixin Feng, Kenji Watanabe, Takashi Taniguchi, Michael F. Crommie, and Feng Wang. Terahertz phonon engineering and spectroscopy with van der waals heterostructures, 2023. URL https://arxiv.org/abs/2310.04939.

[316] Oubo You, Shanjun Liang, Biye Xie, Wenlong Gao, Weimin Ye, Jie Zhu, and Shuang Zhang. Observation of non-abelian thouless pump. *Phys. Rev. Lett.*, 128:244302, Jun 2022. doi: 10.1103/PhysRevLett.128.244302. URL https://link.aps.org/doi/10.1103/PhysRevLett.128.244302.

[317] H. J. Zeiger, J. Vidal, T. K. Cheng, E. P. Ippen, G. Dresselhaus, and M. S. Dresselhaus. Theory for displacive excitation of coherent phonons. *Phys. Rev. B*, 45:768–778, Jan 1992. doi: 10.1103/PhysRevB.45.768. URL https://link.aps.org/doi/10.1103/PhysRevB.45.768.

[318] Cheng-Long Zhang, Su-Yang Xu, Ilya Belopolski, Zhujun Yuan, Ziquan Lin, Bingbing Tong, Guang Bian, Nasser Alidoust, Chi-Cheng Lee, Shin-Ming Huang, Tay-Rong Chang, Guoqing Chang, Chuang-Han Hsu, Horng-Tay Jeng, Madhab Neupane, Daniel S. Sanchez, Hao Zheng, Junfeng Wang, Hsin Lin, Chi Zhang, Hai-Zhou Lu, Shun-Qing Shen, Titus Neupert, M. Zahid Hasan, and Shuang Jia. Signatures of the adler–bell–jackiw chiral anomaly in a weyl fermion semimetal. *Nature Communications*, 7(1), February 2016. ISSN 2041-1723. doi: 10.1038/ncomms10735. URL http://dx.doi.org/10.1038/ncomms10735.

[319] Cheng-Long Zhang, Su-Yang Xu, C. M. Wang, Ziquan Lin, Z. Z. Du, Cheng Guo, Chi-Cheng Lee, Hong Lu, Yiyang Feng, Shin-Ming Huang, Guoqing Chang, Chuang-Han Hsu, Haiwen Liu, Hsin Lin, Liang Li, Chi Zhang, Jinglei Zhang, Xin-Cheng Xie, Titus Neupert, M. Zahid Hasan, Hai-Zhou Lu, Junfeng Wang, and Shuang Jia. Magnetic-tunnelling-induced weyl node annihilation in tap. *Nature Physics*, 13(10):979–986, July 2017. ISSN 1745-2481. doi: 10.1038/nphys4183. URL http://dx.doi.org/10.1038/nphys4183.

[320] Cheng-Long Zhang, Zhujun Yuan, Qing-Dong Jiang, Bingbing Tong, Chi Zhang, X. C. Xie, and Shuang Jia. Electron scattering in tantalum monoarsenide. *Phys. Rev. B*, 95:085202, Feb 2017. doi: 10.1103/PhysRevB.95.085202. URL https://link.aps.org/doi/10.1103/PhysRevB.95.085202.

[321] Chenglong Zhang, Cheng Guo, Hong Lu, Xiao Zhang, Zhujun Yuan, Ziquan Lin, Junfeng Wang, and Shuang Jia. Large magnetoresistance over an extended temperature regime in monophosphides of tantalum and niobium. *Phys. Rev. B*, 92:041203, Jul 2015. doi: 10.1103/PhysRevB.92.041203. URL https://link.aps.org/doi/10.1103/PhysRevB.92.041203.

[322] Furu Zhang, Yang Gao, and Wei Zhang. Three-dimensional topological plasmons in weyl semimetals. *Phys. Rev. B*, 104:205141, Nov 2021. doi: 10.1103/PhysRevB.104.205141. URL https://link.aps.org/doi/10.1103/PhysRevB.104.205141.

[323] Yang Zhang, Hiroaki Ishizuka, Jeroen van den Brink, Claudia Felser, Binghai Yan, and Naoto Nagaosa. Photogalvanic effect in weyl semimetals from first principles. *Phys. Rev. B*, 97:241118, Jun 2018. doi: 10.1103/PhysRevB.97.241118. URL https://link.aps.org/doi/10.1103/PhysRevB.97.241118.

[324] Yinying Zhang and Ctirad Uher. Magnetic and transport properties of fe-doped weyl semimetal co3sn2s2. *Journal of Alloys and Compounds*, 911:165089, August 2022. ISSN 0925-8388. doi: 10.1016/j.jallcom.2022.165089. URL http://dx.doi.org/10.1016/j.jallcom.2022.165089.

[325] Hongbo Zhao and Sumit Mazumdar. Electron-electron interaction effects on the optical excitations of semiconducting single-walled carbon nanotubes. *Phys. Rev. Lett.*, 93:157402, Oct 2004. doi: 10.1103/PhysRevLett.93.157402. URL https://link.aps.org/doi/10.1103/PhysRevLett.93.157402.

[326] R. Zhao, A. Rossi, S. P. Giblin, J. D. Fletcher, F. E. Hudson, M. Möttönen, M. Kataoka, and A. S. Dzurak. Thermal-error regime in high-accuracy gigahertz single-electron pumping. *Phys. Rev. Appl.*, 8:044021, Oct 2017. doi: 10.1103/PhysRevApplied.8.044021. URL https://link.aps.org/doi/10.1103/PhysRevApplied.8.044021.

[327] X. F. Zhao, J. Zhang, S. M. Chen, and W. Xu. Cerenkov acoustic-phonon emission generated electrically from a polar semiconductor. *Journal of Applied Physics*, 105(10), May 2009. ISSN 1089-7550. doi: 10.1063/1.3130400. URL http://dx.doi.org/10.1063/1.3130400.

[328] Hao Zheng, Guoqing Chang, Shin-Ming Huang, Cheng Guo, Xiao Zhang, Songtian Zhang, Jiaxin Yin, Su-Yang Xu, Ilya Belopolski, Nasser Alidoust,

Daniel S. Sanchez, Guang Bian, Tay-Rong Chang, Titus Neupert, Horng-Tay Jeng, Shuang Jia, Hsin Lin, and M. Zahid Hasan. Mirror protected dirac fermions on a weyl semimetal nbp surface. *Phys. Rev. Lett.*, 119: 196403, Nov 2017. doi: 10.1103/PhysRevLett.119.196403. URL https://link.aps.org/doi/10.1103/PhysRevLett.119.196403.

[329] Shaohua Zhou, Changhua Bao, Benshu Fan, Hui Zhou, Qixuan Gao, Haoyuan Zhong, Tianyun Lin, Hang Liu, Pu Yu, Peizhe Tang, Sheng Meng, Wenhui Duan, and Shuyun Zhou. Pseudospin-selective floquet band engineering in black phosphorus. *Nature*, 614(7946):75–80, February 2023. ISSN 1476-4687. doi: 10.1038/s41586-022-05610-3. URL http://dx.doi.org/10.1038/s41586-022-05610-3.

[330] Barton Zwiebach. Quantum physics iii chapter 6: Adiabatic approximation. *MIT OpenCourseWare*, 2018. URL https://ocw.mit.edu/courses/8-06-quantum-physics-iii-spring-2018/resources/mit8_06s18ch6/.